HAL
open science

Variational Multi-Scale stabilized finite elements for the magnetohydrodynamic models of fusion plasmas

José Tarcisio Costa

To cite this version:

José Tarcisio Costa. Variational Multi-Scale stabilized finite elements for the magnetohydrodynamic models of fusion plasmas. Other. COMUE Université Côte d'Azur (2015 - 2019), 2016. English. NNT : 2016AZUR4117 . tel-01419260v2

HAL Id: tel-01419260

https://inria.hal.science/tel-01419260v2

Submitted on 13 Mar 2017

HAL is a multi-disciplinary open access archive for the deposit and dissemination of scientific research documents, whether they are published or not. The documents may come from teaching and research institutions in France or abroad, or from public or private research centers.

L'archive ouverte pluridisciplinaire **HAL**, est destinée au dépôt et à la diffusion de documents scientifiques de niveau recherche, publiés ou non, émanant des établissements d'enseignement et de recherche français ou étrangers, des laboratoires publics ou privés.

École Doctorale de Sciences Fondamentales et Appliquées
Unité de recherche : Sciences

Thèse de doctorat

presentée en vue de l'obtention du
grade de docteur en Mathématiques
de
UNIVERSITÉ NICE SOPHIA ANTIPOLIS

par

José COSTA

Éléments finis stabilisés VMS appliqués aux modèles magnétohydrodynamiques (MHD) des plasmas de fusion

Variational Multi-Scale stabilized Finite Elements for the magnetohydrodynamic models of fusion plasmas

Dirigée par **Boniface Nkonga**

Soutenue le 08 décembre 2016

Devant le jury composé de :

M. Boniface NKONGA	Prof. Université Nice Sophia Antipolis	Dir. de Thèse
M. Bruno DUBROCA	Expert Sénior CEA/DAM Bordeaux	Rapporteur
M. Eric SERRE	Dir. de Recherche CNRS Marseille	Rapporteur
M. Guido HUIJSMANS	Chercheur Com. Européenne/CEA Cadarache	Examinateur
M. Hervé GUILLARD	Dir. de Recherche INRIA Sophia Antipolis	Examinateur

To all those who supported me in this rocky road, and to my mother for always being a light in the dark

"Science never solves a problem without creating ten more"

George Bernard Shaw

"Lasciate ogni speranza, voi ch'entrate"

Dante Alighieri

Acknowledgements

First and foremost, I would like to show my gratitude to Boniface Nkonga. Primarily for giving me the opportunity of working on this subject and then for sharing very patiently his knowledge and passion for the numerical methods. I am sure it has been very challenging for him to make me familiar with this domain. I would also like to thank the members of CASTOR team for the discussions and the experience shared.

Then, I would like to thank Bruno Dubroca and Eric Serre for the precious comments and corrections given to improve this manuscript. Also, Guido Huijsmans and Hervé Guillard for accepting being part of the jury and contributing with my work.

Personally, my heartfelt thanks go to Arturo who supported me more than anyone else during this road that has not always been easy. His encouragements and patience are what made me keep going even when things seemed completely lost. I'm not sure I would have gone through it without his company. I would also like to send my thanks to my friends and family in Brazil who supported me in different ways.

Last but not least, I would like to thank Montserrat Argente from Inria for all the help given, not only on all the bureaucracy issues but also in relieving the stress with the hiking and cultural events to which she never failed to invite me. Also, Elise Estibals for these years of sharing an office and the infinite number of conversations. Finally, to the members of the neighbor ACUMES team for the pieces of advice and insights given during the coffee breaks.

This thesis is dedicated to my mother who, unfortunately, is not present in this special moment of my life. I have no doubts, though, that she would be very proud and would be by my side as she always had been during her time in this world. Her spiritual presence has been like a lighthouse during this adventure.

Contents

Introduction **1**

Introduction (FR) **7**

Résumé **11**

1 Nuclear Fusion and Tokamaks **17**
1.1 Fusion reactions . . . 18
1.2 Magnetic confinement . . . 20
1.3 Tokamaks . . . 22
1.3.1 Characteristics of Tokamaks . . . 23
1.3.1.1 Magnetic configuration . . . 24
1.3.2 Configurations . . . 25
1.3.2.1 Limiter Configuration . . . 26
1.3.2.2 Divertor Configuration . . . 26
1.3.2.3 H-Mode . . . 27
1.3.3 Instabilities . . . 28
1.4 Perspectives: ITER and the future of fusion . . . 30
1.5 Conclusions . . . 32

2 Plasma modeling: Magnetohydrodynamic (MHD) models **33**
2.1 Fundamental plasma models . . . 34
2.1.1 Kinetic model . . . 35
2.1.2 Fluid model: multifluid MHD . . . 37
2.1.3 Maxwell's Equations . . . 41
2.1.4 Bifluid model . . . 42
2.1.5 Magnetic monopoles . . . 42
2.1.5.1 Vector Potential Formulation . . . 43
2.2 Simplified MHD models . . . 45
2.2.1 Full MHD model . . . 45
2.2.1.1 Reformulation of the bi-fluid model . . . 45
2.2.1.2 Quasineutral regime . . . 48
2.2.1.3 Ohm's law in the quasi-neutral regime . . . 50
2.2.1.4 Full MHD in the quasi-neutral regime . . . 50
2.2.2 Ideal MHD . . . 51
2.2.2.1 Ideal MHD under conservative form . . . 52

2.2.2.2 Spectral properties analysis . . . 54
2.2.3 Resistive MHD . . . 56
2.2.4 Reduced MHD models . . . 56
2.2.4.1 Grad-Shafranov (GS) equilibrium . . . 57
2.2.4.2 Reduced Resistive MHD system . . . 59
2.3 Conclusions . . . 64

3 Numerical method: Variational Multi-Scale (VMS) stabilization 67
3.1 Finite element method: model problem . . . 68
3.1.1 Galerkin Method . . . 69
3.1.2 The need of stabilization . . . 70
3.2 VMS-Stabilization and numerical strategy for MHD models . . . 72
3.2.1 Residual-Based Weak form . . . 72
3.2.2 Evaluation of the fine scales . . . 73
3.2.2.1 Stabilization matrix . . . 74
3.2.3 MHD application . . . 77
3.2.4 Numerical strategy . . . 77
3.2.4.1 Vector potential formulation . . . 78
3.2.4.2 Set of interpolated variables . . . 78
3.2.4.3 Stabilized weak formulation . . . 80
3.2.4.4 Finite element approximated space . . . 81
3.2.4.5 Semi-discrete system . . . 84
3.2.4.6 Time stepping . . . 86
3.2.4.7 Discretization in the poloidal plane . . . 88
3.2.4.8 Assembling the system . . . 93
3.3 Conclusions . . . 100

4 Tokamak Equilibrium 103
4.1 Grad Shafranov Equilibrium . . . 104
4.1.1 Input profiles of p and F . . . 104
4.1.2 Solving the GS equation . . . 105
4.1.3 Building the Grid . . . 106
4.1.3.1 Grid discontinuities . . . 110
4.1.4 Establishing the equilibrium . . . 111
4.2 Initializing the simulations . . . 119
4.3 Conclusions . . . 122

5 MHD instabilities: Internal Kink 125
5.1 MHD instabilities: background . . . 126
5.1.0.1 Stability Criterion . . . 126
5.1.0.2 Energy Principle . . . 128
5.2 Resistive Internal Kink Mode . . . 130
5.2.1 Growth Rate Analysis . . . 130
5.2.1.1 Perturbation of the Magnetic Axis . . . 132
5.2.1.2 Effects of the VMS-stabilization . . . 135
5.2.2 Resistive Internal Kink Dynamics . . . 139
5.2.2.1 Magnetic Reconnection . . . 141

5.3 Conclusions 143

6 Divertor Configuration: X-point plasmas 145
6.1 Bohm Criterion 146
6.2 Bohm Boundary Conditions: Implementation 148
6.3 X-point Plasmas: Quasi-stationary equilibriuim 150
6.4 Conclusions 152

Conclusions and Perspectives 155

Conclusions et Perspectives 157

A Details of the evaluations used to derive the Reduced MHD model 161
A.1 For any scalar A, the relation $\nabla\times(\nabla A\times\nabla\phi) = -\nabla\phi(\Delta^* A)+\frac{1}{R^2}\nabla_{\boldsymbol{\xi}}(\partial_\phi A)$ holds. 161
A.2 Derivation of $\boldsymbol{v}\cdot\nabla\boldsymbol{v}$ 162

B Coefficients of the Discrete Fourier Transform 167
B.1 Modes retained when evaluating the RHS 167
B.2 Modes retained when evaluating the Jacobian 168
B.2.1 Non-degenerated cases 168
B.2.2 Degenerated cases 170

List of Figures 173

Bibliography 177

Abstract 185

Introduction

The numerical modeling of physical phenomena is an unavoidable technique that has been widely employed in different scientific domains. The definition of modeling might vary from one domain to another but the principle stays the same: the process of solving physical problems by appropriate approximations of the reality.

The objective of this thesis work concerns the study, design and numerical implementation of a stabilized finite element method that could be applied to different physical problems. More specifically, our goal is to apply this method to problems involving magnetohydrodynamic models of plasmas.

The finite element method was first developed to solve complex elasticity and structural analysis problems in civil and aeronautical engineering but has been since then widely employed outside these domains. Nevertheless, it has been shown that for other applications, namely in fluid mechanics, this technique has limitations. The problem comes from the fact that the finite element method leads to central flux approximations which are known to be numerically unstable. To overcome this difficulty stabilization techniques have been developed giving birth to a new kind of methods known as Stabilized Finite Elements. They were first developed in the end of the 70's to deal with advection diffusion equations [1, 2].

It is now commonly accepted that for flows dominated by convection, numerical schemes must take into account the effects of unresolved scales in order to ensure the stability of the numerical approach. In the context of compressible hydrodynamics, the pioneering work of von Neumann and Richtmyer [3] and its two-dimensional extension by Wilkins [4, 5], unresolved scale effects on coarse scales are formulated as artificial viscosity. Godunov [6] was the first to introduce an explicit evaluation of sub-scale effects on the resolved scales via the solution of the so-called Riemann problems. However, these popular formulations are mainly associated to staggered and centered finite volumes (FV) as well as to Discontinuous Galerkin (DG) formulations. Moreover, as Riemann problems are defined in the directions normal to the mesh faces, the associated numerical stabilization is highly dependent on the mesh topology. This can be very damaging for

flows involving strongly anisotropic processes as it is the case in the high temperature magnetized plasmas. In this context, the high-order Galerkin finite element method (FEM) can provide a useful framework for the numerical approximation. However, it gives rise to centered approximations of the differential operators which is suitable for elliptic like operators but can lead to non-physical behaviors when flows are dominated by the effect of the hyperbolic operators, i.e., convection. Indeed, the Galerkin method does not provide a mechanism for the control of sub-scales effects on the resolved scales or to put in other words, a stabilization.

We are concerned by the numerical modeling of strongly magnetized plasmas in tokamak geometries, particularly the Magnetohydrodynamic (MHD) instabilities. We assume that the characteristic time scales of the simulations under concern, the interaction of the charged gas with the magnetic field, can be described by the compressible MHD equations. The most popular Galerkin finite element codes for simulation of MHD instabilities are NIMROD [7], M3D-C1 [8] and JOREK [9, 10] . The stabilization process in these codes is achieved either by the use of artificial viscosity or by the introduction of additional self-adjoint operators, sometimes presented as preconditioning, semi-implicit or implicit strategies [11–13]. The goal is to parabolize the MHD system through an appropriate decomposition of the hyperbolic operator.

The variational multi-scale (VMS) formulation [1, 14, 15] provides attractive guidelines for the development of stabilized schemes that take into account the hyperbolic nature of the considered systems. Within the VMS framework, stabilization of waves is achieved by an additional contribution in the weak formulation. This contribution mimics the effect of the unresolved scales over the resolved ones. The VMS strategy is residual-based and designed to achieve a numerical stability without compromising the accuracy and the physical behavior of the system. By this way, an upwinding process is introduced which leads to numerical diffusion essentially in the flow direction, so as to avoid cross-wind diffusion effects for multidimensional flows over non-aligned meshes. The critical point of this strategy is the design of a scaling matrix used to adjust the numerical dissipation such as to preserve the order of accuracy of the Galerkin method. VMS-stabilization is very efficient when dealing with smooth solutions. Nevertheless, this is a linear process and, according to Godunov's theorem, it can allow oscillatory approximations of discontinuities. Indeed, low-dissipation schemes might result in spurious Gibbs oscillations associated to spectral truncation in the wavenumber space. Thus, although discontinuity capturing is a nonlinear dissipation it is often used to enforce the total variation stability where the solution develops sharp gradients.

Another issue that must be taken into account in our context is related to the solenoidal constraint on the magnetic field. In fact, the divergence free constraint is formulated

strongly whereas finite element methods are based on the weak formulation. In the present case, we will be concerned by MHD instabilities where the initial conditions come usually from the solution of the so-called Grad-Shafranov (GS) equation on the toroidal component of the vector potential: the magnetic flux. Therefore, if for the MHD system we use the vector potential formulation, the same variable will be interpolated for the GS equilibrium and the evolution of the perturbed system. However, the magnetic field is not uniquely defined in terms of a magnetic vector potential and we need an additional constraint such as the Coulomb gauge. Moreover, the potential formulation can lead to systems with third order derivatives and it can be useful to design finite element functions with continuous gradients over elements (C^1-continuity)

In our applications, the tokamak geometry (3D) is always the tensor product of a 2D poloidal domain and a periodic 1D toroidal domain. Test and trial functions of the finite element strategy are the product of a function of the poloidal coordinates and a function of the toroidal coordinate. In the poloidal plane (2D domain) we consider iso-parametric C^1 bi-cubic splines defined on a curved quadrangulation [9]. The bi-cubic splines have an iso-parametric formulation and the elements in the physical space can be curved quadrangles with four degrees of freedom per vertex and per physical variable. This strategy is very close to the Hermite approach but with more flexibility of the mesh structuration [9]. The degrees of freedom are associated to the mesh vertices so that we can use compressed numerical graph and block formulation to speed-up computations. In the toroidal direction we need periodical representation functions. Most of the computations are performed with sine-cosine expansions and the use of Hermite cubic splines is also an explored option for the poloidal interpolation.

We propose, then, a VMS stabilization strategy specific for time evolving problems and based on time fluctuations. This approach has some similarities with the Taylor-Galerkin (TG) formulation [16–18] and can be simplified to recover the parabolizations that are often used for MHD simulations in tokamaks [11–13, 19]. We will discuss the effect of the vector potential representation of the magnetic field on the weak formulation. The Coulomb gauge condition as well as the boundary conditions are achieved by penalization, added as contributions to the weak formulation. The time step discretization is mainly the Crank-Nicolson scheme so that the global approximation is implicit and its solution is achieved by a linearized approximation. The linearized system is solved by the Generalized Minimal RESidual (GMRES) iterative method, preconditioned by direct solvers based on PASTIX library [20] and applied to the sparse sub-systems describing self interaction of Fourier modes. These strategies have been included in the code JOREK dedicated to simulations of MHD instabilities. Our efforts were mainly directed to the full MHD model.

Organization of the manuscript

This manuscript is basically divided into two parts. The first part, containing Chapters 1, 2 and 3, establishes the fundamental concepts related to our physical problem as well as the models used to describe them and the numerical approximation necessary to find their solutions. The second part, comprising Chapters 4, 5 and 6, presents the results obtained using the model previously established.

In Chapter 1, the basic physics behind the models is presented. It is a basic descriptive chapter showing the context in which the nuclear fusion is dealt with. For that, the practical issues concerning the controlled magnetic fusion are shown starting by the possible way to confine the plasma with the help of magnetic fields. The main characteristics of the device developed as a prototype reactor, the so called tokamak, are shown and the perspectives of this field of research are briefly discussed.

Next, Chapter 2 introduces the mathematical models of the problem. In order to derive them, the most basic plasma model, i.e., the kinetic model is used as a starting point to derive the Magneohydrodynamic (MHD) models. All the steps and assumptions made, such as the quasi-neutral regime and the weak electronic mass, are detailed. Furthermore, Maxwell's equations bring with them the divergence free constraint that must absolutely be treated when going from the analytic model to the numerical approximation. Once the single-fluid full MHD model is obtained further simplifications can be done in order to derive models that can be more easily treated. The first and most simple model derived is the ideal model from which the spectral properties are studied. It is important to do so because this model, in the end, is the model driving the others. Thus, its properties can be extended to the more complex ones without loss of generality. From these equations it is possible to derive one very important equation, the so-called Grad-Shafranov equilibrium. To finish, the reduced resistive model is presented.

Chapter 3 is the core of this work. It comes to give all the numerical background necessary to solve the model shown in the previous chapter. It starts with a general description of the finite element method and explains its need of stabilization. After that, the concepts of the Variational Multi-Scale (VMS) stabilization are shown, going from the explicit evaluation of the fine scales to the discussion about the stabilization parameter that plays a fundamental role in this formulation. The application to our MHD model via the Jacobian operator is then introduced. Next, all the numerical strategy to achieve the discrete formulation of the model is described in details. A main effort is put in the description of the construction of the approximated spaces of the Galerkin formulation considering the axis-symmetry of the problem. Moreover, a way to deal with the boundary conditions is presented. Finally, the assembling of the system

with the help of the so called Bézier finite elements and the Discrete Fourier Transform (DFT) is discussed.

For the results part, Chapter 4 discuss the solution of the Grad-Shafranov equilirium that is used not only as an initial condition of the model but also as a tool to build the grid. In fact, in the MHD context, it is common to use grids that are aligned with the magnetic field and solving the GS equation allows us to properly build them. Next, the equilibrium solution is discussed in terms of the residuals with the help of the results obtained. In this way, a connection between this equation and the full MHD model can be done creating the less amount of numerical noise possible.

Chapter 5 is dedicated to the validation of the stabilized numerical model proposed. For that, a macroscopic MHS instability named internal kink mode is extensively studied. Several of its properties like the growth rate, the dependence of certain phenomena on the resistivity among others were obtained from the simulations and compared with other numerical results already present in the literature and/or theoretical evaluations. A great effort was put in showing how the stabilization has improved considerably the accuracy of the results without interfering in the physical properties of the problem.

Finally, Chapter 6 shows some results obtained for a more complex tokamak configuration in which special boundary conditions must be implemented. This happens because, in this configuration, the plasma can come in touch with a material wall and, hence, the physical phenomena happening around it leads to special constraints for the velocity. Some basic results obtained with this geometry also allowed us to validate the stabilization strategy.

Introduction

La modélisation numérique de phénomènes physiques est une technique incontournable largement utilisée dans différents domaines scientifiques. La définition de modélisation peut varier d'un domaine à l'autre mais son principe reste le même : résoudre des problèmes physiques en utilisant des approximations appropriées de la réalitié.

L'objectif de ce travail de thèse concerne l'étude, conception et mise-en-oeuvre numérique d'une méthode d'éléments finis stabilisés pouvant être appliquée dans différents problèmes physiques. Plus précisement, notre but est d'utiliser cette méthode pour des problèmes liés aux modèles magnétohydrodynamiques de plasmas.

La méthode d'éléments finis a été d'abord developpée pour résoudre des problèmes complexes d'élasticité et d'analyse structurelle en ingénierie civile et aéronautique mais, depuis lors, elle a été largement employée en dehors de ces domaines. Pour d'autres applications, néanmoins, notamment en méchanique des fluides, il a été demontré que cette technique présente des limitations. Le problème advient du fait que l'approche éléments finis mène à des approximations centrées et celles-ci sont connues pour être numériquement instables. Pour surmonter cette difficulté, des techniques de stabilisation ont été developpées donnant naissance à un nouveau type de méthode connu sous le nom d'éléments finis stabilisés. Ces méthodes ont été developpées à la fin des années 70 pour traiter les équations dites d'advection-diffusion [1, 2].

Il est, de nos jours, largement admis que pour le traitement des écoulements dominés par la convection, les schémas numériques doivent tenir compte des effets des échelles non-résolues pour assurer la stabilité de l'approche numérique. Dans le cadre de l'hydrodynamique compressible, les travaux pionniers de von Neumann et Richtmyer [3] et son extension à deux-dimensions faite par Wilkins [4, 5] simulent les effects des échelles non résolues sur des échelles résolues au travers d'une viscosité artificielle. Godunov [6] a été le premier à introduire une évaluation explicite des effects des sous-échelles par la résolution de problèmes dits de Riemman. Toutefois, ces formulations très populaires sont principalement associées à des formulations Volumes Finis (FV) (centrés) et Galerkin discontinu (DG). De plus, étant donné que les problèmes de Riemman sont définis dans les directions

normales aux faces du maillage, la stabilisation numérique est fortement dépendante de la topologie de celui-ci. Cela peut devenir très problématique lorsque l'on traite des écoulements contenant des processus fortement anisotropiques, comme c'est le cas pour les plasmas magnétisés à haute température. Dans ce contexte, la méthode d'éléments finis d'odre élevé du type Galerkin peut fournir le cadre idéal pour l'approche numérique. Toutefois, elle n'est appropriée que lorsque l'on traite des opérateurs du type elliptique et peut mener à de comportements non-physiques quand les écoulements sont dominés par les effets des opérateurs hyperboliques (convection). De fait, la méthode de Galerkin ne fournit pas un mechanisme pour le contrôle des effets des sous-échelles sur les échelles résolues, c'est-à-dire, de la stabilisation.

Nous nous concentrons sur la modélisation numérique des plasmas fortement magnétisés et configurés selon la géometrie des tokamaks, plus particulièrement la modélisation des instabilités magnétohydrodynamiques (MHD). Nous supposons que les temps caractéristiques des simulations concernées, c'est-à-dire les interactions du gaz chargé avec le champ magnétique, peuvent être décrits par les équations de la MHD compressible. Les codes les plus populaires pour la simulation des instabilités MHD des plasmas sont NIMROD [7], M3D-C1 [8] et JOREK [9, 10]. Dans ces codes, la stabilisation est établie, soit par l'utilisation d'une viscosité artificielle soit par l'introduction des opérateurs auto-adjoints, parfois presentés comme des pré-conditionneurs ou comme des strategies semi-implicites ou implicites [11–13]. Le but est de paraboliser le système MHD avec l'aide d'une décomposition appropriée de l'operateur hyperbolique.

La formulation variationnelle multi-échelles (VMS) [1, 14, 15] fournit des lignes directrices attrayantes pour le développement des schémas stabilisés qui prennent en compte la nature hyperbolique des systèmes considérés. Dans le cadre VMS, la stabilisation des ondes est accomplie grâce à une contribution additionnelle dans la formulation faible. La stratégie VMS est basée sur des résidus et conçue pour apporter de la stabilisation numérique sans compromettre la précision et la physique du problème traité. Dans cette stratégie, un processus «upwinding» est introduit conduisant à une diffusion numérique essentiellement dans la direction de l'écoulement de manière à éviter les effets de diffusion «crosswind» pour des écoulements multi-dimensionnels sur des maillages non-alignés. Le point critique de cette stratégie est la conception d'une matrice, dite de «scaling», utilisée pour régler la dissipation numérique de façon à préserver l'ordre de précision de la méthode de Galerkin. La stabilisation VMS est très efficace lorsque l'on traite des solutions régulières. Cependant, il s'agit d'un processus linéaire et, selon le théorème de Godunov, il admet des approximations oscillatoires des discontinuités. En effet, des schémas avec une faible dissipation peuvent créer des oscillations dites de «Gibbs» associées à la troncature dans l'espace des ondes. Par conséquent, même si la capture de

discontinuités est une dissipation non-linéaire, elle est souvent utilisée pour renforcer la stabilisation aux endroits où la solution développe de forts gradients.

De plus, il faut tenir compte de la contrainte solenoïdale du champ magnétique. En réalité, la contrainte de divergence nulle est formulée de manière forte tandis que les méthodes éléments finis sont basées sur des formulations faibles. Dans le cas présent, nous nous concentrons sur des instabilités MHD dont la condition initiale est, normalement, la solution de l'équation de Grad-Shafranov pour la composante toroïdale du potentiel vecteur. Pour cette raison, lorsque nous utilisons la formulation potentiel vecteur pour le système MHD, la même variable sera interpolée pour l'ǵquilibre GS et aussi pour l'évolution du système perturbé. Néanmoins, le champ magnétique n'est pas defini de manière unique en termes d'un potentiel vecteur et, donc, une contrainte additionnelle, connue comme la jauge, se fait nécessaire. Pour notre modèle, la gauge de Coulomb est utilisée. De plus, la formulation potentiel vecteur peut mener à des systèmes contenant des dérivés du troisième ordre et, pour cette raison, la conception des fonctions éléments finis ayant des gradients continus sur les éléments (continuité - C^1) peut être utile.

Dans nos travaux, la géométrie du tokamak (3D) est toujours le produit tensoriel entre un domaine poloïdal 2D et un domaine toroidal 1D périodique. Les fonctions test et les fonctions de base de la stratégie éléments finis seront donc le produit des fonctions des coordonées poloïdales et des fonctions de la coordonée toroïdale (l'angle toroïdal). Sur le plan poloïdal (domaine 2D) nous considérons des splines bi-cubiques C^1 iso-paramétriques définis sur une quadrangulation incurvée [9]. Les splines bi-cubiques ont une formulation iso-paramétrique et les éléments appartenant à l'espace physique peuvent être des quadrangles incurvés ayant quatre degrés de liberté par noeud et par variable. Cette stratégie est similaire à l'approche de Hermite tout en ayant plus de souplesse concernant la structuration du maillage [9]. Les degrés de liberté sont associés aux noeuds du maillage de façon à ce que l'on puisse utiliser des graphes numériques compressés et une formulation en bloc pour accélérer les calculs. Des fonctions périodiques sont nécessaires dans la direction toroïdale. La majorité des calculs sont effectués avec des développements sinus-cosinus et l'utilisation de splines cubiques d'Hermite est aussi une option exploitable pour l'interpolation poloïdale.

Nous proposons, donc, une stratégie de stabilisation VMS pour les problèmes ayant une évolution temporelle et cette stratégie sera basée sur les fluctuations dans le temps. Cette approche comporte des similarités avec la formulation de Taylor-Galerkin (TG) [16–18] et peut être simplifiée afin de récuperer les parabolisations qui sont souvent utilisées dans des simulations MHD pour tokamaks [11–13, 19]. Nous évoquerons les effets de la représentation potentiel vecteur du champ magnétique sur la formulation faible. La discrétisation en temps se fera via le schéma de Crank-Nicholson de façon à ce

que l'approximation globale soit implicite et sa résolution sera accomplie à travers une approximation linéarisée. Ce système linéarisé est résolu par la méthode itérative ≪Generalized Minimal RESidual≫ (GMRES), pré-conditionnée par des solveurs directs basés sur la librairie PASTIX [20] et appliqués aux sous-systèmes creux décrivant l'interaction des modes de Fourier. Ces stratégies ont été inclues dans un code appelé JOREK, dédié aux simulations des instabilités MHD des plasmas de tokamak.

Résumé

Les simulations numériques sont une technique de plus en plus présente dans les domaines scientifiques. Elles ont pour but la résolution des modèles mathématiques représentant des phénomènes physiques divers. Notre but est de contribuer à l'avancement de ce domaine en validant une stratégie de stabilisation pour la méthode éléments finis appliquée aux modèles magnétohydrodynamiques des plasmas de fusion.

La fusion nucléaire est le phénomène par lequel deux noyaux atomiques se rapprochent suffisament pour réagir et former un ou plusiers noyaux différents. L'énergie produite par cette réaction est le résultat de la différence de masse entre les noyoux originaux et les produits. Ces réactions ont lieu naturellement dans le coeur des étoiles où les conditions de pression et température sont propices. Toutefois, elles sont très difficiles de reproduire sur Terre.

Pour le faire, une machine, nommée Tokamak a été developpée visant à attraper les particules sous la forme de plasma via un champ magnétique. Le nom Tokamak est l'acronyme russe de «Chambre Toroïdale avec bobines magnétiques»

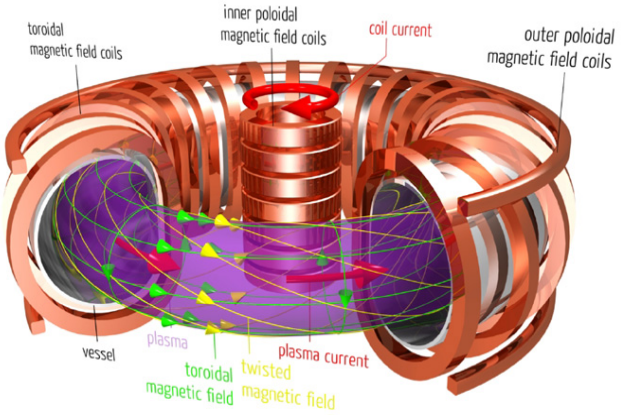

Figure 1: Tokamak

Un rappel aux développements dans le domaine de la fusion contrôlée sont faits dans le chapitre 1. Les propriété des tokamaks ainsi que leurs configurations sont décrites. Aussi, certains phénomènes qui ont lieux dans la machine y sont discutés.

Nous nous concentrons, dans le Chapitre 2, sur l'établissement des modèles de base des plasmas de fusion. Pour la dérivation des modèles dits magnétohydrodynamiques (MHD), nous sommes partis de l'équation de Boltzmann

$$\frac{\partial f_\sigma}{\partial t} + \boldsymbol{u} \cdot \frac{\partial f_\sigma}{\partial \boldsymbol{r}} + \frac{q_\sigma}{m_\sigma}(\boldsymbol{E} + \boldsymbol{u} \times \boldsymbol{B}) \cdot \frac{\partial f_\sigma}{\partial \boldsymbol{u}} = C_\sigma. \tag{1}$$

Ensuite, en utilisant les moments de cette équation, nous avons obtenu un système des lois des conservation concernant la densité, la quantité de mouvement et l'énergie. À ce système viennent se rajouter les équations de Maxwell ainsi que le loi d'Ohm. De plus, des relations pour les termes de transport sont nécessaires. Ensemble, ces équations donnent naissance au système dit bi-fluide. Il est important de souligner que les équations de Maxwell génèrent une difficulté supplémentaire car elles contiennent la contrainte divergence nulle du champ magnétique et cela doit absolument être traité du point de vue numérique. En effet, numériquement

$$\partial_t(\nabla \cdot \boldsymbol{B}) \neq 0 \tag{2}$$

Pour cela, nous présentons la formulation potentiel vecteur. Puis, différentes hypothèses pour la simplification du modèle sont présentées nous permettant d'obtenir le modèle de la MHD complète qui est à la base de notre approximation numérique

$$\begin{cases} \partial_t \rho + \nabla \cdot (\rho \boldsymbol{v}) &= 0, \\ \partial_t \rho \boldsymbol{v} + \nabla \cdot (\rho \boldsymbol{v} \otimes \boldsymbol{v}) &= \boldsymbol{J} \times \boldsymbol{B} - \nabla p - \nabla \cdot \underline{\boldsymbol{\pi}}, \\ \partial_t \rho e + \nabla \cdot (\rho e \boldsymbol{v} + p \boldsymbol{v}) &= (\boldsymbol{J} \times \boldsymbol{B}) \cdot \boldsymbol{v} + \eta \boldsymbol{J}^2 - (\nabla \cdot (\boldsymbol{v} \underline{\boldsymbol{\pi}}) + \nabla \cdot \boldsymbol{Q}), \\ \partial_t \boldsymbol{B} &= -\nabla \times \boldsymbol{E}, \end{cases} \tag{3}$$

avec

$$\rho e = \frac{p}{\gamma - 1} + \frac{1}{2}\rho |\boldsymbol{v}|^2, \tag{4}$$

$$\boldsymbol{J} = \nabla \times \boldsymbol{B}, \tag{5}$$

et la loi d'Ohm qui définira, selon des approximations utilisées, quel type de système sera traité : idéal, résistif ou encore Hall, par exemple. Les modèles idéal et résistif réduit sont, par la suite, obtenus. Le modèle réduit nous permet de dériver l'équation

de Grad-Shafranov qui jouera un rôle important dans nos simulations

$$\Delta^* \psi = -R^2 \frac{dp}{d\psi} - F \frac{dF}{d\psi}. \tag{6}$$

Par la suite, dans le chapitre 3, l'approche numérique est entièrement développée. Cela est fait dans le cadre de la méthode éléments finis pour laquelle le besoin d'une stabilisation est démontré à l'aide d'un problème simple de convection-diffusion. La stabilisation est accomplie via la formulation Variationnelle Multi-Échelles (VMS) pour laquelle une évaluation des échelles non-résolues du système est nécessaire. Pour cela, le système MHD est ré-écrit sous la forme quasi-linéaire

$$\partial_t \boldsymbol{w} + \underline{\boldsymbol{L}}(\boldsymbol{w}, \boldsymbol{\partial})\boldsymbol{w} = 0, \tag{7}$$

où $\underline{\boldsymbol{L}}(\boldsymbol{w}, \boldsymbol{\partial})$ est le Jacobien qui sera au coeur de la stabilisation. L'évaluation des sous-échelles est faite via le résidu $\boldsymbol{R}(\boldsymbol{w}) := \partial_t \boldsymbol{w} + \underline{\boldsymbol{L}}(\boldsymbol{w}, \boldsymbol{\partial})\boldsymbol{w}$. Pour cela, nous considérons les décompositions suivantes

$$\boldsymbol{w} = \overline{\boldsymbol{w}} + \boldsymbol{w}' \text{ and } \boldsymbol{w}^\star = \overline{\boldsymbol{w}}^\star + \boldsymbol{w}^{\star\prime},$$

où $\overline{\boldsymbol{w}}$ represente les échelles résolues et $\boldsymbol{w}'$ celles non-résolues. En plus, nous supposons que les espaces de ces fonctions sont orthogonaux, c'est-à-dire

$$\boldsymbol{\mathcal{S}} = \overline{\boldsymbol{\mathcal{S}}} \oplus \boldsymbol{\mathcal{S}}' \text{ and } \boldsymbol{\mathcal{V}} = \overline{\boldsymbol{\mathcal{V}}} \oplus \boldsymbol{\mathcal{V}}'$$

où $\overline{\boldsymbol{\mathcal{S}}}$ et $\overline{\boldsymbol{\mathcal{V}}}$ sont les espaces des fonctions pour les échelles résolues tandis que $\boldsymbol{\mathcal{S}}'$ et $\boldsymbol{\mathcal{V}}'$ sont ceux des échelles non-résolues.

Ensemble, ces suppositions nous permettent de ré-écrire la formulation faible de notre modèle. Ainsi, la méthode éléments finis prend en compte les effets de ces échelles sur celles résolues

$$\int_{\Omega_{x,h}} \boldsymbol{R}(\boldsymbol{w}) \cdot \boldsymbol{w}^\star - \int_{\Omega_{x,h}} (\underline{\boldsymbol{L}}(\boldsymbol{w}, \boldsymbol{\partial})\delta\boldsymbol{w}) \cdot \underline{\boldsymbol{\mathcal{T}}}(\underline{\boldsymbol{L}}^T(\boldsymbol{w}, \boldsymbol{\partial})\boldsymbol{w}^\star) = 0, \quad \forall \boldsymbol{w}^\star, \in \boldsymbol{\mathcal{W}}_h(\Omega_{x,h}). \tag{8}$$

Différentes options pour la matrice de stabilisation $\underline{\boldsymbol{\mathcal{T}}}$ sont, alors, présentées. Finalement, toute la stratégie numérique, notamment la construction des espaces d'approximation, est detaillée.

Dans le contexte de nos travaux, la géométrie du tokamak est toujours décomposée comme un produit tensoriel entre un domaine poloïdal 2D et un domaine toroïdal 1D pour lequel une decomposition de Fourier est utilisée grâce à la symétrie axiale de la

machine. Pour le domaine 2D, le choix s'est porté sur les éléments finis de Bézier pour lequels une transformation iso-paramétrique est utilisée pour transformer les coordonées tout en utilisant les mêmes fonctions de base utilisées pour les autres variables. Cette construction enforce la continuité C^1 des fonctions test dans l'espace physique. En plus, le fait d'avoir quatre degrés de liberté associés à chaque sommet des éléments rend plus facile la construction du graph compressé qui est utilisé pour résoudre les système numérique plus rapidement. Finallement, les conditions limites ainsi que la jauge de Coulomb pour la formulation potentiel vecteur sont implémentées en utilisant une méthode de pénalisation.

Dans le Chapitre 4, nous nous attaquons à la résolution numérique de l'équilibre de Grad-Shafranov qui servira non seulement à établir nos conditions initiales mais aussi à la construction du maillage poloïdal 2D. Pour la résoudre, des paramètres d'entrée appropriés obtenus par des observations expérimentales sont fournis à l'équation. Celle-ci, écrite en forme faible, mène au système non-linéaire

$$\int_{\Omega_{2D}} \frac{1}{R} \nabla \psi^{(k+1)} \cdot \nabla \psi^{\star} dRdZ = \int_{\Omega_{2D}} \frac{1}{R} \left(F(\psi^{(k)}) \frac{dF(\psi^{(k)})}{d\psi} + R^2 \frac{dp(\psi^{(k)})}{d\psi} \right) \psi^{\star} dRdZ, \quad (9)$$

qui est résolu via la méthode itérative de Picard. Les détails de la construction des maillages sont ensuites donnés. Finalement, la solution est analysée en terme des résidus, avec l'aide des résultats obtenus, de façon à ce que le couplage entre cette equation et le modèle soit fait en créant le minimum de perturbations numériques possible.

Le chapitre 5 est entièrement dédié à la validation du modèle stabilisé proposé. Pour cela, l'instabilité macroscopique MHD dite de «Kink interne» est étudiée. Cette instabilité est liée à la non-uniformité du courant et apparaît dans un plasma lorsque ce courant dépasse une valeur critique. Comme elles se developpent dans des endroits spécifiques du plasma, notamment les surfaces magnétques fermées, elles sont classées comme des instabilités absolues du plasma, en opposition aux processus convectifs.

Plusieurs propriétés de cette instabilité, notamment le taux de croissance et la dépendance entre certains phénomènes et la résistivité, ont été obtenues via les simulations et comparées à d'autres résultats numériques ainsi qu'à des évaluations analytiques. Un grand effort est fait pour démontrer que la stabilisation améliore considérablement la précision des résultats sans pour autant détruire les propriétés physiques du problème.

Finalement, le chapitre 6 présente quelques résultats obtenus pour la géométrie avec point-X. Dans ce cas, des conditions limites spéciales doivent être prises en compte dû au fait que, pour cette configuration, le plasma peut toucher des éléments physiques du tokamak. Dans ce cas, l'intéraction entre le plasma et le matériau mène à une contrainte sur la vitesse de particules arrivant à la zone de contact. En effet, les ions entrant cette

région doivent respecter la condition de Bohm

$$u_{0i} > \left(\frac{k_B T_e}{m_i}\right)^{\frac{1}{2}} = c, \tag{10}$$

où c est la vitesse acoustique ionique que, dans l'approximation mono-fluide, s'écrit sous la forme $c = \sqrt{\gamma T}$. Par conséquent, l'implémentation des conditions limites devient plus délicate. Quelques résultats préliminaires ont été, alors, obtenus dans cette géométrie et nous ont permis, à leur tour, de valider la stratégie de stabilisation.

Chapter 1

Nuclear Fusion and Tokamaks

The current energetic panorama and the projections of an increasing consumption year by year places the energy production discussion in the center of attentions. In fact, the U.S Energy Information Administration's International Energy Outlook 2016 [21] projects that world energy consumption will grow 48% between 2012 and 2040.

This gives rise to concerns about energy security and environmental impacts since fossil fuels account for more than three-quarters of world energy consumption. For this reason, non-fossil fuels like nuclear energy, wind or water generated energy and solar power are expected to grow faster than its non renewable counterparts. Nevertheless, the risks of accidents related to nuclear fission plants, the environmental impact caused by hydroelectric dams and the demanded area necessary for wind turbines or solar panels are still important barriers to the expansion of these sources. In this scenario, one alternative source is gaining more and more ground: the fusion power.

Sometimes called the energy of the stars, fusion power is the energy that could be generated through nuclear fusion reactions, i.e., reactions in which two nuclei of light elements collide and stay joined together as, for example, the reaction shown Figure (1.1). It is the source of light and heat of the stars, including our Sun, and is becoming a very promising source of energy on Earth since, contrary to fission reactions, fusion reactions do not generate long-life radioactive waste. Moreover, it uses as basic ingredients hydrogen atoms (or its isotopes) which is the most abundant element.

Nonetheless, even if this source of energy sounds very tempting, it is a real challenge to reproduce and control it on Earth. In the stars it happens naturally due to their huge gravitational pull related to their great mass that forces the nuclei to be close together improving the chances of the reactions happening. In the end, the equilibrium between the gravitational force and the fusion reactions taking place in the core of the star is

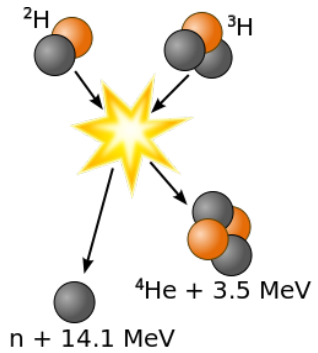

FIGURE 1.1: Illustration of a fusion reaction involving hydrogen isotopes

what makes it stable. The problem is that gravity fields as the ones present in the stars cannot be reproduced on Earth. Thus, another means have to be found in order to achieve a stable reaction.

In this Chapter, we start by introducing the basic concepts of nuclear reactions and how they can produce energy (1.1). After that, a promising alternative to emulate in laboratory the conditions present in the stars is shown (1.2) followed by a detailed description of the device that has been tested as a prototype of what could become the future Nuclear Fusion Reactor (1.3). Finally, the perspectives of the work that is done today in the fusion research field are briefly discussed (1.4).

1.1 Fusion reactions

The fundamental principle behind the production of energy through fusion reactions is the Mass-Energy Equivalence described by Albert Einstein [22] and known worldwide by the expression $E = mc^2$. Basically, it is saying that energy and mass can be interchangeable, i.e., mass is energy and vice-versa. The nuclear fusion reaction is a reaction in which two or more atomic nuclei come close enough to react and form one or more different nuclei. The energy released from this reaction is related to the difference of mass between the original nuclei and the product(s) and this difference comes from the different binding energy of the nuclei before and after the reaction.

These types of reactions were firstly identified as the source of energy production in stars and the detailed discussion were done by Bethe [23–25] and, independently by Weizsäcker [26] in 1938. For the stars with lower central temperature, the proton-proton cycle takes

place

$$H_1^1 + H_1^1 \rightarrow D_1^2 + e^+ + \nu \quad (1.44MeV), \tag{1.1}$$

$$D_1^2 + H_1^1 \rightarrow He_2^3 + \gamma \quad (5.49MeV), \tag{1.2}$$

$$He_2^3 + He_2^3 \rightarrow He_2^4 + 2H_1^1 \quad (12.86MeV), \tag{1.3}$$

where e^+, ν and γ denote in turn a positron, neutrino and gamma ray. The energy outcome is usually given in electron-volt units to avoid carrying the exponential of the scientific notation, $1eV \approx 10^{-19}J$. It is important to remark that, even though it seems like a very small energy, millions of reactions are happening at the same time which gives a considerable amount of energy.

The challenge is that positively charged nuclei have a tendency to repeal one another, thus, for the fusion to happen a certain amount of energy must be given to the system in order to overcome this barrier, known as Coulomb barrier. The probability of two nuclei overcoming it and reacting is usually called the reactivity σv of the elements. It depends on the energy and is shown in Figure (1.2).

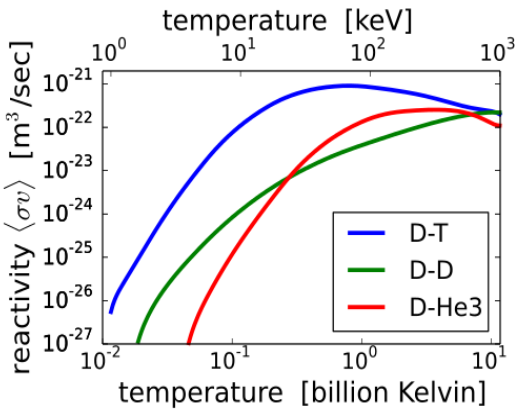

FIGURE 1.2: Reactivity of the three more common reactions as a function of the energy

The figure above states that the reaction having the highest probability of happening at any temperature is the Deuterium-Tritium ($D - T$). In fact, this is also the reaction that releases the highest amount of energy

$$D_1^2 + T_1^3 \rightarrow He_2^4 + n_0^1 \quad (17.6MeV). \tag{1.4}$$

The energetic output is carried by the alpha particle ($\approx 3.5MeV$) and the neutron which carries the rest of the energy. This energy is superior to the energy needed to overcome the Coulomb barrier meaning that a chain reaction can be triggered. However, for the first reaction to happen, the conditions for it, e.g., high pressure and temperature must be attained.

The pressure condition is not easy to be fulfilled in a laboratory and, for this reason, the efforts are mainly directed to the temperature. Indeed, by raising the temperature above a certain threshold it is possible to ionize the atoms. It means that they will absorb enough energy to excite the electrons to the point at which they can overcome the electromagnetic binding with the nucleus. It is important to remark that, in the absence of the huge gravitational pull present in the stars, the temperature necessary for this to happen must be really elevated. Once all the atoms are ionized, matter is in a state known as plasma. If classed by temperature order, plasma is considered the 4th state of matter after solid, liquid and gas. In such a state, ions (positively charged) and electrons are completely separated and, even though the fluid is still a globally neutral fluid, plasmas can be seen as a mix of charged particles. Plasmas compose 99% of the universe. They are present on Earth's ionosphere and magnetosphere, in the solar winds, comets and interstellar media. On Earth's surface, they cannot be found naturally but can be observed in the auroras, also known as northern lights.

The main challenge when dealing with plasmas in laboratory is to find a way to contain it since any vessel used must resist the temperatures that are extremely elevated. For fusion plasmas, for example, it can go up to $10^8 K$. Nonetheless, as mentioned before, plasmas are composed of charged particles, which accordingly to the Lorentz Principle, can be constrained via a magnetic field. In fact, if the magnetic field is constant and no other forces are present, the Lorentz force will cause a particle to be under a constant acceleration perpendicular to both the magnetic field and the particle velocity. This does not affect the particle's motion parallel to the magnetic field but results in circular motion in the plane perpendicular to it. This could avoid the contact between the plasma and any material wall and this strategy is known as magnetic confinement.

1.2 Magnetic confinement

The goal of the controlled fusion is to produce energy from the fusion reactions which need very high temperatures. The problem is that plasmas are basically ionized gases which means that they disperse, if not contained, leading to a considerable reduction in the probability of reactions happening since the goal is to keep the nuclei as close to each other as possible. The challenge becomes then the way to contain the plasma, avoiding its dispersion. Any material vessel, of which the walls would contain it, is out of question due to the temperatures involved. Thus, the magnetic confinement appeared as a possible solution for this problem. Indeed, charged particles can be trapped by magnetic fields in such a way that no contact with any material is needed. Therefore,

the necessary basic initial condition that could lead to a permanent and self-sustained fusion reaction is fulfilled.

If the plasma can be stably contained, the next step consists of heating it in different ways to the point in which the first fusion reaction start. The energy released by this reaction must then be able to compensate the losses and maintain the plasma temperature. To quantify this condition, Lawson introduced in 1957 a criterion known as confinement time τ_E [27] which is a parameter comparing the ratio between the energy produced and the losses of the system

$$\tau_E = \frac{W}{P_{loss}}. \tag{1.5}$$

In some way it is measuring the speed at which the plasma is cooling so as to give the quality of the confinement. The reaction will be sustainable if the heating coming from the alpha particles (charged) is enough to overcome the losses. The neutron energy is the one recovered as the output source of the reactor since neutrons are not constrained by the magnetic field due to the absence of charge.

The Lawson criterion is often written as

$$f(Q) = n_e T \tau_E, \tag{1.6}$$

where n_e is the electronic density, T the temperature and Q is the efficiency of the reactor, i.e.,

$$Q = \frac{E_{produced}}{E_{injected}}. \tag{1.7}$$

When $Q = 1$, the reaction can be self-sustained but no extra energy is being produced. It has been already reached in a device known as JET (Joint European Torus) for approximately $1s$. Nonetheless, to be economically exploitable a device must be able to reach $Q = 50$.

So far, the idea of trapping the particle via magnetic field has been discussed but details of how this can be practically done have not been given. In fact, the point is not only to trap the particles but also keep them trapped so as to reach the conditions for the reactions. Using a straight device for example would lead the particles to eventually hit a wall. The strategy hence is to build a device that could reproduce the properties of an infinite cylinder such that the particles would follow the magnetic lines and no obstacles would appear. Indeed, this can be done with a torus because in this geometry the magnetic lines are bent in such a way that they can close about themselves forming a circle that emulates the idea of an infinite cylinder. This technique is known as fusion by magnetic confinement: it avoids the dispersion of the particles and their contact with the walls. There are different devices in which it has been tested. We however concentrate our discussion on the so called tokamak.

1.3 Tokamaks

After the Second World War, several attempts and strategies were tried in order to achieve the controlled fusion. The one that seemed to be very promising and has been largely exploited up to today is the so called tokamak which is a Russian acronym that stands for Toroidal Chamber with Magnetic Coils. Experimental research with tokamaks started in 1956 in Kurchatov Institute, Moscow by a group of Soviet scientists led by Lev Artsimovich.

The first fusion devices used an electric current to create a poloidal magnetic field that would contain the plasma along a linear axis. After that, in order to improve the technique, studies were concetrated on toroidal devices. It was discovered however that a purely toroidal field is not able to contain the plasma and this is due to the fact that the particles do not only spiral around the field lines but also drift across the field because the magnetic field has a nonzero gradient. This leads to a separation of the electrons and the ions which in turn creates an electric field. The electric field will then induce a new drift pointing outward of the axis of rotation. One way of seeing it is imagining a torus of fluid with the magnetic lines frozen in it. The plasma pressure would tend to expand the torus and the magnetic field outside the plasma is not able to contain it. Thus, the plasma slips between the field lines.

To overcome this difficulty there must be a twist to the field lines in such a way that the flux tubes encircling the axis become, given that there is enough symmetry in the twist, flux surfaces. Some of the outward drift will be then compensated by an inward one on the same flux surface leading to a much improved confinement. This can be done by adding a poloidal component to the toroidal magnetic field. This configuration is known as nested configuration of the magnetic field and a scheme of a tokamak configured this way can be seen in Figure (1.3). More details about the magnetic configuration are given below.

After the establishment of the tokamak technology, bigger and more efficient devices have been built. For example, the already mentioned JET which is part of an European consortium and the reactor is located in England; Asdex-Upgrade located in Germany; Tore Supra in France; and DIIID in the USA capable of getting $Q = 1$. The future tokamak ITER (International Thermonuclear Experimental Reactor) has a goal of reaching a factor $Q = 10$. Details of this project are shown in the end of this chapter.

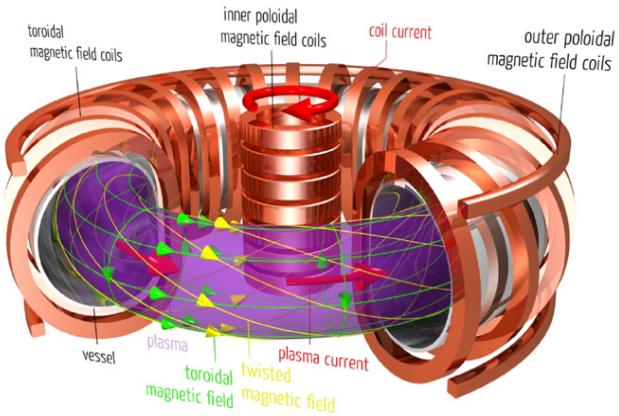

FIGURE 1.3: Tokamak scheme

1.3.1 Characteristics of Tokamaks

As discussed in the previous section, a special configuration of the magnetic field is needed to contain the plasma. Before showing the details of this configuration, let us describe the geometry and the notations often used when dealing with tokamaks.

Geometry and notations

One way to obtain a torus is by performing a rotation on a poloidal section around the Z axis. The toric coordinates are then introduced (R, θ, ϕ) with R the radial coordinate, θ the poloidal coordinate and ϕ the toroidal one. For the toroidal coordinate the notation $\nabla\phi$ is often used where

$$\nabla\phi = \frac{1}{R}\hat{\boldsymbol{\phi}}. \tag{1.8}$$

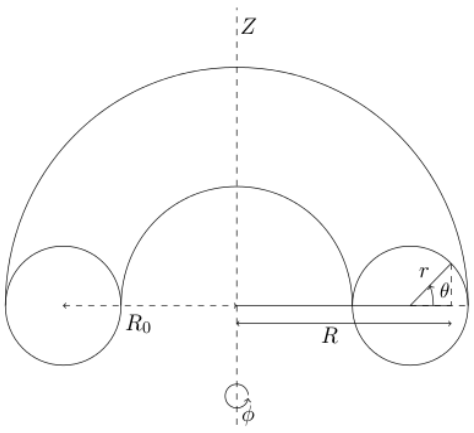

FIGURE 1.4: Toroidal coordinates

The minor radius is given by r while the major radius is R_0 and the ratio $\epsilon \equiv \frac{r}{R_0}$ is known as inverse aspect ratio. When $\epsilon \to 0$ the cylindrical limit of the torus is recovered.

1.3.1.1 Magnetic configuration

It is helpful to decompose the magnetic field in a tokamkak accordingly to the poloidal and toroidal components

$$\boldsymbol{B} = \boldsymbol{B}_\phi \hat{\boldsymbol{\phi}} + \boldsymbol{B}_\theta \hat{\boldsymbol{\theta}}. \tag{1.9}$$

Then, it is useful to introduce the concept of poloidal magnetic flux ψ_θ. For each point P in the space (R, θ, ϕ) it is defined as

$$\psi_\theta = \int_0^{2\pi} \int_0^a (\boldsymbol{B} \cdot \nabla\theta) R dR d\phi, \tag{1.10}$$

which is reduced to

$$\psi_\theta = 2\pi \int_0^a (\boldsymbol{B} \cdot \nabla\theta) R dR \tag{1.11}$$

if there is axis-symmetry.

The poloidal flux is constant over all the surfaces formed by the closed magnetic lines and they are called, in this case, magnetic surfaces. As it can be seen from its expression above, it depends only on R and, for that reason, can be used sometimes as a coordinate reference. A scheme of this configuration of the flux surfaces is shown in Figure (1.5)

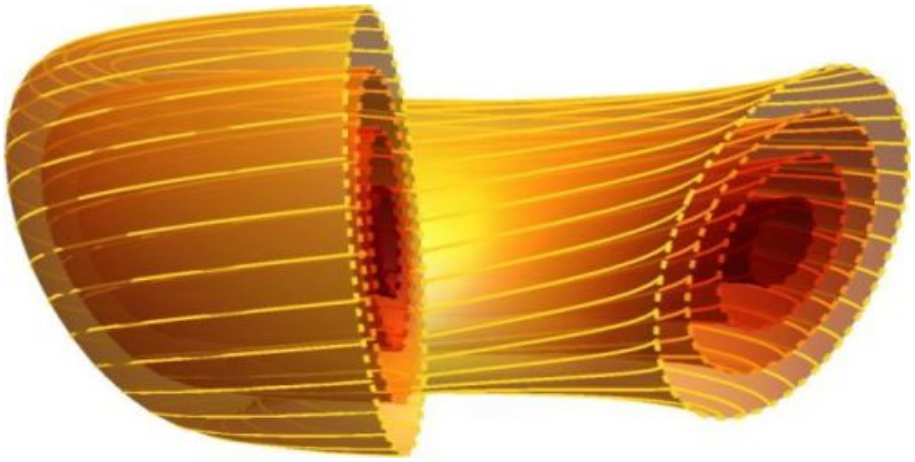

FIGURE 1.5: Scheme of the magnetic field lines forming differente flux surfaces. At each surface ψ_θ is constant [28]

One property of the flux surfaces that is important to know is its safety factor q. This factor gives information about the configuration of the magnetic field lines over a given surface, i.e., it tells if they are open or closed. The closed field lines return to themselves forming a ring while the open field lines reach a wall before doing so. The safety factor

gives, in the end, the number of toroidal turns a line gives for every poloidal one meaning that, if $q \in \mathbb{Z}$, the magnetic lines are closed, otherwise they are open. q is expressed as

$$q(r) = \frac{r\boldsymbol{B}_\phi(R_0)}{R_0\boldsymbol{B}_\theta(r)}. \tag{1.12}$$

The name safety factor comes from the role this parameter plays when dealing with MHD instabilities, some of which will be described in (1.3.3).

The safety factor depends on the radial coordinate, then is is useful to write explicitly this dependence that is called magnetic shear. It is written as

$$s(r) = \frac{r}{q}\frac{dq}{dr}. \tag{1.13}$$

The last important parameter is the ratio between the pressure forces against the magnetic forces. It is called beta β parameter and is defined as

$$\beta = \frac{2p}{|\boldsymbol{B}|^2}. \tag{1.14}$$

With these parameters it is possible to evaluate some characteristics of the confinement.

1.3.2 Configurations

At the beginning of the tokamak research it was realized that if the fusion reaction was successful, the heavier ions resulting from the process, the so called fusion ashes, would be left in the fuel. They are impurities that can cause problems for the ongoing of the reaction since they can lower the temperature of the fuel and can cause some other unexpected reactions. To avoid these problems, the idea of a divertor target was proposed. The idea is: the heavy ions would be flung away due to the centrifugal force, then some absorbing material, the divertor targets, would be put in their way removing them from the fuel. Another function of the divertor would be the prevention of the contact between particles that could occasionally leave the core of the plasma and the wall. It is an important issue because these particles carry a high amount of energy and they could seriously damage the wall. They can also knock out atoms from the material composing the wall which in turn would eventually come back into the plasma core as impurities.

To overcome that, two main configurations using divertors for tokamak were developed. The first one is known as limiter configuration and the second one is simply called

divertor configuration. Nevertheless, due to its particular magnetic configuration, it is often referred to as X-point configuration.

1.3.2.1 Limiter Configuration

During the 80s the limiter configuration became very popular. In this configuration a small piece of material is included in a short distance into the outer edge of the plasma confinement area (Figure (1.6a)). By doing this, the ions going outwards would strike the limiter before hitting the walls and thus would not damage them. This do not solve, on the other hand, the problem of material being deposited in the fuel as the limiter was placed in contact with the plasma. For this reason, another configuration was developed.

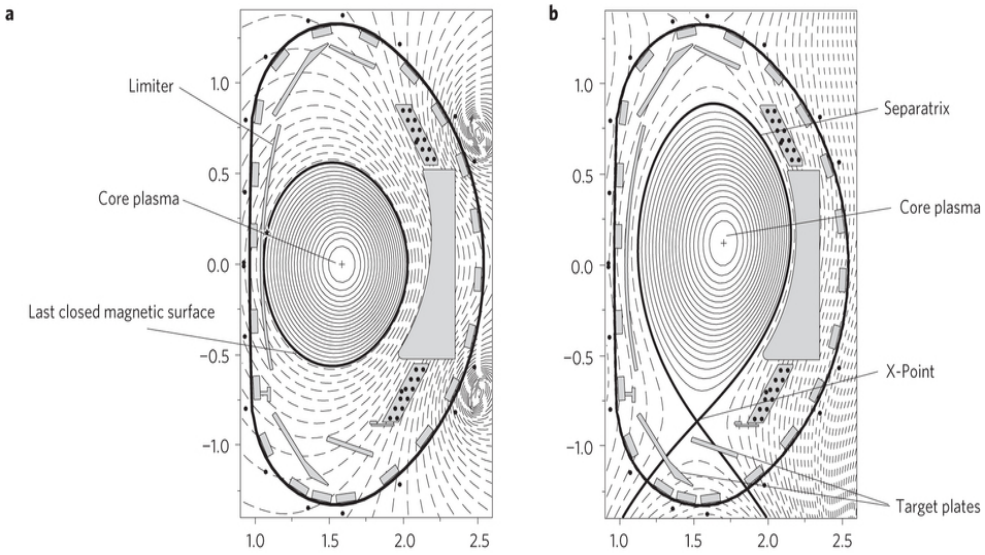

FIGURE 1.6: Scheme showing the main components of a a) limiter plasma and b)X-point plasma [29]

1.3.2.2 Divertor Configuration

In the divertor configuration, the magnetic field is configured in a way that the lower edge of the plasma is deformed such that a small region on the outer edge hits the targets, i.e., the divertors (details in Figure (1.6b)). This creates two different regions inside the device. One where the magnetic lines are closed, i.e., the core plasma that is limited by the last closed magnetic line, known as separatrix; and another one in which the lines are open; known as Scrape-Off layer (SOL). At its bottom, the separatrix has a X-shaped interception and that is why this configuration is often referred to as X-point configuration.

The divertors improve the limiter in several ways, but specially because the modern reactors try to create D-shaped cross-sections making the lower edge of the D the optimal spot for the targets. Here, the particles escape through the separatrix to meet the open lines in the SOL and this allows the divertor to be outside the plasma. This configuration also makes it easier to obtain the more stable H-mode of operation described in the next section.

1.3.2.3 H-Mode

At the beginning of the 80s something very unexpected was observed at the ASDEX tokamak in Germany. In fact, it is intuitive to think that the more you heat the plasma the more it will become unstable since temperature is related to agitation. Nevertheless, the opposite was observed. After increasing the heating power above a certain threshold, an abrupt transition happened and after that the confinement was improved [30]. Indeed, a transport barrier appeared at the inner region of the separatrix improving the confinement time by a factor 2.

This transport bifurcation is the consequence of a self organizing process in the plasma and it is due to the suppression of turbulence on its edge which is, itself, the consequence of the formation of a sheared flow layer and an associated edge radial electric field. It leads to a reduction of transport and a steepening of the edge profiles, forming the so called pedestal region [31]. A scheme of the temperature profile (and as a consequence, the pressure one) before and after the transition is shown in Figure (1.7).

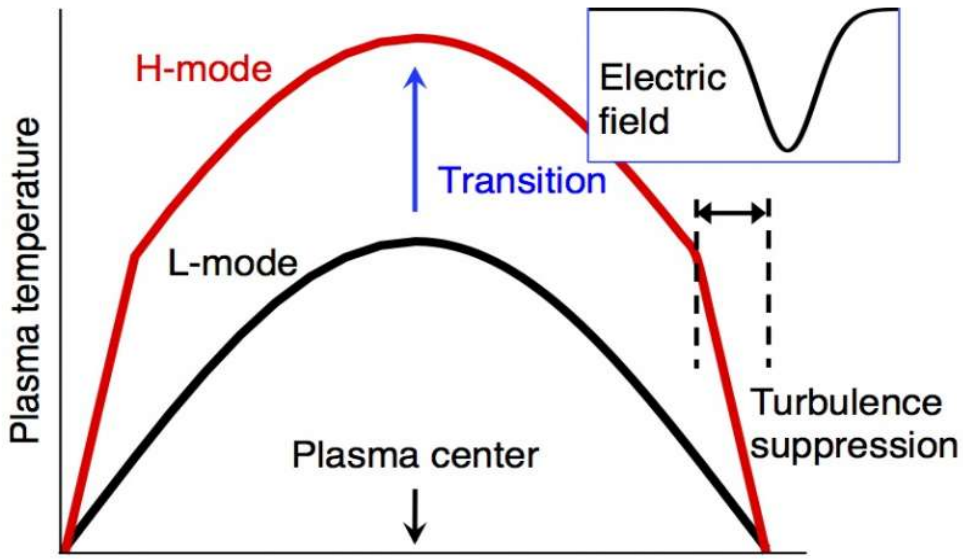

FIGURE 1.7: A scheme of the profiles for L and H-mode. The sharp gradient region, i.e., the pedestal can be clearly seen (the straight part of the red line)[32]

This mode of confinement has received the name H-mode for High confinement mode and its counterpart is called L-mode for Low confinement mode. It has become, since its first observation, the reference mode of operation for the current tokamaks. Nevertheless, it brings some drawbacks with it since very sharp pressure gradients, that can be very unstable, develop near the separatrix creating a turbulence region around the edge of the plasma.

1.3.3 Instabilities

One of the main challenges for the success of the controlled fusion using the magnetic confinement in tokamakas is the development of instabilities. It has been observed since the beginning of the studies with these devices that they are subjected to different kinds of macroscopic instabilities and some of them can be very damaging for the plasma and the machine as well.

Starting from an equilibrium state, the perturbation forces can either lead to a stable state or trigger an instability. When the first happens an oscillation around the equilibrium point is observed that might bring the system back to its original equilibrium, if the oscillations are damped. If, on the other hand, these perturbations are the source of an instability, they create oscillations that have an exponential growth which can make the control of the plasma very difficult.

In a single-fluid model the instabilities are very often caused by current or pressure gradients. They would, thus, be referred to as current mode or pressure mode accordingly to the mechanism behind it (details in Chapter 5).

Pressure related instabilities can be divided into two groups called interchange and ballooning modes. We are more concerned here with the second type. The ballooning mode is a perturbation of the equilibrium between outward directed forces caused by the particle pressure and the curvature drift on one side and inward directed forces exerted by the tangential stress of the field lines on the other side. A certain analogy could be made to the Rayleigh-Taylor instability. They are macroscopic pressure modes evolving slowly along the magnetic field lines. When the presure gradient is steep near the separatrix, ballooning modes could trigger some successive crashes leading to a loss of pressure. These instabilities are known as Edge-localized modes (ELM) [33].

The current driven instabilities are the kink mode instabilities, which can be internal or external. The external ones are the more dangerous to the tokamak operations. In order to avoid them, the safety factor q close to the edge must be high ($\approx 3-5$) which means that the current must decrease very fast around the edge of the plasma. The

internal kink is responsible for instabilities at the plasma core and can trigger another instability called the sawtooth instability.

The edge localized modes which play a crucial role for the operation of the current and future tokamaks and the internal kink, of which more details will be shown on Chapter 5, will be briefly discussed here.

Edge-localized modes (ELM)

Edge localized modes (ELM) are disruptive instabilities happening on the edge of the plasma. They are powerful phenomena that can degrade the whole plasma and sometimes even damage to device. They are the consequence of quasi-periodic relaxations of the transport barrier formed during the transition from L to H mode.

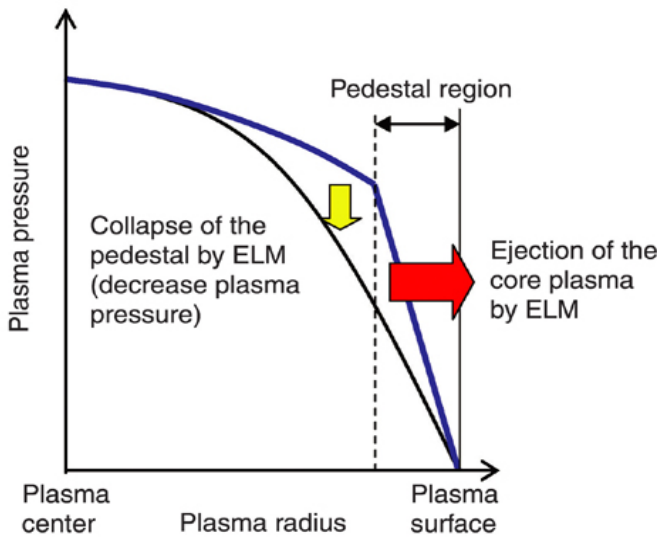

FIGURE 1.8: A scheme of the ELM dynamics: a relaxation of the transport barrier (pedestal) leads to a mass ejection and a possible collapsing of the pressure profile

As shown in Figure (1.8), this relaxation can cause the collapse of the pressure profile as mass ejections through the separatrix take place. This poses major challenges to fusion plasmas because it can damage the walls of the device, specially the divertor targets, as the matter ejected from the plasma core has an elevated temperature.

Research involving prevention of edge localized mode formation is underway. There is, for example, a suggested method of countering this phenomenon by injecting static magnetic noisy energy into the plasma as a containment-stabilization regime which may decrease ELM amplitude [34]. Another strategy consists of using pellet (made from frozen solid fuel) injections to increase the frequency and thereby decrease the severity of ELM bursts.

Internal kink instability

The kink instability occurs in a current carrying plasma when the current exceeds a critical value and it is due to the non-uniformity of the current. Even though this is mainly a current driven instability, the pressure also plays a role. It was shown that if the pressure is sufficiently low the plasma is stable and if it exceeds a threshold value it becomes unstable [35].

This instability can be compared to the twisting of a rubber string, if the twisting exceeds a threshold, the rubber string develops helical deformation. In a tokamak, the twisting of the magnetic field is provided by the poloidal magnetic field produced by the current and similar plasma deformations occur.

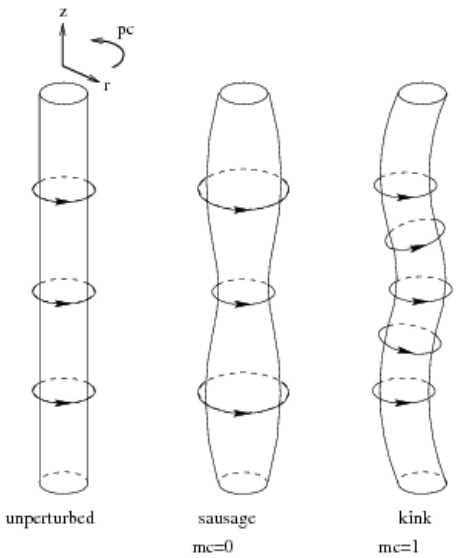

FIGURE 1.9: Deformation caused by a kink instability occurring in a plasma column

The internal kink instability is located at the magnetic mode rational surfaces, i.e, magnetic flux surfaces that are closed. Figure (1.9) shows the shape of the deformation caused by a kink in a plasma column.

As the kink modes develop in fixed zones of the plasma, they are classified as absolute plasma instabilities, as opposed to convective processes. A more detailed description and analysis of this instability will be done in Chapter 5.

1.4 Perspectives: ITER and the future of fusion

Since the beginning of the research concerning tokamaks several different devices have been built and they all contributed at some point to the fusion research field. As the times passes, they have become larger and more complex as well as the phenomena

happening in the plasma they contain. The biggest tokamak in operation today is the already mentioned JET. It has contributed with several results concerning the physics of plasmas. Nevertheless, to achieve not only a stable reaction but also a economically exploitable machine, larger devices are needed.

The International Thermonuclear Experimental Reactor, ITER (which also means The Way in Latin) is under construction in order to prove the viability of the fusion power as a carbon-free and large scale source of energy. The idea for the joint project was launched in 1985 and today there are 35 countries collaborating: China, the European Union, India, Japan, Russia, South Korea and the United States. The installation is being built near to Aix-en-Provence in southern France.

In comparison with JET, it will have a bigger volume and then be able to deal with a more considerable amount of plasma. A representation of the device is shown in Figure (1.10).

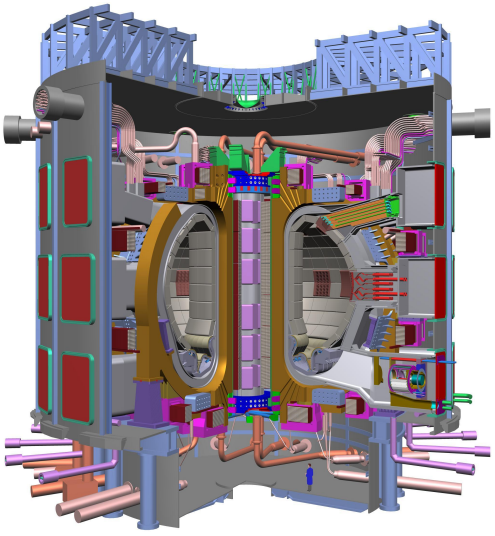

FIGURE 1.10: Representation of the future tokamak [36]

It is important to highlight though that ITER would still be a device built for research purpose only. It means that it will not be able to be economically exploitable and commercialized. For this, a successor has already been planned: DEMO, which would be able to hold a volume even bigger than ITER (Figure (1.11)).

The parameter usually used to measure these devices is the major radius R_0. For JET, it is about $3m$ while for ITER it is planned to be $6m$, DEMO would have a $9m$ major radius. The reason for the increasing in size is that experimental observations have shown that the confinement time is proportional to a power of R, more precisely $R^{1.97}$.

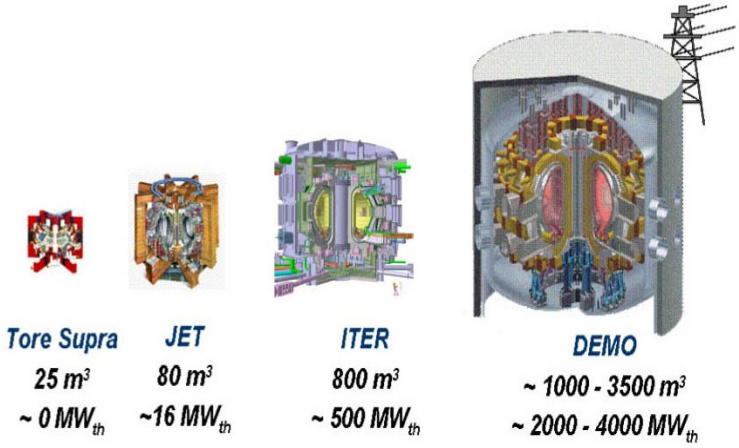

FIGURE 1.11: Comparison between current and future tokamaks

1.5 Conclusions

In this Chapter the basic ideas behind the generation of energy via fusion power were presented. Taking inspiration from the stars, an ambitious quest started more than half a century ago, the quest for a clean source of energy. The concepts involved in the fusion process were briefly described and the challenges related to their reproduction and control in a laboratory have been discussed. At the temperatures needed for fusion to happen, the fuel must be in a fully ionized state called plasma.

Knowing the properties of plasmas allowed researches to come up with an idea to develop a device that could be able to contain it, despite the elevated temperatures. The core of the mechanism is the fact that charged particles such as the ones present in the plasma can be trapped in a magnetic field. This toroidal device called tokamak has been subjected to intense studies since then. Its main characteristics like shape, configuration and certain types of phenomena happening inside, e.g., instabilities were shown. It is important to discuss briefly the macroscopic instabilities occurring in a tokamak because they can be very challenging to deal with and could really prevent the optimal operation of the device. There is a large number of studies related to plasma instabilities.

Finally the perspectives for the future of the fusion domain have been summarized with some details about ITER, the tokamak under construction that is expected to show the viability of this new source of energy. Several challenges still remain concerning the plasma dynamics inside the reactor and that is why the number of studies in this field has been increasing lately.

Chapter 2

Plasma modeling: Magnetohydrodynamic (MHD) models

Magnetohydrodynamics (MHD) is a single-fluid theory describing a charged fluid. Its name and basis are due to the Swedish astrophysicist Hannes Alfvén. In 1942, he published a paper that announced the discovery of the wave that now bears his name [37], and that is now often regarded as marking the birth of magnetohydrodynamics or MHD for short. In interpreting the waves in an associated paper [38], he enunciated a result that has become known as Alfvén's theorem:

Suppose that we have a homogeneous magnetic field in a perfectly conducting fluid[...]. In view of the infinite conductivity, every motion (perpendicular to the field) of the liquid in relation to the lines of force is forbidden because it would give infinite eddy currents. Thus the matter of the liquid is fastened to the lines of force[...]

From the end of the 40s, the studies on the domain of controlled fusion have multiplied. The MHD, that was initially used for studying space plasmas is fast applied to fusion plasmas which provided an experimental frame for it. Until today it is an unavoidable theory for the study of tokamak plasmas. Currently, several codes use MHD equations on their models, namely M3D [39, 40], M3D-C1 [8] which uses C^1 finite-elements, JOREK developed at CEA (French Alternative Energies and Atomic Energy Commission) Cadarache [9, 10] and also BOUT++ [41].

The fundamental concept behind MHD is that magnetic fields can induce currents in a moving conductive fluid, which in turn polarizes the fluid and reciprocally changes the magnetic field itself. The set of equations that describe MHD are a combination of

the Navier-Stokes equations of fluid dynamics and Maxwell's equations of electromagnetism. These differential equations must be solved simultaneously, either analytically or numerically.

This chapter presents the derivation of the different MHD models starting with the fundamental plasma models (2.1) - Kinetic and Fluid models - that are at the basis of the MHD theory. Then, the Full MHD model (2.2) is developed from a multifluid description of the plasma. The aspects of the Maxwell's equations, such as the divergence free constraint, the problems that may rise from it and the possible solutions are discussed (2.1.3). Several elements and assumptions of the model such as the Ohm's law and quasi-neutrality are discussed and their effects on the model are described. Next, by using the Full MHD model in the quasi-neutral regime (2.2.1.4) as the basis model together with the hypothesis that allow it simplifications, the Ideal model (2.2.2), from which the spectral analysis of the system is done, is obtained. Then, the Resistive (2.2.3) and Reduced Resistive (2.2.4) models are presented along with the Grad-Shafranov equilibrium (2.2.4.1) that plays an important role in the discretization of the model.

2.1 Fundamental plasma models

At the microscopic scale, plasmas are composed by particles as, for instance, ions and electrons. Thus, if one wants to model a plasma, the most direct and general way is by the use of a particular model, i.e., a model in which the fundamental principle of dynamics is written for each particle considering that they are submitted to an electromagnetic field. However, as the number of particles present even in a small volume of plasma can be very high, this approach is not always practicable. It is then necessary to use a statistical approach in which plasmas are described in terms of distribution functions f_σ for particles of a given type σ in a seven-dimensional space following the position $\boldsymbol{r}$, the velocity $\boldsymbol{u}$ and the time t. The evolution of the distribution function is described by the kinetic theory. The advantage of this model is that it gives the distribution of the velocities of a particle whithin a fluid element. Nevertheless, this information is not always necessary and, under certain assumptions, it can be simplified leading to a fluid model.

The fluid equations of neutral gases and liquids are usually derived by treating the fluid as a continuous medium and considering the dynamics of a small volume of the fluid. The aim is to develop a macroscopic model that, as far as possible, is independent of the detail of what happens at the molecular level. The same concept can be applied to plasmas, specially since experimentally one seldom makes measurements or observations at the microscopic level. Thus, a macroscopic description is required and it can be obtained

by using the first moments, in the velocity space, of the kinetic formulation. In the resulting model, known as fluid model, the plasma is described in a simpler way by its macroscopic variables, like the density n, the average velocity $\boldsymbol{v}$, the temperature T and so on. It is important to highlight though that the plasma is not really one fluid but at least two, one consisting of ions and the other electrons. The fact that these two fluids are comprised of particles with opposite charges and very unequal masses gives rise to phenomena that do not occur in neutral fluids. Nonetheless, a single fluid description of a plasma is in many situations a useful and plausible model and one that is widely employed.

2.1.1 Kinetic model

The Kinetic or Vlasov model [42–44] is used for a microscopic approach as it studies the behavior of the particles constituting the plasma. At each instant, each particle has a particular position and velocity. It is possible, then, to characterize the instantaneous configuration of a big number of particles by a specific density at each point in the phase-space. For that, a distribution function of each σ particle, denoted $f_\sigma(\boldsymbol{r}, \boldsymbol{u}, t)$ is introduced. It gives the instantaneous density of these particles at the position $\boldsymbol{r}$, having velocity $\boldsymbol{u}$ at the time t. For the sake of compactness and, considering that most numerical tools used to deal with the equations shown in this chapter use normalized quantities in order to simplify the implementation, all the physical constants like ε_0 and μ_0, for example, will not be explicitly written on the equations. The temporal evolution of the distribution function is described by Boltzmann equation [42]

$$\frac{\partial f_\sigma}{\partial t} + \boldsymbol{u} \cdot \frac{\partial f_\sigma}{\partial \boldsymbol{r}} + \frac{q_\sigma}{m_\sigma}(\boldsymbol{E} + \boldsymbol{u} \times \boldsymbol{B}) \cdot \frac{\partial f_\sigma}{\partial \boldsymbol{u}} = C_\sigma, \tag{2.1}$$

where $\boldsymbol{E}$ and $\boldsymbol{B}$ are, respectively, the electric and magnetic fields and C_σ represents the changes in the distribution function due to collisions. The first term gives the temporal variation of f_σ. Then, as $\boldsymbol{r}$ and $\boldsymbol{u}$ are independent, the second term can be written as

$$\boldsymbol{u} \cdot \frac{\partial f_\sigma}{\partial \boldsymbol{r}} = \frac{\partial (\boldsymbol{u} f_\sigma)}{\partial \boldsymbol{r}}. \tag{2.2}$$

It represents the particles convection at the velocity $\boldsymbol{u}$. The last term represents the particles acceleration due to the electromagnetic field

$$\boldsymbol{a}_\sigma = \frac{q_\sigma}{m_\sigma}(\boldsymbol{E} + \boldsymbol{u} \times \boldsymbol{B}), \tag{2.3}$$

where, for each σ particle, q_σ is its charge and m_σ its mass.

The collision term is characterized by

$$C_\sigma = \sum_\alpha C_{\sigma\alpha}(f_\sigma, f_\alpha), \tag{2.4}$$

where $C_{\sigma\alpha}(f_\sigma, f_\alpha)$ represents the exchange between the distribution functions f_σ and f_α due to the collisions between α and σ particles. This operator must satisfy some constraints connected to the conservation of particles density, momentum and energy [42, 43]:

- Collisions cannot change the total number of particles

$$\int C_{\sigma\alpha} d\boldsymbol{u} = 0. \tag{2.5}$$

- Collisions between the same type of particles do not increase the momentum

$$\int m_\sigma \boldsymbol{u} C_{\sigma\sigma} d\boldsymbol{u} = 0. \tag{2.6}$$

  At the same time, collisions between different types of particles do not change the sum of their momenta

$$\int m_\sigma \boldsymbol{u} C_{\sigma\alpha} d\boldsymbol{u} + \int m_\alpha \boldsymbol{u} C_{\alpha\sigma} d\boldsymbol{u} = 0. \tag{2.7}$$

- The same is valid for the energy. Collisions between the same type of particles do not increase the total energy of this type

$$\int m_\sigma \boldsymbol{u}^2 C_{\sigma\sigma} d\boldsymbol{u} = 0. \tag{2.8}$$

  Neither does the sum of the total energies in the case of collisions between different types of particles

$$\int m_\sigma \boldsymbol{u}^2 C_{\sigma\alpha} d\boldsymbol{u} + \int m_\alpha \boldsymbol{u}^2 C_{\alpha\sigma} d\boldsymbol{u} = 0. \tag{2.9}$$

Boltzmann Equation (2.1) allows us to model strong collisional plasmas. If we need, on the other hand, to describe weak collisional, e.g., tokamak plasmas, or collisionless plasmas, Vlasov equation is more suitable because it does not take into account the collision term [42]

$$\frac{\partial f_\sigma}{\partial t} + \boldsymbol{u} \cdot \frac{\partial f_\sigma}{\partial \boldsymbol{r}} + \frac{q_\sigma}{m_\sigma}(\boldsymbol{E} + \boldsymbol{u} \times \boldsymbol{B}) \cdot \frac{\partial f_\sigma}{\partial \boldsymbol{u}} = 0. \tag{2.10}$$

This kinetic formulation is the only truly valid formulation for a plasma. It implies however very heavy calculations and often is not viable. For this reason, it is useful to appeal to a simplified formulation, like for instance the Fluid model. This simplification reduces the velocity space and increases the spatiotemporal scales.

2.1.2 Fluid model: multifluid MHD

This model is obtained from the different moments of the kinetic equation. The plasma will be then described by its macroscopic variables. In the phase-space, the density $n_\sigma(t, \boldsymbol{r})$ of σ particles at the position $\boldsymbol{r}$ and time t is defined by

$$n_\sigma(t, \boldsymbol{r}) = \int_{\mathbb{R}^3} f_\sigma(t, \boldsymbol{r}, \boldsymbol{u}) d\boldsymbol{u}. \tag{2.11}$$

The mean velocity $\boldsymbol{v}$ can be defined by taking into account the 1st order moment of the distribution function

$$n_\sigma(t, \boldsymbol{r})\boldsymbol{v}_\sigma(t, \boldsymbol{r}) = \int_{\mathbb{R}^3} \boldsymbol{u} f_\sigma(t, \boldsymbol{r}, \boldsymbol{u}) d\boldsymbol{u}. \tag{2.12}$$

In the same way, the temperature is defined by the 2nd order moment

$$T_\sigma(t, \boldsymbol{r}) = \frac{1}{n_\sigma} \int_{\mathbb{R}^3} \frac{m_\sigma}{3} (\boldsymbol{u} - \boldsymbol{v}_\sigma)^2 f_\sigma(t, \boldsymbol{r}, \boldsymbol{u}) d\boldsymbol{u}. \tag{2.13}$$

Generally, these macroscopic parameters are different for each type of particle when not in an equilibrium state. By using them we can define a current density $\boldsymbol{J}$

$$\boldsymbol{J} = \sum_\sigma q_\sigma n_\sigma \boldsymbol{v}_\sigma. \tag{2.14}$$

The different moments of the distribution function have been obtained by multiplying it by different powers of $\boldsymbol{u}$ and then performing an integration. The same idea can be applied to the kinetic equation (2.1) in order to obtain conservation equations. Let's consider a generic function $g(\boldsymbol{u})$ such that

$$\int_{\mathbb{R}^3} \left[\frac{\partial f_\sigma}{\partial t} + \nabla_{\boldsymbol{r}} \cdot (\boldsymbol{u} f_\sigma) + \nabla_{\boldsymbol{u}} \cdot (\boldsymbol{a}_\sigma f_\sigma) \right] g(\boldsymbol{u}) d\boldsymbol{u} = \int_{\mathbb{R}^3} \sum_\alpha C_{\sigma\alpha} g(\boldsymbol{u}) d\boldsymbol{u}. \tag{2.15}$$

Then, by taking $g(\boldsymbol{u})$ as being the 0th, 1st and 2nd moments, different relations can be obtained.

Mass continuity equation

At first, for the 0th order moment, $g(\boldsymbol{u}) = 1$ yielding

$$\int_{\mathbb{R}^3} \left[\frac{\partial f_\sigma}{\partial t} + \nabla_{\boldsymbol{r}} \cdot (\boldsymbol{u} f_\sigma) + \nabla_{\boldsymbol{u}} \cdot (\boldsymbol{a}_\sigma f_\sigma) \right] d\boldsymbol{u} = \int_{\mathbb{R}^3} \sum_\alpha C_{\sigma\alpha} d\boldsymbol{u}. \tag{2.16}$$

The derivation terms and the integral can be commuted due to the fact that in the fluid model the variables $\boldsymbol{r}$, $\boldsymbol{u}$ and t are independent. Additionally, accordingly to Gauss theorem the third term on the left hand side will be zero. Finally, combining the above equation with equations (2.11), (2.12) and (2.5) leads to the mass continuity equation for the particles

$$\frac{\partial n_\sigma}{\partial t} + \nabla_{\boldsymbol{r}} \cdot (n_\sigma \boldsymbol{v}_\sigma) = 0 \tag{2.17}$$

Momentum equation

Now, taking $g(\boldsymbol{u}) = \boldsymbol{u}$

$$\int_{\mathbb{R}^3} \boldsymbol{u} \left[\frac{\partial f_\sigma}{\partial t} + \nabla_{\boldsymbol{r}} \cdot (\boldsymbol{u} f_\sigma) + \nabla_{\boldsymbol{u}} \cdot (\boldsymbol{a}_\sigma f_\sigma) \right] d\boldsymbol{u} = \int_{\mathbb{R}^3} \boldsymbol{u} \sum_\alpha C_{\sigma\alpha} d\boldsymbol{u}. \tag{2.18}$$

The second term on the left hand side can be rewritten, since $\nabla_{\boldsymbol{r}} \cdot (f\boldsymbol{u})\boldsymbol{u} = \nabla_{\boldsymbol{r}} \cdot ((\boldsymbol{u} \otimes \boldsymbol{u}) f)$ and a combination with (2.12) leads to

$$\partial_t (n_\sigma \boldsymbol{v}_\sigma) + \nabla_{\boldsymbol{r}} \cdot \int_{\mathbb{R}^3} ((\boldsymbol{u} \otimes \boldsymbol{u}) f_\sigma) d\boldsymbol{u} + \int_{\mathbb{R}^3} \boldsymbol{u} \nabla_{\boldsymbol{u}} \cdot (\boldsymbol{a}_\sigma f_\sigma) d\boldsymbol{u} = \int_{\mathbb{R}^3} \boldsymbol{u} \sum_\alpha C_{\sigma\alpha} d\boldsymbol{u}. \tag{2.19}$$

Now, it is better to work equation (2.19) term by term. The first one is already in a suitable form. To deal with the second a variable change is performed $\boldsymbol{u} = \boldsymbol{v}_\sigma(\boldsymbol{r}, t) + \boldsymbol{\kappa}(\boldsymbol{r}, t)$ where $\boldsymbol{\kappa}$ represents the random part of a given velocity. Thus, $d\boldsymbol{u} = d\boldsymbol{\kappa}$ and knowing that the tensorial product is bilinear, this term can be rewritten in the following way

$$\begin{aligned} \int_{\mathbb{R}^3} ((\boldsymbol{u} \otimes \boldsymbol{u}) f_\sigma) d\boldsymbol{u} \quad = \quad & \int_{\mathbb{R}^3} ((\boldsymbol{v}_\sigma \otimes \boldsymbol{v}_\sigma) f_\sigma) d\boldsymbol{\kappa} + \int_{\mathbb{R}^3} ((\boldsymbol{v}_\sigma \otimes \boldsymbol{\kappa}) f_\sigma) d\boldsymbol{\kappa} \\ & + \int_{\mathbb{R}^3} ((\boldsymbol{\kappa} \otimes \boldsymbol{v}_\sigma) f_\sigma) d\boldsymbol{\kappa} + \int_{\mathbb{R}^3} ((\boldsymbol{\kappa} \otimes \boldsymbol{\kappa}) f_\sigma) d\boldsymbol{\kappa}, \end{aligned} \tag{2.20}$$

which can be simplified by taking into account (2.12) and the relation that comes from it $\int \boldsymbol{\kappa} f_\sigma d\boldsymbol{\kappa} = 0$

$$\int_{\mathbb{R}^3} ((\boldsymbol{u} \otimes \boldsymbol{u}) f_\sigma) d\boldsymbol{u} = n_\sigma (\boldsymbol{v}_\sigma \otimes \boldsymbol{v}_\sigma) + 0 + 0 + \int_{\mathbb{R}^3} ((\boldsymbol{\kappa} \otimes \boldsymbol{\kappa}) f_\sigma) d\boldsymbol{\kappa}. \tag{2.21}$$

Finally, for the third term, an integration by parts in the velocity space yields

$$\int_{\mathbb{R}^3} \boldsymbol{u} \nabla_{\boldsymbol{u}} \cdot (\boldsymbol{a}_\sigma f_\sigma) d\boldsymbol{u} = -\frac{n_\sigma q_\sigma}{m_\sigma} (\boldsymbol{E} + \boldsymbol{v}_\sigma \times \boldsymbol{B}). \tag{2.22}$$

Therefore, the momentum equation for the particles σ is

$$m_\sigma \left[\partial_t(n_\sigma \boldsymbol{v}_\sigma) + \nabla_{\boldsymbol{r}} \cdot (n_\sigma \boldsymbol{v}_\sigma \otimes \boldsymbol{v}_\sigma)\right] - n_\sigma q_\sigma(\boldsymbol{E} + \boldsymbol{v}_\sigma \times \boldsymbol{B}) = \\ -m_\sigma \nabla_{\boldsymbol{r}} \cdot \int_{\mathbb{R}^3} ((\boldsymbol{\kappa} \otimes \boldsymbol{\kappa}) f_\sigma) d\boldsymbol{\kappa} + \int_{\mathbb{R}^3} m_\sigma \boldsymbol{u} \sum_\alpha C_{\sigma\alpha} d\boldsymbol{u}.$$

If f_σ is an isotropic function of $\boldsymbol{\kappa}$, the diagonal terms in the tensor

$$\int_{\mathbb{R}^3} (m_\sigma (\boldsymbol{\kappa} \otimes \boldsymbol{\kappa}) f_\sigma) d\boldsymbol{\kappa}$$

are identical and define, in this case, a scalar pressure p_σ, hence

$$p_\sigma = \int_{\mathbb{R}^3} m_\sigma \frac{|\boldsymbol{\kappa}|^2}{3} f_\sigma d\boldsymbol{\kappa} = n_\sigma T_\sigma.$$

In the end, the momentum equation is

$$m_\sigma \left[\partial_t(n_\sigma \boldsymbol{v}_\sigma) + \nabla_{\boldsymbol{r}} \cdot (n_\sigma \boldsymbol{v}_\sigma \otimes \boldsymbol{v}_\sigma)\right] - n_\sigma q_\sigma(\boldsymbol{E} + \boldsymbol{v}_\sigma \times \boldsymbol{B}) + \nabla_{\boldsymbol{r}} p_\sigma = \nabla_{\boldsymbol{r}} \cdot \underline{\boldsymbol{\pi}}_\sigma + \boldsymbol{R}_\sigma, \quad (2.23)$$

in which $\underline{\boldsymbol{\pi}}_\sigma$ and $\boldsymbol{R}_\sigma$ are, respectively, the viscous stress tensor and the friction coefficient. These two transport coefficients are defined as

$$\underline{\boldsymbol{\pi}}_\sigma = \int_{\mathbb{R}^3} m_\sigma \left(\boldsymbol{\kappa} \otimes \boldsymbol{\kappa} - \frac{|\boldsymbol{\kappa}|^2}{3} \mathbb{I}\right) f_\sigma d\boldsymbol{\kappa}, \quad (2.24)$$

$$\boldsymbol{R}_\sigma = \int_{\mathbb{R}^3} m_\sigma \boldsymbol{\kappa} \sum_\alpha C_{\sigma\alpha} d\boldsymbol{\kappa}. \quad (2.25)$$

Energy Equation

Finally, taking $g(\boldsymbol{u}) = m_\sigma \frac{\boldsymbol{u}\cdot\boldsymbol{u}}{2}$ yields

$$\int_{\mathbb{R}^3} \frac{m_\sigma \boldsymbol{u}^2}{2} \left[\frac{\partial f_\sigma}{\partial t} + \nabla_{\boldsymbol{r}} \cdot (\boldsymbol{u} f_\sigma) + \nabla_{\boldsymbol{u}} \cdot (\boldsymbol{a}_\sigma f_\sigma)\right] d\boldsymbol{u} = \int_{\mathbb{R}^3} \frac{m_\sigma \boldsymbol{u}^2}{2} \sum_\alpha C_{\sigma\alpha} d\boldsymbol{u}. \quad (2.26)$$

The development of the above equation is similar to the one done on the momentum equation and leads to the energy conservation equation

$$\partial_t \rho_\sigma e_\sigma + \nabla_{\boldsymbol{r}} \cdot [(\rho_\sigma e_\sigma + p_\sigma)\boldsymbol{v}_\sigma + \underline{\boldsymbol{\pi}}_\sigma : \boldsymbol{v}_\sigma] - q_\sigma n_\sigma (\boldsymbol{v}_\sigma \cdot \boldsymbol{E}) = \nabla_{\boldsymbol{r}} \cdot \boldsymbol{Q}_\sigma + \boldsymbol{v}_\sigma \cdot \boldsymbol{R}_\sigma + \mathcal{Q}_\sigma, \quad (2.27)$$

with the energy $\rho_\sigma e_\sigma$ defined as

$$\rho_\sigma e_\sigma = m_\sigma n_\sigma \frac{|\boldsymbol{v}_\sigma|^2}{2} + \frac{p_\sigma}{\gamma - 1}, \quad (2.28)$$

in which, $\gamma = \frac{5}{3}$ is the heat capacity ratio. The heat flux $\boldsymbol{Q}_\sigma$ and the heat generated by collisions between particles $\mathcal{Q}_\sigma$ are defined as

$$\boldsymbol{Q}_\sigma = \int_{\mathbb{R}^3} m_\sigma \frac{|\boldsymbol{\kappa}|^2}{2} \boldsymbol{\kappa} f_\sigma d\boldsymbol{\kappa}, \tag{2.29}$$

$$\mathcal{Q}_\sigma = \int_{\mathbb{R}^3} m_\sigma \frac{|\boldsymbol{\kappa}|^2}{2} \sum_{\alpha \neq \sigma} C_{\sigma\alpha} d\boldsymbol{\kappa}. \tag{2.30}$$

Together, these three moments obtained from the kinetic equation generate the following system of conservation laws

$$\begin{cases} \partial_t n_\sigma + \nabla_{\boldsymbol{r}} \cdot (n_\sigma \boldsymbol{v}_\sigma) = 0, \\ m_\sigma \left[\partial_t (n_\sigma \boldsymbol{v}_\sigma) + \nabla_{\boldsymbol{r}} \cdot (n_\sigma \boldsymbol{v}_\sigma \otimes \boldsymbol{v}_\sigma)\right] - n_\sigma q_\sigma (\boldsymbol{E} + \boldsymbol{v}_\sigma \times \boldsymbol{B}) + \nabla_{\boldsymbol{r}} p_\sigma \\ \qquad = \nabla_{\boldsymbol{r}} \cdot \underline{\boldsymbol{\pi}}_\sigma + \boldsymbol{R}_\sigma, \\ \partial_t \rho_\sigma e_\sigma + \nabla_{\boldsymbol{r}} \cdot [(\rho_\sigma e_\sigma + p_\sigma)\boldsymbol{v}_\sigma + \underline{\boldsymbol{\pi}}_\sigma : \boldsymbol{v}_\sigma] - q_\sigma n_\sigma (\boldsymbol{v}_\sigma \cdot \boldsymbol{E}) = \nabla_{\boldsymbol{r}} \cdot \boldsymbol{Q}_\sigma + \boldsymbol{v}_\sigma \cdot \boldsymbol{R}_\sigma + \mathcal{Q}_\sigma. \end{cases} \tag{2.31}$$

The magnetic and electric fields, $\boldsymbol{B}$ and $\boldsymbol{E}$, are described by Maxwell's equations. For the transport coefficients: momentum transfer $\boldsymbol{R}_\sigma$, particle heating $\mathcal{Q}_\sigma$ and heat flux $\boldsymbol{Q}_\sigma$, several different methods are proposed to approach them [43, 45–47]. Their goal has been to give an approximation of these coefficients as a function of the macroscopic data in order to bring closure relations to the fluid models. A widely known method to derive them is the one proposed by Braginskii [43] in which an asymptotic development in small parameters of the kinetic equation is performed followed by a dimensional analysis. Details of these calculations can be found in [48], in which the following relations were obtained for the transport coefficients for ions i and electrons e

$$\text{Electrons:} \begin{cases} \boldsymbol{R}_e = \alpha \delta \boldsymbol{v} + \underline{\boldsymbol{\beta}}^t \boldsymbol{\partial_x} T_e, \\ \mathcal{Q}_e = -\dfrac{3 m_e n_e}{m_i \tau_e} \delta T - \delta \boldsymbol{v} \cdot \boldsymbol{R_e}, \\ \boldsymbol{Q}_e = -\underline{\boldsymbol{\kappa}}_e \boldsymbol{\partial_x} T_e - \underline{\boldsymbol{\beta}}_e^j \delta \boldsymbol{v}, \\ \underline{\boldsymbol{\pi}}_e = \displaystyle\sum_{l=0}^{4} \eta_{el} \underline{\boldsymbol{\Pi}}_l (\boldsymbol{v}_e, \boldsymbol{b}), \end{cases}, \text{ Ions:} \begin{cases} \boldsymbol{R}_i = -\boldsymbol{R}_e, \\ \mathcal{Q}_i = \dfrac{3 m_e n_e}{m_i \tau_e} \delta T, \\ \boldsymbol{Q}_i = -\underline{\boldsymbol{\kappa}}_i \boldsymbol{\partial_x} T_e, \\ \underline{\boldsymbol{\pi}}_i = \displaystyle\sum_{l=0}^{4} \eta_i \underline{\boldsymbol{\Pi}}_l (\boldsymbol{v}_i, \boldsymbol{b}), \end{cases} \tag{2.32}$$

where α and $\underline{\boldsymbol{\beta}}^t$ are perturbation factors related to the difference in the velocities $\delta \boldsymbol{v} = \boldsymbol{v}_e - \boldsymbol{v}_i$ and the temperature, τ_e is the collisional characteristic time, $\eta_{el/i}$ is the viscosity related to electrons/ions, $\underline{\boldsymbol{\Pi}}_l$ are matrices obtained from the development of the constraint tensor proposed in [43] and $\boldsymbol{b}$ is the normalized magnetic field, i.e., $\frac{\boldsymbol{B}}{|\boldsymbol{B}|}$. More explicit relations of these coefficients can be found at the NRL Plasma Formulary (Pages 36-39) [49].

2.1.3 Maxwell's Equations

Plasmas are magnetized fluids and they can be described by the system of Maxwell's equations. This system is composed by Poisson equation, Faraday's and Ampère's law and the equation modeling the absence of magnetic monopoles

$$\begin{cases} \nabla \cdot \boldsymbol{E} &= \dfrac{\rho_q}{\epsilon_0}, \\ \nabla \times \boldsymbol{E} &= -\partial_t \boldsymbol{B}, \\ \nabla \times \boldsymbol{B} - \dfrac{1}{c^2}\partial_t \boldsymbol{E} &= \boldsymbol{J}, \\ \nabla \cdot \boldsymbol{B} &= 0, \end{cases} \tag{2.33}$$

where c is the speed of light

On the MHD context, $\boldsymbol{v} << c$, so the displacement current term $\frac{1}{c^2}\partial_t \boldsymbol{E}$ can be neglected. This non-relativistic context together with the fact that we are interested in low frequency phenomena allow us to write the Ampère's law in such a way that

$$\boldsymbol{J} = \nabla \times \boldsymbol{B}. \tag{2.34}$$

This system is, however, not well posed. To close it, one more relation must be added which is the Ohm's Law.

Ohm's Law

Ohm's law can be derived from the combination of the transport equations for the ionic and electronic velocities

$$n_e m_e \frac{d\boldsymbol{v}_e}{dt} = n_e q_e(\boldsymbol{E} + \boldsymbol{v}_e \times \boldsymbol{B}) - \nabla p_e - \nabla \cdot \underline{\boldsymbol{\pi}}_e + \boldsymbol{R}_e, \tag{2.35}$$

$$n_i m_i \frac{d\boldsymbol{v}_i}{dt} = n_i q_i(\boldsymbol{E} + \boldsymbol{v}_i \times \boldsymbol{B}) - \nabla p_i - \nabla \cdot \underline{\boldsymbol{\pi}}_i + \boldsymbol{R}_i. \tag{2.36}$$

If we multiply the equation (2.36) by the electronic mass, the equation (2.35) by the ionic mass and subtract them, we obtain the following equation known as Ohm's Law

$$\begin{aligned} &m_e n_i m_i \frac{d\boldsymbol{v}_i}{dt} - m_i n_e m_e \frac{d\boldsymbol{v}_e}{dt} = \boldsymbol{E}(m_e n_i q_i - m_i n_e q_e) \\ &+(m_e n_i q_i \boldsymbol{v}_i - m_i n_e q_e \boldsymbol{v}_e) \times \boldsymbol{B} - m_e \nabla p_i + m_i \nabla p_e \\ &-m_e \nabla \cdot \underline{\boldsymbol{\pi}}_i + m_i \nabla \cdot \underline{\boldsymbol{\pi}}_e + m_e \boldsymbol{R}_i - m_i \boldsymbol{R}_e. \end{aligned} \tag{2.37}$$

For MHD studies, we often use a simplified form of (2.37) because we are interested in low-frequency phenomena. Hence, if the characteristic time of the observed phenomenon is much longer than the time in which the electrons and ions are moving, the terms $\frac{d\boldsymbol{v}_e}{dt}$ and $\frac{d\boldsymbol{v}_i}{dt}$ can be neglected. It is important to remark that this is considered a poor approximation because this hypothesis is applied not only on the perpendicular but also on the parallel velocities while these parallel velocities do not generate any magnetic force. With this approximation, (2.37) becomes

$$\begin{aligned} 0 &= \boldsymbol{E}(m_e n_i q_i - m_i n_e q_e) + (m_e n_i q_i \boldsymbol{v}_i - m_i n_e q_e \boldsymbol{v}_e) \times \boldsymbol{B} \\ &-m_e \nabla p_i + m_i \nabla p_e - m_e \nabla \cdot \underline{\boldsymbol{\pi}}_i + m_i \nabla \cdot \underline{\boldsymbol{\pi}}_e - (m_e + m_i)\boldsymbol{R}_e. \end{aligned} \tag{2.38}$$

2.1.4 Bifluid model

Together, the system (2.31), Maxwell's equations and the Ohm's law, give rise to the bi-fluid model, with $\sigma \to i/e$ standing for ions/electrons

$$\begin{cases} \partial_t n_\sigma + \nabla_{\boldsymbol{r}} \cdot (n_\sigma \boldsymbol{v}_\sigma) = 0, \\ m_\sigma \left[\partial_t (n_\sigma \boldsymbol{v}_\sigma) + \nabla_{\boldsymbol{r}} \cdot (n_\sigma \boldsymbol{v}_\sigma \otimes \boldsymbol{v}_\sigma)\right] - n_\sigma q_\sigma (\boldsymbol{E} + \boldsymbol{v}_\sigma \times \boldsymbol{B}) + \nabla_{\boldsymbol{r}} p_\sigma \\ \qquad = \nabla_{\boldsymbol{r}} \cdot \underline{\boldsymbol{\pi}}_\sigma + \boldsymbol{R}_\sigma, \\ \partial_t \rho_\sigma e_\sigma + \nabla_{\boldsymbol{r}} \cdot [(\rho_\sigma e_\sigma + p_\sigma)\boldsymbol{v}_\sigma + \underline{\boldsymbol{\pi}}_\sigma : \boldsymbol{v}_\sigma] - q_\sigma n_\sigma (\boldsymbol{v}_\sigma \cdot \boldsymbol{E}) = \nabla_{\boldsymbol{r}} \cdot \boldsymbol{Q}_\sigma + \boldsymbol{v}_\sigma \cdot \boldsymbol{R}_\sigma + \mathcal{Q}_\sigma, \\ \partial_t \boldsymbol{B} = -\nabla \times \boldsymbol{E}, \end{cases} \tag{2.39}$$

with $\boldsymbol{E}$ and $\boldsymbol{B}$ related by the Ohm's law (2.38) and having the closure relations shown in (2.32). The addition of the Maxwell's equations brings with it one extra difficulty for the discretization of the system wich is the divergence free constraint expressed by $\nabla \cdot \boldsymbol{B} = 0$.

2.1.5 Magnetic monopoles

The equation modeling the absence of magnetic monopoles oversizes the MHD system. For this reason, it is often treated separately. Moreover, it plays an important role when the discretization of these equations is performed using finite elements methods. This equation appears when the divergence operator is applied onto the Faraday's law

$$\begin{aligned} \nabla \cdot (\partial_t \boldsymbol{B} + \nabla \times \boldsymbol{E}) &= 0, \\ \partial_t (\nabla \cdot \boldsymbol{B}) + \cancelto{0}{\nabla \cdot (\nabla \times \boldsymbol{E})} &= 0, \\ \partial_t (\nabla \cdot \boldsymbol{B}) &= 0. \end{aligned} \tag{2.40}$$

This simplification implies that $\nabla \cdot \boldsymbol{B}$ is constant with respect to time. This equation is physically verified but the same cannot be said numerically. Indeed, the problem lies in satisfying it on the discrete level. As shown above, this equation comes when the divergence is applied into Faraday's equation. Nevertheless, numerically, the simplification $\nabla \cdot \nabla \times - = 0$ is not true. Actually, the discrete divergence $\nabla_h \cdot$ of the discrete curl $\nabla_h \times$ is not actually zero, i.e.,

$$\nabla_h \cdot (\nabla_h \times) \neq 0, \tag{2.41}$$

which can create magnetic monopoles

$$\nabla_h \cdot (\nabla_h \times \boldsymbol{E}_h) \neq 0 \Rightarrow \partial_t (\nabla_h \cdot \boldsymbol{B}_h) \approx \rho_m. \tag{2.42}$$

When the magnetic monopoles grow in time, their presence might lead to a non-physical problem [50]. Their effects, for exemple, in the topology of the magnetic field, which is an important parameter for magnetized plasmas, are mentioned by Brackbill and Barnes [51, 52]; and Balsara and Spicer [53].

There are many strategies to overcome this difficulty [54] which can be resumed in: the projection of the magnetic field in a divergence free space, also known as Hodge projection which is not easy to deal with; cleaning the noising effects of the numerical divergence and also the use of Helmholtz decomposition, in which the magnetic field is redefined under a vector potential formulation. This last one is the strategy that is retained here.

2.1.5.1 Vector Potential Formulation

For this formulation, let us consider a decomposition of the magnetic field that is often used for the MHD systems. This is at the basis of the so called Grad-Shafranov equilibrium that is often used as an initial equilibrium for numerical simulations. To obtain the equilibrium the magnetic field is defined as $\boldsymbol{B}_\star = \boldsymbol{F}_\star \nabla\phi + \nabla \times (\psi \nabla \phi)$, where $F_\star \equiv F_\star(\boldsymbol{\xi})$ is a function of the poloidal coordinate in a way that $\boldsymbol{B}_\star$ is divergence-free. By extension of the equilibrium, let us consider a magnetic field defined as

$$\boldsymbol{B} = F_\star \nabla\phi + \nabla \times \boldsymbol{A}, \tag{2.43}$$

where $\boldsymbol{A}$ ia a vector potential. Written in that way though, there is not a unique definition for $\boldsymbol{A}$. In fact, for any scalar function φ the relation below is always valid

$$\boldsymbol{B} = F_\star \nabla\phi + \nabla \times (\boldsymbol{A} + \nabla\varphi). \tag{2.44}$$

When this profile is used, the induction equation becomes

$$\nabla \times (\partial_t(\boldsymbol{A} + \nabla\varphi) + \boldsymbol{E}) = 0. \tag{2.45}$$

Thus, the vector $(\partial_t(\boldsymbol{A} + \nabla\varphi) + \boldsymbol{E})$ is irrotational and there exists a scalar potential function Φ such as

$$\partial_t(\boldsymbol{A} + \nabla\varphi) + \boldsymbol{E} = \nabla\Phi, \tag{2.46}$$

yielding

$$\partial_t \boldsymbol{A} + \boldsymbol{E} = \nabla(\Phi - \partial_t\varphi). \tag{2.47}$$

Hence, an additional ingredient is needed in order to define uniquely the vector potential chosen. This ingredient is what is called gauge condition. Different gauges can be used but we will retain our attention here, in two specific types: the Coulomb and the Weyl gauges.

Coulomb gauge

In this gauge, the vector potential is put under the divergence free condition as well, i.e., $\nabla \cdot \boldsymbol{A} = 0$. In this case, as $\nabla \cdot \boldsymbol{E} = 0$ the evolution of the total scalar potential is given by an elliptic equation

$$-\Delta U = 0 \text{ with } U = -\Phi + \partial_t\varphi. \tag{2.48}$$

This will affect the induction equation in the MHD system. Under the Coulomb gauge it becomes

$$\partial_t \boldsymbol{B} + \nabla \times \boldsymbol{E} = 0 \longrightarrow \partial_t \boldsymbol{A} = -\boldsymbol{E} - \nabla U, \tag{2.49}$$

with $-\Delta U = 0$.

Weyl gauge

The Weyl gauge assumes that the potentials are chosen such that $\Phi = \partial_t\varphi$, which is possible since Φ and φ are independent functions. In this case the induction equation becomes

$$\partial_t \boldsymbol{A} = -\boldsymbol{E}. \tag{2.50}$$

2.2 Simplified MHD models

After the derivation of the fluid model the main objective becomes the derivation of the single-fluid magnetohydrodynamic (MHD) equations. The fundamental assumption of the MHD is that fields and fluids fluctuate on the same time and length scales. Since the plasma is treated as a single fluid, these are necessarily determined by the slower rates of change of the heavy ions. There are several ways of deriving the MHD models depending on the assumptions and approximations used.

2.2.1 Full MHD model

To derive the full MHD system we start by deriving a single-fluid system from a bi-fluid one. This model also contains the Ohm's law and Maxwell's equations. To obtain this model different hypothesis are needed, such as the quasi-neutrality and the very weak electronic mass.

2.2.1.1 Reformulation of the bi-fluid model

In the MHD models, the plasma is treated as a mixing of two fluids: one composed by ions and another composed by electrons. Each one of them is described by (2.39) where σ could stand for electrons - e - or ions - i. From this system it is possible to obtain the system of transport equations for the primitive variables n_σ, $\boldsymbol{v}_\sigma$ and p_σ. The mass continuity equation (2.17) can then be rewritten as

$$\begin{aligned} \frac{\partial n_\sigma}{\partial t} + \boldsymbol{v}_\sigma \cdot \nabla_{\boldsymbol{r}} n_\sigma + n_\sigma \nabla_{\boldsymbol{r}} \cdot \boldsymbol{v}_\sigma &= 0, \\ \frac{dn_\sigma}{dt} + n_\sigma \nabla_{\boldsymbol{r}} \cdot \boldsymbol{v}_\sigma &= 0, \end{aligned} \tag{2.51}$$

where the operator $\frac{d}{dt}$ is the convective derivative associated to each σ particle

$$\frac{d}{dt} = \frac{\partial}{\partial t} + \boldsymbol{v}_\sigma \cdot \nabla_{\boldsymbol{r}}. \tag{2.52}$$

The momentum equation (2.23) can be simplified with the continuity equation (2.17) yielding

$$n_\sigma m_\sigma \frac{d\boldsymbol{v}_\sigma}{dt} = n_\sigma q_\sigma (\boldsymbol{E} + \boldsymbol{v}_\sigma \times \boldsymbol{B}) - \nabla_{\boldsymbol{r}} p_\sigma - \nabla_{\boldsymbol{r}} \cdot \underline{\boldsymbol{\pi}}_\sigma + \boldsymbol{R}_\sigma. \tag{2.53}$$

The energy equation (2.27) can be simplified in a similar way to be rewritten as

$$\frac{dp_\sigma}{dt} + \gamma p_\sigma \nabla_{\boldsymbol{r}} \cdot \boldsymbol{v}_\sigma = (\gamma - 1)(-\nabla_{\boldsymbol{r}} \cdot \boldsymbol{Q}_\sigma + \mathcal{Q}_\sigma - \underline{\boldsymbol{\pi}}_\sigma : \nabla_{\boldsymbol{r}} \boldsymbol{v}_\sigma). \tag{2.54}$$

Therefore, the system of conservative laws yields the system of transport equations

$$\begin{cases} \dfrac{dn_\sigma}{dt} + n_\sigma \nabla_{\boldsymbol{r}} \cdot \boldsymbol{v}_\sigma = 0, \\ n_\sigma m_\sigma \dfrac{d\boldsymbol{v}_\sigma}{dt} = n_\sigma q_\sigma (\boldsymbol{E} + \boldsymbol{v}_\sigma \times \boldsymbol{B}) - \nabla_{\boldsymbol{r}} p_\sigma - \nabla_{\boldsymbol{r}} \cdot \underline{\boldsymbol{\pi}}_\sigma + \boldsymbol{R}_\sigma, \\ \dfrac{dp_\sigma}{dt} + \gamma p_\sigma \nabla_{\boldsymbol{r}} \cdot \boldsymbol{v}_\sigma = (\gamma - 1)(-\nabla_{\boldsymbol{r}} \cdot \boldsymbol{Q}_\sigma + \mathcal{Q}_\sigma - \underline{\boldsymbol{\pi}}_\sigma : \nabla_{\boldsymbol{r}} \boldsymbol{v}_\sigma). \end{cases} \tag{2.55}$$

The electromagnetic variables are the electric field $\boldsymbol{E}$, the magnetic field $\boldsymbol{B}$ and the current density $\boldsymbol{J}$. The fluid variables are the mass density ρ, the fluid velocity $\boldsymbol{v}$, the pressure p and the energy ρe. To obtain the single-fluid equations, the mixed variables below are introduced

$$\begin{aligned} \text{Density: } \rho &\equiv \sum_\sigma m_\sigma n_\sigma = m_e n_e + m_i n_i = \rho_e + \rho_i, \\ \text{Charge: } \rho_q &\equiv \sum_\sigma q_\sigma n_\sigma, \\ \text{Velocity: } \boldsymbol{v} &\equiv \frac{\sum_\sigma m_\sigma n_\sigma \boldsymbol{v}_\sigma}{\sum_\sigma m_\sigma n_\sigma} = \frac{m_e n_e \boldsymbol{v}_e + m_i n_i \boldsymbol{v}_i}{\rho}, \\ \text{Current density: } \boldsymbol{J} &\equiv \sum_\sigma q_\sigma n_\sigma \boldsymbol{v}_\sigma, \\ \text{Pressure: } p &= p_e + p_i, \\ \text{Viscosity tensor: } \underline{\boldsymbol{\pi}} &= \underline{\boldsymbol{\pi}}_e + \underline{\boldsymbol{\pi}}_i, \\ \text{Heat flux: } \boldsymbol{Q} &= \boldsymbol{Q}_e + \boldsymbol{Q}_i, \\ \text{Heat from collisions: } \mathcal{Q} &= \mathcal{Q}_e + \mathcal{Q}_i = \boldsymbol{R}_e \cdot (\boldsymbol{v}_i - \boldsymbol{v}_e). \end{aligned}$$

Now we retake the fluid equations one by one. Starting by multiplying the ionic and electronic mass continuity equations by the ionic and electronic masses m_i and m_e and adding both equations

$$\begin{aligned} \partial_t(\rho_e + \rho_i) + \nabla \cdot (\rho_e \boldsymbol{v}_e + \rho_i \boldsymbol{v}_i) &= 0, \\ \partial_t \rho + \nabla \cdot (\rho \boldsymbol{v}) &= 0. \end{aligned} \tag{2.56}$$

The charge continuity equation can be obtained similarly by multiplying them by their charges, yielding

$$\partial_t \rho_q + \nabla \cdot \boldsymbol{J} = 0. \tag{2.57}$$

The single-fluid momentum equation is obtained by adding both equations for ions and electrons

$$\partial_t \rho \boldsymbol{v} + \nabla \cdot (\rho_e \boldsymbol{v}_e \otimes \boldsymbol{v}_e + \rho_i \boldsymbol{v}_i \otimes \boldsymbol{v}_i) = \rho_q \boldsymbol{E} + \boldsymbol{J} \times \boldsymbol{B} - \nabla p - \nabla \cdot \underline{\boldsymbol{\pi}} + \cancel{\boldsymbol{R}_e + \boldsymbol{R}_i}. \tag{2.58}$$

The electronic and ionic velocities can be redefined as a function of the mixed velocity

$$\boldsymbol{v}_e = \boldsymbol{v} + \frac{\rho_i}{\rho_e}(\boldsymbol{v} - \boldsymbol{v}_i), \tag{2.59}$$

$$\boldsymbol{v}_i = \boldsymbol{v} + \frac{\rho_e}{\rho_i}(\boldsymbol{v} - \boldsymbol{v}_e), \tag{2.60}$$

thus, the momentum equation becomes

$$\partial_t \rho \boldsymbol{v} + \nabla \cdot (\rho \boldsymbol{v} \otimes \boldsymbol{v}) + \nabla \cdot (\boldsymbol{v}_e \otimes \rho_i(\boldsymbol{v} - \boldsymbol{v}_i) + \boldsymbol{v}_i \otimes \rho_e(\boldsymbol{v} - \boldsymbol{v}_e)) = \rho_q \boldsymbol{E} + \boldsymbol{J} \times \boldsymbol{B} - \nabla p - \nabla \cdot \underline{\boldsymbol{\pi}}. \tag{2.61}$$

Finally, to obtain the mixed hydrodynamic energy ρe defined as

$$\rho e = \rho \frac{|\boldsymbol{v}|^2}{2} + \frac{p}{\gamma - 1}, \tag{2.62}$$

we start by adding the ionic and electronic pressure equations

$$\begin{aligned} &\frac{dp}{dt} + \gamma p \nabla \cdot \boldsymbol{v} + \frac{\rho_i}{\rho_e}(\boldsymbol{v} - \boldsymbol{v}_i) \cdot \nabla p_e + \frac{\rho_e}{\rho_i}(\boldsymbol{v} - \boldsymbol{v}_e) \cdot \nabla p_i + \gamma p_e \nabla \cdot \left(\frac{\rho_i}{\rho_e}(\boldsymbol{v} - \boldsymbol{v}_i) \right) \\ &+ \gamma p_i \nabla \cdot \left(\frac{\rho_e}{\rho_i}(\boldsymbol{v} - \boldsymbol{v}_e) \right) = (\gamma - 1)(\mathcal{Q}_e + \mathcal{Q}_i - \underline{\boldsymbol{\pi}}_e : \nabla \boldsymbol{v}_e - \underline{\boldsymbol{\pi}}_i : \nabla \boldsymbol{v}_i - \nabla \cdot \boldsymbol{Q}). \end{aligned} \tag{2.63}$$

The convective derivative of the hydrodynamic energy is

$$\frac{d\rho e}{dt} = \frac{1}{\gamma - 1}\frac{dp}{dt} + \rho \boldsymbol{v} \cdot \frac{d\boldsymbol{v}}{dt} + \frac{|\boldsymbol{v}|^2}{2}\frac{d\rho}{dt}. \tag{2.64}$$

Using the mass continuity (2.56) and pressure (2.63) equations; and replacing the second term of equation (2.64) by the momentum equation (2.61), this energy equation (2.64) becomes

$$\begin{aligned} &\frac{d\rho e}{dt} + \frac{1}{\gamma - 1}\left[\frac{\rho_i}{\rho_e}(\boldsymbol{v} - \boldsymbol{v}_i) \cdot \nabla p_e + \frac{\rho_e}{\rho_i}(\boldsymbol{v} - \boldsymbol{v}_e) \cdot \nabla p_i + \gamma p_e \nabla \cdot \left(\frac{\rho_i}{\rho_e}(\boldsymbol{v} - \boldsymbol{v}_i) \right) \right. \\ &\left. + \gamma p_i \nabla \cdot \left(\frac{\rho_e}{\rho_i}(\boldsymbol{v} - \boldsymbol{v}_e) \right) \right] = -\frac{\gamma}{\gamma - 1} p \nabla \cdot \boldsymbol{v} + \mathcal{Q}_e + \mathcal{Q}_i + \boldsymbol{v} \cdot \nabla p + \boldsymbol{v} \cdot (\boldsymbol{J} \times \boldsymbol{B}) \\ &- (\underline{\boldsymbol{\pi}}_e : \nabla \boldsymbol{v}_e + \underline{\boldsymbol{\pi}}_i : \nabla \boldsymbol{v}_i + \nabla \cdot \boldsymbol{Q}) - \boldsymbol{v} \cdot (\nabla \cdot \underline{\boldsymbol{\pi}}) - \frac{|\boldsymbol{v}|^2}{2}\rho(\nabla \cdot \boldsymbol{v}) + \boldsymbol{v} \cdot (\rho_q \boldsymbol{E}) \\ &- \boldsymbol{v} \cdot (\nabla \cdot (\boldsymbol{v}_e \otimes \rho_i(\boldsymbol{v} - \boldsymbol{v}_i) + \boldsymbol{v}_i \otimes \rho_e(\boldsymbol{v} - \boldsymbol{v}_e))). \end{aligned} \tag{2.65}$$

Thus, the conservation of energy equation can be written as

$$\begin{aligned}
&\partial_t \rho e + \nabla \cdot (\rho e \boldsymbol{v} + p\boldsymbol{v}) + \frac{1}{\gamma - 1}\left[\frac{\rho_i}{\rho_e}(\boldsymbol{v} - \boldsymbol{v}_i) \cdot \nabla p_e + \frac{\rho_e}{\rho_i}(\boldsymbol{v} - \boldsymbol{v}_e) \cdot \nabla p_i \right.\\
&\left. + \gamma p_e \nabla \cdot \left(\frac{\rho_i}{\rho_e}(\boldsymbol{v} - \boldsymbol{v}_i)\right) + \gamma p_i \nabla \cdot \left(\frac{\rho_e}{\rho_i}(\boldsymbol{v} - \boldsymbol{v}_e)\right)\right] = (\boldsymbol{J} \times \boldsymbol{B}) \cdot \boldsymbol{v} - \boldsymbol{v} \cdot (\nabla \cdot \underline{\boldsymbol{\pi}})\\
&+ \mathcal{Q}_e + \mathcal{Q}_i - (\underline{\boldsymbol{\pi}}_e : \nabla \boldsymbol{v}_e + \underline{\boldsymbol{\pi}}_i : \nabla \boldsymbol{v}_i + \nabla \cdot \boldsymbol{Q}) + \boldsymbol{v} \cdot (\rho_q \boldsymbol{E})\\
&- \boldsymbol{v} \cdot (\nabla \cdot (\boldsymbol{v}_e \otimes \rho_i(\boldsymbol{v} - \boldsymbol{v}_i) + \boldsymbol{v}_i \otimes \rho_e(\boldsymbol{v} - \boldsymbol{v}_e))).
\end{aligned} \tag{2.66}$$

Finally, when put together, these equations, Ohm's (2.38) and ideal gas laws (2.62), and Maxwell's equations yield the Full MHD system which is a simplified bi-fluid model

$$\begin{cases}
\partial_t \rho + \nabla \cdot (\rho \boldsymbol{v}) = 0,\\
\partial_t \rho \boldsymbol{v} + \nabla \cdot (\rho \boldsymbol{v} \otimes \boldsymbol{v}) + \nabla \cdot (\boldsymbol{v}_e \otimes \rho_i(\boldsymbol{v} - \boldsymbol{v}_i) + \boldsymbol{v}_i \otimes \rho_e(\boldsymbol{v} - \boldsymbol{v}_e)) = \rho_q \boldsymbol{E}\\
\qquad + \boldsymbol{J} \times \boldsymbol{B} - \nabla p - \nabla \cdot \underline{\boldsymbol{\pi}},\\
\partial_t \rho e + \nabla \cdot (\rho e \boldsymbol{v} + p\boldsymbol{v}) + \frac{1}{\gamma - 1}\left[\frac{\rho_i}{\rho_e}(\boldsymbol{v} - \boldsymbol{v}_i) \cdot \nabla p_e + \frac{\rho_e}{\rho_i}(\boldsymbol{v} - \boldsymbol{v}_e) \cdot \nabla p_i \right.\\
\qquad \left. + \gamma p_e \nabla \cdot \left(\frac{\rho_i}{\rho_e}(\boldsymbol{v} - \boldsymbol{v}_i)\right) + \gamma p_i \nabla \cdot \left(\frac{\rho_e}{\rho_i}(\boldsymbol{v} - \boldsymbol{v}_e)\right)\right] = (\boldsymbol{J} \times \boldsymbol{B}) \cdot \boldsymbol{v}\\
\qquad - \boldsymbol{v} \cdot (\nabla \cdot \underline{\boldsymbol{\pi}}) + \boldsymbol{R}_e \cdot (\boldsymbol{v}_i - \boldsymbol{v}_e) - (\underline{\boldsymbol{\pi}}_e : \nabla \boldsymbol{v}_e + \underline{\boldsymbol{\pi}}_i : \nabla \boldsymbol{v}_i + \nabla \cdot \boldsymbol{Q})\\
\qquad - \boldsymbol{v} \cdot (\nabla \cdot (\boldsymbol{v}_e \otimes \rho_i(\boldsymbol{v} - \boldsymbol{v}_i) + \boldsymbol{v}_i \otimes \rho_e(\boldsymbol{v} - \boldsymbol{v}_e))) + \boldsymbol{v} \cdot (\rho_q \boldsymbol{E}),\\
\partial_t \rho_q + \nabla \cdot \boldsymbol{J} = 0,\\
\partial_t \boldsymbol{B} = -\nabla \times \boldsymbol{E},
\end{cases} \tag{2.67}$$

The same closure relations (2.32) are applied here.

2.2.1.2 Quasineutral regime

To go from the original Maxwell's equations to the low-frequency Maxwell system, it is necessary to make $\epsilon_0 \to 0$. As a consequence, the net charge $\epsilon_0(\nabla \cdot \boldsymbol{E})$ can be neglected, i.e.,

$$\epsilon_0(\nabla \cdot \boldsymbol{E}) \approx 0 \Rightarrow \rho_q = 0. \tag{2.68}$$

This simplification, called plasma quasi-neutrality, is very often used. In the case of a plasma composed only by electrons and ions, it can be written in the following way

$$q_i n_i + q_e n_e = 0, \tag{2.69}$$

where the charges q_i and q_e are defined as

$$q_i = Z_i e \text{ and } q_e = -e, \tag{2.70}$$

and are, respectively, the ion and electron charges.

This hypothesis is basically telling that the electrons will instantaneously compensate the separation of the macroscopic charges to maintain the plasma neutrality. In fact, it is possible to consider the quasi-neutrality in the MHD models because of the assumptions made before concerning the spatiotemporal scales, i.e., the long temporal scales of the phenomena compared to the plasma characteristic times.

Considering a plasma composed by Hydrogen isotopes only, e.g., Deuterium and Tritium leads to

$$n_e = n_i = n, \tag{2.71}$$

which allows some simplifications for the mixed variables in the MHD model, such as the density ρ, the current density $\boldsymbol{J}$, the friction term $\boldsymbol{R}_e$ and also the transport coefficient representing the heat generated by collisions $\mathcal{Q}$. They become, then

$$\begin{aligned}
\rho &= (m_e + m_i)n, && (2.72)\\
\boldsymbol{J} &= en(\boldsymbol{v}_i - \boldsymbol{v_e}), && (2.73)\\
\frac{\boldsymbol{R}_e}{en} &= \eta \boldsymbol{J}, && (2.74)\\
\mathcal{Q} &= \frac{\boldsymbol{R}_e \cdot \boldsymbol{J}}{en} \\
&= \eta \boldsymbol{J}^2, && (2.75)
\end{aligned}$$

in which η represents the electrical resistivity

$$\eta = \frac{\nu_{ei} m_e}{ne^2}. \tag{2.76}$$

These definitions give

$$\begin{aligned}
\boldsymbol{v}_e &= \boldsymbol{v} + \alpha_e \boldsymbol{J}, && (2.77)\\
\boldsymbol{v}_i &= \boldsymbol{v} + \alpha_i \boldsymbol{J}, && (2.78)
\end{aligned}$$

with

$$\begin{aligned}
\alpha_e &= -\frac{m_i}{en(m_i + m_e)}, && (2.79)\\
\alpha_i &= \frac{m_e}{en(m_i + m_e)}. && (2.80)
\end{aligned}$$

2.2.1.3 Ohm's law in the quasi-neutral regime

Taking into account the quasi-neutrality, Ohm's law (2.38) becomes

$$\rho e\boldsymbol{E}+(\rho\boldsymbol{v}e-(m_i-m_e))\boldsymbol{J})\times\boldsymbol{B} = m_e\nabla p_i-m_i\nabla p_e+m_e(\nabla\cdot\underline{\boldsymbol{\pi}}_i)-m_i(\nabla\cdot\underline{\boldsymbol{\pi}}_e)+\frac{\rho}{n}\boldsymbol{R}_e, \quad (2.81)$$

which can be rewritten as

$$\boldsymbol{E}+\boldsymbol{v}\times\boldsymbol{B} = \eta\boldsymbol{J}+\frac{m_i-m_e}{\rho e}\boldsymbol{J}\times\boldsymbol{B}+\frac{1}{\rho e}(m_e\nabla p_i-m_i\nabla p_e+m_e(\nabla\cdot\underline{\boldsymbol{\pi}}_i)-m_i(\nabla\cdot\underline{\boldsymbol{\pi}}_e)). \quad (2.82)$$

Therefore, different MHD models can be derived accordingly to the simplifications that could be done in Ohm's law (2.82) as, for instance, ideal, resistive or Hall MHD

$$\begin{array}{rcrcl} \text{Ideal MHD} & : & \boldsymbol{E}+\boldsymbol{v}\times\boldsymbol{B} & = & 0, \\ \text{Resistive MHD} & : & \boldsymbol{E}+\boldsymbol{v}\times\boldsymbol{B} & = & \eta\boldsymbol{J}, \\ \text{Hall MHD} & : & \boldsymbol{E}+\boldsymbol{v}\times\boldsymbol{B} & = & \eta\boldsymbol{J}+\frac{m_i-m_e}{\rho e}\boldsymbol{J}\times\boldsymbol{B}. \end{array} \quad (2.83)$$

2.2.1.4 Full MHD in the quasi-neutral regime

After applying the quasi-neutrality hypothesis, the Full MHD system (2.67) becomes

$$\left\{\begin{array}{r} \partial_t\rho+\nabla\cdot(\rho\boldsymbol{v})=0, \\ \partial_t\rho\boldsymbol{v}+\nabla\cdot(\rho\boldsymbol{v}\otimes\boldsymbol{v})=\nabla\cdot(\boldsymbol{v}_e\otimes\rho_i\alpha_i\boldsymbol{J}+\boldsymbol{v}_i\otimes\rho_e\alpha_e\boldsymbol{J})+\boldsymbol{J}\times\boldsymbol{B}-\nabla p-\nabla\cdot\underline{\boldsymbol{\pi}}, \\ \partial_t\rho e+\nabla\cdot(\rho e\boldsymbol{v}+p\boldsymbol{v})=\frac{1}{\gamma-1}\left[\frac{m_i}{m_e}\alpha_i\boldsymbol{J}\cdot\nabla p_e+\frac{m_e}{m_i}\alpha_e\boldsymbol{J}\cdot\nabla p_i\right. \\ \left.+\gamma p_e\nabla\cdot\left(\frac{m_i}{m_e}\alpha_i\boldsymbol{J}\right)+\gamma p_i\nabla\cdot\left(\frac{m_e}{m_i}\alpha_e\boldsymbol{J}\right)\right]+(\boldsymbol{J}\times\boldsymbol{B})\cdot\boldsymbol{v}-\boldsymbol{v}\cdot(\nabla\cdot\underline{\boldsymbol{\pi}})+\eta\boldsymbol{J}^2 \\ -(\underline{\boldsymbol{\pi}}_e:\nabla\boldsymbol{v}_e+\underline{\boldsymbol{\pi}}_i:\nabla\boldsymbol{v}_i+\nabla\cdot\boldsymbol{Q})-\boldsymbol{v}\cdot(\nabla\cdot(\boldsymbol{v}_e\otimes\rho_i(\boldsymbol{v}-\boldsymbol{v}_i)+\boldsymbol{v}_i\otimes\rho_e(\boldsymbol{v}-\boldsymbol{v}_e))), \\ \frac{dp_{i/e}}{dt}+\gamma p_{i/e}\nabla\cdot\boldsymbol{v}_{i/e}=(\gamma-1)(-\nabla\cdot\boldsymbol{Q}_{i/e}+\mathcal{Q}_{i/e}-\underline{\boldsymbol{\pi}}_{i/e}:\nabla\boldsymbol{v}_{i/e}), \\ \partial_t\boldsymbol{B}=-\nabla\times\boldsymbol{E}, \end{array}\right. \quad (2.84)$$

with the Ohm's law shown in (2.82)

One last hypothesis that is widely used is the assumption of a weak electronic mass [55], i.e., $m_e \to 0$. With this assumption the mixed velocity simply becomes the ionic velocity

$$\boldsymbol{v}_i = \boldsymbol{v}.$$

This leads to the Full MHD system

$$\begin{cases} \partial_t \rho + \nabla \cdot (\rho \boldsymbol{v}) &= 0, \\ \partial_t \rho \boldsymbol{v} + \nabla \cdot (\rho \boldsymbol{v} \otimes \boldsymbol{v}) &= \boldsymbol{J} \times \boldsymbol{B} - \nabla p - \nabla \cdot \underline{\boldsymbol{\pi}}, \\ \partial_t \rho e + \nabla \cdot (\rho e \boldsymbol{v} + p \boldsymbol{v}) &= (\boldsymbol{J} \times \boldsymbol{B}) \cdot \boldsymbol{v} + \eta \boldsymbol{J}^2 - (\nabla \cdot (\boldsymbol{v} \underline{\boldsymbol{\pi}}) + \nabla \cdot \boldsymbol{Q}), \\ \partial_t \boldsymbol{B} &= -\nabla \times \boldsymbol{E} \end{cases} \tag{2.85}$$

with the following closure relations

$$\rho e = \frac{p}{\gamma - 1} + \frac{1}{2} \rho |\boldsymbol{v}|^2, \tag{2.86}$$

$$\boldsymbol{J} = \nabla \times \boldsymbol{B}, \tag{2.87}$$

together with the expressions for the transport coefficients shown in (2.32) and the Ohm's law chosen from (2.83) accordingly to the kind of system one wants to study. This system is also submitted to the divergence free constraint $\nabla \cdot \boldsymbol{B} = 0$ and implies $\nabla \cdot \boldsymbol{J} = 0$, since $\boldsymbol{J} = \nabla \times \boldsymbol{B}$.

2.2.2 Ideal MHD

The ideal MHD [55, 56] is the single-fluid most basic model allowing the determination of equilibrium and stability plasma properties. In this model, the plasma is a perfect conductor and the goal is to obtain the density, the momentum and the equations of state that describe the macroscopic behavior of a magnetized plasma considering fast time-steps in which the dissipative processes can be neglected. This ideal MHD system is obtained when resistive effects of the current in the full MHD system (2.85) are neglected. For this, the first simplification of Ohm's law in (2.83) is considered and second order terms are neglected. Therefore, the system becomes

$$\begin{cases} \partial_t \rho + \nabla \cdot (\rho \boldsymbol{v}) &= 0, \\ \partial_t \rho \boldsymbol{v} + \nabla \cdot (\rho \boldsymbol{v} \otimes \boldsymbol{v}) &= \boldsymbol{J} \times \boldsymbol{B} - \nabla p, \\ \partial_t \rho e + \nabla \cdot (\rho e \boldsymbol{v} + p \boldsymbol{v}) &= (\boldsymbol{J} \times \boldsymbol{B}) \cdot \boldsymbol{v}, \\ \partial_t \boldsymbol{B} &= -\nabla \times \boldsymbol{E}, \end{cases} , \tag{2.88}$$

with the Ohm's Law being

$$\boldsymbol{E} + \boldsymbol{v} \times \boldsymbol{B} = 0, \tag{2.89}$$

and the other closure relations are the same as in the full MHD system.

2.2.2.1 Ideal MHD under conservative form

In the context of Ideal MHD we retake the system to write it under conservative form. First of all, the product $\rho\boldsymbol{v}$ can be replaced by the momentum vector, i.e., $\boldsymbol{m} \equiv \rho\boldsymbol{v}$. This allows us to rewrite the continuity equation in the following way

$$\partial_t \rho + \nabla \cdot \boldsymbol{m} = 0. \tag{2.90}$$

To deal with the momentum equation, the $\boldsymbol{J} \times \boldsymbol{B}$ term will be evaluated by means of the modified Ampère's law

$$\boldsymbol{J} \times \boldsymbol{B} = (\nabla \times \boldsymbol{B}) \times \boldsymbol{B} = \nabla \cdot (\boldsymbol{B} \otimes \boldsymbol{B}) - \nabla p_m, \tag{2.91}$$

where $p_m = \frac{\boldsymbol{B}\cdot\boldsymbol{B}}{2}$ is the magnetic pressure. Therefore, the momentum equation can be written as

$$\partial_t \boldsymbol{m} + \nabla \cdot \left(\frac{\boldsymbol{m} \otimes \boldsymbol{m}}{\rho} - \boldsymbol{B} \otimes \boldsymbol{B} \right) + \nabla(p + p_m) = 0. \tag{2.92}$$

For the energy equation, it is now necessary to redefine the total energy in order to take into account the magnetic energy as well. Until this point, the total energy was defined as $\rho e = \frac{p}{\gamma-1} + \frac{1}{2}\rho(\boldsymbol{v}\cdot\boldsymbol{v})$ which contains the internal energy term $\rho\varepsilon = \frac{p}{\gamma-1}$ and the kinetic energy $\frac{1}{2}\rho(\boldsymbol{v}\cdot\boldsymbol{v})$. However, the total energy in this context is

$$\mathcal{E} = \rho\varepsilon + \frac{1}{2}\rho(\boldsymbol{v}\cdot\boldsymbol{v}) + \frac{\boldsymbol{B}\cdot\boldsymbol{B}}{2} = \rho e + p_m. \tag{2.93}$$

Thus, the energy equation becomes

$$\partial_t \mathcal{E} - \partial_t p_m + \nabla \cdot ((\mathcal{E} + p - p_m)\boldsymbol{v}) = (\boldsymbol{J} \times \boldsymbol{B}) \cdot \boldsymbol{v}. \tag{2.94}$$

Several algebraic operations must be done then to put this equation in a suitable form. Starting with $\partial_t p_m$

$$\begin{aligned} \partial_t p_m &= \boldsymbol{B} \cdot \partial_t \boldsymbol{B} = -\boldsymbol{B} \cdot (\nabla \times \boldsymbol{E}), \\ &= -\nabla \cdot (\boldsymbol{E} \times \boldsymbol{B}) - \boldsymbol{E} \cdot \boldsymbol{J}, \end{aligned} \tag{2.95}$$

Also,

$$(\boldsymbol{J} \times \boldsymbol{B}) \cdot \boldsymbol{v} = -(\boldsymbol{v} \times \boldsymbol{B}) \cdot \boldsymbol{J} = \boldsymbol{E} \cdot \boldsymbol{J} - (\boldsymbol{v} \cdot \boldsymbol{B}). \tag{2.96}$$

Hence, the energy equation becomes

$$\partial_t \mathcal{E} + \nabla \cdot ((\mathcal{E} + p - p_m)\boldsymbol{v} + \boldsymbol{E} \times \boldsymbol{B}) = 0. \tag{2.97}$$

Finally,

$$\begin{aligned} \boldsymbol{E} \times \boldsymbol{B} &= -(\boldsymbol{v} \times \boldsymbol{B}) \times \boldsymbol{B}, \\ &= -(\boldsymbol{B} \cdot \boldsymbol{v})\boldsymbol{B} + 2p_m \boldsymbol{v}, \end{aligned} \tag{2.98}$$

therefore, the equation becomes

$$\partial_t \mathcal{E} + \nabla \cdot \left((\mathcal{E} + p + p_m) \frac{\boldsymbol{m}}{\rho} - \frac{\boldsymbol{B} \cdot \boldsymbol{m}}{\rho} \boldsymbol{B} \right) = 0. \tag{2.99}$$

The evolution of the magnetic field yields

$$\partial_t \boldsymbol{B} + \nabla \times \boldsymbol{E} = 0, \tag{2.100}$$

$$\partial_t \boldsymbol{B} - \nabla \times (\boldsymbol{v} \times \boldsymbol{B}) = 0, \tag{2.101}$$

$$\partial_t \boldsymbol{B} + \nabla \cdot \left(\frac{\boldsymbol{m} \otimes \boldsymbol{B} - \boldsymbol{B} \otimes \boldsymbol{m}}{\rho} \right) = 0.$$

The resulting single-fluid ideal model written in conservative form is then

$$\left\{ \begin{aligned} \partial_t \rho + \nabla \cdot \boldsymbol{m} &= 0, \\ \partial_t \boldsymbol{m} + \nabla \cdot \left(\tfrac{\boldsymbol{m} \otimes \boldsymbol{m}}{\rho} - \boldsymbol{B} \otimes \boldsymbol{B} \right) + \nabla (p + p_m) &= 0, \\ \partial_t \mathcal{E} + \nabla \cdot \left((\mathcal{E} + p + p_m) \tfrac{\boldsymbol{m}}{\rho} - \tfrac{\boldsymbol{B} \cdot \boldsymbol{m}}{\rho} \boldsymbol{B} \right) &= 0, \\ \partial_t \boldsymbol{B} + \nabla \cdot \left(\tfrac{\boldsymbol{m} \otimes \boldsymbol{B} - \boldsymbol{B} \otimes \boldsymbol{m}}{\rho} \right) &= 0. \end{aligned} \right. \tag{2.102}$$

The equations of state and Ohm's law used are

$$\mathcal{E} = \rho\varepsilon + \frac{1}{2\rho} \boldsymbol{m} \cdot \boldsymbol{m} + \frac{1}{2} \boldsymbol{B} \cdot \boldsymbol{B}, \;\; p = (\gamma - 1)\rho\varepsilon = \rho T \;\text{ and }\; \boldsymbol{E} + \boldsymbol{v} \times \boldsymbol{B} = 0 \tag{2.103}$$

The model described by system (2.102) is a conservative system associated to the conservative variables $\boldsymbol{w}$ and the flux tensor $\underline{\boldsymbol{f}}$

$$\boldsymbol{w} = \begin{pmatrix} \rho \\ \boldsymbol{m} \\ \mathcal{E} \\ \boldsymbol{B} \end{pmatrix} \quad \text{and} \quad \underline{\boldsymbol{f}} = \begin{pmatrix} \boldsymbol{m}^T \\ \frac{1}{\rho}(\boldsymbol{m} \otimes \boldsymbol{m}) + P\mathbb{I} - \boldsymbol{B} \otimes \boldsymbol{B} \\ \mathcal{H}\boldsymbol{m}^T - \frac{1}{\rho}(\boldsymbol{B} \cdot \boldsymbol{m})\boldsymbol{B}^T \\ \frac{1}{\rho}\boldsymbol{m} \otimes \boldsymbol{B} - \frac{1}{\rho}\boldsymbol{B} \otimes \boldsymbol{m} \end{pmatrix}, \tag{2.104}$$

where $P = p + p_m$ is the total pressure and $\mathcal{H} = \frac{\mathcal{E}+P}{\rho}$ the enthalpy. The upper-script$(.^T)$ is used for the transpose of a vector. The ideal MHD system can be written in a compact form

$$\frac{\partial \boldsymbol{w}}{\partial t} + \nabla \cdot \underline{\boldsymbol{f}} = 0. \tag{2.105}$$

2.2.2.2 Spectral properties analysis

To manage the overdimensioning of the system (2.102) due to the divergence free constraint, Powel proposed the addition of source terms to the equations such as [57]

$$\left\{ \begin{array}{rcl} \partial_t \rho + \nabla \cdot \boldsymbol{m} & = & 0 \\ , \partial_t \boldsymbol{m} + \nabla \cdot \left(\frac{\boldsymbol{m} \otimes \boldsymbol{m}}{\rho} - \boldsymbol{B} \otimes \boldsymbol{B} \right) + \nabla (p + p_m) & = & -\boldsymbol{B}(\nabla \cdot \boldsymbol{B}), \\ \partial_t \mathcal{E} + \nabla \cdot \left((\mathcal{E} + p + p_m) \frac{\boldsymbol{m}}{\rho} - \frac{\boldsymbol{B} \cdot \boldsymbol{m}}{\rho} \boldsymbol{B} \right) & = & -(\boldsymbol{v} \cdot \boldsymbol{B})(\nabla \cdot \boldsymbol{B}), \\ \partial_t \boldsymbol{B} + \nabla \cdot \left(\frac{\boldsymbol{m} \otimes \boldsymbol{B} - \boldsymbol{B} \otimes \boldsymbol{m}}{\rho} \right) & = & -\boldsymbol{v}(\nabla \cdot \boldsymbol{B}) \end{array} \right. . \tag{2.106}$$

The goal of this strategy is to turn the system in a strictly hyperbolic one, thus diagonalizable.

The compact form (2.105) can be then rewritten as

$$\partial_t \boldsymbol{w} + \nabla \cdot \underline{\boldsymbol{f}} + \boldsymbol{s}(\boldsymbol{w}) = 0, \tag{2.107}$$

with $\boldsymbol{w}$ being explicitly written as

$$\boldsymbol{w} = (\rho, \rho v_1, \rho v_2, \rho v_3, \mathcal{E}, B_1, B_2, B_3)^T, \tag{2.108}$$

and $\boldsymbol{s}(\boldsymbol{w})$

$$\boldsymbol{s}(\boldsymbol{w}) = \nabla \cdot \boldsymbol{B}(0, \boldsymbol{B}, \boldsymbol{v} \cdot \boldsymbol{B}, \boldsymbol{v})^T. \tag{2.109}$$

Hence, the MHD system can be written in a quasi-linear form

$$\partial_t \boldsymbol{w} + \sum_{i=1}^{3} \underline{\boldsymbol{A}}_i \partial_{x_i} \boldsymbol{w}_i = 0, \tag{2.110}$$

where $\underline{\boldsymbol{A}}_i$ are the Jacobian matrices such that

$$\underline{\boldsymbol{A}}_i = \frac{\partial \boldsymbol{f}_i}{\partial \boldsymbol{w}} + \underline{\boldsymbol{S}}_i, \tag{2.111}$$

and $\underline{\boldsymbol{S}}_i$ is defined by

$$\underline{\boldsymbol{S}}_i = (0, \boldsymbol{B}, \boldsymbol{v}\cdot\boldsymbol{B}, \boldsymbol{v})^T a_i^T, \tag{2.112}$$

with

$$\begin{aligned} a_1^T &= (0,0,0,0,0,1,0,0)^T, & (2.113)\\ a_2^T &= (0,0,0,0,0,0,1,0)^T, & (2.114)\\ a_3^T &= (0,0,0,0,0,0,0,1)^T. & (2.115)\end{aligned}$$

The source term is proportional to $\nabla\cdot\boldsymbol{B}$ which means that it is zero for exact solutions. To obtain the eigenvalues and the eigenvectors of the matrices $\underline{\boldsymbol{A}}_i$, we used the two changes of variables proposed by Jameson [58]. The first change brings the system to the primitive variables

$$\tilde{\boldsymbol{w}} = (\rho, v_1, v_2, v_3, p, B_1, B_2, B_3)^T, \tag{2.116}$$

which changes the quasi-linear form to

$$\partial_t \tilde{\boldsymbol{w}} + \sum_{i=1}^{3} \underline{\tilde{\boldsymbol{A}}}_i \partial_{x_i} \tilde{\boldsymbol{w}}_i = 0, \tag{2.117}$$

with

$$\underline{\tilde{\boldsymbol{A}}}_i = \underline{\tilde{\boldsymbol{M}}}^{-1} \underline{\tilde{\boldsymbol{A}}}_i \underline{\tilde{\boldsymbol{M}}}, \text{ where } \underline{\tilde{\boldsymbol{M}}}^{-1} = \frac{\partial \tilde{\boldsymbol{w}}}{\partial \boldsymbol{w}} \text{ and } \underline{\tilde{\boldsymbol{M}}} = \frac{\partial \boldsymbol{w}}{\partial \tilde{\boldsymbol{w}}}. \tag{2.118}$$

Given a normal vector $\boldsymbol{n} = (n_1, n_2, n_3)^T$, the jacobian matrix $\underline{\tilde{\boldsymbol{A}}} = \sum_{i=1}^{3} n_i \underline{\tilde{\boldsymbol{A}}}_i$ is

$$\underline{\tilde{\boldsymbol{A}}} = \begin{pmatrix} v_n & n_1\rho & n_2\rho & n_3\rho & 0 & 0 & 0 & 0 \\ 0 & v_n & 0 & 0 & \frac{n_1}{\rho} & \frac{n_1B_1-B_n}{\rho} & \frac{n_1B_2}{\rho} & \frac{n_1B_3}{\rho} \\ 0 & 0 & v_n & 0 & \frac{n_2}{\rho} & \frac{n_2B_1}{\rho} & \frac{n_2B_2-B_n}{\rho} & \frac{n_2B_3}{\rho} \\ 0 & 0 & 0 & v_n & \frac{n_3}{\rho} & \frac{n_3B_1}{\rho} & \frac{n_3B_2}{\rho} & \frac{n_3B_3-B_n}{\rho} \\ 0 & n_1\rho\gamma p & n_2\rho\gamma p & n_3\rho\gamma p & v_n & 0 & 0 & 0 \\ 0 & n_1B_1 - B_n & n_2B_1 & n_3B_1 & 0 & v_n & 0 & 0 \\ 0 & n_1B_2 & n_2B_2 - B_n & n_3B_2 & 0 & 0 & v_n & 0 \\ 0 & n_1B_3 & n_2B_3 & n_3B_3 - B_n & 0 & 0 & 0 & v_n \end{pmatrix}.$$

After that, another change of variables is performed in order to obtain a symmetric matrix (Details in [58]) that will have the following eigenvalues

$$\begin{aligned} \lambda &= \boldsymbol{v}\cdot\boldsymbol{n}, & (2.119)\\ \lambda &= \boldsymbol{v}\cdot\boldsymbol{n} \pm c_a, & (2.120)\\ \lambda &= \boldsymbol{v}\cdot\boldsymbol{n} \pm c_f, & (2.121)\\ \lambda &= \boldsymbol{v}\cdot\boldsymbol{n} \pm c_s, & (2.122)\end{aligned}$$

where

$$c_a^2 = \frac{\boldsymbol{B}\cdot\boldsymbol{n}}{\rho},\ \ c_f^2 = \frac{1}{2}\left(c^2 + \frac{\boldsymbol{B}\cdot\boldsymbol{B}}{\rho} + \sqrt{\left(c^2 + \frac{\boldsymbol{B}\cdot\boldsymbol{B}}{\rho}\right)^2 - 4c^2\frac{(\boldsymbol{B}\cdot\boldsymbol{n})^2}{\rho}}\right), \tag{2.123}$$

$$c^2 = \frac{\gamma p}{\rho},\ \ c_s^2 = \frac{1}{2}\left(c^2 + \frac{\boldsymbol{B}\cdot\boldsymbol{B}}{\rho} - \sqrt{\left(c^2 + \frac{\boldsymbol{B}\cdot\boldsymbol{B}}{\rho}\right)^2 - 4c^2\frac{(\boldsymbol{B}\cdot\boldsymbol{n})^2}{\rho}}\right). \tag{2.124}$$

They are associated, respectively, to advection, Alfvén, fast accoustic and slow accoustic waves. It is important to remark that through the change of variables λ are also eigenvalues of the conservative system. All eigenvalues are real making the MHD system a hyperbolic one. However, in some cases the eigenvalues can coincide which means that it is not a strictly hyperbolic system. Indeed, the MHD equations are not convex and in some cases the characteristic fields are neither really linear nor linearly degenerated [59].

2.2.3 Resistive MHD

The goal of the Resistive MHD is to extend the temporal scale beyond the electronic collision time so the dissipative effects due to the electrical resistivity can be taken into account. In this system, the resistivity term η is assumed to be different from zero. The complete system of the resistive MHD is then written as

$$\begin{cases} \partial_t\rho + \nabla\cdot(\rho\boldsymbol{v}) &= 0, \\ \partial_t\rho\boldsymbol{v} + \nabla\cdot(\rho\boldsymbol{v}\otimes\boldsymbol{v}) &= \boldsymbol{J}\times\boldsymbol{B} - \nabla p - \nabla\cdot\underline{\boldsymbol{\pi}}, \\ \partial_t\rho e + \nabla\cdot(\rho e\boldsymbol{v} + p\boldsymbol{v}) &= (\boldsymbol{J}\times\boldsymbol{B})\cdot\boldsymbol{v} + \eta\boldsymbol{J}^2 - (\nabla\cdot(\boldsymbol{v}\underline{\boldsymbol{\pi}}) + \nabla\cdot\boldsymbol{Q}), \\ \partial_t\boldsymbol{B} &= -\nabla\times\boldsymbol{E}, \end{cases} \tag{2.125}$$

with the same closure relations as the Ideal MHD system, with the difference that the Ohm's Law here takes into account the resistive term, i.e.,

$$\boldsymbol{E} + \boldsymbol{v}\times\boldsymbol{B} = \eta\boldsymbol{J}. \tag{2.126}$$

2.2.4 Reduced MHD models

The first article introducing the reduced MHD system in a cylindrical geometry and supposing a weak pressure in the plasma was written by Strauss in 1976 [60]. After

that, other articles introduced the toroidal effects [61, 62] or a stronger plasma pressure [63].

In the Reduced MHD model the number of scalar fields evolving in time is reduced. As a consequence an analytical treatment is viable and the calculations are more reasonable if a numerical simulation is needed. Hence, from the complete MHD system, it is possible to obtain the reduced resistive MHD system and the Grad-Shafranov (GS) equilibrium equation.

2.2.4.1 Grad-Shafranov (GS) equilibrium

In a tokamak a strong magnetic field is used in the toroidal direction to confine the plasma. It is possible to decompose this field onto a toroidal $\boldsymbol{B}_\phi$ and a poloidal $\boldsymbol{B}_\theta$ directions [64]

$$\begin{aligned} \boldsymbol{B} &= \boldsymbol{B}_\phi + \boldsymbol{B}_\theta, \\ &= F\nabla\phi + \nabla\psi \times \nabla\phi, \\ &= F\nabla\phi + \nabla \times (\psi\nabla\phi), \end{aligned} \tag{2.127}$$

with F being a scalar that is time-independent but could depend on the poloidal coordinates, ψ the magnetic flux and ϕ corresponds to the coordinate of the toroidal direction.

Now, applying this definition to the Maxwell's equation $\nabla \times \boldsymbol{B} = \boldsymbol{J}$ yields the current density

$$\begin{aligned} \boldsymbol{J} &= \nabla \times (F\nabla\phi + \nabla\psi \times \nabla\phi) = \nabla \times (F\nabla\phi) + \nabla \times (\nabla\psi \times \nabla\phi) \\ &= \nabla F \times \nabla\phi + \nabla \times (\nabla\psi \times \nabla\phi). \end{aligned}$$

For the second term, we can use the relation that holds for any scalar A (Appendix A)

$$\nabla \times (\nabla A \times \nabla\phi) = -\nabla\phi(\Delta^* A) + \frac{1}{R^2}\nabla_{\boldsymbol{\xi}}(\partial_\phi A), \tag{2.128}$$

where $\nabla_{\boldsymbol{\xi}}$ is the gradient operator of a poloidal section in cylindrical coordinates, i.e. $\nabla_{\boldsymbol{\xi}} = \nabla R\partial_R + \nabla Z\partial_Z$. The operator Δ^* is the second-order Grad-Shafranov operator defined by

$$\Delta^*\psi = R\nabla_{\boldsymbol{\xi}} \cdot \left(\frac{1}{R}\nabla_{\boldsymbol{\xi}}\psi\right). \tag{2.129}$$

Hence, the current is

$$\boldsymbol{J} = \left(\nabla F \times \nabla\phi - j_\phi\nabla\phi + \boldsymbol{J}^\star\right), \tag{2.130}$$

where j_ϕ and $\boldsymbol{J}^\star$ are defined as

$$j_\phi = \Delta^*\psi \text{ and } \boldsymbol{J}^\star = \frac{1}{R^2}\nabla_{\boldsymbol{\xi}}\left(\partial_\phi\psi\right). \tag{2.131}$$

Moreover, the plasma here is treated as an ideal axis-symmetric single-fluid to which a stationary condition is added. The Grad-Shafranov equation [65, 66] models a plasma equilibrium in which the pressure gradient is compensated by the Lorentz force [9, 55, 67–69]. It is a static equilibrium and thus, it does not present a temporal evolution ($\partial_t = 0$) and the plasma velocity is assumed to be zero. With these assumptions, the idel MHD system (2.88) becomes

$$\begin{cases} \nabla p &= \boldsymbol{J} \times \boldsymbol{B}, \\ \boldsymbol{J} &= \nabla \times \boldsymbol{B}, \\ \nabla \cdot \boldsymbol{B} &= 0. \end{cases} \tag{2.132}$$

Grad-Shafranov equation is a nonlinear elliptical differential equation obtained by adding the toroidal symmetry condition [65] which reduces the magnetic field to its poloidal component, i.e., $\boldsymbol{B} = \boldsymbol{B}_\theta = \nabla \times (\psi \nabla \phi)$. Hence, the equation modeling the absence of magnetic monopoles becomes

$$\nabla \cdot \boldsymbol{B} = \frac{1}{R}\partial_R(RB_R) + \partial_z B_z = 0, \tag{2.133}$$

with

$$\begin{aligned} B_R &= -\frac{1}{R}\partial_z \psi, \\ B_Z &= \frac{1}{R}\partial_R \psi. \end{aligned}$$

The current (2.130) is used to obtain the equation describing the equilibrium between the pressure gradient and the Lorentz force $\nabla p = \boldsymbol{J} \times \boldsymbol{B}$. Its projection onto the magnetic field and the current are zero,

$$\boldsymbol{B} \cdot \nabla p = 0 \quad \Rightarrow \boldsymbol{e}_\phi \cdot (\nabla \psi \times \nabla p) = 0, \tag{2.134}$$

$$\boldsymbol{J} \cdot \nabla p = 0 \quad \Rightarrow \boldsymbol{e}_\phi \cdot (\nabla \psi \times \nabla F) = 0. \tag{2.135}$$

These implications lead to an important conclusion: p and F are functions depending on the magnetic flux ψ. The Grad-Shafranov equation is then obtained by introducing these two flux functions - $p(\psi)$ and $F(\psi)$ - into the projection of the momentum equation onto $\nabla \psi$ as follows

$$\begin{aligned} \nabla \psi \cdot \nabla p &= \nabla \psi \cdot (\boldsymbol{J} \times \boldsymbol{B}), \\ &= \boldsymbol{J} \cdot ((F \nabla \phi + \nabla \psi \times \nabla \phi) \times \nabla \psi), \\ &= -(\nabla F \cdot \nabla \psi)\frac{F}{R^2} - \frac{1}{R^2}\Delta^* \psi (\nabla \psi \cdot \nabla \psi), \end{aligned}$$

yielding

$$\Delta^*\psi = -R^2\frac{dp}{d\psi} - F\frac{dF}{d\psi}. \tag{2.136}$$

This equation holds for whichever functions p and F. The choice made for these functions altogether with the one made for the boundary conditions for ψ determines which plasma equilibrium will be obtained.

2.2.4.2 Reduced Resistive MHD system

Now, replacing the magnetic field definition (2.127) into the Faraday's law shown on system (2.125) yields the induction equation,

$$\nabla \times (\nabla\phi\partial_t\psi + \boldsymbol{E}) = 0, \tag{2.137}$$

which, with the introduction of the arbitrary electric potential U, becomes

$$\nabla\phi\partial_t\psi + \boldsymbol{E} = -F_0\nabla U. \tag{2.138}$$

It is important to remark the difference between the scaling factor F_0 which is constant and the toroidal component F of the magnetic field. In fact, F is a function of the poloidal coordinates $\boldsymbol{\xi}$ that will be profiled as a function of the equilibrium state.

The equation above is the starting point to obtain the velocity profile. The electric field in (2.138) is given by the Ohm's law shown in (2.125), which is

$$\boldsymbol{E} = -\boldsymbol{v} \times \boldsymbol{B} + \eta\boldsymbol{J}. \tag{2.139}$$

Then, performing a cross product with $\nabla\phi$ on equation (2.138) leads to

$$(\nabla\phi\partial_t\psi - \boldsymbol{v} \times \boldsymbol{B} + \eta\boldsymbol{J} = -F_0\nabla U) \times \nabla\phi. \tag{2.140}$$

The temporal derivative term contains a $\nabla\phi\times\nabla\phi$, which is zero. The second is rewritten with the help of the vector identity $\boldsymbol{a} \times (\boldsymbol{b} \times \boldsymbol{c}) = (\boldsymbol{a} \cdot \boldsymbol{c})\boldsymbol{b} - (\boldsymbol{a} \cdot \boldsymbol{b})\boldsymbol{c}$, yielding

$$-(\boldsymbol{v} \times \boldsymbol{B}) \times \nabla\phi = (\nabla\phi \cdot \boldsymbol{B})\boldsymbol{v} - (\nabla\phi \cdot \boldsymbol{v})\boldsymbol{B}. \tag{2.141}$$

Thus, considering the definition of $\boldsymbol{B}$ given in (2.127), equation (2.140) becomes

$$\frac{F}{R^2}\boldsymbol{v} - (\boldsymbol{v} \cdot \nabla\phi)\boldsymbol{B} = -F_0\nabla U \times \nabla\phi - \eta\boldsymbol{J} \times \nabla\phi. \tag{2.142}$$

This is a vector relation that can be projected onto the toroidal direction. When it is done it comes out that there is no constraint on the toroidal component of the velocity.

In other words $(\boldsymbol{v} \cdot \nabla\phi)$ is a free parameter in the previous relation. Therefore, the velocity can be profiled as

$$\boldsymbol{v} = \vartheta \boldsymbol{B} + \frac{R^2 F_0}{F} \nabla\phi \times \nabla U + \boldsymbol{v}'_\perp, \tag{2.143}$$

where

$$\vartheta = \frac{R^2}{F}(\boldsymbol{v} \cdot \nabla\phi) \text{ and } \boldsymbol{v}'_\perp = \frac{R^2}{F} \nabla\phi \times (\eta \boldsymbol{J}). \tag{2.144}$$

Taking into account the fact that the reduced field has been separated into toroidal and poloidal components and knowing that the velocity evolution is strongly dependent on the magnetic field behavior, the same idea is applied to the velocity profile, giving the following formulation

$$\boldsymbol{v} = \vartheta F \nabla\phi + \boldsymbol{v}_\perp, \tag{2.145}$$

in which

$$\boldsymbol{v}_\perp = \vartheta(\nabla\psi \times \nabla\phi) + \frac{R^2 F_0}{F} \nabla\phi \times \nabla U + \boldsymbol{v}'_\perp. \tag{2.146}$$

In this context some relations can be derived that will be useful in order to write the equations in a more compact way. For any scalar function A, the following relations hold

$$\begin{aligned}
\boldsymbol{B} \cdot \nabla A &= F \nabla\phi \cdot \nabla A + (\nabla\psi \times \nabla\phi) \cdot \nabla A, \\
\nabla \cdot \boldsymbol{v} &= F \nabla\phi \cdot \nabla\vartheta + (\nabla\psi \times \nabla\phi) \cdot \nabla\vartheta + \nabla\left(\frac{R^2 F_0}{F}\right) \cdot (\nabla\psi \times \nabla U) + \nabla \cdot \boldsymbol{v}'_\perp, \\
\nabla \cdot (\boldsymbol{v} A) &= F \nabla\phi \cdot \nabla(\vartheta A) + (\nabla\psi \times \nabla\phi) \cdot \nabla(\vartheta A) + \nabla\left(\frac{R^2 F_0 A}{F}\right) \cdot (\nabla\psi \times \nabla U) + \nabla \cdot (\boldsymbol{v}'_\perp A), \\
\boldsymbol{v} \cdot \nabla A &= F \vartheta \nabla\phi \cdot \nabla A + \vartheta(\nabla\psi \times \nabla\phi) \cdot \nabla A + \frac{R^2 F_0}{F}(\nabla\psi \times \nabla U) \cdot \nabla A + \boldsymbol{v}'_\perp \cdot \nabla A.
\end{aligned}$$

Let's start by the derivation of the equation describing the evolution of the magnetic flux ψ. In order to obtain it we project equation (2.138) onto the toroidal direction $\nabla\phi$, yielding

$$\partial_t \psi(\nabla\phi \cdot \nabla\phi) + \boldsymbol{E} \cdot \nabla\phi = -F_0 \nabla U \cdot \nabla\phi, \tag{2.147}$$

the term $\boldsymbol{E}\cdot\nabla\phi$ can be evaluated by using the Ohm's Law (2.125), leading to

$$\begin{aligned}
\boldsymbol{E}\cdot\nabla\phi &= (-\boldsymbol{v}\times\boldsymbol{B}+\eta\boldsymbol{J})\cdot\nabla\phi \\
&= (\boldsymbol{B}\times\boldsymbol{v})\cdot\nabla\phi - \frac{1}{R^2}\eta j_\phi, \\
&= \cancelto{0}{(F\nabla\phi\times\boldsymbol{v})\cdot\nabla\phi} + ((\nabla\psi\times\nabla\phi)\times\boldsymbol{v})\cdot\nabla\phi - \frac{1}{R^2}\eta j_\phi, \\
&= ((\nabla\psi\cdot\boldsymbol{v})\nabla\phi - (\nabla\psi\cdot\nabla\phi)\boldsymbol{v})\cdot\nabla\phi - \frac{1}{R^2}\eta j_\phi, \\
&= \frac{1}{R^2}(\boldsymbol{v}\cdot\nabla\psi) - (\boldsymbol{v}\cdot\nabla\phi)(\nabla\phi\cdot\nabla\psi) - \frac{1}{R^2}\eta j_\phi,
\end{aligned}$$

hence,

$$\begin{aligned}
\frac{1}{R^2}\partial_t\psi + \frac{1}{R^2}(\boldsymbol{v}\cdot\nabla\psi) - (\boldsymbol{v}\cdot\nabla\phi)(\nabla\phi\cdot\nabla\psi) - \frac{1}{R^2}\eta j_\phi &= -F_0\nabla U\cdot\nabla\phi, \\
\partial_t\psi + (\boldsymbol{v} - R^2(\boldsymbol{v}\cdot\nabla\phi)\nabla\phi)\cdot\nabla\psi) - \eta j_\phi + F_0\partial_\phi U &= 0,
\end{aligned}$$

which gives the most general form of the induction equation for Reduced MHD,

$$\partial_t\psi + \boldsymbol{v}_\perp\cdot\nabla\psi = \eta j_\phi - F_0\partial_\phi U. \tag{2.148}$$

For the energy equation, the starting point is also the equation present in system (2.125), which is

$$\partial_t\rho e + \nabla\cdot(\rho e\boldsymbol{v} + p\boldsymbol{v}) = (\boldsymbol{J}\times\boldsymbol{B})\cdot\boldsymbol{v} + \eta\boldsymbol{J}^2 - \boldsymbol{v}\cdot(\nabla\cdot\underline{\boldsymbol{\pi}}) - \underline{\boldsymbol{\pi}}:\nabla\boldsymbol{v} - \nabla\cdot\boldsymbol{Q}. \tag{2.149}$$

Using the definition $\rho e = \frac{p}{\gamma-1} + \frac{1}{2}\rho(\boldsymbol{v}\cdot\boldsymbol{v})$

$$\begin{aligned}
\frac{1}{\gamma-1}(\partial_t p + \nabla\cdot(p\boldsymbol{v})) + \nabla\cdot(p\boldsymbol{v}) + \boldsymbol{v}\cdot\partial_t(\rho\boldsymbol{v}) + \nabla\cdot\left(\frac{\rho}{2}(\boldsymbol{v}\cdot\boldsymbol{v})\boldsymbol{v}\right) - \frac{\boldsymbol{v}\cdot\boldsymbol{v}}{2}\partial_t\rho = \\
(\boldsymbol{J}\times\boldsymbol{B})\cdot\boldsymbol{v} + \eta\boldsymbol{J}^2 - \boldsymbol{v}\cdot(\nabla\cdot\underline{\boldsymbol{\pi}}) - \underline{\boldsymbol{\pi}}:\nabla\boldsymbol{v} - \nabla\cdot\boldsymbol{Q},
\end{aligned}$$

this can be rewritten as

$$\begin{aligned}
\frac{1}{\gamma-1}(\partial_t p + \nabla\cdot(p\boldsymbol{v})) + \nabla\cdot(p\boldsymbol{v}) + \boldsymbol{v}\cdot\partial_t(\rho\boldsymbol{v}) + \nabla\cdot((\rho\boldsymbol{v}\otimes\boldsymbol{v})\boldsymbol{v}) - \frac{\boldsymbol{v}\cdot\boldsymbol{v}}{2}\partial_t\rho - \nabla\cdot\left(\rho\boldsymbol{v}\frac{\boldsymbol{v}\cdot\boldsymbol{v}}{2}\right) = \\
(\boldsymbol{J}\times\boldsymbol{B})\cdot\boldsymbol{v} + \eta\boldsymbol{J}^2 - \boldsymbol{v}\cdot(\nabla\cdot\underline{\boldsymbol{\pi}}) - \underline{\boldsymbol{\pi}}:\nabla\boldsymbol{v} - \nabla\cdot\boldsymbol{Q},
\end{aligned}$$

which will lead to

$$\begin{aligned}
\frac{1}{\gamma-1}(\partial_t p + \nabla\cdot(p\boldsymbol{v}) + (\gamma-1)p(\nabla\cdot\boldsymbol{v})) = \\
-\boldsymbol{v}\cdot(\partial_t(\rho\boldsymbol{v}) + \nabla\cdot(\rho\boldsymbol{v}\otimes\boldsymbol{v}) + \nabla p - (\boldsymbol{J}\times\boldsymbol{B}) + (\nabla\cdot\underline{\boldsymbol{\pi}})) \\
-\frac{\boldsymbol{v}\cdot\boldsymbol{v}}{2}(\partial_t\rho + \nabla\cdot(\rho\boldsymbol{v})) + \eta\boldsymbol{J}^2 - \underline{\boldsymbol{\pi}}:\nabla\boldsymbol{v} - \nabla\cdot\boldsymbol{Q},
\end{aligned}$$

in which it is possible to identify the momentum equation (first term on RHS) and the continuity equation (second term in RHS) written in the conservative form. This means that the total energy equation can be written in a pressure formulation as

$$\partial_t p + \boldsymbol{v} \cdot \nabla p + \gamma p (\nabla \cdot \boldsymbol{v}) = (\gamma - 1)(\eta \boldsymbol{J}^2 - \nabla \cdot \boldsymbol{Q} - \underline{\boldsymbol{\pi}} : \nabla \boldsymbol{v}). \tag{2.150}$$

Finally, the momentum equation in system (2.125) can be reformulated under the assumptions made here for the magnetic field

$$\partial_t \rho \boldsymbol{v} + \nabla \cdot (\rho \boldsymbol{v} \otimes \boldsymbol{v}) = \boldsymbol{J} \times \boldsymbol{B} - \nabla p - \nabla \cdot \underline{\boldsymbol{\pi}}. \tag{2.151}$$

As, $\nabla \cdot (\rho \boldsymbol{v} \otimes \boldsymbol{v}) = \rho \boldsymbol{v} \cdot \nabla \boldsymbol{v} + \boldsymbol{v} \nabla \cdot (\rho \boldsymbol{v})$, the previous equation can be rewritten as

$$\rho \left(\partial_t \boldsymbol{v} + \boldsymbol{v} \cdot \nabla \boldsymbol{v} \right) = \boldsymbol{J} \times \boldsymbol{B} - \nabla p - \nabla \cdot \underline{\boldsymbol{\pi}}. \tag{2.152}$$

Then, in the context where the velocity writes as $\boldsymbol{v} = \vartheta \boldsymbol{B} + \boldsymbol{w}_{2D}$ the equation (2.152) becomes

$$\rho \boldsymbol{B} \partial_t \vartheta + \rho \vartheta \partial_t \boldsymbol{B} + \rho \partial_t \boldsymbol{w}_{2D} + \rho \boldsymbol{v} \cdot \nabla \boldsymbol{v} = \boldsymbol{J} \times \boldsymbol{B} - \nabla p - \nabla \cdot \underline{\boldsymbol{\pi}}. \tag{2.153}$$

Let's consider a projection applied onto a direction $\boldsymbol{N}$, which can be a function of time and spatial coordinates. It yields

$$\begin{aligned} \rho (\boldsymbol{N} \cdot \boldsymbol{B}) \partial_t \vartheta + \rho \vartheta (\boldsymbol{N} \cdot \partial_t \boldsymbol{B}) \quad &+ \quad \rho (\boldsymbol{N} \cdot \partial_t \boldsymbol{w}_{2D}) + \rho \boldsymbol{N} \cdot (\boldsymbol{v} \cdot \nabla \boldsymbol{v}) \\ &= \quad \boldsymbol{N} \cdot (\boldsymbol{J} \times \boldsymbol{B} - \nabla p) - \boldsymbol{N} \cdot (\nabla \cdot \underline{\boldsymbol{\pi}}). \end{aligned} \tag{2.154}$$

To obtain the Reduced MHD system, we will consider the context in which $F \approx F_0$ and $\boldsymbol{v}'_\perp = 0$. Some special attention, however, must be paid concerning the approximation of F. A careful look at the above equation shows that the Grad-Shafranov equilibrium is present (the term $(\boldsymbol{J} \times \boldsymbol{B} - \nabla p)$). This equilibrium is given by equation (2.136) using the magnetic field defined in (2.127) in which F is present without assuming $F \approx F_0$. This equilibrium is used as an initial condition for the numerical simulations and therefore, it must be preserved. This means that, the evaluation of the current $\boldsymbol{J} = \nabla \times \boldsymbol{B}$ must not take into account the approximation for F.

On the other hand, an explicit storage of F for the numerical strategy can be avoided if the projections of the momentum equation are orthogonal to $\frac{1}{R^2} F \nabla F$. For instance

$$\nabla \phi \cdot \left(\frac{1}{R^2} F \nabla F \right) = 0 \text{ and } \nabla \phi \cdot \nabla \times \left(R^2 \frac{1}{R^2} F \nabla F \right), \tag{2.155}$$

indeed

$$R^2 \frac{1}{R^2} F \nabla F = \nabla \left(\frac{F^2}{2} \right), \tag{2.156}$$

and the curl of a gradient is always zero.

In this case, to derive the momentum equation projections we use the relation $\boldsymbol{v} \cdot \nabla \boldsymbol{v} = \nabla \frac{|\boldsymbol{v}|^2}{2} - \boldsymbol{v} \times \boldsymbol{\Omega}$, in which $\boldsymbol{\Omega} = \nabla \times \boldsymbol{v}$. Hence, if the velocity profile considered is $\boldsymbol{v} = \vartheta F \nabla \phi + \boldsymbol{v}_{2D}$, this term becomes (see Appendix A).

$$(\boldsymbol{v} \cdot \nabla \boldsymbol{v}) = \nabla \phi (\boldsymbol{v} \cdot \nabla (F\vartheta)) + \nabla_{\boldsymbol{\xi}} \left(\tfrac{|\boldsymbol{v}|^2}{2} \right) - \tfrac{1}{R^2} \nabla_{\boldsymbol{\xi}} \left(\tfrac{F^2 \vartheta^2}{2} \right) - \tfrac{F\vartheta}{R^2} \nabla \phi \times \mathbb{H}_{2D} + \Omega_\phi \mathbb{V}_{2D}, \tag{2.157}$$

where

$$\begin{aligned} R\mathbb{V}_{2D} &= \vartheta \nabla_{\boldsymbol{\xi}} \psi - R^2 \nabla_{\boldsymbol{\xi}} U && (2.158) \\ R\Omega_\phi &= R^2 \omega - \vartheta j_\phi - \nabla_{\boldsymbol{\xi}} \vartheta \cdot \nabla_{\boldsymbol{\xi}} \psi && (2.159) \\ \mathbb{H}_{2D} &= \vartheta \nabla_{\boldsymbol{\xi}} (\partial_\phi \psi) - R^2 \nabla_{\boldsymbol{\xi}} (\partial_\phi U) + \partial_\phi \vartheta \nabla_{\boldsymbol{\xi}} \psi. && (2.160) \end{aligned}$$

Therefore the projection of the momentum equation writes

$$\begin{aligned} &\rho (\boldsymbol{N} \cdot \boldsymbol{B}) \partial_t \vartheta + \rho \vartheta (\boldsymbol{N} \cdot \partial_t \boldsymbol{B}) + \rho (\boldsymbol{N} \cdot \partial_t \boldsymbol{w}_{2D}) + (F_0 \boldsymbol{N} \cdot \nabla \phi) \rho \boldsymbol{v} \cdot \nabla \vartheta \\ &+ \rho \boldsymbol{N} \cdot \left(\nabla_{\boldsymbol{\xi}} \left(\frac{|\boldsymbol{v}|^2}{2} \right) - \frac{1}{R^2} \nabla_{\boldsymbol{\xi}} \left(\frac{F^2 \vartheta^2}{2} \right) - \frac{F\vartheta}{R^2} \nabla \phi \times \mathbb{H}_{2D} + \Omega_\phi \mathbb{V}_{2D} \right) \\ &\qquad = \boldsymbol{N} \cdot (\boldsymbol{J} \times \boldsymbol{B} - \nabla p) - \boldsymbol{N} \cdot (\nabla \cdot \underline{\boldsymbol{\pi}}). \end{aligned} \tag{2.161}$$

From this equation, two projections can be obtained, one that will give an equation for ϑ and another U. For the first one we make $\boldsymbol{N} = R^2 \nabla \phi$ yielding

$$\rho F_0 \partial_t \vartheta + F_0 \vartheta (\partial_t \rho + \nabla \cdot (\rho \boldsymbol{v})) + F_0 \rho \boldsymbol{v} \cdot \nabla \vartheta = -\partial_\phi \left(\frac{|\nabla_{\boldsymbol{\xi}} \psi|^2}{2R^2} \right) - \partial_\phi p - R^2 \nabla \phi \cdot (\nabla \cdot \underline{\boldsymbol{\pi}}). \tag{2.162}$$

to obtain this equation, the following relations were used

$$\partial_t \left(\frac{F_0}{R^2} \right) = 0, \quad \nabla \phi \cdot \boldsymbol{w}_{2D} = 0 \text{ and } R^2 \nabla \phi \cdot \boldsymbol{v} = F_0 \vartheta. \tag{2.163}$$

Finally, for the evolution of U is given by

$$\begin{aligned} &\nabla \phi \cdot \left(\nabla \times \left(R^2 \left(\rho \boldsymbol{B} \partial_t \vartheta + \rho \vartheta \partial_t \boldsymbol{B} + \rho \partial_t \boldsymbol{w}_{2D} + \rho \nabla_{\boldsymbol{\xi}} \left(\frac{|\boldsymbol{v}|^2}{2} \right) \right) \right) \right) \\ &\nabla \phi \cdot \left(\nabla \times \left(R^2 \left(-\frac{1}{R^2} \nabla_{\boldsymbol{\xi}} \left(\frac{F^2 \vartheta^2}{2} \right) - \frac{F_0 \vartheta}{R^2} \nabla \phi \times \mathbb{H}_{2D} + \Omega_\phi \mathbb{V}_{2D} \right) \right) \right) \\ &\qquad = \nabla \phi \cdot \left(\nabla \times \left(R^2 ((\boldsymbol{J} \times \boldsymbol{B} - \nabla p) - \nabla \cdot \underline{\boldsymbol{\pi}}) \right) \right). \end{aligned} \tag{2.164}$$

Therefore, the extended reduced resistive MHD model is

$$\begin{cases} \partial_t \psi + \boldsymbol{v}_\perp \cdot \nabla \psi - \eta j_\phi + F_0 \partial_\phi U = 0, \\ \partial_t \rho + \nabla \cdot (\rho \boldsymbol{v}) = 0, \\ \rho F_0 \partial_t \vartheta + F_0 \vartheta (\partial_t \rho + \nabla \cdot (\rho \boldsymbol{v})) + F_0 \rho \boldsymbol{v} \cdot \nabla \vartheta = -\partial_\phi \left(\dfrac{|\nabla_{\boldsymbol{\xi}} \psi|^2}{2R^2} \right) \\ -\partial_\phi p - R^2 \nabla \phi \cdot (\nabla \cdot \underline{\boldsymbol{\pi}}), \\ \nabla \phi \cdot \left(\nabla \times \left(R^2 \left(\rho \boldsymbol{B} \partial_t \vartheta + \rho \vartheta \partial_t \boldsymbol{B} + \rho \partial_t \boldsymbol{w}_{2D} + \rho \nabla_{\boldsymbol{\xi}} \left(\dfrac{|\boldsymbol{v}|^2}{2} \right) \right) \right) \right) \\ \nabla \phi \cdot \left(\nabla \times \left(R^2 \left(-\dfrac{1}{R^2} \nabla_{\boldsymbol{\xi}} \left(\dfrac{F^2 \vartheta^2}{2} \right) - \dfrac{F_0 \vartheta}{R^2} \nabla \phi \times \mathbb{H}_{2D} + \Omega_\phi \mathbb{V}_{2D} \right) \right) \right) \\ = \nabla \phi \cdot \left(\nabla \times \left(R^2 ((\boldsymbol{J} \times \boldsymbol{B} - \nabla p) - \nabla \cdot \underline{\boldsymbol{\pi}}) \right) \right), \\ \partial_t p + \boldsymbol{v} \cdot \nabla p + \gamma p (\nabla \cdot \boldsymbol{v}) = (\gamma - 1)(\eta \boldsymbol{J}^2 - \nabla \cdot \boldsymbol{Q} - \underline{\boldsymbol{\pi}} : \nabla \boldsymbol{v}) \end{cases} \tag{2.165}$$

2.3 Conclusions

This chapter started by showing the fundamental plasma models that can be used to simulate a plasma. The fluid model, a simplification of the kinetic model was obtained and its extension, known as Magnetohydrodynamic model has been developed.

A few MHD models were obtained using as basis the fluid description of a plasma. For that, different assumptions and hypothesis were made concerning properties of a plasma, in general; and more precisely plasmas in a tokamak. Some of these assumptions have a strongly theoretical basis while a few others have been based on weaker arguments. However, MHD models have had been tested and verified with experimental results for almost 50 years now and their validity is widely established and accepted. One of its most important applications today is the study of instabilities occurring in a hot plasma that can constrain the operation of a tokamak.

Having this in mind a full MHD model was derived, however, it is still a very complex model containing several independent variables and fields that must be treated. For this reason, approximations and simplified models have been used for theoretical and numerical studies. These are known as Reduced models and the Reduced Resistive one was obtained here. To obtain it, extra assumptions concerning the fields, e.g., strong toroidal magnetic field, were taken into account. Also, we obtained a special equilibrium condition that is largely used for numerical simulation, called the Grad-Shafranov equilibrium. Maxwell's equations bring an extra difficulty to the problem:

the divergence free constraint that is not directly satisfied at discrete level. Hence some strategies to overcome it are discussed, in particular the Helmholtz decomposition.

Having derived the models, ou goal becomes the methods that can be used to solve them numerically. We concentrate our efforts on the Finite Element Method (FEM) for which we derived a stabilization in the framework of the Variational Multi-Scale (VMS) formulation.

Chapter 3

Numerical method: Variational Multi-Scale (VMS) stabilization

The simulation of magnetohydrodyamic plasmas involves flows dominated by convection. Thus, numerical schemes have to take into consideration the effects that the unresolved (fine) scales over the resolved ones. Some pioneering works used to mimic those effects with the help of a numerical viscosity. It was after, that an explicit evaluation of the sub-scales was introduced by Godunov. This involved finding the solution of Riemann problems on the finite volume context. The main disadvantage of this formulation, though, it that the Riemann problems are highly dependent on the mesh topology because they are defined in the direction normal to the mesh faces.

This becomes very problematic when the flow to be treated comprises strong anisotropies as it is the case of magnetized plasmas. In order to overcome that, Finite Element Formulation can establish a very useful framework, the problem is that it can lead to non-physical behavior when dealing with hyperbolic operators. For this reason, different stabilization techniques have been developed to avoid this limitation. We concentrate our efforts here on the Variational Mutli-Scale (VMS) Stabilization.

The idea behind the variational multi-scale (VMS) formulation [1, 14, 15] is to emulate the effects of the unresolved scales over the resolved scales in order to stabilize the waves. The strategy is residual-based and is designed to achieve numerical stability without compromising the physical instabilities that are the object of study and accuracy. The main goal is to avoid crosswind diffusion effects by introducing a upwinding process which leads to numerical diffusion essentially in the flow direction. This is achieved by adding a contribution to the weak formulation. The critical point is the design of a scaling matrix that adjusts the numerical dissipation but preserves the order of accuracy of the Galerkin method.

In this chapter the formalism of the finite element problem is described (3.1) followed by the justification for the need of stabilization when dealing with these types of scheme (3.1.2). Then, a particular stabilization strategy, e.g., Variational Multi-scale is introduced and its properties are discussed (3.2). Finally, the details of the numerical strategy, as for example, the spatial and temporal discretization are shown (3.2.4)

3.1 Finite element method: model problem

To study and understand the basics of the finite elements method (FEM), let us take a look at a general model problem. More details will be given further is the chapter. The goal here is to introduce the concepts that will be used to develop the stabilization. Let be Ω a $\mathbb{R}^2$ regular domain of which the boundary is noted Γ and an equation written in the compact form

$$\partial_t \boldsymbol{w} + \mathcal{L}(\boldsymbol{\partial}, \boldsymbol{w}) = \boldsymbol{f}, \quad \text{in } \Omega, \quad \forall t > 0, \tag{3.1}$$

where $\boldsymbol{w}$ is the vector containing the variables of the system, which are functions of the space variables $\boldsymbol{x} = (x_1, x_2, x_3)^T$, and $\mathcal{L}$ a linear application. We assume that Dirichlet type condition is verified at the boundary, i.e.

$$\boldsymbol{w}(\boldsymbol{x}, t) = \boldsymbol{g}(\boldsymbol{x}) \quad \forall \boldsymbol{x} \in \Gamma, \quad \forall t > 0 \tag{3.2}$$

and that an initial condition closes the problem

$$\forall \boldsymbol{x} \in \Omega, \quad \boldsymbol{w}(\boldsymbol{x}, 0) = \boldsymbol{w}^0(\boldsymbol{x}). \tag{3.3}$$

To obtain the weak formulation of the problem, this equation is multiplied by a function, called test function $\boldsymbol{w}^\star$, which is assumed to be regular enough, and integrated over the domain Ω

$$\int_\Omega (\partial_t \boldsymbol{w} + \mathcal{L}(\boldsymbol{\partial}, \boldsymbol{w})) \cdot \boldsymbol{w}^\star = \int_\Omega \boldsymbol{f} \cdot \boldsymbol{w}^\star. \tag{3.4}$$

This yields the variational formulation of this problem

$$\left\{ \begin{array}{rcll} & \text{Find } \boldsymbol{w} \text{ such as} & & \\ \partial_t(\boldsymbol{w}, \boldsymbol{w}^\star) + a(\boldsymbol{w}, \boldsymbol{w}^\star) & = & l(\boldsymbol{w}^\star), & \forall \boldsymbol{w}^\star, \\ \boldsymbol{w}(\boldsymbol{x}, 0) & = & \boldsymbol{w}^0(\boldsymbol{x}), & \forall \boldsymbol{x} \in \Omega, \\ \boldsymbol{w}(\boldsymbol{x}, t) & = & \boldsymbol{g}(\boldsymbol{x}), & \forall \boldsymbol{x} \in \Gamma, \end{array} \right. \tag{3.5}$$

where a and l are functions associated to the problem, $(.,.)$ is the L^2 scalar product, and $\boldsymbol{w}^0$ and $\boldsymbol{g}$ are functions of $L^2(\Omega)$.

3.1.1 Galerkin Method

The Galerkin method consists of a projection of the variational formulation from a continuous (infinite dimensional) domain to a discretized (finite dimensional) one. For that, the domain Ω is discretized through a division into elements Ω_e. The total number of elements on the new domain Ω_h is $\mathcal{N}_{el}$, i.e.,

$$\Omega_h = \bigcup_{1}^{\mathcal{N}_{el}} \Omega_e. \tag{3.6}$$

These elements cover all the domain and they are connected either by a segment or a node. Hence, the Galerkin method is the search of the unknowns in the same approximated spaces $\boldsymbol{\mathcal{V}}_h$.

$$\begin{cases} \text{Find } \boldsymbol{w}_e \in \boldsymbol{\mathcal{V}}_h \text{ such as} & & & \\ \partial_t(\boldsymbol{w}_e, \boldsymbol{w}_e^\star) + a(\boldsymbol{w}_e, \boldsymbol{w}_e^\star) & = & l(\boldsymbol{w}_e^\star), & \forall \boldsymbol{w}_e^\star \in \boldsymbol{\mathcal{V}}_h \subset L^2(\Omega), \\ \boldsymbol{w}_e(\boldsymbol{x}, 0) & = & \boldsymbol{w}_e^0(\boldsymbol{x}), & \forall \boldsymbol{x} \in \Omega, \\ \boldsymbol{w}_e(\boldsymbol{x}, t) & = & \boldsymbol{g}_e(\boldsymbol{x}), & \forall \boldsymbol{x} \in \Gamma, \end{cases} \tag{3.7}$$

This system is discrete in space but continuous in time and can be written in the matrix form

$$\underline{\boldsymbol{M}}\partial_t \boldsymbol{W} + \sum_p \sum_q \underline{\boldsymbol{K}}^{p,q} \boldsymbol{W} = \boldsymbol{F}, \tag{3.8}$$

where $\boldsymbol{W}$ it the vector of unknowns on the nodes of the domain, $\underline{\boldsymbol{M}}$ is the mass matrix, $\boldsymbol{F}$ the vector containing the source terms and $\underline{\boldsymbol{K}}$ represents the matrices associated to the differential terms. The details for the assembly of these matrices will be described later in the chapter.

The time discretization for this kind of model problems is generally based on a finite differences approximation in the interval $[0, T_f]$ with a time-step Δt

$$\underline{\boldsymbol{M}} \frac{\boldsymbol{W}^{n+1} - \boldsymbol{W}^n}{\Delta t} + \underline{\boldsymbol{K}}(\theta \boldsymbol{W}^{n+1} + (1-\theta)\boldsymbol{W}^n) = \theta \boldsymbol{F}^{n+1} + (1-\theta)\boldsymbol{F}^n, \tag{3.9}$$

with $\theta \in [0, 1]$ the so called method parameter: $\theta = 0$ gives the forward Euler scheme, $\theta = 1$ the backward Euler scheme and $\theta = 1/2$ the Crank-Nicholson scheme, which is 2nd-order, differently from the Euler schemes that are 1st-order.

One good advantage of the finite elements method is that the integrals of the weak formulation can be split into separated contributions from each element because the basis functions are nonzero only on the elements bordering the node where the unknown is evaluated giving rise to sparse matrices. This is not true however when a spectral decomposition is applied.

3.1.2 The need of stabilization

The FEM was first developed to deal with deformation problems in solid mechanics. The development of the stabilized methods began later when the finite elements have started to be used outside the solid mechanics domain, as for instance, fluid mechanics. In fact, deformation problems are usually simpler to be treated, since they generally lead to symmetrical and coercive operators. In fluid mechanics, however, specially when dealing with advection dominated fluxes, this technique needs to be improved. To overcome this difficulty, the solution consists in adding to the discrete variational formulation an extra term that will ensure the numerical stability while keeping the consistency of the method. This kind of methods were first introduced in the of the $70s$ to deal with the advection-diffusion equations [1, 2].

The stabilized finite element methods can be divided into two categories: Petrov-Galerkin methods and Multi-scale methods which include the Variational Multi-scale method (VMS) [70] but also the projection method [71, 72], the algebraic subgrid scale methods (ASGS) [70, 73] among others.

To illustrate that, let us consider a simple example of the onset of the numerical instability by using the 1D convection-diffusion equation without source term, i.e.,

$$-u\frac{d\phi}{dx} + k\frac{d^2\phi}{dx^2} = 0. \tag{3.10}$$

This equation will be discretized on the domain shown on Figure (3.1b) with the following Dirichlet boundary conditions

$$\phi = 0 \text{ at } x = 0, \tag{3.11}$$

$$\phi = \overline{\phi} \text{ at } x = 2l \tag{3.12}$$

The analytic solution of Equation (3.10) is

$$\phi = Ae^{\frac{u}{k}x} + B, \tag{3.13}$$

where the constant A and B come from the boundary conditions.

A numerical solution is attempted with the mesh shown in Figure (3.1a). As expected the Galerkin finite element formulation gives the same system of equations as a central finite differences scheme

$$-u\frac{\phi_3 - \phi_1}{2l} + k\frac{\phi_3 - 2\phi_2 + \phi_1}{l^2} = 0, \tag{3.14}$$

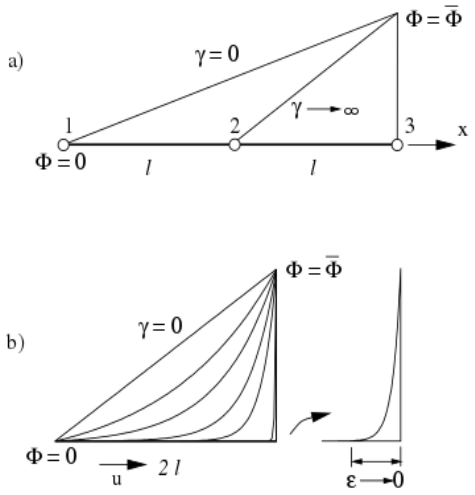

FIGURE 3.1: Simple $1D$ convection-diffusion example: a)two element discretization and b)analytic solution

into which the boundary conditions $\phi_1 = 0$ and $\phi_3 = \overline{\phi}$ are replaced, leading to

$$\phi_2 = \frac{1}{2}(1-\gamma)\overline{\phi}, \tag{3.15}$$

where $\gamma = \frac{ul}{2k}$ is the so called element Péclet number.

A careful look at Equation (3.15) shows that for $\gamma = 0$, the pure diffusive case, the solution $\phi_2 = \frac{\overline{\phi}}{2}$ coincides with the exact liner distribution shown in Figure (3.1b). Nevertheless, it is clear, as well, that ϕ_2 becomes negative for $\gamma > 1$ leading to non-physical results because $\phi_2 \geq 0 \ \ \forall u, k$ as it can be seen from the exact analytic solution.

It is clear from this test that the standard numerical schemes fail for high values of the Péclet number. This is due to the fact of them being central fluxes approximation, which are known to be numerically unstable. In fact, the solution will improve if mesh refinement is performed as a small value of the element length will also reduce the cell Péclet number. This leads however to prohibitive small element sizes for large values of the velocity.

This was a simple problem that can be generalized when dealing with FEM because the way in which the discretization is performed will always lead to a central flux approximated system. Therefore, the lack of a strategy to stabilize these models will lead to non physical results. This is the reason why finite elements methods, in general, are followed by a stabilization scheme. Here, we developed the Variational Multi-scale stabilization shown in the next section.

3.2 VMS-Stabilization and numerical strategy for MHD models

As said before, the VMS method is a procedure that seeks to rectify the fact that Galerkin method in not a robust approach when dealing with multi-scale phenomena. The idea behind the VMS method is not complex: sum decomposition of the solution into coarse (resolved) $\overline{\boldsymbol{w}}$ and fine (subgrid) $\boldsymbol{w}'$ scales are considered $\boldsymbol{w} = \overline{\boldsymbol{w}} + \boldsymbol{w}'$ where $\overline{\boldsymbol{w}}$ is solved numerically. Then, an attempt is made to eliminate analytically $\boldsymbol{w}'$ from the resolved problem. The fine scales are driven by the residual of the coarse scales and for this reason a residual-based weak form of the system of equations is written.

To develop the stabilization strategy, we consider here the ideal MHD system written on the conservative form (2.102) because this is the system essentially driving the full MHD model. The main difference being the Ohm's law considered and the transport terms that are not present on the Ideal model. It is useful here ot reformulate this system in a quasi linear form such as

$$\partial_t \boldsymbol{w} + \underline{\boldsymbol{L}}(\boldsymbol{w}, \boldsymbol{\partial})\boldsymbol{w} = 0, \tag{3.16}$$

This is the general system that will be solved and for that, a stabilization strategy will be developed.

3.2.1 Residual-Based Weak form

The system (2.102) can be reformulated if we define a residual $\boldsymbol{R}(\boldsymbol{w})$ function, where

$$\boldsymbol{R}(\boldsymbol{w}) := \partial_t \boldsymbol{w} + \underline{\boldsymbol{L}}(\boldsymbol{w}, \boldsymbol{\partial})\boldsymbol{w}, \tag{3.17}$$

and thus $\boldsymbol{R}(\boldsymbol{w}) = 0$. Therefore, the weak formulation for a space domain $\Omega_{x,h}$ can be written as

$$\int_{\Omega_{x,h}} \boldsymbol{R}(\boldsymbol{w}) \cdot \boldsymbol{w}^\star = 0, \quad \forall \boldsymbol{w}^\star \in \boldsymbol{\mathcal{W}}_h(\Omega_{x,h}). \tag{3.18}$$

The construction of the finite element space $\boldsymbol{\mathcal{W}}_h$ will be treated later. This simple formulation (3.18) is not satisfactory in the tokamak plasmas context for at least to reasons. First, the MHD system is subjected to a divergence free constraint on the magnetic field and this is not included on the previous formulation. The second reason is that the plasma flows in this case are convection dominated and as the formulation (3.18) in general is not upwinded, it will develop spurious waves. The solution for the first point was discussed in (2.1.5) and the solution for the second is the use of the VMS stabilization strategy.

3.2.2 Evaluation of the fine scales

For the MHD system shown in (2.102) the main operator to be stabilized is $\underline{\boldsymbol{L}}(\boldsymbol{w}, \boldsymbol{\partial})$. For that, let us follow the procedure described at the beginning of this section to find an expression for the effects of the fine scales over the coarse ones. Let's consider a decomposition of $\boldsymbol{w}$ as

$$\boldsymbol{w} = \overline{\boldsymbol{w}} + \boldsymbol{w}', \tag{3.19}$$

where $\overline{\boldsymbol{w}}$ represents de coarse scales and $\boldsymbol{w}'$ represent the fine scales. In the same way, let

$$\boldsymbol{w}^\star = \overline{\boldsymbol{w}}^\star + \boldsymbol{w}^{\star\prime}. \tag{3.20}$$

Let $\boldsymbol{\mathcal{S}} = \overline{\boldsymbol{\mathcal{S}}} \oplus \boldsymbol{\mathcal{S}}'$ and $\boldsymbol{\mathcal{V}} = \overline{\boldsymbol{\mathcal{V}}} \oplus \boldsymbol{\mathcal{V}}'$ where $\overline{\boldsymbol{\mathcal{S}}}$ and $\overline{\boldsymbol{\mathcal{V}}}$ are the trial solution and the weighting function spaces, respectively, for coarse scales while $\boldsymbol{\mathcal{S}}'$ and $\boldsymbol{\mathcal{V}}'$ are the ones for the fine scales. We assume $\boldsymbol{\mathcal{S}}' = \boldsymbol{\mathcal{V}}'$. The objective is to derive an equation governing $\overline{\boldsymbol{w}}$ and for that a expression for $\boldsymbol{w}'$ must be found.

The residual and the test function can then be rewritten as $\boldsymbol{R}(\overline{\boldsymbol{w}} + \boldsymbol{w}')$ and $\overline{\boldsymbol{w}}^\star + \boldsymbol{w}^{\star\prime}$, respectively, yielding the following weak formulation

$$\int_{\Omega_{x,h}} \boldsymbol{R}(\overline{\boldsymbol{w}} + \boldsymbol{w}') \cdot (\overline{\boldsymbol{w}}^\star + \boldsymbol{w}^{\star\prime}) = 0, \quad \forall \overline{\boldsymbol{w}} \in \overline{\boldsymbol{\mathcal{S}}}, \boldsymbol{w}' \in \boldsymbol{\mathcal{S}}', \overline{\boldsymbol{w}}^\star \in \overline{\boldsymbol{\mathcal{V}}}, \boldsymbol{w}^{\star\prime} \in \boldsymbol{\mathcal{V}}'. \tag{3.21}$$

The assumption made before concerning the orthogonality of the spaces $\overline{\boldsymbol{\mathcal{S}}}$ and $\boldsymbol{\mathcal{S}}'$; and $\overline{\boldsymbol{\mathcal{V}}}$ and $\boldsymbol{\mathcal{V}}'$, allows the separation of this weak form into two different problems

$$\left\{ \begin{array}{rcl} \displaystyle\int_{\Omega_{x,h}} \boldsymbol{R}(\overline{\boldsymbol{w}} + \boldsymbol{w}') \cdot \overline{\boldsymbol{w}}^\star & = & 0 \quad \forall \overline{\boldsymbol{w}} \in \overline{\boldsymbol{\mathcal{S}}}, \boldsymbol{w}' \in \boldsymbol{\mathcal{S}}', \overline{\boldsymbol{w}}^\star \in \overline{\boldsymbol{\mathcal{V}}} \\ \displaystyle\int_{\Omega_{x,h}} \boldsymbol{R}(\overline{\boldsymbol{w}} + \boldsymbol{w}') \cdot \boldsymbol{w}^{\star\prime} & = & 0 \quad \forall \overline{\boldsymbol{w}} \in \overline{\boldsymbol{\mathcal{S}}}, \boldsymbol{w}' \in \boldsymbol{\mathcal{S}}', \boldsymbol{w}^{\star\prime} \in \boldsymbol{\mathcal{V}}' \end{array} \right. . \tag{3.22}$$

Performing a Taylor expansion on the residual yields

$$\boldsymbol{R}(\overline{\boldsymbol{w}} + \boldsymbol{w}') \approx \boldsymbol{R}(\overline{\boldsymbol{w}}) + \underline{\boldsymbol{L}}(\overline{\boldsymbol{w}}, \boldsymbol{\partial})\boldsymbol{w}', \tag{3.23}$$

which can be replaced in the first weak form shown in (3.22) leading to

$$\begin{aligned} \int_{\Omega_{x,h}} \boldsymbol{R}(\overline{\boldsymbol{w}} + \boldsymbol{w}') \cdot \overline{\boldsymbol{w}}^\star &= \int_{\Omega_{x,h}} \boldsymbol{R}(\overline{\boldsymbol{w}}) \cdot \overline{\boldsymbol{w}}^\star + \int_{\Omega_{x,h}} (\underline{\boldsymbol{L}}(\overline{\boldsymbol{w}}, \boldsymbol{\partial})\boldsymbol{w}') \cdot \overline{\boldsymbol{w}}^\star \\ &= \int_{\Omega_{x,h}} \boldsymbol{R}(\overline{\boldsymbol{w}}) \cdot \overline{\boldsymbol{w}}^\star - \int_{\Omega_{x,h}} \boldsymbol{w}' \cdot (\underline{\boldsymbol{L}}^T(\overline{\boldsymbol{w}}, \boldsymbol{\partial})\overline{\boldsymbol{w}}^\star). \end{aligned} \tag{3.24}$$

To obtain Equation (3.24) an integration by parts has been done. Therefore, the most general weak formulation related to the coarse, i.e, resolved scales is

$$\int_{\Omega_{x,h}} \boldsymbol{R}(\overline{\boldsymbol{w}}) \cdot \overline{\boldsymbol{w}}^{\star} - \int_{\Omega_{x,h}} \boldsymbol{w}' \cdot (\underline{\boldsymbol{L}}^{T}(\overline{\boldsymbol{w}}, \boldsymbol{\partial})\overline{\boldsymbol{w}}^{\star}) = 0. \tag{3.25}$$

Now, an evaluation of the fine scale $\boldsymbol{w}'$ must be done and for that let us consider the second equation in (3.22). Applying the same expansion of the residual in it leads to

$$\int_{\Omega_{x,h}} (\boldsymbol{R}(\overline{\boldsymbol{w}}) + \underline{\boldsymbol{L}}(\overline{\boldsymbol{w}}, \boldsymbol{\partial})\boldsymbol{w}') \cdot \boldsymbol{w}^{\star\prime} = 0, \tag{3.26}$$

which is an equation for solving the fine, i.e., unresolved scales. This equation is true for whichever $\boldsymbol{w}^{\star\prime}$ which allows us the consider the following equality

$$\boldsymbol{R}(\overline{\boldsymbol{w}}) + \underline{\boldsymbol{L}}(\overline{\boldsymbol{w}}, \boldsymbol{\partial})\boldsymbol{w}' = 0. \tag{3.27}$$

To solve this problem, projectors related to the coarse and fine spaces can be used leading to a dual problem that can be solved with the aid of Green's function [74] yielding

$$\boldsymbol{w}' = \underline{\boldsymbol{M}}'\boldsymbol{R}(\overline{\boldsymbol{w}}), \tag{3.28}$$

where $\boldsymbol{R}(\overline{\boldsymbol{w}})$ is the residual of the coarse scales and $\underline{\boldsymbol{M}}' = -(\underline{\boldsymbol{L}}(\overline{\boldsymbol{w}}, \boldsymbol{\partial}))^{-1}$. It is important to remark that this result is possible because of the assumption that the fine and coarse scales are linearly independent.

3.2.2.1 Stabilization matrix

As the description from now on concerns only the coarse scale system, the bar/prime notation is abandoned such that the writing of the equation is lighter. The result (3.28) obtained in the previous section concerning the fine scales is.

$$\boldsymbol{w}' = -(\underline{\boldsymbol{L}}(\boldsymbol{w}, \boldsymbol{\partial}))^{-1}\boldsymbol{R}(\boldsymbol{w}). \tag{3.29}$$

Although this is the formal definition of $\underline{\boldsymbol{M}}'$, the operator $\underline{\boldsymbol{L}}(\boldsymbol{w}, \boldsymbol{\partial})$ is not always simple to invert and algebraic formulations are often used via the introduction of the intrinsic time-scale stabilization matrix $\underline{\boldsymbol{\mathcal{T}}}$. The applications under concern are MHD instabilities, hence we propose to use a modified algebraic closure where the fine scales are related to the advection of time fluctuations of the state $\boldsymbol{w}$, i.e.

$$\boldsymbol{w}' \approx \underline{\boldsymbol{\mathcal{T}}}(\underline{\boldsymbol{L}}(\boldsymbol{w}, \boldsymbol{\partial})\delta\boldsymbol{w}). \tag{3.30}$$

A very simple analysis shows, for usual VMS approaches, that the matrix $\underline{\boldsymbol{\mathcal{T}}}$ satisfies the scaling estimation in matrix norm

$$||\underline{\boldsymbol{L}}(\boldsymbol{w},\boldsymbol{\partial})||_\infty||\underline{\boldsymbol{\mathcal{T}}}||_\infty \approx 1, \tag{3.31}$$

such that it is possible to set the stabilization matrix as $\underline{\boldsymbol{\mathcal{T}}} \approx (\underline{\boldsymbol{L}}(\boldsymbol{w},\boldsymbol{\partial}))^{-1}$. However this is only a formal definition that is very difficult to use in practice. This is why the derivation of the stabilization matrix has been a subject of extensive research over the last decades.

The weak formulation will the be written as

$$\int_{\Omega_{x,h}} \boldsymbol{R}(\boldsymbol{w})\cdot\boldsymbol{w}^\star - \int_{\Omega_{x,h}} (\underline{\boldsymbol{L}}(\boldsymbol{w},\boldsymbol{\partial})\delta\boldsymbol{w})\cdot\underline{\boldsymbol{\mathcal{T}}}(\underline{\boldsymbol{L}}^T(\boldsymbol{w},\boldsymbol{\partial})\boldsymbol{w}^\star) = 0, \quad \forall \boldsymbol{w}^\star, \in \boldsymbol{\mathcal{W}}_h(\Omega_{x,h}). \tag{3.32}$$

where $\underline{\boldsymbol{L}}^T(\boldsymbol{w},\boldsymbol{\partial})$ is the adjoint of $\underline{\boldsymbol{L}}(\boldsymbol{w},\boldsymbol{\partial})$. In fact, several classical stabilized methods are generalized Galerkin methods written almost as (3.32). The main difference is in the choice of the stabilization operator. For instance, the VMS approach uses the adjoint of the Jacobian while SUPG methods use $\underline{\boldsymbol{L}}$ itself.

Options for the stabilization matrix

Up to now, the definitions of $\underline{\boldsymbol{\mathcal{T}}}$ mostly rely on heuristic arguments. An optimal way to choose it is still an open question and problem dependent. For instance, when the $1D$ advection-diffusion steady case is considered, the following definition of $\underline{\boldsymbol{\mathcal{T}}}$ yields a nodally exact solution [75]

$$\underline{\boldsymbol{\mathcal{T}}} = \frac{h_e}{2||a||}\left(\coth(P_e) - \frac{1}{P_e}\right), \qquad P_e = \frac{||a||h_e}{2\kappa}, \tag{3.33}$$

where h_e is a measure of the local length scale, also know as element length, a is the flow velocity, κ the diffusivity and P_e the Péclet number. Different definitions of h_e can be used; in the literature, it is common to use the element length aligned with the flow velocity. By analogy with the definition (3.33), when dealing with convection dominated systems of equation and iso-parametric finite elements, the stabilization tensor is defined as

$$\underline{\boldsymbol{\mathcal{T}}} \equiv \underline{\boldsymbol{\mathcal{T}}}_{ad} = \frac{||\frac{\partial\boldsymbol{x}}{\partial\boldsymbol{\zeta}}||_2}{||\Lambda||_\infty}\mathbb{I}, \tag{3.34}$$

where Λ is the diagonal matrix of the system's eigenvalues and $\boldsymbol{\zeta}$ the local parameter coordinates that scale as unity, so that $||\frac{\partial\boldsymbol{x}}{\partial\boldsymbol{\zeta}}||_2$ is a local length. This derivation assumes the isotropy of wave propagation and does not take into account occasional anisotropies of the grid for large aspect ratios. This choice affects booth the smoothness of the results

in regions containing large variations of the solution and the conditioning of the discrete system. To overcome this limitation, a recovery technique is proposed in [76] and [77].

A different definition of $\underline{\boldsymbol{\mathcal{T}}}$ parameter has been proposed by Tezduyar and Senga in [78] to take into account occasional anisotropies related to the density gradient. In the MHD context, anisotropies are driven by the magnetic field, thus, sharing some similarities with the formulation in [78]. We propose, the following estimation of the stabilization parameter

$$\underline{\boldsymbol{\mathcal{T}}} \equiv \underline{\boldsymbol{\mathcal{T}}}_{tz} = \left(\sum_{i \in \vartheta(e)} c_f \left| \frac{\boldsymbol{B} \cdot \nabla \mathcal{N}_i}{||\boldsymbol{B}||} \right| + |\boldsymbol{v} \cdot \nabla \mathcal{N}_i| \right)^{-1} \mathbb{I}, \tag{3.35}$$

where $\vartheta(e)$ is the set containing of the elements, $\mathcal{N}_i$ is the discrete test function (Further details (3.2.4.4)) and c_f the fast accoustic speed.

More general strategies were proposed and used in the context of space-time GLS [79], SUPG formulations [80–83] and the residual distribution scheme [84]. These approaches use the fact that, for any nonzero vector $\boldsymbol{n}$, the matrix $\underline{\boldsymbol{L}}_\star(\boldsymbol{w}, \boldsymbol{n})$ is diagonalizable, i.e., $\underline{\boldsymbol{L}}_\star(\boldsymbol{w}, \boldsymbol{n}) \equiv \underline{\mathbb{P}\boldsymbol{\Lambda}\mathbb{P}}^{-1}$. Therefore, the stabilization matrix is estimated as

$$\underline{\boldsymbol{\mathcal{T}}} \equiv \underline{\boldsymbol{\mathcal{T}}}_{GLS} = \left(\sum_{i \in \vartheta(e)} \underline{\mathbb{P}}(\boldsymbol{w}, \nabla \mathcal{N}_i) |\underline{\boldsymbol{\Lambda}}(\boldsymbol{w}, \nabla \mathcal{N}_i)| \underline{\mathbb{P}}^{-1}(\boldsymbol{w}, \nabla \mathcal{N}_i) \right)^{-1}. \tag{3.36}$$

This option requires a set of matrix inversions at each time step. Unfortunately, the MHD system can produce a non-diagonizable matrix, so that this option is generally not retained.

A more interesting way to consider the magnetic field anisotropy is to use the following decomposition

$$\underline{\boldsymbol{L}}^T(\boldsymbol{w}, \boldsymbol{\partial}) = \underline{\boldsymbol{L}}_{\boldsymbol{B}}^T(\boldsymbol{w}, \boldsymbol{\partial}) + \underline{\boldsymbol{L}}_\star^T(\boldsymbol{w}, \boldsymbol{\partial}), \tag{3.37}$$

where

$$\underline{\boldsymbol{L}}_{\boldsymbol{B}}^T(\boldsymbol{w}, \boldsymbol{\partial}) = \underline{\boldsymbol{L}}^T \left(\boldsymbol{w}, \frac{\boldsymbol{B}\boldsymbol{B} \cdot \boldsymbol{\partial}}{\boldsymbol{B} \cdot \boldsymbol{B}} \right) \quad \text{and} \quad \underline{\boldsymbol{L}}_\star^T(\boldsymbol{w}, \boldsymbol{\partial}) = \underline{\boldsymbol{L}}^T \left(\boldsymbol{w}, \boldsymbol{\partial} - \frac{\boldsymbol{B}\boldsymbol{B} \cdot \boldsymbol{\partial}}{\boldsymbol{B} \cdot \boldsymbol{B}} \right). \tag{3.38}$$

A similar decomposition is used for $\underline{\boldsymbol{L}}(\boldsymbol{w}, \boldsymbol{\partial})$ and it is assumed that it is a decomposition in orthogonal spaces. Therefore, the stabilization is reformulated as

$$\begin{aligned} \int_{\Omega_{x,h}} \underline{\boldsymbol{\mathcal{T}}}\underline{\boldsymbol{L}}(\boldsymbol{w}, \boldsymbol{\partial}) \delta \boldsymbol{w} \cdot \underline{\boldsymbol{L}}^T(\boldsymbol{w}, \boldsymbol{\partial}) \boldsymbol{w}^\star \approx & \int_{\Omega_{x,h}} \underline{\boldsymbol{\mathcal{T}}}_{\boldsymbol{B}} \underline{\boldsymbol{L}}_{\boldsymbol{B}}(\boldsymbol{w}, \boldsymbol{\partial}) \delta \boldsymbol{w} \cdot \underline{\boldsymbol{L}}_{\boldsymbol{B}}^T(\boldsymbol{w}, \boldsymbol{\partial}) \boldsymbol{w}^\star \\ & + \int_{\Omega_{x,h}} \underline{\boldsymbol{\mathcal{T}}}_\star \underline{\boldsymbol{L}}_\star(\boldsymbol{w}, \boldsymbol{\partial}) \delta \boldsymbol{w} \cdot \underline{\boldsymbol{L}}_\star^T(\boldsymbol{w}, \boldsymbol{\partial}) \boldsymbol{w}^\star, \end{aligned}$$

having $\underline{\boldsymbol{\mathcal{T}}}_{\boldsymbol{B}}$ and $\underline{\boldsymbol{\mathcal{T}}}_{\star}$ constructed as usual, although different strategies could be used, taking into account the anisotropy of the magnetized plasmas.

3.2.3 MHD application

An application of the stabilization strategy to MHD models can now be discussed, since the basis of the strategy are settled. For that, we are going to consider the ideal MHD model shown in (2.102). It is important to remark, that the ideal MHD system, even if it is simplified is the system driving to full MHD model. It means that the translation from the ideal stabilized system to the full one is straightforward. The general weak formulation of the system is written as

$$\int_{\Omega_{x,h}} \boldsymbol{R}(\boldsymbol{w}) \cdot \boldsymbol{w}^{\star} - \int_{\Omega_{x,h}} (\underline{\boldsymbol{\mathcal{T}}}\underline{\boldsymbol{L}}(\boldsymbol{w}, \boldsymbol{\partial})\delta\boldsymbol{w}) \cdot (\underline{\boldsymbol{L}}^{T}(\boldsymbol{w}, \boldsymbol{\partial})\boldsymbol{w}^{\star}) = 0 \tag{3.39}$$

The Jacobian of (2.102) can be written as

$$\underline{\boldsymbol{L}}(\boldsymbol{w}, \boldsymbol{\partial}) = \left(\begin{array}{c|c|c|c} 0 & \boldsymbol{\partial}^T & 0 & \boldsymbol{0}^T \\ \hline -\frac{\boldsymbol{m}}{\rho^2}\boldsymbol{m}\cdot\boldsymbol{\partial} + \frac{\partial P}{\partial \rho}\boldsymbol{\partial} & \begin{array}{c}\frac{1}{\rho}\boldsymbol{m}\otimes\boldsymbol{\partial} + \frac{1}{\rho}\boldsymbol{m}\cdot\boldsymbol{\partial} \\ + \left(\frac{\partial P}{\partial \boldsymbol{m}}\otimes\boldsymbol{\partial}\right)^T\end{array} & \frac{\partial P}{\partial \mathcal{E}}\boldsymbol{\partial} & \begin{array}{c}\boldsymbol{B}\otimes\boldsymbol{\partial} - \boldsymbol{B}\cdot\boldsymbol{\partial} \\ + \left(\frac{\partial P}{\partial \boldsymbol{B}}\otimes\boldsymbol{\partial}\right)^T\end{array} \\ \hline \begin{array}{c}\frac{\partial \mathcal{H}}{\partial \rho}\boldsymbol{m}\cdot\boldsymbol{\partial} \\ + \frac{\boldsymbol{B}\cdot\boldsymbol{m}}{\rho^2}\boldsymbol{B}\cdot\boldsymbol{\partial}\end{array} & \begin{array}{c}\left(\frac{\partial \mathcal{H}}{\partial \boldsymbol{m}}\right)^T\boldsymbol{m}\cdot\boldsymbol{\partial} + \mathcal{H}\boldsymbol{\partial}^T \\ - \frac{\boldsymbol{B}^T}{\rho}\boldsymbol{B}\cdot\boldsymbol{\partial}\end{array} & \frac{\partial \mathcal{H}}{\partial \mathcal{E}}\boldsymbol{m}\cdot\boldsymbol{\partial} & \begin{array}{c}\left(\frac{\partial \mathcal{H}}{\partial \boldsymbol{B}}\right)^T\boldsymbol{m}\cdot\boldsymbol{\partial} \\ - \frac{\boldsymbol{B}\cdot\boldsymbol{m}}{\rho}\boldsymbol{\partial}^T - \frac{\boldsymbol{m}^T}{\rho}\boldsymbol{B}\cdot\boldsymbol{\partial}\end{array} \\ \hline -\frac{\boldsymbol{B}\boldsymbol{m}\cdot\boldsymbol{\partial} - \boldsymbol{m}\boldsymbol{B}\cdot\boldsymbol{\partial}}{\rho^2} & \frac{\boldsymbol{B}\otimes\boldsymbol{\partial} - \boldsymbol{B}\otimes\boldsymbol{\partial}}{\rho} & \boldsymbol{0} & \frac{\boldsymbol{m}\cdot\boldsymbol{\partial} - \boldsymbol{m}\otimes\boldsymbol{\partial}}{\rho} \end{array}\right). \tag{3.40}$$

Its spectral properties were shown in (2.2.2.2). Its adjoint is

$$\underline{\boldsymbol{L}}^{T}(\boldsymbol{w}, \boldsymbol{\partial}) = \left(\begin{array}{c|c|c|c} 0 & -\frac{\boldsymbol{m}^T}{\rho^2}\boldsymbol{m}\cdot\boldsymbol{\partial} + \frac{\partial P}{\partial \rho}\boldsymbol{\partial}^T & \frac{\partial \mathcal{H}}{\partial \rho}\boldsymbol{m}\cdot\boldsymbol{\partial} + \frac{\boldsymbol{B}\cdot\boldsymbol{m}}{\rho^2}\boldsymbol{B}\cdot\boldsymbol{\partial} & -\frac{\boldsymbol{B}^T\boldsymbol{m}\cdot\boldsymbol{\partial} - \boldsymbol{m}^T\boldsymbol{B}\cdot\boldsymbol{\partial}}{\rho^2} \\ \hline \boldsymbol{\partial} & \begin{array}{c}\frac{1}{\rho}(\boldsymbol{m}\otimes\boldsymbol{\partial})^T + \frac{1}{\rho}\boldsymbol{m}\cdot\boldsymbol{\partial} \\ + \frac{\partial P}{\partial \boldsymbol{m}}\otimes\boldsymbol{\partial}\end{array} & \left(\frac{\partial \mathcal{H}}{\partial \boldsymbol{m}}\right)\boldsymbol{m}\cdot\boldsymbol{\partial} + \mathcal{H}\boldsymbol{\partial} - \frac{\boldsymbol{B}}{\rho}\boldsymbol{B}\cdot\boldsymbol{\partial} & \frac{(\boldsymbol{B}\otimes\boldsymbol{\partial})^T - \boldsymbol{B}\otimes\boldsymbol{\partial}}{\rho} \\ \hline 0 & \frac{\partial P}{\partial \mathcal{E}}\boldsymbol{\partial}^T & \frac{\partial \mathcal{H}}{\partial \mathcal{E}}\boldsymbol{m}\cdot\boldsymbol{\partial} & \boldsymbol{0}^T \\ \hline \boldsymbol{0} & \begin{array}{c}(\boldsymbol{B}\otimes\boldsymbol{\partial}) - \boldsymbol{B}\cdot\boldsymbol{\partial} \\ + \left(\frac{\partial P}{\partial \boldsymbol{B}}\otimes\boldsymbol{\partial}\right)\end{array} & \left(\frac{\partial \mathcal{H}}{\partial \boldsymbol{B}}\right)\boldsymbol{m}\cdot\boldsymbol{\partial} - \frac{\boldsymbol{B}\cdot\boldsymbol{m}}{\rho}\boldsymbol{\partial} - \frac{\boldsymbol{m}}{\rho}\boldsymbol{B}\cdot\boldsymbol{\partial} & \frac{\boldsymbol{m}\cdot\boldsymbol{\partial} - (\boldsymbol{m}\otimes\boldsymbol{\partial})^T}{\rho} \end{array}\right). \tag{3.41}$$

Both operators are going to be used in order to develop the numerical strategy to solve the full MHD system.

3.2.4 Numerical strategy

Before discussing all the details of the discretization of this system, it is important to describe briefly how the possible solution for the divergence free constraint is implemented. After that, the numerical method with the stabilization already taken into account is discussed in details.

3.2.4.1 Vector potential formulation

As discussed in Section (2.1.5) there are different ways of solving the problem related to the divergence free constraint. The option retained here however is the vector potential formulation, specially because simulations of MHD instabilities inside tokamaks generally start from the Grad-Shafranov equilibrium (Section (2.2.4.1)) which is an equation for the magnetic flux ψ. This variable is the toroidal component of the vector potential. Hence, it is natural to introduce a vector potential $\boldsymbol{A}$ and redefine de magnetic field as $\boldsymbol{B} = \nabla \times \boldsymbol{A}$, so that $\nabla \cdot \boldsymbol{B} = 0$. This vector potential is not uniquely defined, however, and this is a tricky situation in computations subjected to numerical overflow. To define it uniquely, a Gauge must be chosen and the one chosen here is the Coulomb gauge which simply sets $\nabla \cdot \boldsymbol{A} = 0$ (Section (2.1.5.1)). This condition is applied here under a penalized weak form defined with $(\nabla \cdot \boldsymbol{A}) \cdot (\nabla \cdot \boldsymbol{A}^\star)$. This penalty is activated whe the approximated space for $\boldsymbol{A}$ is not divergence free. This approximation space is spanned by the test functions $\boldsymbol{A}^\star$.

3.2.4.2 Set of interpolated variables

So far, we have been dealing with the MHD by means of the conservative variables $\rho, \boldsymbol{m}, \mathcal{E}$ and the potential vector $\boldsymbol{A}$ has been introduced to deal with the solenoid condition coming from Maxwell's equation $\nabla \cdot \boldsymbol{B} = 0$. This works well for general plasmas but can be problematic when dealing with tokamaks. As described in Chapter 1, the plasma inside a tokamak is divided into two regions by the separatrix: the core region where most of the plasma is located and the Scrap-off layer (SOL) which has very low density and pressure. Hence, extract information related to the temperature, which is a physical quantity that is actually measured in experimental tokamaks, can be quite delicate. In order to avoid critical issues during the inversion of the equation of state, interpolations are often applied to the following physical variables $\boldsymbol{Y}$

$$\boldsymbol{Y} = \begin{pmatrix} \rho \\ \boldsymbol{v} \\ T \\ \boldsymbol{A} \end{pmatrix} \quad \text{so that} \quad \boldsymbol{w} = \begin{pmatrix} \rho \\ \boldsymbol{m} = \rho \boldsymbol{v} \\ \mathcal{E} = \frac{\rho T}{\gamma - 1} + \frac{1}{2}\boldsymbol{v} \cdot \boldsymbol{v} + \frac{1}{2}\boldsymbol{B} \cdot \boldsymbol{B} \\ \boldsymbol{B} = \nabla \times \boldsymbol{A} \end{pmatrix}. \tag{3.42}$$

Therefore, the derivatives of $\boldsymbol{w}$ must be reformulated in terms of the derivatives of $\boldsymbol{Y}$, as

$$\begin{aligned}
\boldsymbol{\partial}\rho &\rightarrow \boldsymbol{\partial}\rho, && (3.43)\\
\boldsymbol{\partial}\boldsymbol{m} &\rightarrow \boldsymbol{v}(\boldsymbol{\partial}\rho) + \rho(\boldsymbol{\partial}\boldsymbol{v}), && (3.44)\\
\boldsymbol{\partial}\mathcal{E} &\rightarrow \frac{T}{\gamma-1}\left(\boldsymbol{\partial}\rho + \frac{\boldsymbol{v}\cdot\boldsymbol{v}}{2}\right) + \rho\boldsymbol{v}\cdot(\boldsymbol{\partial}\boldsymbol{v}) + \frac{\rho}{\gamma-1}(\boldsymbol{\partial}T) + \boldsymbol{B}\cdot(\nabla\times\boldsymbol{A}), && (3.45)\\
\boldsymbol{\partial}\boldsymbol{B} &\rightarrow \nabla\times\boldsymbol{A}, && (3.46)
\end{aligned}$$

which can be written in a more compact way as

$$\boldsymbol{\partial}\boldsymbol{w} = \underline{\boldsymbol{M}}(\boldsymbol{Y})\underline{\boldsymbol{Rot}}(\boldsymbol{\partial}\boldsymbol{Y}), \tag{3.47}$$

where

$$\underline{\boldsymbol{M}}(\boldsymbol{Y}) = \begin{pmatrix} 1 & 0 & 0 & 0 \\ \boldsymbol{v} & \rho\mathbb{I} & 0 & 0 \\ \frac{T}{\gamma-1} + \frac{\boldsymbol{v}\cdot\boldsymbol{v}}{2} & \rho\boldsymbol{v}^T & \frac{\rho}{\gamma-1} & \boldsymbol{B}^T \\ 0 & 0 & 0 & \mathbb{I} \end{pmatrix} \quad \text{and} \quad \underline{\boldsymbol{Rot}}(\boldsymbol{\partial}\boldsymbol{Y}) = \begin{pmatrix} \boldsymbol{\partial}\rho \\ \boldsymbol{\partial}\boldsymbol{v} \\ \boldsymbol{\partial}T \\ \nabla\times\boldsymbol{A} \end{pmatrix}. \tag{3.48}$$

The interpolation implies that every numerical approximation using the physical variables must have its integrals reformulated accordingly to the change of variables because the whole formulation up this point has been derived from the conservative equations. For instance, the time derivative becomes

$$\begin{aligned}
\int_{\Omega_{x,h}} \partial_t\boldsymbol{w}\cdot\boldsymbol{w}^\star &= \int_{\Omega_{x,h}} (\underline{\boldsymbol{M}}(\boldsymbol{Y})\underline{\boldsymbol{Rot}}(\partial_t\boldsymbol{Y}))\cdot\boldsymbol{w}^\star = \int_{\Omega_{x,h}} \underline{\boldsymbol{Rot}}\,(\underline{\boldsymbol{M}}(\boldsymbol{Y})\partial_t\boldsymbol{Y})\cdot\boldsymbol{w}^\star \\
&= \int_{\Omega_{x,h}} (\underline{\boldsymbol{M}}(\boldsymbol{Y})\partial_t\boldsymbol{Y})\cdot\underline{\boldsymbol{Rot}}(\boldsymbol{w}^\star) + \int_{\partial\Omega_{x,h}} \underline{\boldsymbol{G}}(\boldsymbol{n}\cdot\boldsymbol{w}^\star) \\
&= \int_{\Omega_{x,h}} (\underline{\boldsymbol{M}}(\boldsymbol{Y})\partial_t\boldsymbol{Y})\cdot\tilde{\boldsymbol{w}}^\star + \int_{\partial\Omega_{x,h}} (\boldsymbol{n}\times\partial_t\boldsymbol{A})\cdot\boldsymbol{B}^\star,
\end{aligned}$$

where the test vector functions are defined as

$$\boldsymbol{w}^\star = \begin{pmatrix} \rho^\star \\ \boldsymbol{m}^\star \\ \mathcal{E}^\star \\ \boldsymbol{B}^\star \end{pmatrix} \quad \text{and} \quad \tilde{\boldsymbol{w}}^\star = \begin{pmatrix} \rho^\star \\ \boldsymbol{m}^\star \\ \mathcal{E}^\star \\ \boldsymbol{J}^\star \end{pmatrix} \quad \text{with} \quad \boldsymbol{J}^\star = \nabla\times\boldsymbol{B}^\star.$$

3.2.4.3 Stabilized weak formulation

To obtain the final numerical stabilized formulation for the MHD system, the interpolation developed before is applied to the residual weak form (3.32) and additional contributions are added to take into account the boundary conditions as penalty integrals. Thus, the VMS-stabilized finite element takes the following compact form

$$\begin{aligned}\int_{\Omega_{x,h}}(\underline{\boldsymbol{M}}(\boldsymbol{Y})\partial_t\boldsymbol{Y})\cdot\tilde{\boldsymbol{w}}^\star - \int_{\Omega_{x,h}}\underline{\boldsymbol{F}}:(\boldsymbol{\partial}\odot\boldsymbol{w}^\star) + \int_{\Omega_{x,h}}\underline{\boldsymbol{G}}:(\boldsymbol{\partial}\odot\boldsymbol{w}^\star) - \frac{1}{\epsilon}\int_{\partial\Omega_{x,h}}(\nabla\cdot\boldsymbol{A})\cdot(\nabla\cdot\boldsymbol{A}^\star)\\ + \int_{\partial\Omega_{x,h}}\underline{\boldsymbol{F}}:(\boldsymbol{n}\odot\boldsymbol{w}^\star) - \int_{\partial\Omega_{x,h}}\underline{\boldsymbol{G}}:(\boldsymbol{n}\odot\boldsymbol{w}^\star) + \frac{1}{\epsilon}\int_{\partial\Omega_{x,h}}(\boldsymbol{n}\times\partial_t\boldsymbol{A})\cdot\boldsymbol{B}^\star\\ + \frac{1}{\epsilon}\int_{\partial\Omega_{x,h}}\boldsymbol{S}(\boldsymbol{w},\boldsymbol{w}_b,\boldsymbol{w}^\star) = \int_{\Omega_{x,h}}(\underline{\boldsymbol{L}}(\boldsymbol{w},\boldsymbol{\partial})\delta\boldsymbol{w})\cdot\underline{\boldsymbol{\mathcal{T}}}(\underline{\boldsymbol{L}}^T(\boldsymbol{w},\boldsymbol{\partial})\boldsymbol{w}^\star).\end{aligned} \tag{3.49}$$

We have defined a new operator $\odot$ in order to write it in the most compact form. It acts between a vector having size d, which is the space dimension (also the dimensions of the vector quantities $\boldsymbol{v}$ and $\boldsymbol{B}$), and a state vector of size N_v, where N_v is the total number of scalar variables (size of $\boldsymbol{w}$), resulting in a $N_v \times d$ tensor. The resulting tensors are defined as follow

$$(\boldsymbol{\partial}\odot\boldsymbol{w}^\star) = \begin{pmatrix}\boldsymbol{\partial}\rho^\star\\ \boldsymbol{\partial}\otimes\boldsymbol{m}^\star\\ \boldsymbol{\partial}\mathcal{E}^\star\\ \boldsymbol{\partial}\times\boldsymbol{B}^\star\end{pmatrix}, \quad \text{and} \quad (\boldsymbol{n}\odot\boldsymbol{w}^\star) = \begin{pmatrix}\boldsymbol{n}\rho^\star\\ \boldsymbol{n}\otimes\boldsymbol{m}^\star\\ \boldsymbol{n}\mathcal{E}^\star\\ \boldsymbol{n}\times\boldsymbol{B}^\star\end{pmatrix},$$

with

$$(\boldsymbol{\partial}\otimes\boldsymbol{m}) = \begin{pmatrix}\partial_1 m_1 & \partial_1 m_2 & \partial_1 m_3\\ \partial_2 m_1 & \partial_2 m_2 & \partial_2 m_3\\ \partial_3 m_1 & \partial_3 m_2 & \partial_3 m_3\end{pmatrix}. \tag{3.50}$$

Also,

$$(\boldsymbol{m}\otimes\boldsymbol{\partial})^T = \begin{pmatrix}m_1\partial_1 & m_2\partial_1 & m_3\partial_1\\ m_1\partial_2 & m_2\partial_2 & m_3\partial_2\\ m_1\partial_3 & m_2\partial_3 & m_3\partial_3\end{pmatrix}, \tag{3.51}$$

which implies

$$(\boldsymbol{m}\otimes\boldsymbol{\partial})^T\boldsymbol{m}^\star = \begin{pmatrix}m_1\partial_1 m_1^\star & m_2\partial_1 m_2^\star & m_3\partial_1 m_3^\star\\ m_1\partial_2 m_1^\star & m_2\partial_2 m_2^\star & m_3\partial_2 m_3^\star\\ m_1\partial_3 m_1^\star & m_2\partial_3 m_2^\star & m_3\partial_3 m_3^\star\end{pmatrix} = (\boldsymbol{\partial}\boldsymbol{m}^\star)\boldsymbol{m}. \tag{3.52}$$

The hyperbolic flux tensor $\underline{\boldsymbol{F}}$ related to convection and the elliptic flux tensor $\underline{\boldsymbol{G}}$ related ot diffusion have the size $N_v \times d$. They are written as

$$\underline{\boldsymbol{F}} = \begin{pmatrix} \rho \boldsymbol{v} \\ \rho \boldsymbol{v} \otimes \boldsymbol{v} + P\mathbb{I} - \boldsymbol{B} \otimes \boldsymbol{B} \\ \rho \mathcal{H} \boldsymbol{v} - \boldsymbol{B} \cdot \boldsymbol{v} \boldsymbol{B} \\ -\boldsymbol{v} \times \boldsymbol{B} \end{pmatrix}, \quad \underline{\boldsymbol{G}} = \begin{pmatrix} g_\rho \\ g_{\boldsymbol{m}} \\ g_{\mathcal{E}} \\ g_{\boldsymbol{B}} \end{pmatrix}.$$

So far, the boundary conditions have not been discussed. However, they are fundamental to define the true nature of the system we want to solve. Depending on the boundary conditions chosen one can switch from one problem to another. For the case in question, the boundary conditions are of Dirichlet type, which means that for each state of $\boldsymbol{w}$, a value is enforced on the boundary of the domain, noted $\boldsymbol{w}_b$. These conditions are then applied in the form of penalty integrals following the boundary. The vector $\boldsymbol{S}$ containing the condition is

$$\boldsymbol{S}(\boldsymbol{w}, \boldsymbol{w}_b, \boldsymbol{w}^\star) = \begin{pmatrix} (\rho - \rho_b)\rho^\star \boldsymbol{\mathcal{X}}(\partial\Omega^\rho_{x,h}) \\ \rho(\boldsymbol{v} - \boldsymbol{v}_b) \cdot \boldsymbol{m}^\star \boldsymbol{\mathcal{X}}(\partial\Omega^{\boldsymbol{v}}_{x,h}) + (\rho \boldsymbol{v} - \boldsymbol{m}_b) \cdot \boldsymbol{m}^\star \boldsymbol{\mathcal{X}}(\partial\Omega^{\boldsymbol{m}}_{x,h}) \\ \rho(T - T_b)\mathcal{E}^\star \boldsymbol{\mathcal{X}}(\partial\Omega^T_{x,h}) + (p - p_b)\mathcal{E}^\star \boldsymbol{\mathcal{X}}(\partial\Omega^p_{x,h}) \\ (\boldsymbol{A} - \boldsymbol{A}_b) \cdot \boldsymbol{J}^\star \boldsymbol{\mathcal{X}}(\partial\Omega^{\boldsymbol{A}}_{x,h}) + (\boldsymbol{B} - \boldsymbol{B}_p) \cdot \boldsymbol{B}^\star \boldsymbol{\mathcal{X}}(\partial\Omega^{\boldsymbol{B}}_{x,h}) \end{pmatrix}, \tag{3.53}$$

where, for any subset $\boldsymbol{\mathcal{Y}}$ of the boundary $\partial\Omega_{x,h}$, $\boldsymbol{\mathcal{X}}(\boldsymbol{\mathcal{Y}})$ is the characteristic function of $\boldsymbol{\mathcal{Y}}$. It is also assumed that the boundaries do not overlap so that, for example, the pressure and the temperature are always penalized over different subsets.

3.2.4.4 Finite element approximated space

It is important to remark that, even though the tokamak is a 3D device, its geometry has symmetrical properties that can be exploited when working with finite elements. Hence, we start by making a cut of the torus in a way that 2D elements can be used in each poloidal plane and a spectral Fourier representation can be used in the toroidal direction. The transformation used is:

$$\boldsymbol{x} \equiv \boldsymbol{x}(R, \phi, Z) \rightarrow \boldsymbol{x} \equiv \boldsymbol{x}(\boldsymbol{\xi}, \phi) \quad \text{with} \quad \boldsymbol{\xi} \in \Omega_{2D} \quad \text{and} \quad \phi \in [0, 2\pi[. \tag{3.54}$$

Having this in mind, an approximated space for the test functions in (3.2.4.3) must be derived. Let's consider a scalar function defined on the domain Ω_x which will be interpolated in an approximated finite element as described by the Galerkin method on (3.1.1). By taking into account the toroidal symmetry, the space $\boldsymbol{\mathcal{V}}_h$ can be decomposed

as

$$\boldsymbol{\mathcal{V}}_h(\Omega_{x,h}) \equiv \boldsymbol{\mathcal{V}}_h(\boldsymbol{\Omega}_{2D}) \times \boldsymbol{\mathcal{V}}_h([0, 2\pi[). \tag{3.55}$$

The space $\boldsymbol{\mathcal{V}}_h(\Omega_{x,h})$ is spanned by the test functions $\mathcal{N}_i$.

It is useful now to introduce the cylindrical coordinates (R, ϕ, Z) that contain the poloidal coordinates $\boldsymbol{\xi} = (R, Z)^T$ with $\boldsymbol{\xi} \in \Omega_{2D}$ and the toroidal coordinate $\phi \in [0, 2\pi[$. Therefore, the integrals that must be solved to obtain the matrix elements in the finite elements formulation become:

$$\int_{\boldsymbol{\Omega}_{3D}} (\cdots)\, d\boldsymbol{x} = \int_0^{2\pi} d\phi \int_{\boldsymbol{\Omega}_{2D}} (\cdots) R d\boldsymbol{\xi} \tag{3.56}$$

and

$$\int_{\partial\boldsymbol{\Omega}_{3D}} (\cdots)\, dS_x = \int_0^{2\pi} d\phi \int_{\partial\boldsymbol{\Omega}_{2D}} (\cdots) R dS_{\boldsymbol{\xi}}. \tag{3.57}$$

And this, because there is a non-singular mapping between the Cartesian coordinate $\boldsymbol{x}$ and the cylindrical coordinates. In the expression above R is the Jacobian of the transformation. It is important to remark that for tokamak applications the position $R = 0$ is almost always out of the domain is a way that there is no problem of singularity.

It is desirable then, to represent the functions according to cylindrical variables $(\boldsymbol{\xi}, \phi)$ since all the vector quantities, e.g. $(\boldsymbol{v}, \boldsymbol{m}, \boldsymbol{B}, \boldsymbol{A}, \boldsymbol{m}^\star, \boldsymbol{A}^\star, \boldsymbol{B}^\star, \cdots)$ are also related the the three unit orthogonal vectors $(\hat{\boldsymbol{R}}, \hat{\boldsymbol{\phi}}, \hat{\boldsymbol{Z}})$. For example

$$\boldsymbol{m}^\star(\boldsymbol{\xi}, \phi) := m_R^\star(\boldsymbol{\xi}, \phi)\hat{\boldsymbol{R}} + m_\phi^\star(\boldsymbol{\xi}, \phi)\hat{\boldsymbol{\phi}} + m_Z^\star(\boldsymbol{\xi}, \phi)\hat{\boldsymbol{Z}}. \tag{3.58}$$

The tricky point is that the vectors $\hat{\boldsymbol{R}}$ and $\hat{\boldsymbol{\phi}}$ are also functions of the coordinates ϕ. Formally, the space representing vectors can be described as

$$\vec{\boldsymbol{\mathcal{V}}}_h(\Omega_{x,h}) := \boldsymbol{\mathcal{V}}_h(\Omega_{x,h})\hat{\boldsymbol{R}}(\phi) \oplus \boldsymbol{\mathcal{V}}_h(\Omega_{x,h})\hat{\boldsymbol{\phi}}(\phi) \oplus \boldsymbol{\mathcal{V}}_h(\Omega_{x,h})\hat{\boldsymbol{Z}}. \tag{3.59}$$

This holds true for all vector quantities of the system, except for one: the vector potential. In the context of MHD instabilities, the initial condition is computed from the solution of the Grad Shafranov equilibrium described in (2.2.4.1) in which ψ is the toroidal component of the vector potential, associated to $\nabla\phi$ that is not unitary as $\nabla\phi = \frac{1}{R}\hat{\boldsymbol{\phi}}$. Hence, the vector variable $\boldsymbol{A}$ is represented in a slightly different space as to avoid numerical perturbations related to the projection onto a normalized basis. Therefore, the space for the vector potential is

$$\vec{\boldsymbol{\mathcal{V}}}_h(\Omega_{x,h}) := \boldsymbol{\mathcal{V}}_h(\Omega_{x,h})\hat{\boldsymbol{R}}(\phi) \oplus \boldsymbol{\mathcal{V}}_h(\Omega_{x,h})\frac{1}{R}\hat{\boldsymbol{\phi}}(\phi) \oplus \boldsymbol{\mathcal{V}}_h(\Omega_{x,h})\hat{\boldsymbol{Z}}, \tag{3.60}$$

which yields

$$\boldsymbol{A}(t,\boldsymbol{\xi},\phi) := A_R(t,\boldsymbol{\xi},\phi)\hat{\boldsymbol{R}} + \psi(t,\boldsymbol{\xi}\phi)\nabla\phi + A_Z(t,\boldsymbol{\xi},\phi)\hat{\boldsymbol{Z}}, \tag{3.61}$$

with $\psi(t,\boldsymbol{\xi},\phi) = RA_\phi(t,\boldsymbol{\xi},\phi)$.

Special attention must be paid to the gradients of vectors as $\boldsymbol{\partial m}^\star$, for example, due to the dependence on polar coordinates. The following explicit relations will be used for the gradients of $\hat{\boldsymbol{R}}$ and $\hat{\boldsymbol{\phi}}$

$$\boldsymbol{\partial}\hat{\boldsymbol{R}} = \frac{1}{R}\hat{\boldsymbol{\phi}}\otimes\hat{\boldsymbol{\phi}} \text{ and } \boldsymbol{\partial}\hat{\boldsymbol{\phi}} = \frac{1}{R}\hat{\boldsymbol{R}}\otimes\hat{\boldsymbol{\phi}}.$$

This yields for any vector $\boldsymbol{Y} = Y_R\hat{\boldsymbol{R}} + Y_\phi\hat{\boldsymbol{\phi}} + Y_Z\hat{\boldsymbol{Z}}$, the gradient

$$\boldsymbol{\partial Y} = \hat{\boldsymbol{R}}\otimes\boldsymbol{\partial}Y_R + \hat{\boldsymbol{\phi}}\otimes\boldsymbol{\partial}Y_\phi + \hat{\boldsymbol{Z}}\otimes\boldsymbol{\partial}Y_Z + \frac{Y_R}{R}\hat{\boldsymbol{\phi}}\otimes\hat{\boldsymbol{\phi}} - \frac{Y_\phi}{R}\hat{\boldsymbol{R}}\otimes\hat{\boldsymbol{\phi}}, \tag{3.62}$$

where each component $\boldsymbol{\partial}Y_m$ is defined, in cylindrical basis

$$\boldsymbol{\partial}Y_m = \hat{\boldsymbol{R}}\partial_R Y_m + \hat{\boldsymbol{\phi}}\frac{1}{R}\partial_\phi Y_m + \hat{\boldsymbol{Z}}\partial_Z Y_m. \tag{3.63}$$

As said before, the finite element space $\boldsymbol{\mathcal{V}}_h(\Omega_x,h)$ is constructed as a tensor product of poloidal ($2D$) and toroidal ($1D$) functions. The approximated poloidal space is spanned by functions $\psi_{i_{2D}}$ while the toroidal space is spanned by functions C_{i_ϕ} as

$$\boldsymbol{\mathcal{V}}_h(\Omega_{2D}) \equiv SPAN(\psi_{i_{2D}}(\boldsymbol{\xi})) \quad\text{and}\quad \boldsymbol{\mathcal{V}}_h([0,2\pi[) \equiv SPAN(C_{i_\phi}(\phi)),$$

where $i_{2D} = 1,\cdots,N_{i_{2D}}$ and $i_\phi = 1,\cdots,N_{i_\phi}$. $N_{i_{2D}}$ and N_{i_ϕ} are the dimensions of the poloidal and toroidal spaces.

The global approximation space is then defined as

$$\boldsymbol{\mathcal{V}}_h(\Omega_{x,h}) = SPAN(\mathcal{N}_i(\boldsymbol{\xi},\phi) = \psi_{i_{2D}}(\boldsymbol{\xi})C_{i_\phi}(\phi)), \tag{3.64}$$

where $i \equiv i(i_{2D},i_\phi) = 1,\cdots,N_{i_{2D}}N_{i_\phi}$

In the Galerkin method used here the variables $\boldsymbol{Y}$ and the test functions $\boldsymbol{w}^\star$ and $\tilde{\boldsymbol{w}}^\star$ belong all to the same space $\overrightarrow{\boldsymbol{\mathcal{W}}}(\Omega_{x,h})$

$$\overrightarrow{\boldsymbol{\mathcal{W}}}(\Omega_{x,h}) := \boldsymbol{\mathcal{V}}_h(\Omega_{x,h}) \times \overrightarrow{\boldsymbol{\mathcal{V}}}_h(\Omega_{x,h}) \times \boldsymbol{\mathcal{V}}_h(\Omega_{x,h}) \times \overrightarrow{\boldsymbol{\mathcal{V}}}_h(\Omega_{x,h}). \tag{3.65}$$

This space is spanned by the test functions

$$\begin{aligned}
\boldsymbol{w}^{\star}{}_{\rho,i} &= \begin{pmatrix} \mathcal{N}_i \\ 0 \\ 0 \\ 0 \end{pmatrix}, \boldsymbol{w}^{\star}{}_{v_R,i} = \begin{pmatrix} 0 \\ \mathcal{N}_i\hat{\boldsymbol{R}} \\ 0 \\ 0 \end{pmatrix}, \boldsymbol{w}^{\star}{}_{v_\phi,i} = \begin{pmatrix} 0 \\ \mathcal{N}_i\hat{\boldsymbol{\phi}} \\ 0 \\ 0 \end{pmatrix}, \boldsymbol{w}^{\star}{}_{v_Z,i} = \begin{pmatrix} 0 \\ \mathcal{N}_i\hat{\boldsymbol{Z}} \\ 0 \\ 0 \end{pmatrix} \\
\boldsymbol{w}^{\star}{}_{\mathcal{E},i} &= \begin{pmatrix} 0 \\ 0 \\ \mathcal{N}_i \\ 0 \end{pmatrix}, \boldsymbol{w}^{\star}{}_{A_R,i} = \begin{pmatrix} 0 \\ 0 \\ 0 \\ \mathcal{N}_i\hat{\boldsymbol{R}} \end{pmatrix}, \boldsymbol{w}^{\star}{}_{A_\phi,i} = \begin{pmatrix} 0 \\ 0 \\ 0 \\ \mathcal{N}_i\hat{\boldsymbol{\phi}} \end{pmatrix}, \boldsymbol{w}^{\star}{}_{A_Z,i} = \begin{pmatrix} 0 \\ 0 \\ 0 \\ \mathcal{N}_i\hat{\boldsymbol{Z}} \end{pmatrix}
\end{aligned}, \tag{3.66}$$

with $\mathcal{N}_i \in \boldsymbol{\mathcal{V}}_h(\Omega_{x,h})$.

The primitive variable $\boldsymbol{Y}(t, \boldsymbol{\xi}, \phi)$ can be decomposed as

$$\boldsymbol{Y}(t, \boldsymbol{\xi}, \phi) = \sum_{j=1}^{N_{i_{2D}} N_{i_\phi}} \boldsymbol{Y}_j(t)\mathcal{N}_j(\boldsymbol{\xi}, \phi), \tag{3.67}$$

where $\boldsymbol{Y}_j(t)$ is the unknown vector associated to the test function $\mathcal{N}_j(\boldsymbol{\xi}, \phi)$

$$\boldsymbol{Y}_j = \begin{pmatrix} \rho_j(t) \\ v_{R,j}(t)\hat{\boldsymbol{R}} + v_{\phi,j}(t)\hat{\boldsymbol{\phi}} + v_{Z,j}(t)\hat{\boldsymbol{Z}} \\ T_j(t) \\ A_{R,j}(t)\hat{\boldsymbol{R}} + \psi_j(t)\nabla\phi + A_{Z,j}(t)\hat{\boldsymbol{Z}} \end{pmatrix}, \tag{3.68}$$

which can be written to show all its components

$$\boldsymbol{Y}_j \equiv (\rho_j, v_{R,j}, v_{\phi,j}, v_{Z,j}, T_j, A_{R,j}, \psi_j, A_{Z,j})^T. \tag{3.69}$$

3.2.4.5 Semi-discrete system

To obtain the evolution of the unknown vector $\boldsymbol{Y}_j$, projections of the weak formulation shown in (3.2.4.3) following the vector test functions (3.66) have been performed, leading to the following semi-discrete system (it is discretized in space but not in time).

$$\begin{aligned}
\sum_j \int_{\Omega_{x,h}} \underline{\boldsymbol{M}}_{ij}(\underline{\boldsymbol{Y}})\partial_t \boldsymbol{Y}_j - \int_{\Omega_{x,h}} \boldsymbol{\Phi}_i^{\boldsymbol{F}}(\underline{\boldsymbol{Y}}) + \int_{\Omega_{x,h}} \boldsymbol{\Phi}_i^{\boldsymbol{G}}(\underline{\boldsymbol{Y}}) + \int_{\Omega_{x,h}} \boldsymbol{\Phi}_i^{\boldsymbol{F},R\phi}(\underline{\boldsymbol{Y}}) - \int_{\Omega_{x,h}} \boldsymbol{\Phi}_i^{\boldsymbol{G},R\phi}(\underline{\boldsymbol{Y}}) + \frac{1}{\epsilon}\int_{\Omega_{x,h}} \boldsymbol{\Phi}_i^{\boldsymbol{A}}(\underline{\boldsymbol{Y}}) \\
+ \int_{\partial\Omega_{x,h}} \boldsymbol{\Psi}_i^{\boldsymbol{F}}(\underline{\boldsymbol{Y}}) - \int_{\partial\Omega_{x,h}} \boldsymbol{\Psi}_i^{\boldsymbol{G}}(\underline{\boldsymbol{Y}}) + \frac{1}{\epsilon}\int_{\partial\Omega_{x,h}} \boldsymbol{\Psi}_i^{\partial_t \boldsymbol{A}}(\underline{\boldsymbol{Y}}) + \frac{1}{\epsilon}\int_{\partial\Omega_{x,h}} \boldsymbol{\Psi}_i^{\boldsymbol{S}}(\underline{\boldsymbol{Y}}) = \int_{\Omega_{x,h}} \boldsymbol{\Psi}_i^{VMS}(\overline{\underline{\boldsymbol{Y}}}, \delta\underline{\boldsymbol{Y}})
\end{aligned}, \tag{3.70}$$

where $\underline{\boldsymbol{M}}_{ij} = \mathcal{N}_i\mathcal{N}_j\underline{\boldsymbol{M}}(\underline{\boldsymbol{Y}})$ is the non-integrated mass matrix, which is not diagonal and depends on the variable $\boldsymbol{Y}$. The large vector $\underline{\boldsymbol{Y}}$ contains all the unknown vectors $\boldsymbol{Y}_j$.

The fluxes are defined as

$$\boldsymbol{\Phi}_i^{\underline{\boldsymbol{F}}}(\underline{\boldsymbol{Y}}) = \begin{pmatrix} \rho(\boldsymbol{v}\cdot\nabla\mathcal{N}_i) \\ \rho\boldsymbol{v}(\boldsymbol{v}\cdot\nabla\mathcal{N}_i) + P\nabla\mathcal{N}_i - \boldsymbol{B}(\boldsymbol{B}\cdot\nabla\mathcal{N}_i) \\ \rho\mathcal{H}(\boldsymbol{v}\cdot\nabla\mathcal{N}_i) - \boldsymbol{B}\cdot\boldsymbol{v}(\boldsymbol{B}\cdot\nabla\mathcal{N}_i) \\ -(\boldsymbol{v}\times\boldsymbol{B})\mathcal{N}_i \end{pmatrix}, \quad \boldsymbol{\Phi}_i^{\underline{\boldsymbol{G}}}(\underline{\boldsymbol{Y}}) = \begin{pmatrix} g_\rho\cdot\nabla\mathcal{N}_i \\ g_{\boldsymbol{m}}\nabla\mathcal{N}_i \\ g_{\mathcal{E}}\cdot\nabla\mathcal{N}_i \\ g_{\boldsymbol{B}}\mathcal{N}_i \end{pmatrix} \tag{3.71}$$

The contributions associated to $\boldsymbol{\Phi}_i^{\underline{\boldsymbol{F}}}$ and $\boldsymbol{\Phi}_i^{\underline{\boldsymbol{G}}}$ do not take into account the variation of $\hat{\boldsymbol{R}}$ and $\hat{\boldsymbol{\phi}}$ on the polar plane. This variation in taken into account on the fluxes, $\boldsymbol{\Phi}_i^{\underline{\boldsymbol{F}},R\phi}$ and $\boldsymbol{\Phi}_i^{\underline{\boldsymbol{G}},R\phi}$

$$\boldsymbol{\Phi}_i^{\underline{\boldsymbol{F}},R\phi}(\underline{\boldsymbol{Y}}) = \begin{pmatrix} 0 \\ (\rho v_\phi^2 + P - B_\phi^2)\hat{\boldsymbol{R}} - (\rho v_R v_\phi - B_R B_\phi)\hat{\boldsymbol{\phi}} \\ 0 \\ 0 \end{pmatrix}, \tag{3.72}$$

$$\boldsymbol{\Phi}_i^{\underline{\boldsymbol{G}},R\phi}(\underline{\boldsymbol{Y}}) = \begin{pmatrix} 0 \\ (g_{\boldsymbol{m}} : (\hat{\boldsymbol{\phi}}\otimes\hat{\boldsymbol{\phi}}))\hat{\boldsymbol{R}} - (g_{\boldsymbol{m}} : (\hat{\boldsymbol{R}}\otimes\hat{\boldsymbol{\phi}}))\hat{\boldsymbol{\phi}} \\ 0 \\ 0 \end{pmatrix} \tag{3.73}$$

The Coulomb condition is enforced when the approximation space is not divergence free, yielding

$$\boldsymbol{\Phi}_i^{\boldsymbol{A}}(\underline{\boldsymbol{Y}}) = \begin{pmatrix} 0 \\ 0 \\ 0 \\ (\nabla\cdot\boldsymbol{A})\left(\left(\partial_R\mathcal{N}_i + \frac{\mathcal{N}_i}{R}\right)\hat{\boldsymbol{R}} + \frac{\partial_\phi\mathcal{N}_i}{R}\hat{\boldsymbol{\phi}} + \partial_Z\mathcal{N}_i\hat{\boldsymbol{Z}}\right) \end{pmatrix}, \tag{3.74}$$

where the relations $\nabla\cdot\hat{\boldsymbol{R}} = \frac{1}{R}$ and $\nabla\cdot\hat{\boldsymbol{\phi}} = 0$ were used.

In order to simplify the formulation, let us express the fluxes as functions of the state $\underline{\boldsymbol{Y}}$, the gradient of the test function $\nabla\mathcal{N}_i$ and the test function itself $\mathcal{N}_i$, i.e.

$$\boldsymbol{\Phi}_i^{\underline{\boldsymbol{F}}}(\underline{\boldsymbol{Y}}) = \boldsymbol{\Phi}^{\underline{\boldsymbol{F}}}(\underline{\boldsymbol{Y}}, \nabla\mathcal{N}_i, \mathcal{N}_i) \text{ and } \boldsymbol{\Phi}_i^{\underline{\boldsymbol{D}}}(\underline{\boldsymbol{Y}}) = \boldsymbol{\Phi}^{\underline{\boldsymbol{D}}}(\underline{\boldsymbol{Y}}, \nabla\mathcal{N}_i, \mathcal{N}_i). \tag{3.75}$$

Therefore, the associated boundary fluxes use the same functions except for the gradient that is replaced by a vector multiplying the test function, such as

$$\boldsymbol{\Psi}_i^{\underline{\boldsymbol{F}}}(\underline{\boldsymbol{Y}}) = \boldsymbol{\Psi}^{\underline{\boldsymbol{F}}}(\underline{\boldsymbol{Y}}, \mathcal{N}_i\boldsymbol{n}, \mathcal{N}_i) \text{ and } \boldsymbol{\Psi}_i^{\underline{\boldsymbol{D}}}(\underline{\boldsymbol{Y}}) = \boldsymbol{\Psi}^{\underline{\boldsymbol{D}}}(\underline{\boldsymbol{Y}}, \mathcal{N}_i\boldsymbol{n}, \mathcal{N}_i), \tag{3.76}$$

where $\boldsymbol{n}$ represents the outward unit normal vector at the boundary. The boundary conditions flux becomes then

$$\boldsymbol{\Psi}_i^S = \begin{pmatrix} (\rho - \rho_b)\mathcal{N}_i \boldsymbol{\mathcal{X}}(\partial\Omega_{x,h}^{\rho}) \\ \rho(\boldsymbol{v} - \boldsymbol{v}_b)\mathcal{N}_i \boldsymbol{\mathcal{X}}(\partial\Omega_{x,h}^{\boldsymbol{v}}) + (\rho\boldsymbol{v} - \boldsymbol{m}_b)\mathcal{N}_i \boldsymbol{\mathcal{X}}(\partial\Omega_{x,h}^{\boldsymbol{m}}) \\ \rho(T - T_b)\mathcal{N}_i \boldsymbol{\mathcal{X}}(\partial\Omega_{x,h}^{T}) + (p - p_b)\mathcal{N}_i \boldsymbol{\mathcal{X}}(\partial\Omega_{x,h}^{p}) \\ (\boldsymbol{A} - \boldsymbol{A}_b)\mathcal{N}_i \boldsymbol{\mathcal{X}}(\partial\Omega_{x,h}^{\boldsymbol{A}}) + (\boldsymbol{B} - \boldsymbol{B}_p)\mathcal{N}_i \boldsymbol{\mathcal{X}}(\partial\Omega_{x,h}^{\boldsymbol{B}}) \end{pmatrix}. \tag{3.77}$$

The formulation with the vector potential produces a boundary contribution associated to the time derivative of $\boldsymbol{A}$. When the degree of freedom associated to the index i is on the boundary, we have

$$\boldsymbol{\Psi}_i^{\partial_t \boldsymbol{A}}(\underline{\boldsymbol{Y}}) = \begin{pmatrix} 0 \\ 0 \\ 0 \\ \boldsymbol{n} \cdot (\partial_t \boldsymbol{A} \times \hat{\boldsymbol{R}})\mathcal{N}_i \hat{\boldsymbol{R}} + \boldsymbol{n} \cdot (\partial_t \boldsymbol{A} \times \hat{\boldsymbol{\phi}})\mathcal{N}_i \hat{\boldsymbol{\phi}} + \boldsymbol{n} \cdot (\partial_t \boldsymbol{A} \times \hat{\boldsymbol{Z}})\mathcal{N}_i \hat{\boldsymbol{Z}} \end{pmatrix}. \tag{3.78}$$

Finally, the stabilization is defined as

$$\boldsymbol{\Phi}_i^{VMS}(\overline{\underline{\boldsymbol{Y}}}, \delta\boldsymbol{Y}) = \left(\begin{array}{c} \underline{\boldsymbol{L}}(\overline{\boldsymbol{w}}, \boldsymbol{\partial})\delta\boldsymbol{w} \cdot \underline{\boldsymbol{L}}^T(\overline{\boldsymbol{w}}, \boldsymbol{\partial})\boldsymbol{w}^{\star}{}_{\rho,i} \\ \hline \underline{\boldsymbol{L}}(\overline{\boldsymbol{w}}, \boldsymbol{\partial})\delta\boldsymbol{w} \cdot \underline{\boldsymbol{L}}^T(\overline{\boldsymbol{w}}, \boldsymbol{\partial})\boldsymbol{w}^{\star}{}_{v_R,i}\hat{\boldsymbol{R}} + \underline{\boldsymbol{L}}(\overline{\boldsymbol{w}}, \boldsymbol{\partial})\delta\boldsymbol{w} \cdot \underline{\boldsymbol{L}}^T(\overline{\boldsymbol{w}}, \boldsymbol{\partial})\boldsymbol{w}^{\star}{}_{v_\phi,i}\hat{\boldsymbol{\phi}} \\ +\underline{\boldsymbol{L}}(\overline{\boldsymbol{w}}, \boldsymbol{\partial})\delta\boldsymbol{w} \cdot \underline{\boldsymbol{L}}^T(\overline{\boldsymbol{w}}, \boldsymbol{\partial})\boldsymbol{w}^{\star}{}_{v_Z,i}\hat{\boldsymbol{Z}} \\ \hline \underline{\boldsymbol{L}}(\overline{\boldsymbol{w}}, \boldsymbol{\partial})\delta\boldsymbol{w} \cdot \underline{\boldsymbol{L}}^T(\overline{\boldsymbol{w}}, \boldsymbol{\partial})\boldsymbol{w}^{\star}{}_{\mathcal{E},i} \\ \hline \underline{\boldsymbol{L}}(\overline{\boldsymbol{w}}, \boldsymbol{\partial})\delta\boldsymbol{w} \cdot \underline{\boldsymbol{L}}^T(\overline{\boldsymbol{w}}, \boldsymbol{\partial})\boldsymbol{w}^{\star}{}_{A_R,i}\hat{\boldsymbol{R}} + \underline{\boldsymbol{L}}(\overline{\boldsymbol{w}}, \boldsymbol{\partial})\delta\boldsymbol{w} \cdot \underline{\boldsymbol{L}}^T(\overline{\boldsymbol{w}}, \boldsymbol{\partial})\boldsymbol{w}^{\star}{}_{A_\phi,i}\hat{\boldsymbol{\phi}} \\ +\underline{\boldsymbol{L}}(\overline{\boldsymbol{w}}, \boldsymbol{\partial})\delta\boldsymbol{w} \cdot \underline{\boldsymbol{L}}^T(\overline{\boldsymbol{w}}, \boldsymbol{\partial})\boldsymbol{w}^{\star}{}_{A_Z,i}\hat{\boldsymbol{Z}} \end{array}\right), \tag{3.79}$$

where the fluctuation is approximated by the variation in the current time-step. The quantities $\delta\boldsymbol{w}$ linked to $\delta\underline{\boldsymbol{Y}}$ by the matrix $\underline{\boldsymbol{M}}(\overline{\underline{\boldsymbol{Y}}})$ evaluated at the beginning of the time-step are

$$\delta\underline{\boldsymbol{Y}} \approx \underline{\boldsymbol{Y}}^{n+1} - \underline{\boldsymbol{Y}}^{n} \text{ and } \delta\boldsymbol{w} \approx \underline{\boldsymbol{M}}(\overline{\underline{\boldsymbol{Y}}})\delta\underline{\boldsymbol{Y}}. \tag{3.80}$$

3.2.4.6 Time stepping

The time discretization is done following a procedure similar to the one shown in (3.9). For that, let us simplify the notation by using the following block matrix, block vector and block right-hand side

$$\underline{\mathbb{M}}_{ij}^{\delta t}(\underline{\boldsymbol{Y}}) = \int_{\Omega_{x,h}} \underline{\boldsymbol{M}}_{ij}(\underline{\boldsymbol{Y}}), \qquad \underline{\boldsymbol{VMS}}_i(\overline{\underline{\boldsymbol{Y}}}, \delta\underline{\boldsymbol{Y}}) = -\int_{\Omega_{x,h}} \boldsymbol{\Phi}_i^{VMS}(\overline{\underline{\boldsymbol{Y}}}, \delta\underline{\boldsymbol{Y}}) \tag{3.81}$$

and

$$\begin{aligned}\underline{\boldsymbol{RHS}}_i(\underline{\boldsymbol{Y}}) = \int_{\Omega_{x,h}} \boldsymbol{\Phi}_i^{\boldsymbol{F}}(\underline{\boldsymbol{Y}}) - \int_{\Omega_{x,h}} \boldsymbol{\Phi}_i^{\boldsymbol{G}}(\underline{\boldsymbol{Y}}) - \int_{\Omega_{x,h}} \boldsymbol{\Phi}_i^{\boldsymbol{F},R\phi}(\underline{\boldsymbol{Y}}) + \int_{\Omega_{x,h}} \boldsymbol{\Phi}_i^{\boldsymbol{G},R\phi}(\underline{\boldsymbol{Y}}) - \frac{1}{\epsilon}\int_{\Omega_{x,h}} \boldsymbol{\Phi}_i^{\boldsymbol{A}}(\underline{\boldsymbol{Y}}) \\ - \int_{\partial\Omega_{x,h}} \boldsymbol{\Psi}_i^{\boldsymbol{F}}(\underline{\boldsymbol{Y}}) + \int_{\partial\Omega_{x,h}} \boldsymbol{\Psi}_i^{\boldsymbol{G}}(\underline{\boldsymbol{Y}}) - \frac{1}{\epsilon}\int_{\partial\Omega_{x,h}} \boldsymbol{\Psi}_i^{\partial_t \boldsymbol{A}}(\underline{\boldsymbol{Y}}) - \frac{1}{\epsilon}\int_{\partial\Omega_{x,h}} \boldsymbol{\Psi}_i^{\boldsymbol{S}}(\underline{\boldsymbol{Y}})\end{aligned} . \tag{3.82}$$

The semi-discrete system (3.70) is then a nonlinear system that can be written as

$$\underline{\mathbb{M}}^{\delta t}(\underline{\boldsymbol{Y}})\partial_t \underline{\boldsymbol{Y}} + \underline{\boldsymbol{VMS}}(\overline{\underline{\boldsymbol{Y}}}, \delta\underline{\boldsymbol{Y}}) = \underline{\boldsymbol{RHS}}(\underline{\boldsymbol{Y}}). \tag{3.83}$$

To discretize this system, we consider the most general two-step time integration method, like in [85]. For that, six unknowns are introduced: p_-, p_0, p_+, q_-, q_0 and q_+. Hence

$$\begin{aligned}p_-\underline{\mathbb{M}}^{\delta t}(\underline{\boldsymbol{Y}}^{n-1})\underline{\boldsymbol{Y}}^{n-1} + p_0\underline{\mathbb{M}}^{\delta t}(\underline{\boldsymbol{Y}}^{n})\underline{\boldsymbol{Y}}^{n} + p_+\underline{\mathbb{M}}^{\delta t}(\underline{\boldsymbol{Y}}^{n+1})\underline{\boldsymbol{Y}}^{n+1} + \underline{\boldsymbol{VMS}}(\overline{\underline{\boldsymbol{Y}}^n}, \delta\underline{\boldsymbol{Y}}) \\ = \delta t\left(q_-\underline{\boldsymbol{RHS}}(\underline{\boldsymbol{Y}}^{n-1}) + q_0\underline{\boldsymbol{RHS}}(\underline{\boldsymbol{Y}}^{n}) + q_+\underline{\boldsymbol{RHS}}(\underline{\boldsymbol{Y}}^{n+1})\right)\end{aligned} , \tag{3.84}$$

where $\delta t = t^{n+1} - t^n$ which can be different from δt^n that is defined as $t^n - t^{n-1}$. We can perform a Taylor expansion in the expression above up to second order, to get

$$\begin{aligned}p_-\left(\underline{\mathbb{M}}^{\delta t}(\underline{\boldsymbol{Y}}^{n-1})\underline{\boldsymbol{Y}}^{n-1} - \delta t^n\underline{\mathbb{M}}^{\delta t}(\underline{\boldsymbol{Y}}^{n})\partial_t\underline{\boldsymbol{Y}}^{n} + \frac{1}{2}\delta t^n\underline{\mathbb{M}}^{\delta t}(\underline{\boldsymbol{Y}}^{n})\partial_t^2\underline{\boldsymbol{Y}}^{n}\right) + p_0\underline{\mathbb{M}}^{\delta t}(\underline{\boldsymbol{Y}}^{n})\partial_t\underline{\boldsymbol{Y}}^{n} \\ p_+\left(\underline{\mathbb{M}}^{\delta t}(\underline{\boldsymbol{Y}}^{n})\underline{\boldsymbol{Y}}^{n} + \delta t\underline{\mathbb{M}}^{\delta t}(\underline{\boldsymbol{Y}}^{n})\partial_t\underline{\boldsymbol{Y}}^{n} + \frac{1}{2}\delta t^n\underline{\mathbb{M}}^{\delta t}(\underline{\boldsymbol{Y}}^{n})\partial_t^2\underline{\boldsymbol{Y}}^{n}\right) \\ = \delta t\left(q_-(\underline{\boldsymbol{RHS}}(\underline{\boldsymbol{Y}}^{n}) - \delta t^n\underline{\boldsymbol{RHS}}(\partial_t\underline{\boldsymbol{Y}}^{n})) + q_0\underline{\boldsymbol{RHS}}(\underline{\boldsymbol{Y}}^{n}) + q_-(\underline{\boldsymbol{RHS}}(\underline{\boldsymbol{Y}}^{n}) + \delta t\underline{\boldsymbol{RHS}}(\partial_t\underline{\boldsymbol{Y}}^{n}))\right)\end{aligned} . \tag{3.85}$$

To leading order on the time step, $p_- + p_0 + p_+ = 0$. To first order, it is enough to use the relation $\underline{\mathbb{M}}^{\delta t}(\underline{\boldsymbol{Y}}^{n})\partial_t\underline{\boldsymbol{Y}}^{n} = \underline{\boldsymbol{RHS}}(\underline{\boldsymbol{Y}}^{n})$ to get

$$\frac{p_+\delta t - p_-\delta t^n}{\delta t} = q_- + q_0 + q_+. \tag{3.86}$$

If we rewrite the variables as $\zeta \equiv p_-$, $\beta \equiv -q_-$ and $\theta \equiv q_+$, the solution for the coefficients are

$$p_0 = -(1 + \zeta(1 + r)), \quad p_+ = 1 + \zeta r, \quad q_- = 1 + \beta - \theta, \tag{3.87}$$

where $r = \frac{\delta t^n}{\delta_t}$. Therefore, the one-step and two-step schemes can be written in its most general form as

$$\begin{aligned}(1-\zeta r)\frac{\underline{\mathbb{M}}^{\delta t}(\underline{\boldsymbol{Y}}^{n+1})\underline{\boldsymbol{Y}}^{n+1} - \underline{\mathbb{M}}^{\delta t}(\underline{\boldsymbol{Y}}^{n})\underline{\boldsymbol{Y}}^{n}}{\delta t} + \underline{\boldsymbol{VMS}}(\overline{\underline{\boldsymbol{Y}}}, \delta\underline{\boldsymbol{Y}}) - \theta\underline{\boldsymbol{RHS}}(\underline{\boldsymbol{Y}}^{n} + \delta\underline{\boldsymbol{Y}}) \\ = -\zeta\frac{\underline{\mathbb{M}}^{\delta t}(\underline{\boldsymbol{Y}}^{n})\underline{\boldsymbol{Y}}^{n} - \underline{\mathbb{A}}^{\delta t}(\underline{\boldsymbol{Y}}^{n-1})\underline{\boldsymbol{Y}}^{n-1}}{\delta t^n} + (1-\theta+\beta)\underline{\boldsymbol{RHS}}(\underline{\boldsymbol{Y}}^{n}) - \beta\underline{\boldsymbol{RHS}}(\underline{\boldsymbol{Y}}^{n-1})\end{aligned} . \tag{3.88}$$

For $\zeta = \beta = 0$ the above scheme includes the $\theta-$scheme shown in (3.9).

Note that the proposed VMS stabilization is related to the Taylor-Galerkin formulation and always contains an implicit contribution. Therefore, the forward Euler scheme is no more an explicit scheme. We can say that it is an implicit stabilization of the forward Euler scheme. Moreover, the approximation $\underline{\mathbb{M}}^{\delta t}(\underline{\boldsymbol{Y}}^{n+1}) \approx \underline{\mathbb{M}}^{\delta t}(\underline{\boldsymbol{Y}}^{n}) = \underline{\mathbb{M}}(\underline{\boldsymbol{Y}}^{n})$ can be used in (3.89) yielding

$$\begin{aligned}\underline{\mathbb{M}}\left((1-\zeta r)\left(\frac{\delta\underline{\boldsymbol{Y}}}{\delta t}\right)+\zeta\left(\frac{\partial\underline{\boldsymbol{Y}}}{\partial t}\right)^{n}\right) &= \underline{\boldsymbol{VMS}}(\overline{\underline{\boldsymbol{Y}}},\delta\underline{\boldsymbol{Y}})-\theta\underline{\boldsymbol{RHS}}(\underline{\boldsymbol{Y}}^{n}+\delta\underline{\boldsymbol{Y}})\\ &\quad+(1-\theta+\beta)\underline{\boldsymbol{RHS}}(\underline{\boldsymbol{Y}}^{n})-\beta\underline{\boldsymbol{RHS}}(\underline{\boldsymbol{Y}}^{n-1}),\end{aligned} \tag{3.89}$$

where $\delta\underline{\boldsymbol{Y}} = \underline{\boldsymbol{Y}}^{n+1} - \underline{\boldsymbol{Y}}^{n}$ and

$$\left(\frac{\partial\underline{\boldsymbol{Y}}}{\partial t}\right)^{n} = \frac{\underline{\boldsymbol{Y}}^{n}-\underline{\boldsymbol{Y}}^{n-1}}{t^{n}-t^{n-1}}. \tag{3.90}$$

For compactness, let us define $\underline{\boldsymbol{\mathcal{R}}}$, defined as

$$\underline{\boldsymbol{\mathcal{R}}}(\underline{\boldsymbol{Y}},\delta\underline{\boldsymbol{Y}}) = \underline{\boldsymbol{VMS}}(\overline{\underline{\boldsymbol{Y}}},\delta\underline{\boldsymbol{Y}})-\theta\underline{\boldsymbol{RHS}}(\underline{\boldsymbol{Y}}^{n}+\delta\underline{\boldsymbol{Y}})+(1-\theta+\beta)\underline{\boldsymbol{RHS}}(\underline{\boldsymbol{Y}}^{n})-\beta\underline{\boldsymbol{RHS}}(\underline{\boldsymbol{Y}}^{n-1}), \tag{3.91}$$

such that the temporal discretization can be written as

$$\underline{\mathbb{M}}\left((1-\zeta r)\left(\frac{\delta\underline{\boldsymbol{Y}}}{\delta t}\right)+\zeta\left(\frac{\partial\underline{\boldsymbol{Y}}}{\partial t}\right)^{n}\right) = \underline{\boldsymbol{\mathcal{R}}}(\underline{\boldsymbol{Y}},\delta\underline{\boldsymbol{Y}}). \tag{3.92}$$

3.2.4.7 Discretization in the poloidal plane

The discretization of the poloidal plane is done with the aid of a $2D$ finite element basis using the Bézier formalism described below.

Bézier Formalism

There are several different formalism concerning FEM, as for instance Lagrangian elements used in the code NIMROD [7] or triangular finite elements with C^1 continuity as described in [86]. We will describe here the fourth-order Galerkin method based on the Bézier formalism as proposed in [9]. Let's start with an introduction about Bézier surfaces.

Bézier Surfaces

Bézier surfaces were first described in 1962 by the French engineer Pierre Bézier who used them to design automobile bodies. They are constructed with a family of polynomials called Bernstein polynomials. A Bézier surface, as a Bézier curve, is defined by a set of control points that stretch the surface towards them as if each had an attractive force.

Bézier surfaces can be of any degree, but bi-cubic Bézier surfaces generally provide enough degrees of freedom for most applications.

The simplest Bézier object corresponds to curves defined as

$$P(s) = \sum_{i=1}^{n} P_i B_i^n(s), \quad 0 \leq s \leq 1, \tag{3.93}$$

in which $P_i(x_1, x_2, x_3)$ is a set of control points belonging to the $3D$ space where the coordinates are expressed and $B_i^n(s)$ are the Bernstein Polynomials [87], defined as

$$B_i^n(s) = C_n^i s^i (1-s)^{n-i}, \text{ where } C_i^n = \frac{n!}{i!(n-i)!} \text{ for } 0 \leq i \leq n. \tag{3.94}$$

As an example, a degree $n = 3$ yields,

$$\begin{cases} B_0^3(s) &= (1-s)^3, \\ B_1^3(s) &= 3(1-s)^2 s, \\ B_2^3(s) &= 3(1-s)s^2, \\ B_3^3(s) &= s^3, \end{cases} \tag{3.95}$$

It is important to remark that even if it is a $3D$ curve, only one parameter s is necessary to locate a point on it. The curve shape will be defined directly by the position of the control points as shown in Figure (3.2).

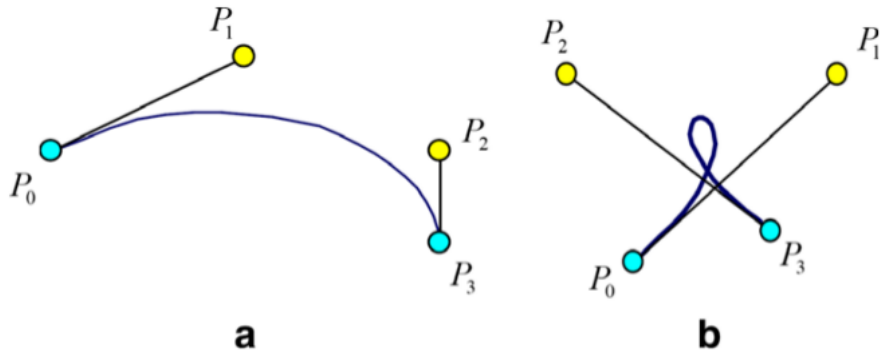

FIGURE 3.2: Examples of Bézier curves with $P_i \in \mathbb{R}^2$

It is possible to extend the parametrization (3.93) to a bicubic rectangular patch as

$$P(s,t) = \sum_{i=0}^{3} \sum_{j=0}^{3} P_{i,j} B_i^3(s) B_j^3(t), \text{ for } 0 \leq s, t \leq n. \tag{3.96}$$

This definition yields 16 control points which will be evenly distributed into four sets associated to each corner of the patch as shown in Figure (3.3).

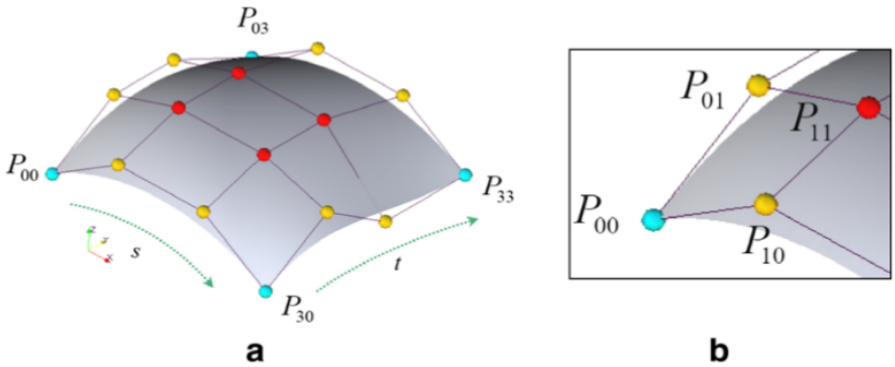

FIGURE 3.3: Bézier patch with $P_{ij} \in \mathbb{R}^3$ and detail of the corner.

Continuity between adjacent Bézier Patches

Let's consider two surfaces named S and S', as shown in Figure (3.4). The parametrization of the common edge writes

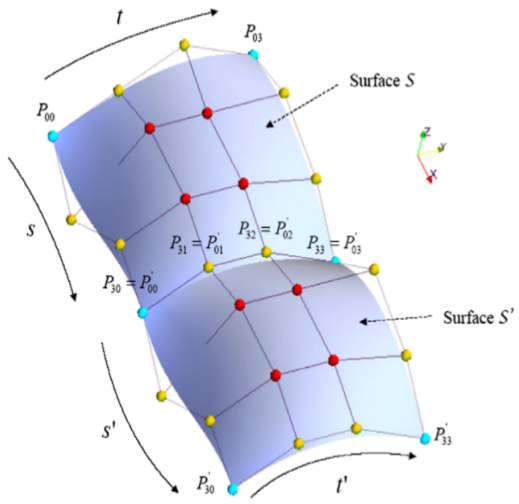

FIGURE 3.4: Continuity between two adjacent Bézier patches

$$E(t) = P(1,t) = \sum_{j=0}^{3} P_{3,j} B_j^3(t) \text{ and } E'(t') = P'(0,t') = \sum_{j=0}^{3} P'_{0,j} B_j^3(t'). \tag{3.97}$$

The first level of continuity comes from the equality $E(t) = E'(t'), \forall t = t'$, which yields

$$P_{3,j} = P'_{0,j}, \forall j \tag{3.98}$$

In summary, this result is telling that S and S' share the same control points at the common edge. This also leads to the equality of tangent vectors associated to direction t

$$\left(\frac{\partial P}{\partial t}\right)_{s=1}(t) = \left(\frac{\partial P'}{\partial t'}\right)_{s'=1}(t'), \forall t = t'. \tag{3.99}$$

Another continuity that must be verified is the continuity of surface gradients. For that, let us consider a point $P = P'$ located at the common boundary $E = E'$. The planes Π and Π' tangent to the surfaces S and S' at $P = P'$ are generated by a basis of two vectors $\left(\frac{\partial P}{\partial s}\right)$ and $\left(\frac{\partial P}{\partial t}\right)$; and $\left(\frac{\partial P'}{\partial s'}\right)$ and $\left(\frac{\partial P'}{\partial t'}\right)$, respectively. To fulfill the tangent plane condition, we must have $\Pi = \Pi'$ on the edge. As Equation (3.99) already provides a relation for the coordinate t, the condition becomes the reinforcement of the coplanarity of $\left(\frac{\partial P}{\partial s}\right)$, $\left(\frac{\partial P}{\partial t}\right)$and $\left(\frac{\partial P'}{\partial s'}\right)$ at any point of the common edge, i.e., for each $P(t)$ along the edge, real numbers $k_1(t), k_2(t)$ and $k_3(t)$ must be found, such that

$$k_1(t)\left(\frac{\partial P}{\partial s}\right) + k_2(t)\left(\frac{\partial P}{\partial t}\right) + k_3(t)\left(\frac{\partial P'}{\partial s'}\right) = 0. \tag{3.100}$$

The necessary and sufficient condition to satisfy (3.100) used here is detailed in [88]. For the case where the control points are alligned over the edge, the following relations hold

$$\exists \lambda_j \in \mathbb{R} | P_{3,j} - P'_{1,j} = \lambda_j P_{s,j} - P_{3,j}. \tag{3.101}$$

Therefore, each derivative in (3.100) can be written as

$$\left(\frac{\partial P}{\partial s}\right)_{s=1} = \sum_{j=0}^{3} 3(P_{3,j} - P_{2,j}) B_j^3(t), \tag{3.102}$$

$$\left(\frac{\partial P'}{\partial s'}\right)_{s'=0} = \sum_{j=0}^{3} 3\lambda_j (P_{3,j} - P_{2,j}) B_j^3(t), \tag{3.103}$$

$$\left(\frac{\partial P}{\partial t}\right)_{s=1} = \sum_{j=0}^{3} 3P_{3,j} \frac{dB_j^3}{dt}(t). \tag{3.104}$$

If $k_2(t)$ is taken to be zero and knowing that the Bernstein polynomials are linearly independent, it yields

$$\lambda_j = \lambda, \forall j \tag{3.105}$$

with λ an arbitrary constant coefficient. Finally, the alignment condition writes

$$P_{3,j} - P'_{1,j} = \lambda P_{2,j} - P_{3,j} \quad \forall j \in (0, ..., 3). \tag{3.106}$$

This condition is retained for the formulation of the finite element problem.

Bézier finite elements

For the finite element formulation we suppose that a domain Ω is decomposed into $\mathcal{N}_{el}$ quadrilateral cells parametrized with a Bézier approach. Then, the integrals of the weak

form are not evaluated in the classical coordinates of the problem but goes under a coordinate transformation to a unit square, called reference element, as in Figure (3.5).

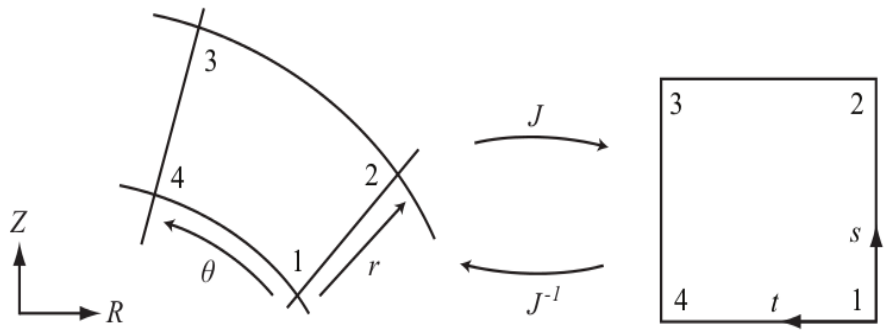

FIGURE 3.5: Scheme of the transformation from a curved element to the reference square element

An iso-parametric formulation is used in which the coordinates are transformed by means of the same basis functions used for other variables. An arbitrary quantity is expanded on this reference element as

$$P(s,t) = \sum_{i=1}^{4}\sum_{j=1}^{4} p_{i,j}\sigma_{i,j}b_{i,j}(s,t), \quad 0 \leq s,t \leq 1, \tag{3.107}$$

where the first sum runs over the four vertices, while the second one runs over the four basis function $b_{i,j}$ per vertex, which come from the Bernstein polynomials described in the previous section. σ arranges the continuity through the elements (also described in previous section) and $p_{i,j}$, are the unknowns living on the vertices. The basis functions are zero in all elements, excepting the ones to which the vertex belongs. Also, all the basis functions labeled i vanish on the two edges opposite to the vertex i.

This iso-parametric construction enforces the C^1 continuity of the test functions in the physical space, also, having four degrees of freedom associated to each vertex makes the construction of the compressed graph that is used to speed-up the solving of the numerical scheme easier.

The iso-parametric transformation used to map the square to any curved element $\boldsymbol{e}$ of the physical space is written as

$$\begin{cases} R_e(\boldsymbol{\zeta}) &= \displaystyle\sum_{j_{2D}\in\vartheta(\boldsymbol{e})} R_{j_{2D}}\hat{\psi}_{m_{\boldsymbol{e}(j_{2D})}}(\boldsymbol{\zeta}) \\ Z_e(\boldsymbol{\zeta}) &= \displaystyle\sum_{j_{2D}\in\vartheta(\boldsymbol{e})} Z_{j_{2D}}\hat{\psi}_{m_{\boldsymbol{e}(j_{2D})}}(\boldsymbol{\zeta}) \end{cases} \tag{3.108}$$

The parameters $R_{j_{2D}}$ and $R_{j_{2D}}$ of this interpolation are inputs of the MHD computation. They are designed by the meshing process to ensure that the transformation is non-singular (injection) and that the mapped element in the physical space can be curved. This allows the mesh to be aligned either with the curved boundary or the flux surfaces given by the initial equilibrium. The function $m_{\boldsymbol{e}}(j_{2D})$ changes the global numbering (j_{2D}) to a local numbering in the set $\left\{1, \cdots, \widehat{N}_{dof}\right\}$ where $\widehat{N}_{dof}$ is the number of unknowns associated to the reference element. In the present context of the bi-cubic interpolation over square, we have $\widehat{N}_{dof} = 16$. However, contrary to the classical cubic Bézier, the unknowns of the current basis are located at the vertices of the square such as to ensure the C^1 continuity when crossing the edges of physical elements. This localization of the unknowns also allows the derivation of the compressed numerical graph, useful for computational efficiency.

In order to solve the integrals to be able to assembly the system, the toroidal decomposition must be taken into account toghether with the poloidal representation shown here. For this, Fourier basis functions are used due to the axis-symmetry of the system. The details are shown below.

3.2.4.8 Assembling the system

The integrals to be evaluated in equation (3.70) will be achieved accordingly to the cylindrical transformation and the parametric mapping. For any function $\boldsymbol{Y}$, the integral is approximated as a sum of integrals over the poloidal elements and the local mapping used. They are evaluated by Gauss quadrature. For the toroidal part, the details of the discretization will be given here. We consider the finite element formulation where the test functions $\mathcal{N}_i$ and $\mathcal{N}_j$ are written as

$$\mathcal{N}_i = \psi_{i_{2D}}(\boldsymbol{\xi}) C_{i_\phi}(\phi), \quad \forall i_{2D}, i_\phi \tag{3.109}$$

$$\mathcal{N}_j = \psi_{j_{2D}}(\boldsymbol{\xi}) C_{j_\phi}(\phi), \quad \forall j_{2D}, j_\phi \tag{3.110}$$

The right hand side $\underline{\boldsymbol{\mathcal{R}}}$ defined in (3.91) can then be decomposed as

$$\underline{\boldsymbol{\mathcal{R}}}_i = \int_0^{2\pi} \int_{\Omega_{2D}} R \underline{\widehat{\boldsymbol{\mathcal{R}}}}_i d\boldsymbol{\xi} d\phi, \tag{3.111}$$

and

$$\underline{\widehat{\boldsymbol{\mathcal{R}}}}_i \equiv \underline{\widehat{\boldsymbol{\mathcal{R}}}}^{(00)}(\boldsymbol{Y}, \mathcal{N}_i) + \underline{\widehat{\boldsymbol{\mathcal{R}}}}^{(01)}(\boldsymbol{Y}, \partial_\phi \mathcal{N}_i) + \underline{\widehat{\boldsymbol{\mathcal{R}}}}^{(10)}(\partial_\phi \boldsymbol{Y}, \mathcal{N}_i) + \underline{\widehat{\boldsymbol{\mathcal{R}}}}^{(11)}(\partial_\phi \boldsymbol{Y}, \partial_\phi \mathcal{N}_i), \tag{3.112}$$

where $\underline{\widehat{\boldsymbol{\mathcal{R}}}}^{(kl)}$ are often nonlinear functions of the first variables, i.e., either $\boldsymbol{Y}$ or $\partial_\phi \boldsymbol{Y}$ and linear functions of the second variable (either $\mathcal{N}_i$ or $\partial_\phi \mathcal{N}_i$). Then, using (3.109) yields

$$\underline{\widehat{\boldsymbol{\mathcal{R}}}}_i \equiv \underline{\widehat{\boldsymbol{\mathcal{R}}}}^{(00)}(\boldsymbol{Y}, \psi_{i_{2D}})C_{i_\phi} + \underline{\widehat{\boldsymbol{\mathcal{R}}}}^{(01)}(\boldsymbol{Y}, \psi_{i_{2D}})\partial_\phi C_{i_\phi} + \underline{\widehat{\boldsymbol{\mathcal{R}}}}^{(10)}(\partial_\phi \boldsymbol{Y}, \psi_{i_{2D}})C_{i_\phi} + \underline{\widehat{\boldsymbol{\mathcal{R}}}}^{(11)}(\partial_\phi \boldsymbol{Y}, \psi_{i_{2D}})\partial_\phi C_{i_\phi}.$$

The functions $\boldsymbol{Y}$ and $\partial_\phi \boldsymbol{Y}$ depend on the discrete unknowns $\tilde{\boldsymbol{Y}}(t)$ as follows

$$\begin{aligned} \boldsymbol{Y} \equiv \boldsymbol{Y}(\tilde{\boldsymbol{Y}}) &= \sum_k \boldsymbol{Y}_k \psi_{k2D}(\boldsymbol{\xi}) C_{k\phi}(\phi) &= \boldsymbol{\psi}^T \tilde{\boldsymbol{Y}}_{3D} \boldsymbol{C} \\ \partial_\phi \boldsymbol{Y} \equiv \partial_\phi \boldsymbol{Y}(\tilde{\boldsymbol{Y}}) &= \sum_k \boldsymbol{Y}_k \psi_{k2D}(\boldsymbol{\xi}) \partial_\phi C_{k\phi}(\phi) &= \boldsymbol{\psi}^T \tilde{\boldsymbol{Y}}_{3D} \partial_\phi \boldsymbol{C} \end{aligned} . \tag{3.113}$$

The make the notation a lighter, let us use the following form

$$\underline{\widehat{\boldsymbol{\mathcal{R}}}}_i \equiv \underline{\widehat{\boldsymbol{\mathcal{R}}}}^{(00)}_{i_{2D}} C_{i_\phi} + \underline{\widehat{\boldsymbol{\mathcal{R}}}}^{(01)}_{i_{2D}} C_{i_\phi} + \underline{\widehat{\boldsymbol{\mathcal{R}}}}^{(10)}_{i_{2D}} \partial_\phi C_{i_\phi} + \underline{\widehat{\boldsymbol{\mathcal{R}}}}^{(11)}_{i_{2D}} \partial_\phi C_{i_\phi} = \underline{\widehat{\boldsymbol{\mathcal{R}}}}^{(0)}_{i_{2D}} C_{i_\phi} + \underline{\widehat{\boldsymbol{\mathcal{R}}}}^{(1)}_{i_{2D}} \partial_\phi C_{i_\phi}. \tag{3.114}$$

It is important to remark that as $\boldsymbol{Y}$ is a function of ϕ, $\underline{\widehat{\boldsymbol{\mathcal{R}}}}^{(0)}_{i_{2D}}$ and $\underline{\widehat{\boldsymbol{\mathcal{R}}}}^{(1)}_{i_{2D}}$ are also functions of ϕ. Therefore,

$$\underline{\boldsymbol{\mathcal{R}}}_i \equiv \underline{\boldsymbol{\mathcal{R}}}_i(\tilde{\boldsymbol{Y}}) = \int_0^{2\pi} \left(\int_{\Omega_{2D}} \underline{\widehat{\boldsymbol{\mathcal{R}}}}^{(0)}_{i_{2D}} R d\boldsymbol{\xi} \right) C_{i_\phi} d\phi + \int_0^{2\pi} \left(\int_{\Omega_{2D}} \underline{\widehat{\boldsymbol{\mathcal{R}}}}^{(1)}_{i_{2D}} R d\boldsymbol{\xi} \right) \partial_\phi C_{i_\phi} d\phi. \tag{3.115}$$

For a given $\tilde{\boldsymbol{Y}} = \tilde{\boldsymbol{Y}}^n$, these integrals are evaluated by numerical integration associated to integration points in the poloidal plane and toroidal direction. The finite element discrete formulation writes

$$\sum_j \underline{\mathbb{M}}_{ij} \frac{d\tilde{\boldsymbol{Y}}_j}{dt} = \underline{\boldsymbol{\mathcal{R}}}_i(\tilde{\boldsymbol{Y}}) \quad \forall i. \tag{3.116}$$

This is a nonlinear ordinary differential system that can be approximated by a numerical integration in time. Then, using the time stepping shown in (3.92) yields

$$\sum_j \underline{\mathbb{M}}_{ij}(\tilde{\boldsymbol{Y}}^n) \left((1-\zeta r) \left(\frac{\delta \tilde{\boldsymbol{Y}}_j}{\delta t} \right) + \zeta \left(\frac{\partial \tilde{\boldsymbol{Y}}_j}{\partial t} \right)^n \right) = \underline{\boldsymbol{\mathcal{R}}_i}. \tag{3.117}$$

The nonlinear system (3.117) can be solved by a Newton procedure, where at each step the following nonlinear system is inverted

$$\sum_j \left((1-\zeta r) \underline{\mathbb{M}}^{(m)}_{ij} - \theta \delta t \underline{\mathbb{A}}^{(m)}_{ij} \right) \boldsymbol{\mathcal{X}}^{m+1}_j = \delta t \boldsymbol{\mathcal{R}}_i \left(\tilde{\boldsymbol{Y}}^{(m)} \right) + \zeta \delta t \sum_j \underline{\mathbb{M}}^{(m)}_{ij} \left(\frac{\partial \tilde{\boldsymbol{Y}}_j}{\partial t} \right)^n, \tag{3.118}$$

where the intermediate states are defined as $\tilde{\boldsymbol{Y}}^{(m)} = \tilde{\boldsymbol{Y}}^n + \boldsymbol{\mathcal{X}}^m$. The initial value of the Newton procedure is seto to zero, i.e., $\boldsymbol{\mathcal{X}}^0 = 0$ and the Jacobian of the right hand

side is $\underline{\mathbb{A}}_{ij}(\tilde{\boldsymbol{Y}}) = \frac{\partial \boldsymbol{\mathcal{R}}_i}{\partial \boldsymbol{Y}_j}(\tilde{\boldsymbol{Y}})$, so that $\underline{\mathbb{A}}_{ij}^{(m)} = \underline{\mathbb{A}}_{ij}\left(\tilde{\boldsymbol{Y}}^{(m)}\right)$. Similarly, $\underline{\mathbb{M}}_{ij}^{(m)} = \underline{\mathbb{M}}_{ij}\left(\tilde{\boldsymbol{Y}}^{(m)}\right)$. In the Newton procedure, the state $\tilde{\boldsymbol{Y}}^{n+1}$ is defined as the limit, when it exists, of the sequence $\boldsymbol{\mathcal{X}}^m$. In practice though, a truncation at a step M is used

$$\tilde{\boldsymbol{Y}}^{n+1} = \boldsymbol{\mathcal{X}}^M. \tag{3.119}$$

In principle, M is a dynamic parameter that is chosen in order to ensure that, for a given norm, the error $\left|\left|\boldsymbol{\mathcal{X}}^M - \lim_{m\to\infty} \boldsymbol{\mathcal{X}}^m\right|\right|$ is small. The linearized implicit scheme always assume that $\tilde{\boldsymbol{Y}}^{n+1} = \boldsymbol{\mathcal{X}}^1$. Thus,

$$\sum_j \left((1-\zeta r)\underline{\mathbb{M}}_{ij}^n - \theta\delta t \underline{\mathbb{A}}_{ij}^n\right)\delta\tilde{\boldsymbol{Y}} = \delta t \boldsymbol{\mathcal{R}}_i\left(\tilde{\boldsymbol{Y}}^n\right) + \zeta\delta t \sum_j \underline{\mathbb{M}}_{ij}^n \left(\frac{\partial \tilde{\boldsymbol{Y}}_j}{\partial t}\right)^n. \tag{3.120}$$

Accordingly to the decomposition of the RHS, the Jacobian is

$$\widehat{\underline{\mathbb{A}}}_{ij} = \frac{\partial \widehat{\boldsymbol{\mathcal{R}}}_i}{\partial \boldsymbol{Y}_j} = \widehat{\underline{\mathbb{A}}}^{00}_{i_{2D}j_{2D}} C_{i_\phi} C_{j_\phi} + \widehat{\underline{\mathbb{A}}}^{01}_{i_{2D}j_{2D}} C_{i_\phi}\partial_\phi C_{j_\phi} + \widehat{\underline{\mathbb{A}}}^{10}_{i_{2D}j_{2D}} \partial_\phi C_{i_\phi} C_{j_\phi} + \widehat{\underline{\mathbb{A}}}^{11}_{i_{2D}j_{2D}} \partial_\phi C_{i_\phi}\partial_\phi C_{j_\phi}, \tag{3.121}$$

where

$$\begin{aligned}
\widehat{\underline{\mathbb{A}}}^{00}_{i_{2D}j_{2D}} &= \frac{\partial \widehat{\underline{\boldsymbol{\mathcal{R}}}}^{(00)}_{i_{2D}}}{\partial(\tilde{\boldsymbol{Y}}_j C_{j_\phi})}, & \widehat{\underline{\mathbb{A}}}^{01}_{i_{2D}j_{2D}} &= \frac{\partial \widehat{\underline{\boldsymbol{\mathcal{R}}}}^{(01)}_{i_{2D}}}{\partial(\tilde{\boldsymbol{Y}}_j C_{j_\phi})}, \\
\widehat{\underline{\mathbb{A}}}^{10}_{i_{2D}j_{2D}} &= \frac{\partial \widehat{\underline{\boldsymbol{\mathcal{R}}}}^{(10)}_{i_{2D}}}{\partial(\tilde{\boldsymbol{Y}}_j \partial_\phi C_{j_\phi})}, & \widehat{\underline{\mathbb{A}}}^{11}_{i_{2D}j_{2D}} &= \frac{\partial \widehat{\underline{\boldsymbol{\mathcal{R}}}}^{(11)}_{i_{2D}}}{\partial(\tilde{\boldsymbol{Y}}_j \partial_\phi C_{j_\phi})}.
\end{aligned} \tag{3.122}$$

Therefore

$$\begin{aligned}
\underline{\mathbb{A}}_{ij} = &\int_0^{2\pi}\left(\int_{\Omega_{2D}} \widehat{\underline{\mathbb{A}}}^{00}_{i_{2D}j_{2D}} R d\boldsymbol{\xi}\right) C_{i_\phi} C_{j_\phi} d\phi + \int_0^{2\pi}\left(\int_{\Omega_{2D}} \widehat{\underline{\mathbb{A}}}^{01}_{i_{2D}j_{2D}} R d\boldsymbol{\xi}\right) C_{i_\phi}\partial_\phi C_{j_\phi} d\phi \\
&+ \int_0^{2\pi}\left(\int_{\Omega_{2D}} \widehat{\underline{\mathbb{A}}}^{10}_{i_{2D}j_{2D}} R d\boldsymbol{\xi}\right) \partial_\phi C_{i_\phi} C_{j_\phi} d\phi + \int_0^{2\pi}\left(\int_{\Omega_{2D}} \widehat{\underline{\mathbb{A}}}^{11}_{i_{2D}j_{2D}} R d\boldsymbol{\xi}\right) \partial_\phi C_{i_\phi}\partial_\phi C_{j_\phi} d\phi.
\end{aligned}$$

Now, coming back to the expression (3.115) it is possible to write a RHS associated to a poloidal element $\boldsymbol{e}_{2D}$ as follows

$$\underline{\boldsymbol{\mathcal{R}}}_i^{\boldsymbol{e}_{2D}} \equiv \underline{\boldsymbol{\mathcal{R}}}_i^{\boldsymbol{e}_{2D}}(\tilde{\boldsymbol{Y}}) = \int_0^{2\pi}\left(\int_{\Omega_{2D}} \widehat{\underline{\boldsymbol{\mathcal{R}}}}^{(0)}_{i_{2D}} R d\boldsymbol{\xi}\right) C_{i_\phi} d\phi + \int_0^{2\pi}\left(\int_{\Omega_{2D}} \widehat{\underline{\boldsymbol{\mathcal{R}}}}^{(1)}_{i_{2D}} R d\boldsymbol{\xi}\right) \partial_\phi C_{i_\phi} d\phi. \tag{3.123}$$

The integrals related to the $2D$ poloidal elements are numerically evaluated via Gauss quadrature formulas while the toroidal part can be evaluated either by a Riemann sum with equidistant toroidal angles ϕ_p or by Discrete Fourier Transform (DFT). When

Riemann sum is used, we obtain

$$\underline{\boldsymbol{R}}_i = \frac{2\pi}{N_p}\sum_{p=1}^{N_p}\underline{\widehat{\boldsymbol{\mathcal{R}}}}^{(0)}_{i_{2D},p}C_{i_\phi,p} + \frac{2\pi}{N_p}\sum_{p=1}^{N_p}\underline{\widehat{\boldsymbol{\mathcal{R}}}}^{(1)}_{i_{2D},p}\partial_\phi C_{i_\phi,p}, \tag{3.124}$$

with $\phi_p = \frac{2(p-1)\pi}{N_p}$. The integration on the poloidal element use a reference square element $\hat{\boldsymbol{e}}$ as described in Section (3.2.4.7). Thus,

$$\begin{aligned}\underline{\widehat{\boldsymbol{\mathcal{R}}}}^{(k)}_{i_{2D},p} &= \int_{\boldsymbol{e}_{2D}}\underline{\widehat{\boldsymbol{\mathcal{R}}}}^{(k)}_{i_{2D}}(\boldsymbol{\xi},\phi_p)Rd\boldsymbol{\xi} = \int_{\hat{\boldsymbol{e}}}\underline{\widehat{\boldsymbol{\mathcal{R}}}}^{(k)}_{i_{2D}}(\boldsymbol{\xi}(\boldsymbol{\zeta}),\phi_p)R(\boldsymbol{\zeta})\mathcal{J}_{\boldsymbol{e}_{2D}}(\boldsymbol{\zeta})d\boldsymbol{\zeta}\\ &\approx \sum_{\boldsymbol{g}_{2D}}^{N_{\boldsymbol{g}_{2D}}}\omega_{\boldsymbol{g}_{2D}}\mathcal{J}_{\boldsymbol{g}_{2D}}R_{\boldsymbol{g}_{2D}}\underline{\widehat{\boldsymbol{\mathcal{R}}}}^{(k)}_{i_{2D}}(\boldsymbol{\zeta}_{\boldsymbol{g}_{2D}},\phi_p),\end{aligned} \tag{3.125}$$

where $\boldsymbol{g}_{2D}$ is the Gaussian weigth and $\boldsymbol{\zeta}_{\boldsymbol{g}_{2D}}$ the associated samplig points. The Jacobian os the mapping $\mathcal{J}_{\boldsymbol{e}_{2D}}$ is

$$\mathcal{J}_{\boldsymbol{e}_{2D}} = \partial_s R\partial_t Z - \partial_t R\partial_s Z. \tag{3.126}$$

Using Discrete Fourier Transform to assembly the system

In the context of Fourier decomposition, to speed up the computation, one can use the Discrete Fourier Transform (DFT). Before describing the method, let us consider a context of *sine/cosine* functions for $C_{i_\phi}(\phi)$, where $1 \leq i_\phi \leq N_\phi$ because a relation can be obtained that will be used in the estimation of the RHS and Jacobians using DFT. Let be

$$C_1(\phi) = 1, \quad C_{2m}(\phi) = cos(m\phi), \quad C_{2m+1}(\phi) = sin(m\phi), \quad \forall m > 0, \tag{3.127}$$

then,

$$C_{2m}(\phi) - iC_{2m+1}(\phi) = e^{-im\phi}. \tag{3.128}$$

Indeed, one can write

$$\underline{\boldsymbol{\mathcal{R}}}^{(k)}_{i_{2D},2m} - i\underline{\boldsymbol{\mathcal{R}}}^{(k)}_{i_{2D},2m+1} = (-im)^k\int_0^{2\pi}\underline{\widehat{\boldsymbol{\mathcal{R}}}}^{(k)}_{i_{2D}}(\phi)e^{-im\phi}d\phi. \tag{3.129}$$

Now, the DFT can be used to estimate the integral. The input is a set of reals stored as

$$\underline{\widehat{\boldsymbol{\mathcal{R}}}}^{(k)}_{i_{2D},1},\cdots,\underline{\widehat{\boldsymbol{\mathcal{R}}}}^{(k)}_{i_{2D},p},\cdots,\underline{\widehat{\boldsymbol{\mathcal{R}}}}^{(k)}_{i_{2D},N_p}. \tag{3.130}$$

The output of the Real-to-complex DFT is a set of complexes

$$Z_0^{(k)}, \cdots, Z_m^{(k)}, \cdots, Z_{\frac{N_p+1}{2}-1}^{(k)}, \tag{3.131}$$

where the number of integration points N_p is greater than the number of toroidal test functions N_ϕ. The output of the DFT is an approximation of

$$Z_m^{(k)} \approx \int_0^{2\pi} \underline{\widehat{\boldsymbol{\mathcal{R}}}}_{i_{2D}}^{(k)}(\phi) e^{-im\phi} d\phi, \tag{3.132}$$

thus

$$\underline{\boldsymbol{\mathcal{R}}}_{i_{2D},2m}^{(k)} - i\underline{\boldsymbol{\mathcal{R}}}_{i_{2D},2m+1}^{(k)} = (-im)^k Z_m^{(k)}. \tag{3.133}$$

Putting it in a different way

$$\begin{aligned} \underline{\boldsymbol{\mathcal{R}}}_{i_{2D},1}^{(k)} &= \boldsymbol{RE}\left((-i0)^k Z_0^{(k)}\right), \\ \underline{\boldsymbol{\mathcal{R}}}_{i_{2D},2m}^{(k)} &= \boldsymbol{RE}\left((-im)^k Z_m^{(k)}\right), \\ \underline{\boldsymbol{\mathcal{R}}}_{i_{2D},2m+1}^{(k)} &= -\boldsymbol{IM}\left((-im)^k Z_m^{(k)}\right), \end{aligned} \tag{3.134}$$

this is true for all m such that $0 < m < \frac{N_\phi+1}{2}$. $\boldsymbol{RE}$ and $\boldsymbol{IM}$ stand for the real and imaginary part of the result.

Only the first modes of the DFT are retained to avoid aliasing phenomena when dealing with non-linearities. More explicitly coefficients are shown in Appendix B.

The same strategy shown here can be applied to evaluate the different coefficients of the Jacobian

$$\begin{aligned} \underline{\mathbb{A}}_{ij} = &\int_0^{2\pi} \underline{\widehat{\mathbb{A}}}_{i_{2D}j_{2D}}^{00} C_{i_\phi} C_{j_\phi} d\phi + \int_0^{2\pi} \underline{\widehat{\mathbb{A}}}_{i_{2D}j_{2D}}^{01} C_{i_\phi} \partial_\phi C_{j_\phi} d\phi \\ &+ \int_0^{2\pi} \underline{\widehat{\mathbb{A}}}_{i_{2D}j_{2D}}^{10} \partial_\phi C_{i_\phi} C_{j_\phi} d\phi + \int_0^{2\pi} \underline{\widehat{\mathbb{A}}}_{i_{2D}j_{2D}}^{11} \partial_\phi C_{i_\phi} \partial_\phi C_{j_\phi} d\phi. \end{aligned}$$

Taking the evaluation of

$$\underline{\mathbb{A}}_{ij}^{kl} = \int_0^{2\pi} \underline{\widehat{\mathbb{A}}}_{i_{2D}j_{2D}}^{kl}(\phi) \partial_\phi^k C_{i_\phi} \partial_\phi^k C_{j_\phi} d\phi, \tag{3.135}$$

with an input

$$\underline{\widehat{\mathbb{A}}}_{i_{2D}j_{2D}}^{kl}(\phi_1), \cdots, \underline{\widehat{\mathbb{A}}}_{i_{2D}j_{2D}}^{kl}(\phi_{N_p}). \tag{3.136}$$

The output is then a set of complexes

$$Z_0^{(kl)}, \cdots, Z_m^{(kl)}, \cdots, Z_{\frac{N_p+1}{2}-1}^{(kl)} \quad \text{where} \quad Z_m^{(kl)} \approx \int_0^{2\pi} \underline{\widehat{\mathbb{A}}}_{i_{2D}j_{2D}}^{kl}(\phi) e^{-im\phi} d\phi. \tag{3.137}$$

On the other hand

$$\begin{aligned}
\underline{\mathbb{A}}^{kl}_{2m,2n} &= \int_0^{2\pi} \underline{\widehat{\mathbb{A}}}^{kl}_{i_{2D}j_{2D}}(\phi)\partial^k_\phi cos(m\phi)\partial^l_\phi cos(n\phi)d\phi,\\
\underline{\mathbb{A}}^{kl}_{2m+1,2n} &= \int_0^{2\pi} \underline{\widehat{\mathbb{A}}}^{kl}_{i_{2D}j_{2D}}(\phi)\partial^k_\phi sin(m\phi)\partial^l_\phi cos(n\phi)d\phi,\\
\underline{\mathbb{A}}^{kl}_{2m,2n+1} &= \int_0^{2\pi} \underline{\widehat{\mathbb{A}}}^{kl}_{i_{2D}j_{2D}}(\phi)\partial^k_\phi cos(m\phi)\partial^l_\phi sin(n\phi)d\phi,\\
\underline{\mathbb{A}}^{kl}_{2m+1,2n+1} &= \int_0^{2\pi} \underline{\widehat{\mathbb{A}}}^{kl}_{i_{2D}j_{2D}}(\phi)\partial^k_\phi sin(m\phi)\partial^l_\phi sin(n\phi)d\phi,
\end{aligned}$$

Therefore

$$\left\{\begin{aligned}
\underline{\mathbb{A}}^{kl}_{2m,2n} - \underline{\mathbb{A}}^{kl}_{2m+1,2n+1} - i(\underline{\mathbb{A}}^{kl}_{2m,2n+1} + \underline{\mathbb{A}}^{kl}_{2m+1,2n}) &= (-i)^{k+l}m^k n^l Z^{(kl)}_{m+n}\\
\underline{\mathbb{A}}^{kl}_{2m,2n} + \underline{\mathbb{A}}^{kl}_{2m+1,2n+1} + i(\underline{\mathbb{A}}^{kl}_{2m,2n+1} - \underline{\mathbb{A}}^{kl}_{2m+1,2n}) &= i^{k+l}(-1)^k m^k n^l Z^{(kl)}_{m-n}\\
\underline{\mathbb{A}}^{kl}_{2m,2n} + \underline{\mathbb{A}}^{kl}_{2m+1,2n+1} - i(\underline{\mathbb{A}}^{kl}_{2m,2n+1} - \underline{\mathbb{A}}^{kl}_{2m+1,2n}) &= i^{k+l}(-1)^l m^k n^l Z^{(kl)}_{n-m}
\end{aligned}\right. \tag{3.138}$$

Only the first equation and one of the two seconds, depending if $m \geq n$ or $m < n$, are retained. Again, more explicit coefficients are shown in Appendix B.

To conclude, the degenerated cases must be treated. The first one is the case in which $i_\phi = 1$ and $j_\phi > 1$. Hence, as $i = (i_{2D}, 1)$ and $C_1 = 1$

$$\underline{\mathbb{A}}_{ij} = \int_0^{2\pi} \underline{\widehat{\mathbb{A}}}^{0l}_{i_{2D}j_{2D}}(\phi)C_{j_\phi}d\phi + \int_0^{2\pi} \underline{\widehat{\mathbb{A}}}^{01}_{i_{2D}j_{2D}}(\phi)\partial_\phi C_{j_\phi}d\phi, \tag{3.139}$$

with

$$\underline{\mathbb{A}}^{0l}_{1,j_\phi} = \int_0^{2\pi} \underline{\widehat{\mathbb{A}}}^{00}_{i_{2D}j_{2D}}(\phi)\partial^l_\phi C_{j_\phi}d\phi. \tag{3.140}$$

Then, for $n > 1$ the following relation can be derived

$$\underline{\mathbb{A}}^{0l}_{1,2n} + i\underline{\mathbb{A}}^{0l}_{1,2n+1} = (-in)^l \int_0^{2\pi} \underline{\widehat{\mathbb{A}}}^{0l}_{i_{2D}j_{2D}}(\phi)e^{-in\phi}d\phi = (-in)^l Z^{0l}_n. \tag{3.141}$$

A similar decomposition holds for the case in which $i_\phi > 1$ and $j_\phi = 1$, yielding for $m > 1$

$$\underline{\mathbb{A}}^{k0}_{2m,1} + i\underline{\mathbb{A}}^{k0}_{2m+1,1} = (-im)^k \int_0^{2\pi} \underline{\widehat{\mathbb{A}}}^{k0}_{i_{2D}j_{2D}}(\phi)e^{-im\phi}d\phi = (-im)^k Z^{k0}_m. \tag{3.142}$$

Finally, when $i_\phi = \jmath_\phi = 1$

$$\underline{\mathbb{A}}_{ij} = Z^{00}_0. \tag{3.143}$$

As before, more explicit coefficients for the degenerated cases can be found in Appendix B.

Evaluating the boundary integrals

To evaluate the boundary integrals we need an estimation of the normal in the physical space. Such a boundary can be parametrized either by the reference coordinate s or t. When it is parametrized with the coordinate s, for example, we obtain

$$R_{l_{2D}}(s) = \sum_{j\in\vartheta(l_{2D})} R_j \mathcal{N}_j(s,t^\star) \text{ and } Z_{l_{2D}}(s) = \sum_{j\in\vartheta(l_{2D})} Z_j \mathcal{N}_j(s,t^\star),$$

where $l_{2D} = \partial \boldsymbol{e}_{2D} \cap \partial\Omega_{2D} \neq \emptyset$, is used for any curved edge at the physical boundary associated to the element $\boldsymbol{e}_{2D}$. In this case $t = t^\star$ where $t^\star$ is either zero or one. Thus, any infinitesimal length dl associated to the boundary, is written as

$$dl = \sqrt{(dR(s))^2 + (dZ(s))^2} = \left(\sqrt{\partial_s R)^2 + (\partial_s Z)^2}\right) ds, \tag{3.144}$$

which yields the Jacobian of the transformation $\mathcal{J}_l(s) = \sqrt{\partial_s R)^2 + (\partial_s Z)^2}$. Therefore, for any function $\boldsymbol{\Psi}$, the boundary integral is

$$\begin{aligned} \int_{\partial\Omega_{x,h}} \boldsymbol{\Psi}(\boldsymbol{Y}) &= \int_0^{2\pi} R d\phi \int_{\partial\Omega_{x,h}} \boldsymbol{\Psi}(\boldsymbol{Y}) dl = \int_0^{2\pi} \sum_{l_{2D}} \int_0^1 R_{l_{2D}}(s) \mathcal{J}_{l_{2D}}(s) \boldsymbol{\Psi}(\boldsymbol{Y}) ds \\ &\approx \sum_{g_\phi}^{N_{g_\phi}} \frac{2\pi}{N_{g_\phi}} \sum_{l_{2D}} \sum_{g_s=1}^{N_{g_s}} \omega_{g_s} R_{l_{2D}}(s_{g_s}) \mathcal{J}_{l_{2D}}(S_{g_s}) \boldsymbol{\Psi}(\boldsymbol{Y}(s_{g_s})). \end{aligned} \tag{3.145}$$

Most of the integrals computed are linear functions of the outward normal $\boldsymbol{n}$. In the case of the parametrization with s, the associated poloidal coordinate is given by

$$\boldsymbol{\xi}(s) = R_{l_{2D}}(s)\hat{\boldsymbol{R}} + Z_{l_{2D}}(s)\hat{\boldsymbol{Z}}. \tag{3.146}$$

Thus, the tangent vector $\partial_s \boldsymbol{\xi}$ and the unit normal are orthogonal yielding

$$\boldsymbol{n} = n_R \hat{\boldsymbol{R}} + n_Z \hat{\boldsymbol{Z}} = \pm \frac{\partial_s Z_{l_{2D}} \hat{\boldsymbol{Z}} - \partial_s R_{l_{2D}} \hat{\boldsymbol{R}}}{\mathcal{J}_l} = \frac{1}{\mathcal{J}_l} \tilde{\boldsymbol{n}}. \tag{3.147}$$

The sign of the normal is fixed be the orientation of the reference axis used for the boundary mapping. For example, the sign is positive when the boundary mapped with s corresponds to $t^\star = 0$; and negative for $t^\star = 1$. Therefore, any linear surface integral

to the outward normal can be reformulated as

$$\begin{aligned}\int_{\partial\Omega_{x,h}}(\underline{\boldsymbol{L}}(\underline{\boldsymbol{Y}})\boldsymbol{n}) &= \int_0^{2\pi}\sum_{l_{2D}}\int_0^1 R_{l_{2D}}(s)\mathcal{J}_{l_{2D}}(s)(\underline{\boldsymbol{L}}(\underline{\boldsymbol{Y}})\boldsymbol{n})ds \\ &\approx \sum_{g_\phi}^{N_{g_\phi}}\frac{2\pi}{N_{g_\phi}}\sum_{l_{2D}}\sum_{g_s=1}^{N_{g_s}}\omega_{g_s}R_{l_{2D}}(s_{g_s})\mathcal{J}_{l_{2D}}(S_{g_s})(\underline{\boldsymbol{L}}(\underline{\boldsymbol{Y}}(s_{g_s}))\tilde{\boldsymbol{n}}(s_{g_s})).\end{aligned} \tag{3.148}$$

Similar formulas hold when the parametrization is defined with the reference coordinate t.

3.3 Conclusions

This chapter started with the discussion of the finite element formalism used to solve several problems numerically. The general model problem has given an idea of the procedure and the nuances of this type of scheme, specially the Galerkin formulation. This was, however a very general description of the method.

Once the scheme had been discussed, a special characteristic of this kind of discretization method was introduced: the need of stabilization. In fact, FEM (and central finite difference, for example) always lead to central flux approximations that are numerically unstable. The simple $1D$ convection-diffusion equation has shown that. Therefore, a stabilization strategy must always follow the finite element method.

In this chapter, the Variational Multi-Scale (VMS) strategy was derived in order to be applied to our MHD model. As usual for the stabilization strategies, a term is added to the weak formulation to ensure the stability of the method. For that, an evaluation of the fine scale was done such that the weak form of the system could be modified to achieve an stable scheme. This lead to an approximation of the stabilization term, since its formal definition leads to the inversion of a matrix that might not be diagonalizable, containing a parameter known as stabilization matrix. Nevertheless, up to today there is no general definition for this parameter. Thus, some options were discussed here. Also, the way in which the divergence free condition discussed in the previous chapter could be overcome numerically was shown in more details.

To finish, the whole detailed numerical strategy was described, going from the interpolation of the conservative variables in order to avoid singularity problems, passing through the spatial and temporal discretization of the system using a special type of finite element, called Bézier elements. It is important to describe the details of the Bézier formalism because the way in which the discrete system will be assembled is related to the formalism behind it. The stabilization term as well as the divergence free constraint

were already included in the numerical scheme. The method for solving the resultant integrals numerically has been described and, finally, the boundary conditions and the way to implement them have been also discussed.

All the ingredients necessary to solve the MHD models are set. From now on, results obtained using the models and the strategy developed here will be shown.

Chapter 4

Tokamak Equilibrium

Axis-symmetric equilibria are at the basis of the analysis of instabilities and transport phenomena in tokamaks. The Grad-Shafranov equilibrium, in particular, is a very powerful concept when dealing with magnetohydrodynamic simulations. In fact, it can be used as an initial equilibrium configuration for different MHD models, e.g., Reduced or Full MHD. The idea is to use this equilibrium to provide the initial conditions of different simulations. Once it is obtained, the system can be perturbed in such a way as to develop the desired physical instabilities one wants to study.

Nevertheless, solving the Grad-Shafranov equation and connecting it with the MHD model is not as trivial as it appears to be. Indeed, as the equation is solved under the Galerkin formulation, some details concerning the approximated spaces of the finite element technique have to be considered carefully. The main goal at first, is to obtain initial conditions that are stable enough as to keep the plasma in its original configuration when no perturbations or flows ($\boldsymbol{v} = 0$) are added. It means that the transition between the numerical solution of the equilibrium and the data used as initial conditions of the MHD system must generate the less amount of numerical noise as possible.

In this Chapter we describe in details the formulation used to solve the Grad-Shafranov Equilibrium (4.1) and how it can be used to build the grids necessary for the numerical analysis of the MHD models (4.1.3). A detailed discussion of the characteristics of the grids is also presented. Finally, the effects of the numerical formulation of the GS equation and the impacts it can have on the initial conditions, based on the results obtained, are discussed (4.1.4).

4.1 Grad Shafranov Equilibrium

In order to compute MHD instabilities in tokamak geometries, we very often start with an initial condition that is a solution of the static MHD equilibrium without flow, i.e., $\boldsymbol{v} = 0$. This equilibrium is given by the Grad-Shafranov equation derived in Chapter 2 (Section (2.2.4.1)). The equation is

$$\Delta^* \psi = -R^2 \frac{dp}{d\psi} - F \frac{dF}{d\psi}. \tag{4.1}$$

At this point the functions $p(\psi)$ and $F(\psi)$ are completely arbitrary and should be defined from additional considerations associated to device under concern. When these functions are nonlinear, there is no theoretical guarantee of the existence and/or uniqueness of the previous equation, even when equipped with Dirichlet boundary conditions.

4.1.1 Input profiles of p and F

The idea is then to design these functions from a fitting over experimental data hoping that, in that case, a solution for this equation could be found. The fitting assumes polynomial profiles for the density and the temperature leading thus to a profile for the pressure. Also, a profile is fitted for $F^2(\psi)$, the reason for using the square is that it makes it easier to obtain the term $F\frac{dF}{d\psi}$ used in the Grad-Shafranov equation. By doing $F^2(\psi) = \tilde{G}(\psi)$, the profiles are defined as

$$\begin{aligned}
\tilde{\rho}(\psi, \psi_\star, \psi_\times) &\approx \tilde{\rho}^{(0)} \left(1 + \sum_{s=1}^{s_p} \tilde{\rho}^{(s)} \overline{\psi}^s \right), \\
\tilde{T}(\psi, \psi_\star, \psi_\times) &\approx \tilde{T}^{(0)} \left(1 + \sum_{s=1}^{s_p} \tilde{T}^{(s)} \overline{\psi}^s \right), \\
\tilde{G}(\psi, \psi_\star, \psi_\times) &\approx \tilde{G}^{(0)} + 2(\psi_\times - \psi_\star) \sum_{s=1}^{s_f} \tilde{G}^{(s)} \frac{\overline{\psi}^s}{s},
\end{aligned} \tag{4.2}$$

where $\tilde{\rho}^{(s)}$, $\tilde{T}^{(s)}$ and $\tilde{G}^{(s)}$ are fitting parameters. The normalized magnetic flux $\overline{\psi}$ is defined as

$$\overline{\psi} \equiv \overline{\psi}(\psi) = \frac{\psi - \psi_\star}{\psi_\times - \psi_\star}, \tag{4.3}$$

where $\psi_\star$ and $\psi_\times$ are given values of the poloidal flux at the magnetic axis and at a specific flux surface (to be chosen), respectively. This specific flux surface can be a separatrix, in the case of X-point plasmas or the last closed magnetic surface for limiter plasmas. From the equation of state $p = \rho T$ and the profile $\tilde{G}(\psi)$, we obtain the following

estimations

$$\begin{aligned}
\frac{dp(\psi)}{d\psi} &\approx \left(\frac{d\tilde{\rho}}{d\psi}\right)\tilde{T} + \tilde{\rho}\left(\frac{d\tilde{T}}{d\psi}\right) \approx \frac{1}{\psi_\times - \psi_\star}\left(\left(\frac{\partial\tilde{\rho}}{\partial\overline{\psi}}\right)\tilde{T} + \tilde{\rho}\left(\frac{\partial\tilde{T}}{\partial\overline{\psi}}\right)\right), \\
F(\psi)\frac{dF(\psi)}{d\psi} &\approx \frac{1}{2}\frac{\partial\tilde{G}}{\partial\psi} \approx \frac{1}{2(\psi_\times - \psi_\star)}\frac{\partial\tilde{G}}{\partial\overline{\psi}} = \sum_{s=1}^{s_f}\tilde{G}^{(s)}\overline{\psi}^{s-1},
\end{aligned} \tag{4.4}$$

where the partial derivative is evaluated for fixed $\psi_\star$ and $\psi_\times$.

4.1.2 Solving the GS equation

The Galerkin finite element method is used to approximate the Grad-Shafranov equation. The weak form of (4.1) is then

$$-\int_{\Omega_{2D}}\left(\frac{1}{R^2}\Delta^*\psi\right)\psi^\star RdRdZ = \int_{\Omega_{2D}}\left(\frac{FF'}{R^2} + p'\right)\psi^\star RdRdZ, \tag{4.5}$$

where $\psi^\star \in \Omega_{2D}$ is a test function, $F' = \frac{dF}{d\psi}$ and $p' = \frac{dp}{d\psi}$. Equation (4.5) can be rewritten more explicitly as

$$-\int_{\Omega_{2D}}\left(\nabla\cdot\left(\frac{1}{R}\nabla\psi\right)\right)\psi^\star dRdZ = \int_{\Omega_{2D}}\left(\frac{FF'}{R} + Rp'\right)\psi^\star dRdZ. \tag{4.6}$$

In order to reduce the derivative order of the LHS an integration by parts is performed, yielding

$$\int_{\Omega_{2D}}\left(\frac{1}{R}\nabla\psi\right)\cdot\nabla\psi^\star dRdz = \int_{\Omega_{2D}}\frac{1}{R}\left(FF' + R^2p'\right)\psi^\star dRdZ + \cancelto{0}{\int_{\Gamma_{2D}}\frac{\psi^\star}{R}\nabla\psi\cdot\boldsymbol{\tilde{n}}dRdz}. \tag{4.7}$$

The last term on the RHS is considered to be zero because homogeneous Dirichlet boundary conditions are used. This non-linear system is solved by Picard iterations, by inverting the following linear system for $\psi^{(k+1)}$

$$\int_{\Omega_{2D}}\frac{1}{R}\nabla\psi^{(k+1)}\cdot\nabla\psi^\star dRdZ = \int_{\Omega_{2D}}\frac{1}{R}\left(F(\psi^{(k)})\frac{dF(\psi^{(k)})}{d\psi} + R^2\frac{dp(\psi^{(k)})}{d\psi}\right)\psi^\star dRdZ. \tag{4.8}$$

The quantities $\psi_\star^{(k+1)} \equiv \psi_\star(\psi^{(k+1)})$, and $\psi_\times^{(k+1)} \equiv \psi_\times(\psi^{(k+1)})$ are computed at each step. When the Picard iterations converge, which is always the case for our applications, an approximated solution ψ^{eq} of the Grad Shafranov equation is obtained.

Very often, when solving numerically the MHD models for tokamak plasmas, it is useful to have a grid that is aligned with the flux surfaces. Hence, the Grad-Shafranov equilibrium can be used to build this grid, since it is solved for ψ which is constant over a given flux surface.

4.1.3 Building the Grid

In order to build a proper grid aligned with the flux surfaces, a new parameter must be given as an input to the Grad-Shafranov equation: the flux contour. This paramater is defined by two properties which are the geometrical form of the poloidal contour and the value of ψ on it. If limiter plasmas (near circular) are considered, the value of ψ might be constant over the entire contour. Nevertheless, if X-point plasmas are considered it can be more complicated. This contour will give the boundary of the computational domain and it will be used to generate an initial unaligned grid on which the equilibrium will be computed. To determine the form of the contour, the following parametrization is considered

$$R = \begin{cases} cos(\theta + \mathbb{T}_u sin(\theta) + \mathbb{Q}_u sin(2\theta)), & 0 \leq \theta < \pi, \\ cos(\theta + \mathbb{T}_l sin(\theta) + \mathbb{Q}_l sin(2\theta)), & \pi \leq \theta < 2\pi, \end{cases} \tag{4.9}$$

$$Z = \mathbb{E} sin(\theta), \tag{4.10}$$

where $\mathbb{T}_{u/l}$ and $\mathbb{Q}_{u/l}$ are the plasma upper/lower triangularities and quadrangularities, respectively; and $\mathbb{E}$ is the plasma ellipticity. These parameters may be varied to modify the final geometry of ψ that will be solved by the Grad-Shafranov equation. The poloidal angle θ is the angle seen from the geometric center. The value of ψ on this contour, for the more complex cases, is given by a function related to characteristics of the problem under investigation.

Once the domain is defined with these parameters, the equilibrium is then solved and a first ψ^{eq} is found. This value is then used to rebuild the grid that will be aligned with the flux surfaces this time. Figure (4.1) shows both grids (unaligned and aligned) for both configurations: limiter and X-point.

The construction of the aligned grid for the limiter case is relatively simple and direct. Nevertheless, this is not the case when dealing with X-point plasmas and the grid must be built step by step. The flux aligned construction will be described here when ψ^{eq} have a single saddle point, i.e., the X-point having coordinates $\boldsymbol{\xi} = \boldsymbol{\xi}_\times$ and value $\psi = \psi_\times$; and a single extremum, i.e., the magnetic axis with $\boldsymbol{\xi} = \boldsymbol{\xi}_c$ and $\psi = \psi_c$. We assume that $\psi_c < \psi_\times$, that the magnetic axis and the saddle point are not at the boundary of the

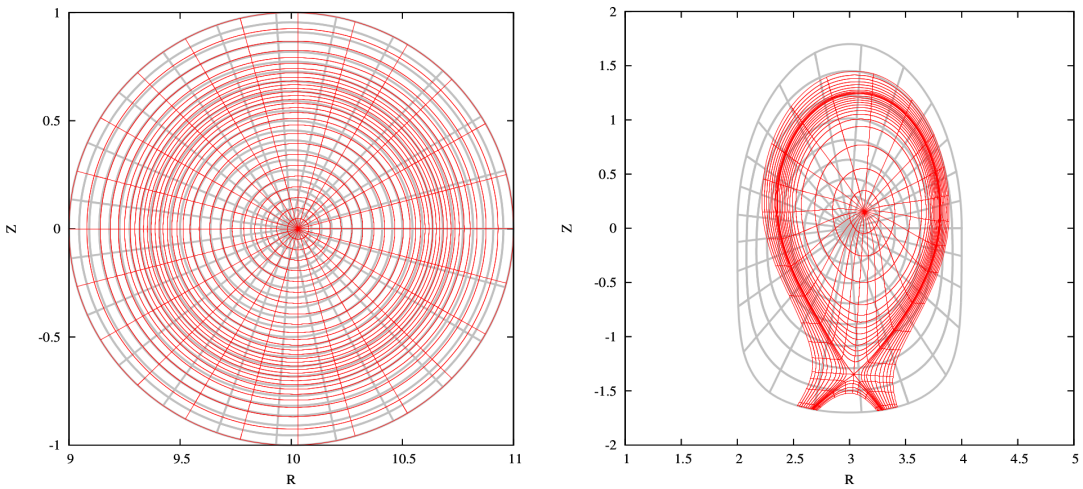

FIGURE 4.1: Unaligned meshes (grey) and aligned ones (red) for both, limiter and divertor, configurations.

domain and that the surface associated to the saddle point (the separatrix) cross the divertor plates at two different points $\boldsymbol{\xi}_\times^l$ and $\boldsymbol{\xi}_\times^r$.

In this way, the separatrix can be decomposed as a closed curve $\mathcal{S}(\boldsymbol{\xi}_\times, \boldsymbol{\xi}_\times)$, and two smooth curves $\mathcal{S}(\boldsymbol{\xi}_\times, \boldsymbol{\xi}_\times^l)$ and $\mathcal{S}(\boldsymbol{\xi}_\times, \boldsymbol{\xi}_\times^r)$ connecting $\boldsymbol{\xi}_\times$ to $\boldsymbol{\xi}_\times^l$ and to $\boldsymbol{\xi}_\times^r$, respectively. Moreover, there exists a value ψ_b greater than $\psi_\times$ such that the associated flux surface is a smooth curve $\mathcal{S}(\boldsymbol{\xi}_b^l, \boldsymbol{\xi}_b^r)$, where $\boldsymbol{\xi}_b^l$ and $\boldsymbol{\xi}_b^r$ are on the divertor plates. Similarly, there is a ψ_b smaller than $\psi_\times$ that is used for the construction of an isoline curve $\mathcal{S}(\boldsymbol{\xi}_p^l, \boldsymbol{\xi}_p^r)$, where $\boldsymbol{\xi}_p^l$ and $\boldsymbol{\xi}_p^r$ are also on the divertor plates. All these coordinate points can be seen in Figure (4.2).

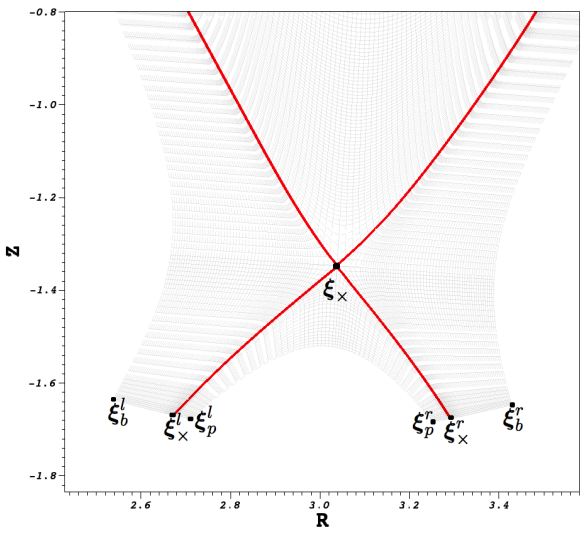

FIGURE 4.2: Coordinate points used to define the boundaries of the different domains of the plasma

There are also lines associated to divertor plates, denoted by $\mathcal{D}(\boldsymbol{\xi}_b^l, \boldsymbol{\xi}_\times^l)$, $\mathcal{D}(\boldsymbol{\xi}_\times^l, \boldsymbol{\xi}_p^l)$, $\mathcal{D}(\boldsymbol{\xi}_b^r, \boldsymbol{\xi}_\times^r)$ and $\mathcal{D}(\boldsymbol{\xi}_\times^r, \boldsymbol{\xi}_p^r)$. It is important to highlight that these considerations are natural properties of the flux ψ associated to the plasma equilibrium in tokamaks. The entire domain is then divided into three sub-domains Ω_c, Ω_s and Ω_p of the physical space associated, respectively to the plasma core, the Scrape-Off Layer and the private region. The boundary of these sub-domains are defined as

$$\begin{aligned}
\partial\Omega_c &= \mathcal{S}(\boldsymbol{\xi}_\times, \boldsymbol{\xi}_\times), \\
\partial\Omega_s &= \mathcal{S}(\boldsymbol{\xi}_\times^l, \boldsymbol{\xi}_\times) \cup \mathcal{S}(\boldsymbol{\xi}_\times, \boldsymbol{\xi}_\times) \cup \mathcal{S}(\boldsymbol{\xi}_\times, \boldsymbol{\xi}_\times^r) \cup \mathcal{D}(\boldsymbol{\xi}_\times^r, \boldsymbol{\xi}_b^r) \cup \mathcal{S}(\boldsymbol{\xi}_b^r, \boldsymbol{\xi}_b^l) \cup \mathcal{D}(\boldsymbol{\xi}_b^l, \boldsymbol{\xi}_\times^l), \\
\partial\Omega_p &= \mathcal{S}(\boldsymbol{\xi}_\times^l, \boldsymbol{\xi}_\times) \cup \mathcal{S}(\boldsymbol{\xi}_\times, \boldsymbol{\xi}_\times^r) \cup \mathcal{D}(\boldsymbol{\xi}_\times^r, \boldsymbol{\xi}_p^r) \cup \mathcal{S}(\boldsymbol{\xi}_p^r, \boldsymbol{\xi}_p^l) \cup \mathcal{D}(\boldsymbol{\xi}_p^l, \boldsymbol{\xi}_\times^l).
\end{aligned}$$

These sub-domains can be seen in Figure (4.3) in which the red line represents the separatrix.

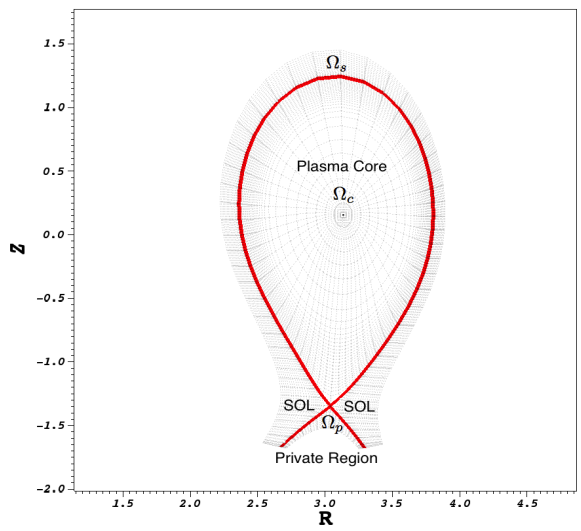

FIGURE 4.3: Scheme with the differente domains of the plasma. The red line represents the separatrix wich is defined as $\mathcal{S}^{sep} = \mathcal{S}(\boldsymbol{\xi}_\times^l, \boldsymbol{\xi}_\times) \cup \mathcal{S}(\boldsymbol{\xi}_\times, \boldsymbol{\xi}_\times) \cup \mathcal{S}(\boldsymbol{\xi}_\times, \boldsymbol{\xi}_\times^r)$

The subdomain Ω_c of the plasma core can be recovered by a polar mapping centered at $\boldsymbol{\xi}_c$. The sub-domains Ω_p and Ω_s, on the other hand, can be obtained by curved mappings of a originally rectangular domain.

Mapping the plasma core

A set of values $\psi_{c,k}$ associated to the plasma core is defined such that

$$\psi_c < \psi_{c,2} < \cdots < \psi c, k < \psi_{c,k+1} < \cdots \psi_{c,K_c-1} < \psi_\times. \tag{4.11}$$

Then, $\mathcal{S}_{c,k}$, for $k = 2, \cdots, K_c - 1$, are isolines curves of the plasma core associated to the values $\psi_{c,k}$. Moreover, there are $\mathcal{S}_{c,1}$ associated to the magnetic axis and $\mathcal{S}_{c,K_c} = \mathcal{S}(\boldsymbol{\xi}_\times, \boldsymbol{\xi}_\times)$. Now, let us consider the following distribution of angles

$$\theta_1 = 0 < \theta_2 < \cdots < \theta_m < \theta_{m+1} < \theta_{M_c} < 2\pi, \tag{4.12}$$

and a set of half-lines $\mathcal{T}_{c,m}$, $m = 1, \cdots, M_c$ associated to the plasma center $\boldsymbol{\xi}_c$ and the angle θ_m. By convention the half-line $\mathcal{T}_{c,1}$ contains the saddle point $\boldsymbol{\xi}_\times$. Intersections of $\mathcal{S}_{c,k}$ and $\mathcal{T}_{c,m}$ are then used to derive an iso-parametric representation that gives a quadrangular meshing of the plasma core, aligned with the flux surfaces.

Mapping the private region

Similarly to the core, a set of values $\psi_{p,k}$ is defined such as

$$\psi_p < \psi_{p,2} < \cdots < \psi p, k < \psi_{p,k+1} < \cdots \psi_{p,K_p-1} < \psi_\times. \tag{4.13}$$

Then, $\mathcal{S}_{p,k}$, for $k = 2, \cdots, K_p - 1$, are curves of the private region associated to the values $\psi_{p,k}$. The curves $\mathcal{S}_{p,1}$ and $\mathcal{S}_{p,K_p}$ are defined as

$$\mathcal{S}_{p,1} \equiv \mathcal{S}(\boldsymbol{\xi}_p^l, \boldsymbol{\xi}_p^r) \quad \text{and} \quad \mathcal{S}_{p,K_p} \equiv \mathcal{S}(\boldsymbol{\xi}_\times^l, \boldsymbol{\xi}_\times) \cup \mathcal{S}(\boldsymbol{\xi}_\times, \boldsymbol{\xi}_\times^r). \tag{4.14}$$

Let us consider a clockwise oriented distribution of $2M_p + 1$ points on the curve $\mathcal{S}_{p,1}$ and also on the curve $\mathcal{S}_{p,K_p}$ such that the distributions contain the points $\boldsymbol{\xi}_\times^l$, $\boldsymbol{\xi}_\times$, $\boldsymbol{\xi}_\times^r$, $\boldsymbol{\xi}_p^l$ and $\boldsymbol{\xi}_p^r$. The lines connecting the points belonging to $\mathcal{S}_{p,1}$ and the ones belonging $\mathcal{S}_{p,K_p}$ will give the quandrangular meshing of this region. One extra assumption made is that the distribution of the curve $\mathcal{S}_{p,1}$ is such that the line coming from $\boldsymbol{\xi}_\times$ is at the middle of this curve.

Mapping the SOL

Again, associated to the SOL, a set of values $\psi_{s,k}$ is defined such as

$$\psi_\times < \psi_{s,2} < \cdots < \psi s, k < \psi_{s,k+1} < \cdots \psi_{s,K_s-1} < \psi_b. \tag{4.15}$$

Then, $\mathcal{S}_{s,k}$, for $k = 2, \cdots, K_s - 1$, are curves of the private region associated to the values $\psi_{s,k}$. The curves $\mathcal{S}_{s,1}$ and $\mathcal{S}_{p,K_s}$ are defined as

$$\mathcal{S}_{s,1} \equiv \mathcal{S}(\boldsymbol{\xi}_\times^l, \boldsymbol{\xi}_\times) \cup \mathcal{S}(\boldsymbol{\xi}_\times, \boldsymbol{\xi}_\times) \cup \mathcal{S}(\boldsymbol{\xi}_\times, \boldsymbol{\xi}_\times^r) \quad \text{and} \quad \mathcal{S}_{p,K_s} \equiv \mathcal{S}(\boldsymbol{\xi}_b^l, \boldsymbol{\xi}_b^r). \tag{4.16}$$

As the divertor targets are a conformal mesh, the points distribution on the curves $\mathcal{S}(\boldsymbol{\xi}^l_\times, \boldsymbol{\xi}_\times)$, $\mathcal{S}(\boldsymbol{\xi}_\times, \boldsymbol{\xi}_\times)$ and $\mathcal{S}(\boldsymbol{\xi}_\times, \boldsymbol{\xi}^r_\times)$ should coincide between the patches. Therefore, by using the already defined distribution of points on $\mathcal{S}_{s,1}$ with the duplication of the saddle point. Thus, the total number of points on this curve is $M_s = M_c + 2M_p + 1$. With this predefined distribution on $\mathcal{S}_{s,1}$ we can design an appropriated distribution of M_s points on all the other curves $\mathcal{S}_{s,k}$, for $k > 1$.

Finally, by construction the three sub-domains can be joined without generating singularities or discontinuities everywhere, except at the saddle point. The coordinates of this point are shared by four frames, the core, the SOL (2 frames) and the private region were merged there. This discontinuity and the singularity at the axis must be treated carefully.

4.1.3.1 Grid discontinuities

Looking at both the grids, the X-point one shown in Figure (4.4 (left)), and the circular one shown in Figure (4.5) it is clear that the grids present singularity problems. The magnetic axis for both grids and the X-point as well for the X-point grid. As it can be seen, more than four elements are meeting at those points, hence, a particular treatment must be done.

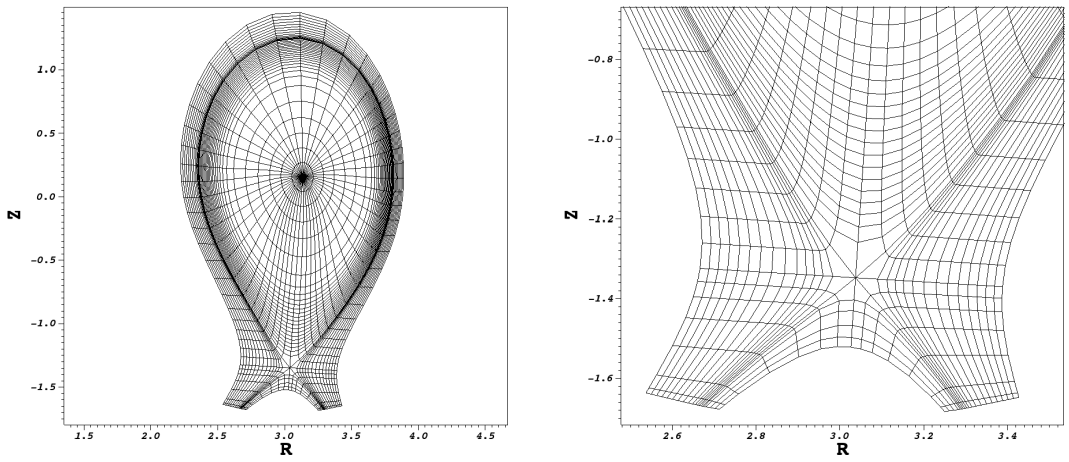

FIGURE 4.4: Example of a X-point grid (left) with the detail of the separation between two regions below and above the X-point (right)

For the magnetic axis, the strategy chosen consists in considering this point not as a node but an infinitesimally small circle such that all the nodes in it are the corner of two surfaces. This is a palliative solution though because when the radius of the circle tends to zero and we are dealing with vector quantities, it becomes very problematic (more details will be given below).

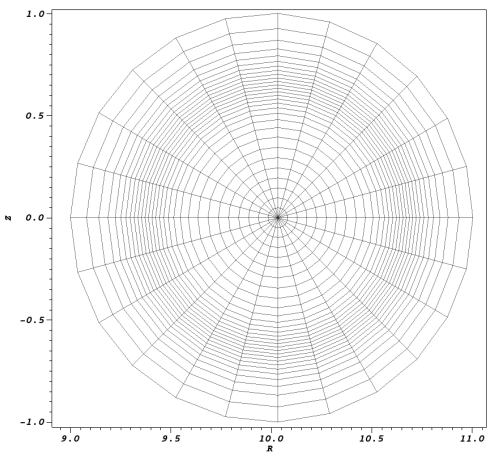

FIGURE 4.5: Example of an aligned circular grid

For the X-point, this strategy is not valid because ψ has a saddle point at this place causing the circle method to yield five nodes elements, which is not possible. Therefore, the continuity at the X-point is only partially satisfied for the derivatives.

4.1.4 Establishing the equilibrium

After using the Grad-Shafranov equation to build a grid aligned with the flux surfaces, an equilibrium must be calculated to be used as the initial condition for the simulations. Indeed, this equilibrium is established again by the Grad-Shfranov equation using the same procedure as before with the difference that the ψ used for the input profiles now is the ψ^{eq} used to build the grid. After solving the equation, a second ψ^{eq} is obtained which will be the flux potential used to initialize the simulation, i.e, $\psi^{(0)}$.

It is important however to discuss before how this equilibrium is achieved and how it can affect the simulation. In fact, theoretically, if the simulation is started from a static equilibrium without flow as the one given by the Grad-Shafranov equation and no perturabation is applied, the plasma is supposed to stay in equilibrium since there will be no forces acting on it. This is due to the fact that, in the case where $\boldsymbol{v} = 0$, the moment equation is reduced to

$$0 = \boldsymbol{J}^{(0)} \times \boldsymbol{B}^{(0)} - \nabla p^{(0)}. \tag{4.17}$$

Taking the field coming from the GS equation as $\boldsymbol{B}^{(0)} = F(\psi^{(0)})\nabla\phi + \nabla\psi^{(0)} \times \nabla\phi$ yields

$$\boldsymbol{J}^{(0)} = -\Delta^*\psi^{(0)}\nabla\phi + \nabla F(\psi^{(0)}) \times \nabla\phi = -\Delta^*\psi^{(0)}\nabla\phi + \frac{\partial F}{\partial \psi^{(0)}}\nabla\psi^{(0)} \times \nabla\phi, \tag{4.18}$$

leading to

$$\boldsymbol{J}^{(0)} \times \boldsymbol{B}^{(0)} = -\frac{1}{R^2}\left(\Delta^*\psi^{(0)} + F(\psi^{(0)})\frac{\partial F}{\partial \psi^{(0)}}\right)\nabla\psi^{(0)}. \tag{4.19}$$

Moreover,

$$\nabla p^{(0)} = \frac{\partial p^{(0)}}{\partial \psi^{(0)}}\nabla\psi^{(0)}. \tag{4.20}$$

Finally, the residual of the momentum equation is

$$\overline{\mathcal{R}}^{\boldsymbol{m}} = \frac{1}{R^2}\left(\Delta^*\psi^{(0)} + R^2\frac{\partial p^{(0)}}{\partial \psi^{(0)}} + F(\psi^{(0)})\frac{\partial F}{\partial \psi^{(0)}}\right)\nabla\psi^{(0)}, \tag{4.21}$$

which is, analytically equals to zero since the terms between brackets are equivalent to the Grad-Shafranov equation.

The problem though is that all the equations here are solved under a Finite Element formulation, which means that only their weak forms are solved. It is important then to look at these residuals through the point of view of the weak form. Let's define the residual of the Grad Shafranov equation in its weak form as $\overline{\mathcal{R}}_i^{GS}$

$$\overline{\mathcal{R}}_i^{GS} = \frac{1}{a_i}\int_{\Omega_{2D}}\left(\Delta^*\psi^{(0)} + R^2\frac{\partial p^{(0)}}{\partial \psi^{(0)}} + F(\psi^{(0)})\frac{\partial F}{\partial \psi^{(0)}}\right)\mathcal{N}_i R dR dZ, \tag{4.22}$$

where a_i is the surface area of the element.

Similarly, the momentum equation residual can be written as

$$\overline{\mathcal{R}}_i^{\boldsymbol{m}} = \frac{1}{a_i}\int_{\Omega_{2D}}\frac{1}{R^2}\left(\Delta^*\psi^{(0)} + R^2\frac{\partial p^{(0)}}{\partial \psi^{(0)}} + F(\psi^{(0)})\frac{\partial F}{\partial \psi^{(0)}}\right)\nabla\psi^{(0)}\mathcal{N}_i R dR dZ. \tag{4.23}$$

As it can be seen, the weak formulation leads to two main differences between these two residuals. The first one is the factor $\frac{1}{R^2}$, which in principle is not supposed to be a problem since the terms insde the brackets are supposed to be zero. For the weak form however, a stop criterion ϵ was chosen for the numerical solution of the system, this means that at the equilibirum the residual is supposed to be $\overline{\mathcal{R}}_i^{GS} \approx \epsilon$. The absolute value of this residual is shown in Figure (4.6) for the circular case (left) and X-point case (right). They were both obtained for $\epsilon = 10^{-7}$.

There are however perturbations in the results and the details can be seen in Figure (4.7) for the circular case. The perturbation at the magnetic axis is $\approx 10^{-8} < \epsilon$ which is pretty reasonable, meaning that at the beginning of the simulations, at least, it can be neglected.

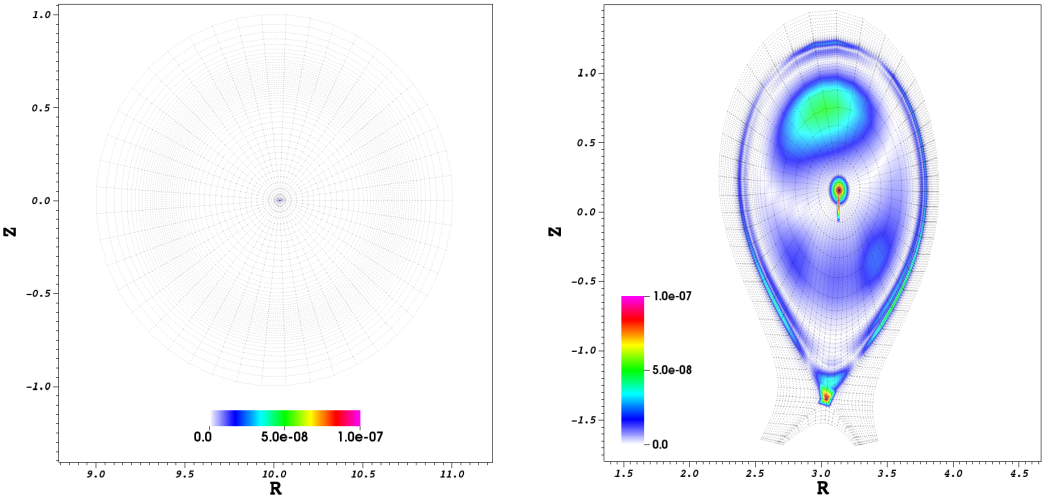

FIGURE 4.6: Residual of the Grad-Shafranov equation $\overline{\mathcal{R}}_i^{GS}$ over the domain for two different grids. A polar grid (left) and a X-point one (right). They were obtained for stop criterion $\epsilon = 10^{-7}$. Around the singularities, however this value can go up to 10^{-3} for the X-point grid. This can be seen in more details in Figures (4.7) and (4.8)

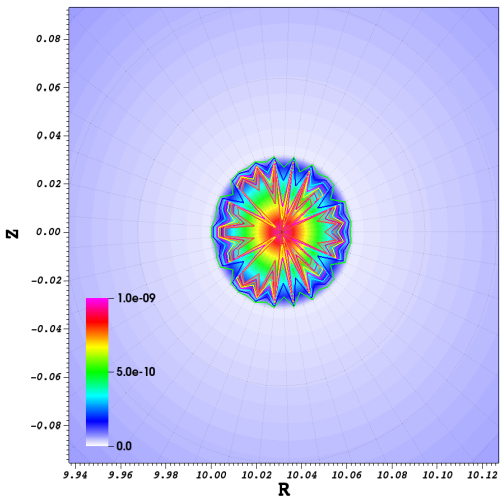

FIGURE 4.7: Perturbation of the residual of the GS equation at the magnetic axis. Its maximum value is $\approx 10^{-8} < \epsilon$

For the X-point though (Figure (4.8)), this is more delicate and the reason is twofold. First, there is not only one but two delicate points, the axis and the X-point and the perturbations at these regions reach a value of $\approx 10^{-3}$ which is four orders of magnitude greater than the convergence criterion.

For the momentum equation residual however there is a $\nabla\psi^{(0)}$ that can cause problems. In fact, this residual can be written as $\overline{\mathcal{R}}_i^{\boldsymbol{m}} \approx \frac{1}{R^2}\epsilon\nabla\psi^{(0)}$. Well, when neither ϵ nor $\nabla\psi^{(0)}$ tend to zero, there is absolutely no reason for $\overline{\mathcal{R}}_i^{\boldsymbol{m}}$ to be zero. Figure (4.9) shows the values of $\nabla\psi^{(0)}$ over the domain and it can be clearly seen that it is not negligible

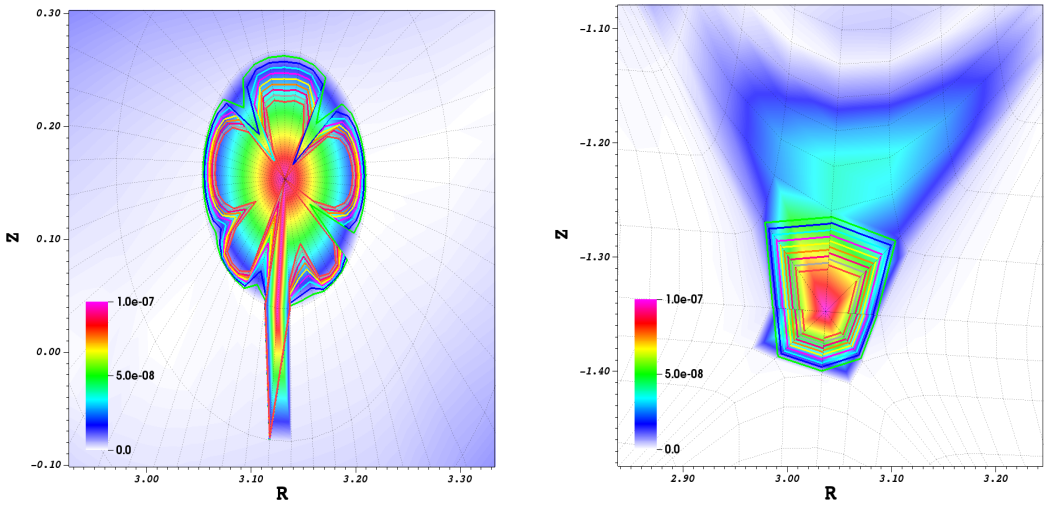

FIGURE 4.8: Perturbations of the equilibrium related ot the singularities of the grid: one at the magnetic axis (left) and one at the X-point (right). Their maximum residual is $\approx 10^{-3}$.

which means that it affects the residual of the momentum equation. It is important to highlight though that at the sensitive point - the axis and the X-point - the values of the gradient are very small compared to other regions. Hopefully, this characteristic will act in such a way to reduce the perturbations around these regions.

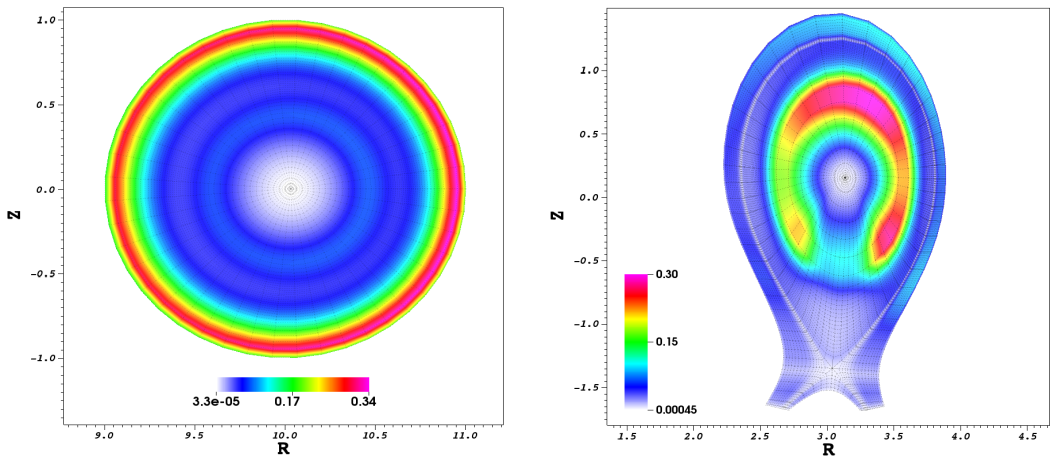

FIGURE 4.9: The norm of $\nabla\psi^{(0)}$ for both grids: poloidal (left) and X-point (right)

This residual, $\overline{\mathcal{R}}_i^{\boldsymbol{m}}$, was obtained and is shown in Figure (4.10). It is clear that it does not correspond exactly to $\overline{\mathcal{R}}_i^{GS}$ and the effect of $\nabla\psi^{(0)}$ can be clearly seen. Indeed, around the axis, the perturbation was considerably attenuated, except for a particular region of the X-point mesh.

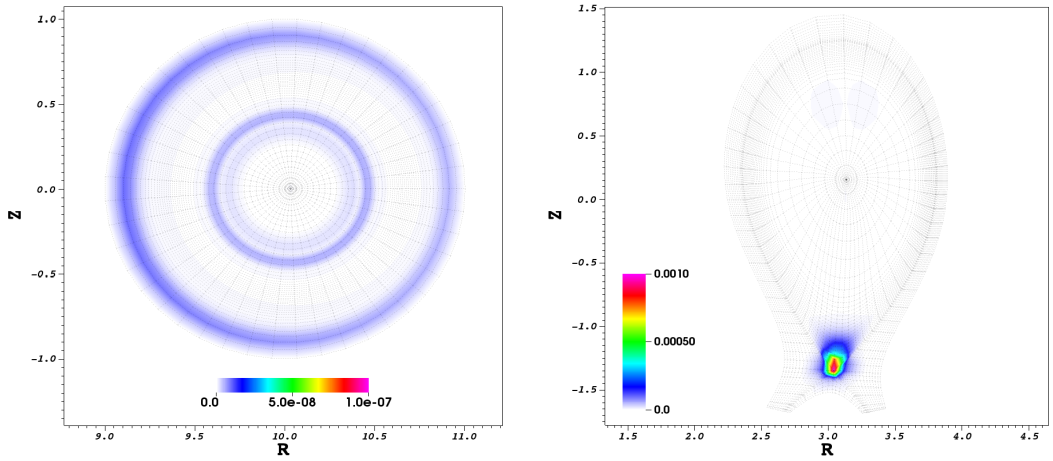

FIGURE 4.10: Residual od the momentum equation, $\overline{\mathcal{R}}_i^{\boldsymbol{m}}$, for the poloidal (left) and X-point grids (right). The difference from the previous residual can be clearly seen. The perturbations, however were attenuated, for the poloidal case it is $\approx 10^{-9}$ and for the X-point case $\approx 5.10^{-4}$

In the end, these differences between $\overline{\mathcal{R}}_i^{GS}$ and $\overline{\mathcal{R}}_i^{\boldsymbol{m}}$ create a numerical perturbation since one cannot be sure that the equilibrium conditions established before will be fulfilled during the evolution of the MHD equations. For the poloidal cases (limiter configuration) the order of magnitude of the perturbations can be completely neglected at the beginning since its maximum value is still smaller than the convergence criterion chosen. It means that simulations in this case are more numerically stable. For the X-point (divertor configuration), on the other hand, the same cannot be said. As the perturbation can go up to $\approx 10^{-4}$, it can be problematic to the simulations. For some of the test cases it may be negligible vis-à-vis the velocity fields developed when then simulation is run but the only way to be sure is by analyzing carefully the residuals before running the code.

In fact, there are no sure and definitive ways to avoid these problems and it has been shown that they can interfere in the evolution of the MHD instability if they are not treated (Details in Chapter 5). For the magnetic axis however, some palliative techniques (in addition to the infinitesimal circle described above) have been used to improve the evolution of the equations. The strategy consists in restraining the derivatives of the variables on the nodes belonging to the infinitesimal circle. It has to be done because the derivatives ∂_R and ∂_Z for any variable are related, in this context, to directional derivatives following either the direction s or t described in Section (3.2.4.7). A representation of these orientations on the nodes is shown in Figure (4.11)

The problem is that the radius of the circle is supposed to tend to zero meaning that these points altogether converge to only one and, in this case, the scheme becomes inconsistent at this point because it has derivatives pointing in different directions at

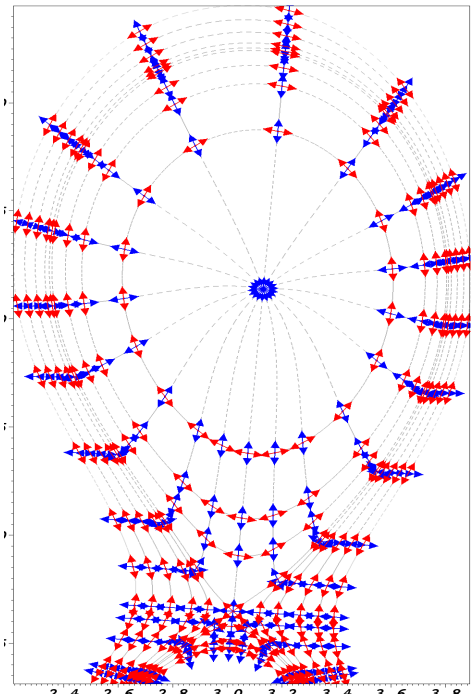

FIGURE 4.11: Orientation related to the nodes associated to the global mesh

the same node. This conflict of directions can be seen in Figure (4.12) for both regions, the center (left) and X-point (right).

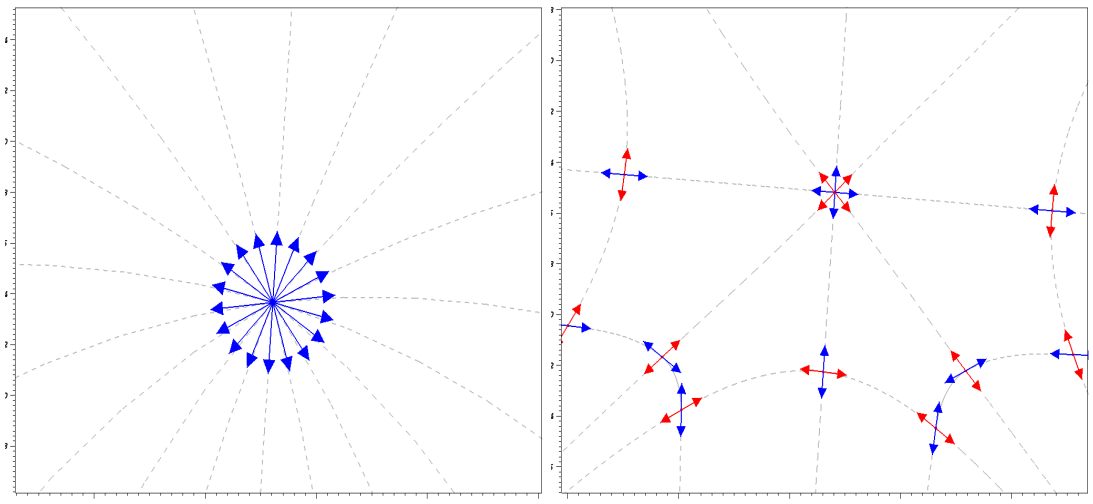

FIGURE 4.12: Orientations related to the particular points of the grid: the magnetic axis (left) and the X-point (right)

In fact, at the X-point, four different frames of reference (Figure (4.13)) are put together, one from the private region domain Ω_p, one from the plasma core Ω_c and two from the Scrape-Off Layer (SOL) Ω_s. This is a result of the construction of the grid itself. As the entire domain must be separated to be constructed, at some point they must be put together in order to generate the grid for the calculations. As a result, the X-point node

has 16 degrees of freedom per scalar variable and that is what it is hard to deal with the discontinuity at this point. It is an unavoidable characteristic of the grid.

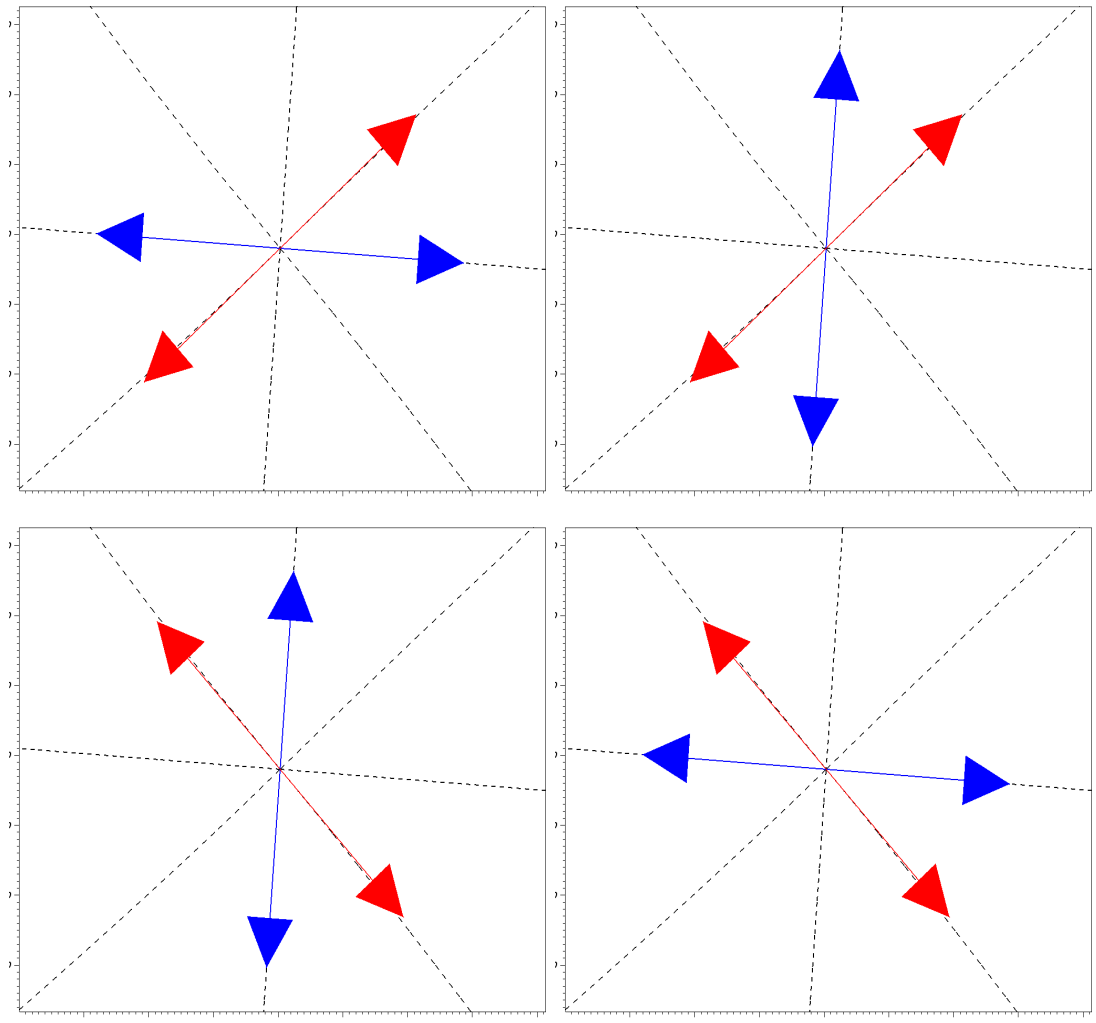

FIGURE 4.13: Four different frames meeting at the X-point. As a consequence, this node has 16 degrees of freedom per variable

If we are dealing only with scalar quantities, as it is the case for the Reduced MHD model, this is not a problem since there are no directions assigned to scalar quantities. This is not the case, unfortunately, for the full MHD model, in which the velocity and the magnetic fields are treated as actual vector fields. It is then necessary to put the derivatives to zero. The problem is that it while it improves the evolution of the plasma, it creates a perturbation on the residuals. For the limiter case, this new perturbation is still negligible ($\approx 10^{-8}$ (4.14)) allowing us to use it without further problems.

Another way to overcome this difficulty is to physically assume a hole in the middle of the plasma, i.e, enlarging the radius of the circle. This can be very useful if the phenomena one wants to study is not related to plasma flow close to the center, as it

is the case of some instabilities like the Edge-localized modes. On the other hand, the internal kink instability can be very tricky to simulate since it comprises the movement of the entire plasma column.

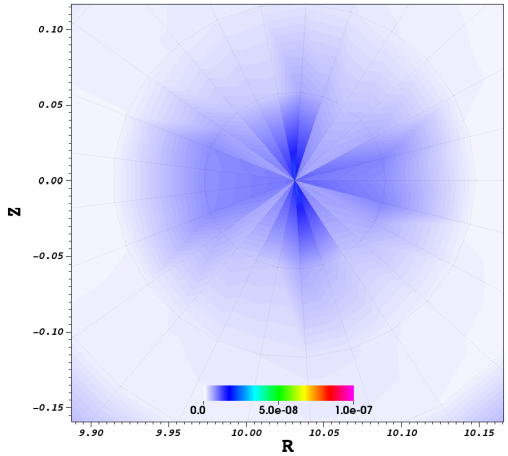

FIGURE 4.14: Perturbation around the center due to the derivatives conditions. Its maximum value is $\approx 10^{-8}$.

For the divertor configuration, though, it has problematic consequences. The effects are shown in Figure (4.15), which can be compared to Figure (4.10 (right)). The perturbation around the center has actually been increased to a value $\approx 10^{-3}$. Furthermore, for the X-point nothing can be done, as it was said before. This means that for the X-point configuration there is no way of treating these perturbations.

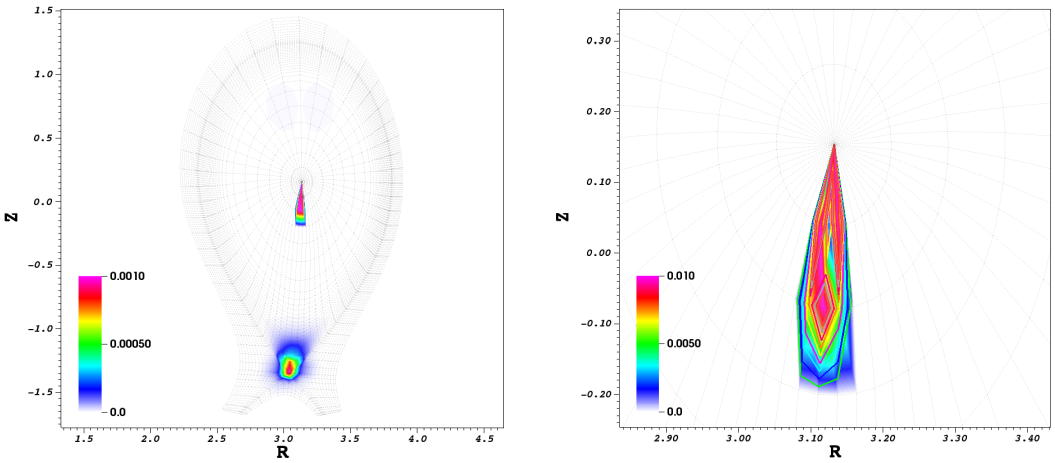

FIGURE 4.15: Residual od the momentum equation, $\overline{\mathcal{R}}_i^m$ when the derivatives of all variables on the nodes belonging to the center are fixed as zero. In this case, the perturbation value goes from $\approx 5 \times 10^{-4}$ to $\approx 10^{-3}$ as it can be seen in the detail (right)

4.2 Initializing the simulations

After establishing the equilibrium form the Grad-Shafranov Equation, the initial conditions of the simulations must be initialized. For that, the same input profiles (fitted experimentally) shown in Equation (4.2) are used for $\psi^{(0)}$

$$\begin{cases} \rho^{(0)} &= \tilde{\rho}(\psi^{(0)}, \psi_\star^{(0)}, \psi_\times^{(0)}), \\ T^{(0)} &= \tilde{T}(\psi^{(0)}, \psi_\star^{(0)}, \psi_\times^{(0)}), \\ p^{(0)} &= \rho^{(0)} T^{(0)}, \\ \boldsymbol{v}^{(0)} &= 0, \\ \boldsymbol{A}^{(0)} &= \psi^{(0)} \nabla \phi. \end{cases}$$

A poloidal cut of the density (left) and the potential vector (right) profiles at the equilibrium for the circular configuration are shown in Figure (4.16). The temperature profile has basically the same shape as the density one since their fitting is made in a similar fashion.

They were obtained for the following values of the input parameters, when $s_p = 1$ and $s_f = 2$

$$\begin{cases} \tilde{\rho}^{(0)} = 1, & \tilde{\rho}^{(1)} = -9 \times 10^{-1}, \\ \tilde{T}^{(0)} = 2 \times 10^{-3}, & \tilde{T}^{(1)} = -8 \times 10^{-1}, \\ \tilde{G}^{(0)} = 100, & \tilde{G}^{(1)} = 2, \quad \tilde{G}^{(2)} = -2. \end{cases} \tag{4.24}$$

Therefore, the profiles are

$$\rho^{(0)} = 1 - 9 \times 10^{-1} \left(\overline{\psi}^{(0)}\right), \tag{4.25}$$

$$T^{(0)} = 2 \times 10^{-3} - 1.6 \times 10^{-3} \left(\overline{\psi}^{(0)}\right), \tag{4.26}$$

$$p^{(0)} = 2 \times 10^{-3} - 3.4 \times 10^{-3} \left(\overline{\psi}^{(0)}\right) + 1.44 \times 10^{-3} \left(\overline{\psi}^{(0)}\right)^2, \tag{4.27}$$

where $\overline{\psi}^{(0)}$ is obtained from Equation (4.3) with $\psi = \psi^{(0)}$, $\psi_\times = 0$ and $\psi_\star = -0.4792$.

For the X-point configuration, the parameters were chose in a way that the initial profiles (Figure (4.17)) would be similar to the experimental one observed in JET. For this, the parameters were

$$\begin{cases} \tilde{\rho}^{(0)} = 9.5 \times 10^{-1}, & \tilde{\rho}^{(1)} = 2.5 \times 10^{-1}, \\ \tilde{T}^{(0)} = 1.197 \times 10^{-1}, & \tilde{T}^{(1)} = -6.67 \times 10^{-1}, \\ \tilde{G}^{(0)} = 81, & \tilde{G}^{(1)} = 4.8, \quad \tilde{G}^{(2)} = -4.8. \end{cases} \tag{4.28}$$

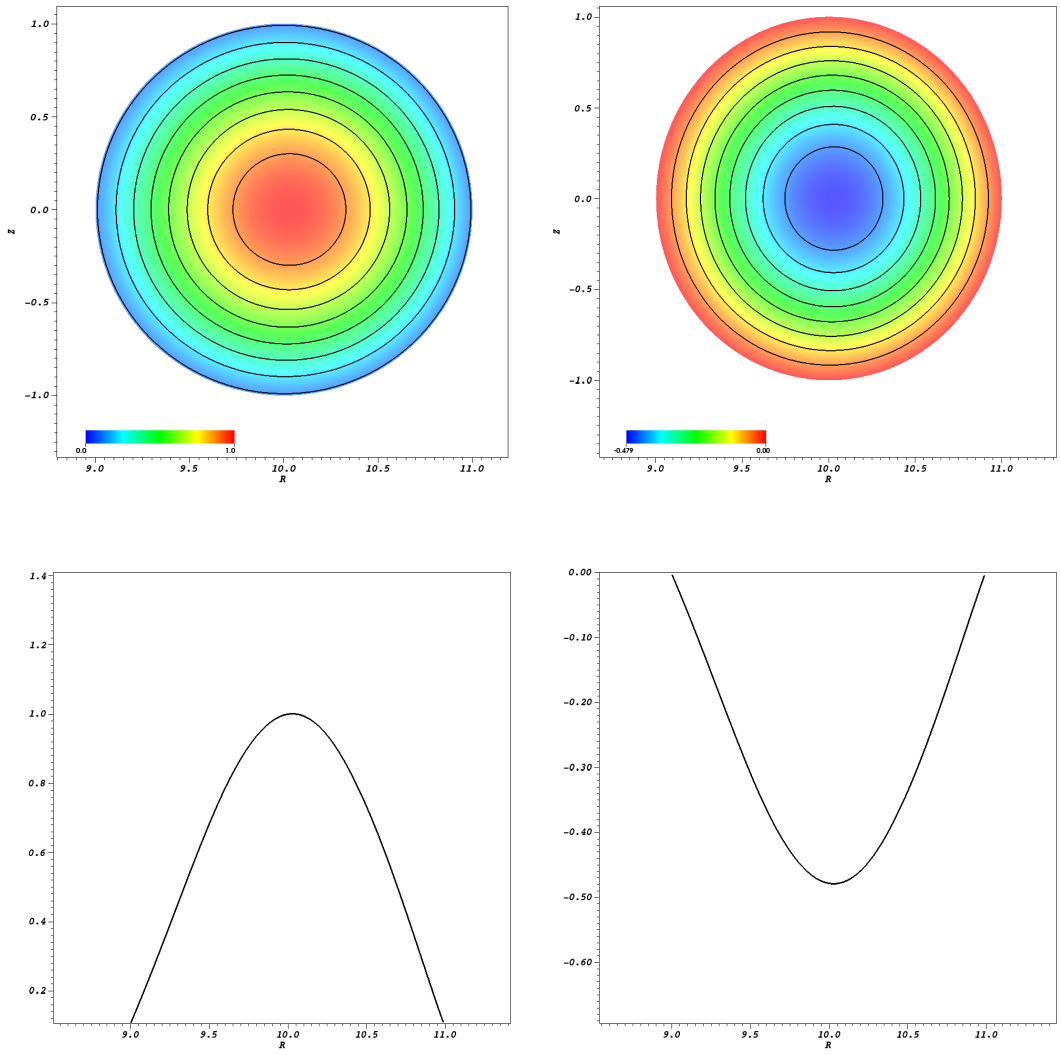

FIGURE 4.16: Density and magnetic fluw profiles used to initialize the circular plasma simulations

The profiles are

$$\rho^{(0)} = 9.5 \times 10^{-1} - 2.375 \times 10^{-1} \left(\overline{\psi}^{(0)}\right), \tag{4.29}$$

$$T^{(0)} = 1.197 \times 10^{-1} - 7.984 \times 10^{-1} \left(\overline{\psi}^{(0)}\right), \tag{4.30}$$

$$p^{(0)} \approx 1.114 \times 10^{-1} - 7.869 \times 10^{-1} \left(\overline{\psi}^{(0)}\right) + 1.869 \times 10^{-1} \left(\overline{\psi}^{(0)}\right)^2, \tag{4.31}$$

where, in this case $\overline{\psi}^{(0)}$ is obtained from Equation (4.3) with $\psi = \psi^{(0)}$, $\psi_\times = -0.4578$ and $\psi_\star = -1.2827$.

It is possible to see that the density, hence the pressure as well, has in this case a sharp gradient close to the separatrix, i.e., the pedestal region. This is related to the H-mode

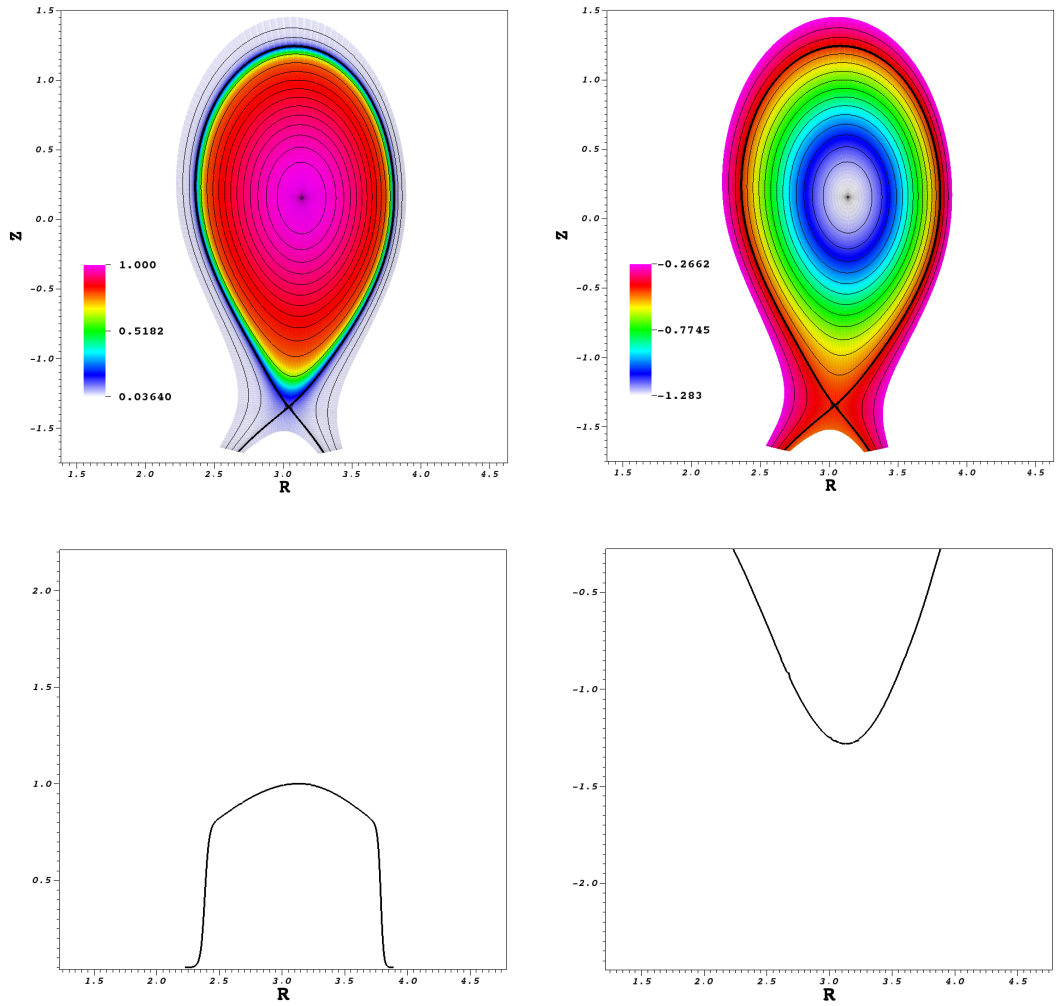

FIGURE 4.17: Density and potential flux profiles for the X-point plasma. The black lines represent the flux surfaces and the bold one, the separatrix. In the cut for the density (bottom-left), it is possible to identify the pedestal region by its sharp gradient.

of operation present when dealing with X-point plasmas. The details of this mode were shown in Chapter 1 (Section (1.3.2.3)). It is important to highlight though that, in order the reproduce the physical characteristic of the H-mode, in which the plasma density falls drastically in the SOL, these profiles must be multiplied by a cutt-off. Indeed, it is given by

$$f_i^{cut}(\overline{\psi}, \hat{\psi}, \sigma_n) = \frac{1}{2} - \frac{1}{2} tanh\left(\frac{\overline{\psi} - \hat{\psi}}{\sigma_n}\right), \tag{4.32}$$

where i stands for the function to which it must me applied, e.g., density, temperature or $F\frac{dF}{d\psi}$ (notice that, it is not applied in $\tilde{G}$ but in FF' directly); and $\hat{\psi}$ and σ_n are related

to these functions as well. For the profiles shown here, these values are

$$\tilde{\rho} \rightarrow \hat{\psi} = 0.96 \text{ and } \sigma_n = 0.06, \tag{4.33}$$

$$\tilde{T} \rightarrow \hat{\psi} = 0.96 \text{ and } \sigma_n = 0.06, \tag{4.34}$$

$$FF' \rightarrow \hat{\psi} = 1 \text{ and } \sigma_n = 0.03. \tag{4.35}$$

Furthermore, it is also necessary to ensure that no plasma is present in the private region. For that, an extra cutt-off, depending on the Z coordinate (to ensure that it will act only below the X-point) is applied

$$g_i^{cut}(Z, Z_\times, \sigma_Z) = \frac{1}{2} - \frac{1}{2} tanh\left(\frac{Z_\times - Z}{\sigma_Z}\right), \tag{4.36}$$

where $Z_\times$ is the Z coordinate of the X-point and σ_Z is

$$\tilde{\rho} \rightarrow \sigma_Z = 0.1, \tag{4.37}$$

$$\tilde{T} \rightarrow \sigma_Z = 0.05, \tag{4.38}$$

$$FF' \rightarrow \sigma_Z = 0.1. \tag{4.39}$$

In the end, the profiles for the X-point cases, are

$$\begin{cases} \rho_\times^{(0)} = \rho^{(0)} f_\rho^{cut} g_\rho^{cut}, \\ T_\times^{(0)} = T^{(0)} f_T^{cut} g_T^{cut}, \end{cases} \tag{4.40}$$

and the same is done for FF' before inserting it in the Grad-Shafranov equation.

4.3 Conclusions

This chapter has established the necessary basis for the simulations of tokamak instabilities. As it has been shown, the Grad-Shafranov equilibrium is a very important characteristic of the plasma that can be used not only to generate the initial conditions of the calculation but also the construction of a proper grid domain in which the MHD system under the Finite Element Formulation can be evaluated.

The input of the GS equation is given by fittings of the density, the temperature and the magnetic potential that are based on experimental observation that have been done inside tokamaks in operation. From that, a first evaluation is done from which a ψ^{eq} is obtained. This allows the construction of the aligned grids. It was shown however that this construction has some problems related to the characteristics of ψ^{eq} itself, e.g., the singularities related to the maximum and the saddle points of the potential flux.

For the maximum value in the magnetic axis, palliative solutions can be found that help attenuate the numerical noise at this region. For example, that fact of considering a infinitesimal circle instead of a single node. It was shown that for circular plasmas, the noise is about 10^{-8}, which is negligible. For the X-point however, the situation is more complicated. Indeed, in this case, both perturbations, the one from the axis and the one from the X-point are harder to deal with. For saddle-point, the construction of the grid itself generates an over-determination of this node since four different frames of referece are joined there. Moreover, as it is a saddle point and not a maximum or a minimum, like the axis, the infinitesimal circle technique cannot be applied. For the axis it was shown that fixing the values of the derivatives of all the scalar variables increases the noise around this area, although, it might be a solution when the evolution of the equations comprises vector quantities and the frames of the center disturb it.

For the Reduced MHD models, this discontinuity problems are not so severe because we are only dealing with scalar variables and the fact that different frames of reference join together is less critic since scalar variables have no direction. Unfortunately, this is not the case for the Full MHD model for which even the circle technique can become problematic when there is movement of the plasma around this region. In fact, when there is movement and the derivatives are forced to zero, the scheme becomes inconsistent and usually, the calculation diverges.

The effects of these initial perturbations on the simulation of plasma instabilities will be discussed in the following chapter since they will affect in some way all the simulations initialized in the way described here.

Chapter 5

MHD instabilities: Internal Kink

The behavior of dynamical systems is very often divided into two categories: stable or unstable. This division describes basically what will be the effects on the equilibrium state if small perturbations are applied to the system. If this perturbation gives rise to a force that tend to restore the equilibrium, the system is said to be in stable equilibrium. If, on the other hand, the forces pushes the system further and further from the equilibrium, it is called unstable equilibrium.

In the plasma context, instabilities can be divided into two main groups: microscopic and macroscopic. To describe the microscopic instabilities, one can use the Kinetic model since they are mainly originated by the changes on the distribution functions. These instabilities are, in general, less disruptive than the macroscopic ones which can be discussed within the framework of the MHD system. The study of turbulence is an unavoidable subject when dealing with tokamak plasmas since they can damage the confinement.

These macroscopic instabilities can be classified as pressure and current driven accordingly to the main mechanism triggering them. One example of the current-driven instabilities is the kink modes. They can be further subdivided in internal and external. Our efforts here are concentrated on the internal kink instability.

In this Chapter we start by establishing an analytic background of the main macroscopic instabilities (5.1). Then, an extensive and detailed study of the resistive internal kink instability is performed in order to validate our numerical scheme. It starts with the analysis of the characteristic growth rates of this phenomenon (5.2.1), in which the effects of the VMS stabilization strategy will be discussed (5.2.1.2). After that, different characteristics of the kink modes dynamics, e.g., dependence on the magnetic Reynolds

number, movement of the column and magnetic reconnection are shown as numerical validations of the scheme (5.2.2).

5.1 MHD instabilities: background

In Chapter 4 we have studied the equilibrium of tokamak plasmas. It is known, however, through observations that tokamak plasmas could be unstable accordingly to some of its characteristics, e.g., the pressure gradient, the ratio between the poloidal and toroidal magnetic fields, among others. In order to simulate these instabilities, a perturbation is added to the initial equilibrium and the forces created by this perturbation may lead to a growth of its amplitude, which is defined as an instability. On the other hand, when the forces due to the initial perturbation lead the system to a permanent oscillation around the equilibrium or eventually bring it back to the initial state, it is a stable case.

5.1.0.1 Stability Criterion

To explicitly study the instabilities using the MHD models, it is useful to express each variable as a decomposition containing an equilibrium part $\boldsymbol{w}_0$ and a perturbation term, $\tilde{\boldsymbol{w}}$ i,e.

$$\rho(\boldsymbol{x},t) = \rho_0(\boldsymbol{x}) + \tilde{\rho}(\boldsymbol{x},t), \tag{5.1}$$

$$\boldsymbol{v}(\boldsymbol{x},t) = \boldsymbol{v}_0(\boldsymbol{x}) + \tilde{\boldsymbol{v}}(\boldsymbol{x},t) = \tilde{\boldsymbol{v}}(\boldsymbol{x},t), \tag{5.2}$$

$$p(\boldsymbol{x},t) = p_0(\boldsymbol{x}) + \tilde{p}(\boldsymbol{x},t), \tag{5.3}$$

$$\boldsymbol{B}(\boldsymbol{x},t) = \boldsymbol{B}_0(\boldsymbol{x}) + \tilde{\boldsymbol{B}}(\boldsymbol{x},t), \tag{5.4}$$

where $\boldsymbol{x} \equiv \boldsymbol{x}(R,\phi,Z) = \boldsymbol{x}(\boldsymbol{\xi},\phi)$ and $\boldsymbol{v}_0 = 0$ because we are starting from the Grad-Shafranov equilibrium without flow. Ignoring products of the perturbations yields, to first order, the following equations

$$\partial_t\tilde{\rho} = -\tilde{\boldsymbol{v}}\cdot\nabla\rho_0 - \rho_0(\nabla\cdot\tilde{\boldsymbol{v}}), \tag{5.5}$$

$$\partial_t\tilde{\boldsymbol{v}} = -\nabla\tilde{p} + (\nabla\times\boldsymbol{B}_0)\times\tilde{\boldsymbol{B}} + (\nabla\times\tilde{\boldsymbol{B}})\times\boldsymbol{B}_0, \tag{5.6}$$

$$\partial_t\tilde{p} = -\tilde{\boldsymbol{v}}\cdot\nabla p_0 - \gamma p_0(\nabla\cdot\tilde{\boldsymbol{v}}), \tag{5.7}$$

$$\partial_t\tilde{\boldsymbol{B}} = \nabla\times(\tilde{\boldsymbol{v}}\times\boldsymbol{B}_0). \tag{5.8}$$

A close look at these equations shows that on the RHS, $\tilde{\boldsymbol{v}}$ is the only time-dependent variable. It is possible then to integrate these equations partially with respect to time. It is also convenient to choose the constants of integration such as $\tilde{\rho}(\boldsymbol{x},0) = \tilde{p}(\boldsymbol{x},0) =$

$\tilde{\boldsymbol{B}}(\boldsymbol{x},0) = 0$. It means that we start from the equilibrium and disturb it dynamically with a non-zero $\tilde{\boldsymbol{v}}(\boldsymbol{x},0)$. After the integration, the equations become

$$\tilde{\rho}(\boldsymbol{x},t) = -\boldsymbol{\varsigma}(\boldsymbol{x},t)\cdot\nabla\rho_0(\boldsymbol{x}) - \rho_0(\boldsymbol{x})(\nabla\cdot\boldsymbol{\varsigma}(\boldsymbol{x},t)), \tag{5.9}$$

$$\tilde{p}(\boldsymbol{x},t) = -\boldsymbol{\varsigma}(\boldsymbol{x},t)\cdot\nabla p_0(\boldsymbol{x}) - \gamma p_0(\boldsymbol{x})(\nabla\cdot\boldsymbol{\varsigma}(\boldsymbol{x},t)), \tag{5.10}$$

$$\tilde{\boldsymbol{B}}(\boldsymbol{x},t) = \nabla\times(\boldsymbol{\varsigma}(\boldsymbol{x},t)\times\boldsymbol{B}_0(\boldsymbol{x})), \tag{5.11}$$

where the displacement vector is defined as

$$\boldsymbol{\varsigma}(\boldsymbol{x},t) \equiv \int_0^t \tilde{\boldsymbol{v}}(\boldsymbol{x},t)dt. \tag{5.12}$$

From (5.12), $\partial_t\boldsymbol{\varsigma} = \tilde{\boldsymbol{v}}(\boldsymbol{x},t)$ such that the initial conditions on $\boldsymbol{\varsigma}$ are

$$\boldsymbol{\varsigma}(\boldsymbol{x},0) = 0 \text{ and } \partial_t\boldsymbol{\varsigma}(\boldsymbol{x},0) = \boldsymbol{v}(\boldsymbol{x},0) \neq 0 \tag{5.13}$$

Therefore, replacing (5.11) and (5.10) in (5.6) yields

$$\rho_0\frac{\partial^2\boldsymbol{\varsigma}}{\partial t^2} = \boldsymbol{F}(\boldsymbol{\varsigma}(\boldsymbol{x},t)), \tag{5.14}$$

where $\boldsymbol{F}(\boldsymbol{\varsigma}(\boldsymbol{x},t))$ is the force operator and can be written as a function of the equilibrium variables and $\boldsymbol{\varsigma}$ as

$$\boldsymbol{F}(\boldsymbol{\varsigma}) = (\nabla\times\boldsymbol{B}_0)\times\boldsymbol{Q} + (\nabla\times\boldsymbol{Q})\times\boldsymbol{B}_0 + \nabla(\boldsymbol{\varsigma}\cdot\nabla p_0 + \gamma p_0(\nabla\cdot\boldsymbol{\varsigma})), \tag{5.15}$$

in which $\boldsymbol{Q} = \nabla\times(\boldsymbol{\varsigma}\times\boldsymbol{B}_0)$.

The equilibrium configuration establishes ρ_0, p_0 and $\boldsymbol{B}_0$. Thus, Equation (5.14) together with the boundary conditions and the initial values given in (5.13) will determine the evolution of the displacement vector and therefore the evolution of the perturbations $\tilde{\rho}$, $\tilde{p}$, $\tilde{\boldsymbol{B}}$ and $\tilde{\boldsymbol{v}}$. This is the initial value stability problem.

To solve this problem, we assume that in the displacement vector the time and the space can be separated as $\boldsymbol{\varsigma}(\boldsymbol{x},t) = \boldsymbol{\varsigma}(\boldsymbol{x})T(t)$. Thus, the stability problem becomes

$$\frac{\partial^2 T}{\partial t^2} = -\omega^2 T, \tag{5.16}$$

$$-\omega^2\rho_0\boldsymbol{\varsigma}(\boldsymbol{x}) = \boldsymbol{F}(\boldsymbol{\varsigma}(\boldsymbol{x})), \tag{5.17}$$

where the separation constant is chosen to be $-\omega^2$ such that $T(t) = e^{-i\omega t}$.

Therefore, the stability problem becomes

$$-\omega^2\rho_0\boldsymbol{\varsigma}(\boldsymbol{x}) = \boldsymbol{F}(\boldsymbol{\varsigma}(\boldsymbol{x})), \tag{5.18}$$

for $\boldsymbol{\varsigma}(\boldsymbol{x},t) = \boldsymbol{\varsigma}(\boldsymbol{x})e^{-i\omega t}$. Equation (5.18) is called the normal mode eigenvalue equation.

Now, the force operator is self-adjoint [55] which means that for two arbitrary displacement vectors $\boldsymbol{\varsigma}$ and $\boldsymbol{\iota}$, the following relation holds

$$\int \boldsymbol{\varsigma}\cdot\boldsymbol{F}(\boldsymbol{\varsigma})d\boldsymbol{x} = \int \boldsymbol{\iota}\cdot\boldsymbol{F}(\boldsymbol{\iota})d\boldsymbol{x}, \tag{5.19}$$

the integration being over the plasma volume. Thus, taking the scalar product of (5.18) with $\boldsymbol{\varsigma}^*$ (the complex conjugate of $\boldsymbol{\varsigma}$) and integrating it all over the domain yields

$$-\omega^2\int \rho_0(\boldsymbol{\varsigma}\cdot\boldsymbol{\varsigma}^*)d\boldsymbol{x} = \int \boldsymbol{F}(\boldsymbol{\varsigma})\cdot\boldsymbol{\varsigma}^* d\boldsymbol{x}. \tag{5.20}$$

If, on the other hand, we consider the complex conjugate of (5.18) and take the scalar product with $\boldsymbol{\varsigma}$, we obtain

$$-(\omega^*)^2\int \rho_0(\boldsymbol{\varsigma}^*\cdot\boldsymbol{\varsigma})d\boldsymbol{x} = \int \boldsymbol{F}(\boldsymbol{\varsigma}^*)\cdot\boldsymbol{\varsigma})d\boldsymbol{x}. \tag{5.21}$$

Finally, subtracting (5.20) from (5.21) yields

$$(\omega^2-(\omega^*)^2)\int \rho_0|\boldsymbol{\varsigma}^2|d\boldsymbol{x} = \int(\boldsymbol{F}(\boldsymbol{\varsigma}^*)\cdot\boldsymbol{\varsigma}-\boldsymbol{F}(\boldsymbol{\varsigma})\cdot\boldsymbol{\varsigma}^*)d\boldsymbol{x} \tag{5.22}$$

which, considering the self-adjointness of $\boldsymbol{F}$ leads to $\omega^2 = (\omega^*)^2$. This means that ω^2 is real which implies that $\boldsymbol{\varsigma}$ is also real because $\boldsymbol{F}$ in Equation (5.18) is real. Therefore, two scenarios are possible

$$\text{if}\ \begin{cases} \omega^2 > 0 & \rightarrow \quad \text{Pure oscillation (stability)}, \\ \omega^2 < 0 & \rightarrow \quad \text{Exponential growth (instability)}. \end{cases} \tag{5.23}$$

5.1.0.2 Energy Principle

The ideal MHD equations compose a dissipationless system meaning that they conserve energy and that a stable equilibrium corresponds to a minimum of the potential energy W. This idea is at the basis of the so called energy principle which states

If there exists a displacement $\boldsymbol{\varsigma}$ for which the change in potential energy is $\delta W < 0$, the equilibrium is unstable.

As we are dealing with a static initial equilibrium the change in the kinetic energy is $\frac{1}{2}\int \rho_0(\partial_t \boldsymbol{\varsigma}\cdot\partial_t\boldsymbol{\varsigma})d\boldsymbol{x}$. Knowing that $\boldsymbol{\varsigma}(\boldsymbol{x},t)=\boldsymbol{\varsigma}\boldsymbol{x}e^{-i\omega t}$ yields

$$K(\boldsymbol{\varsigma},\boldsymbol{\varsigma}) = -\frac{\omega^2}{2}\int \rho_0(\boldsymbol{\varsigma}\cdot\boldsymbol{\varsigma})d\boldsymbol{x}, \tag{5.24}$$

$$= \frac{1}{2}\int \boldsymbol{\varsigma}\cdot\boldsymbol{F}(\boldsymbol{\varsigma})d\boldsymbol{x}. \tag{5.25}$$

Therefore, by conservation of energy

$$\delta W(\boldsymbol{\varsigma},\boldsymbol{\varsigma}) = -\frac{1}{2}\int \boldsymbol{\varsigma}\cdot\boldsymbol{F}(\boldsymbol{\varsigma})d\boldsymbol{x}, \tag{5.26}$$

which allows us to write the variational formulation of the stability problem (5.18)

$$\omega^2 = \frac{\delta W(\boldsymbol{\varsigma},\boldsymbol{\varsigma})}{K(\boldsymbol{\varsigma},\boldsymbol{\varsigma})}. \tag{5.27}$$

A more explicit form of δW can be obtained when the assumption of a plasma bounded by a perfectly conducting wall is made. In this case, the only boundary condition to be taken into account is $\boldsymbol{n}\cdot\boldsymbol{\varsigma}_{wall}=0$, where $\boldsymbol{n}$ is the normal pointing outwards from the wall. Then, defining a parallel and perpendicular components for all the vector quantities, i.e, $\boldsymbol{X}=\boldsymbol{X}_\perp + X_\parallel\boldsymbol{b}$, where $\boldsymbol{b}=\boldsymbol{B}/|\boldsymbol{B}|$ leads to a simplification of the expression for δW.

In the end, the intuitive form of δW is [89]

$$\begin{aligned}\delta W(\boldsymbol{\varsigma},\boldsymbol{\varsigma}) = & \frac{1}{2}\int \left(|\boldsymbol{Q}_\perp|^2 + |\boldsymbol{B}|^2(\nabla\cdot\boldsymbol{\varsigma}_\perp + 2\boldsymbol{\varsigma}_\perp\cdot\boldsymbol{\kappa}) + \gamma p_0(\nabla\cdot\boldsymbol{\varsigma})^2\right)d\boldsymbol{x} \\ - & \frac{1}{2}\int \left(2(\boldsymbol{\varsigma}_\perp\cdot\nabla p_0)(\boldsymbol{\varsigma}_\perp\cdot\boldsymbol{\kappa}) + j_\parallel\boldsymbol{Q}_\perp\cdot(\boldsymbol{\varsigma}_\perp\times\boldsymbol{b})\right)d\boldsymbol{x},\end{aligned} \tag{5.28}$$

where $\boldsymbol{\kappa}=\boldsymbol{b}\cdot\nabla\boldsymbol{b}$ is the field line curvature. Let us analyze all the terms of Equation (5.28) separately. The $|\boldsymbol{Q}_\perp|^2$ term represents the shear Alfvén wave and it computes the energy required to bend the field lines. The second term stands for the compressional Alfvén wave, i.e., the energy required to compress magnetic fiels lines and the term $\gamma p_0(\nabla\cdot\boldsymbol{\varsigma})^2$ represents the sound wave. These terms are strictly positive and thus stabilizing, in fact they correspond to three natural wave modes supported by the MHD system. The second integral however is composed by destabilizing terms. The instabilities arising from them are classified as pressure-driven (the first term has a ∇p_0) and current-driven (the second has $j_\parallel$) instabilities.

The current-driven instabilities are the so-called kink modes. They are macroscopic instabilities with low toroidal and poloidal wave numbers (n,m), where $\boldsymbol{\varsigma}(\boldsymbol{x})=\boldsymbol{\varsigma}(R)e^{i(m\theta+n\phi)}$. The resistive internal kink mode is the instability studied in this chapter.

5.2 Resistive Internal Kink Mode

The idea is to develop a rigorous numerical study of the resistive internal kink instability in order to validate the numerical scheme - VMS-Stabilized Finite Element - presented in Chapter 3. For that, we consider a low-β plasma (Details in Chapter 1) at a toroidal symmetrical equilibrium. This means that the magnetic pressure is larger than the hydrodynamic pressure.

The parameters to obtain the equilibrium are the ones shown in Chapter 4, Section (4.2). The initial profiles are shown in Figure (4.16).

This equilibrium was then perturbed by a initial $\tilde{\boldsymbol{v}} = 10^{-12}\overline{\psi}(1-\overline{\psi})$ applied at the $n = 1$ harmonic of the toroidal velocity. It means that the initial velocity becomes

$$\boldsymbol{v}_{\phi}^{(n=1)} = \tilde{\boldsymbol{v}} = 10^{-12}\overline{\psi}(1-\overline{\psi}). \tag{5.29}$$

This perturbation is shown in Figure (5.1).

After this initialization, the numerical method shown in Chapter 3 was used for the Full-MHD model to evolve the equations and then observe the development of the instability. Two Fourier modes $n = 0$ and $n = 1$, giving $cos(0)$, $cos(\phi)$ and $sin(\phi)$ were considered. A reverse aspect-ratio $\epsilon = 0.1$ was considered and the safety factor q monotonically increases from 0.73 at the axis to 1.6 at the plasma edge as it is shown in Figure (5.2). With these parameters, $\beta \approx 4 \times 10^{-3}$.

The resistive internal kink is related to the resonant surface $q = 1$ and the magnetic flux associated to it is $\psi = -0.229$. It is important to identify this surface because an important characteristic of the internal kink mode is the development of a layer around it.

To ensure that we are observing the internal kink, the first characteristic analyzed was the growth rate.

5.2.1 Growth Rate Analysis

To analyze the growth rate of the instability a simulation was launched with the parameters described in the previous section for a Magnetic Reynolds number $S = 10^8$. It is important to remark that the magnetic Reynolds number is inversely proportional to the resistivity η meaning that it affects the current and therefore the kink instability itself. The simulations have been performed over a poloidal grid like the one shown in Figure (4.5) containing $N_\psi = 40$ radial and $N_\theta = 32$ poloidal elements. For the first

FIGURE 5.1: Initial data for $3D$ computation with the density and magnetic stramlines (top) and perturbation of the first Fourier mode of the velocity (bottom). The perturbation has an order of magnitude of 10^{-12}.

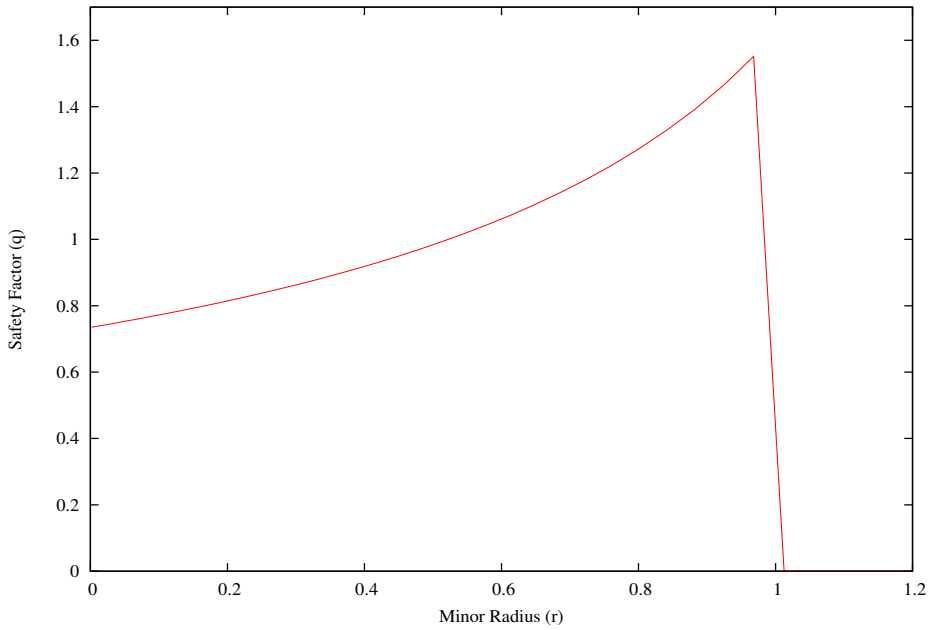

FIGURE 5.2: Safety factor as a function of the minor radius r. Its minimum value is 0.73 at the center and its maximum is 1.6 at the edge. The sharp decreasing at the end is a consequence of getting near to the wall

try the condition over the derivatives at the magnetic axis was disabled. This choice was made because as explained in section (4.1.4) that condition degrades a little bit the residual. The results for this configuration are shown below.

5.2.1.1 Perturbation of the Magnetic Axis

The idea was then, analyze what would happen if the derivatives at the central nodes were free to evolve. Figure (5.3) shows the kinetic energy evolution for the mode $n = 0$ and the cosine component of $n = 1$.

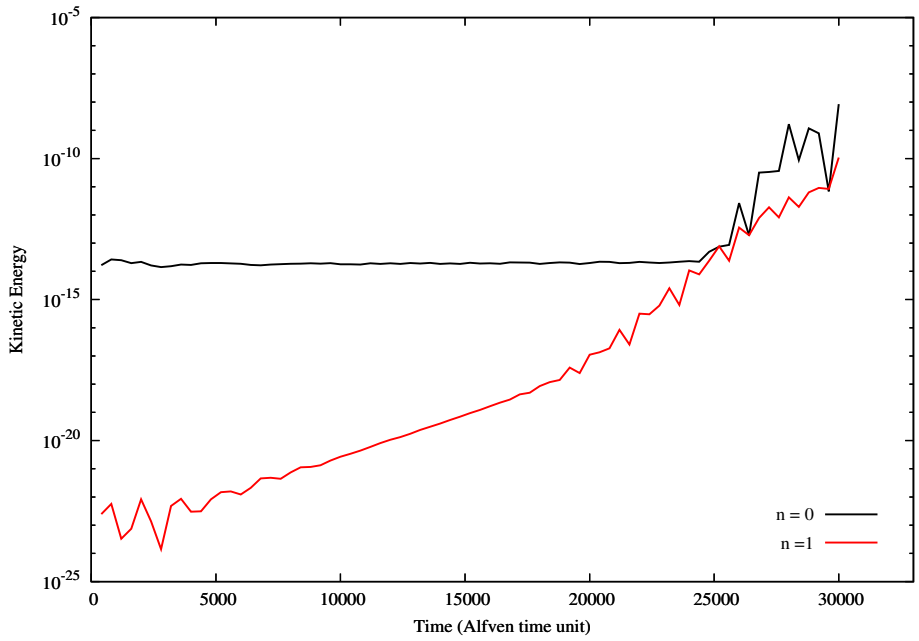

FIGURE 5.3: Kinetic energy evolution of the Fourier modes for an internal kink simulation. The oscillations at the beginning are expected but not those at the end which are a result of numerical noise related to the singularity of the grid

As it can be seen, the kinetic energy of the mode $cos(\phi)$ is completely unstable presenting oscillations in the growing phase that also interfere with mode $n = 0$ after a while. It is important to remark that the oscillations at the beginning, until $t_A \approx 9000$ are expected because up to this point the instability has not yet been triggered, thus, the plasma tends to oscillate around the equilibrium. The final oscillations, however, are completely unexpected and their characteristics, e.g., lack of periodicity and nonuniform amplitude indicate that their origin might be numerical noise. Indeed, Figure (5.4) shows the norm of the poloidal velocity profile at $t = 2.5 \times 10^4 t_A$ (left) and $t = 3 \times 10^4 t_A$ (right) as well as the details of the vector field close to the magnetic axis. The dotted red line identifies the surface for which $q = 1$.

If the center is not considered, the maximum value of the norm of the velocity fields is $|\boldsymbol{v}_\theta| = (v_R^2 + v_Z^2)^{\frac{1}{2}} \approx 10^{-11}$. Around the center, however, its maximum value reaches $|\boldsymbol{v}_\theta| \approx 10^{-8}$. With these perturbations, it was impossible to observe the dynamics of the internal kink mode.

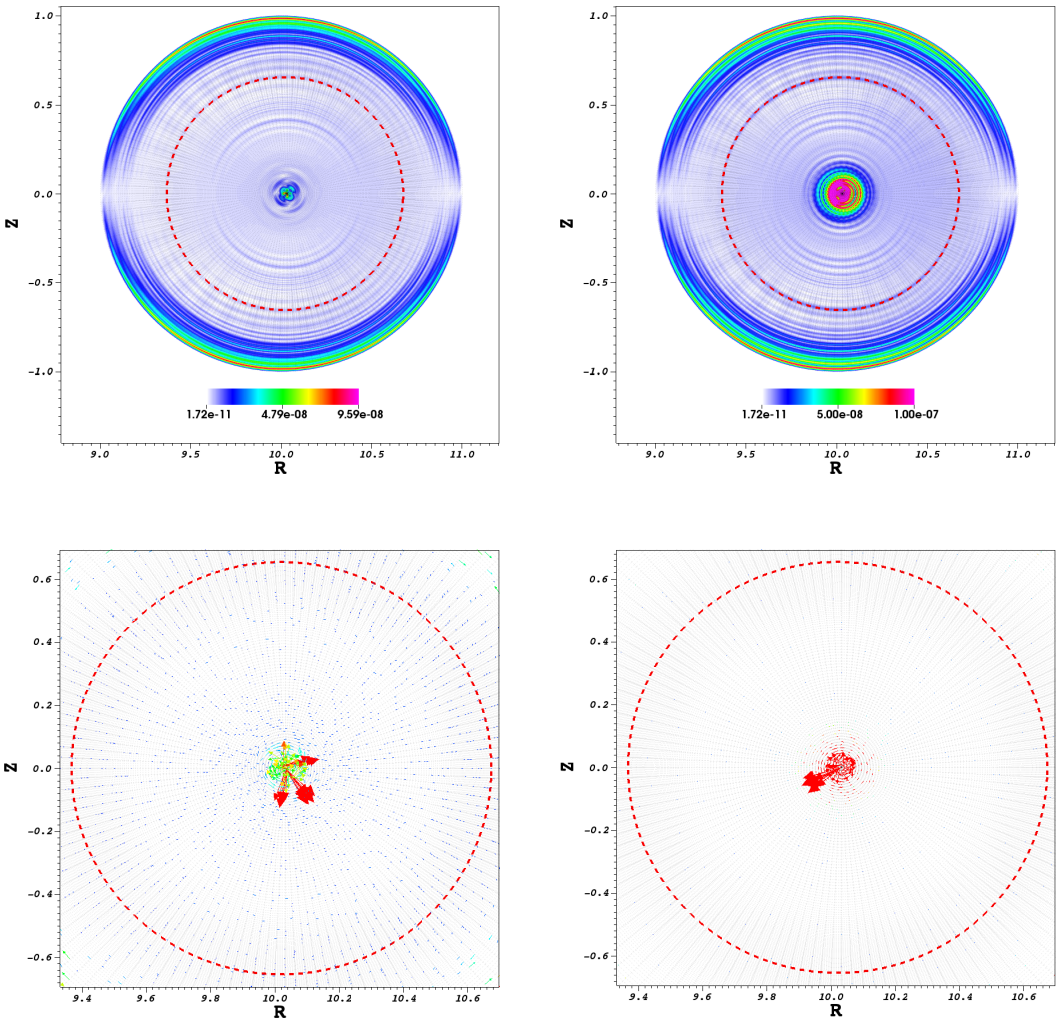

FIGURE 5.4: The abolute value of the poloidal velocity (top) for two different times - $2.5 \times 10^4 t_A$ (left) and $3 \times 10^4 t_A$ (right)- shows that the instabilities are located close to the singularity at the center. The vector shape of the field for the same time-steps are shown (below). The red dotted line represents the surface $q = 1$ where $\psi = -0.229$

It is important to highlight though that this problem, as explained in Section (4.1.4), is only characteristic of the vector quantities because they are related to the directional frames of reference of the grid. The scalar quantities, as shown in Figure (5.5), do not present this perturbed behavior.

After these results, the next logical step is add the conditions on the derivatives and run the simulations again for the same parameters exactly. The energy evolution for this case is shown in Figure (5.6).

As expected, the oscillation at the beginning are still there. Nevertheless, the growth part of the instability can be clearly identified now and it verifies the theoretical value expected [90] for a resistive internal kink. Figure (5.7) shows the poloidal velocity profile

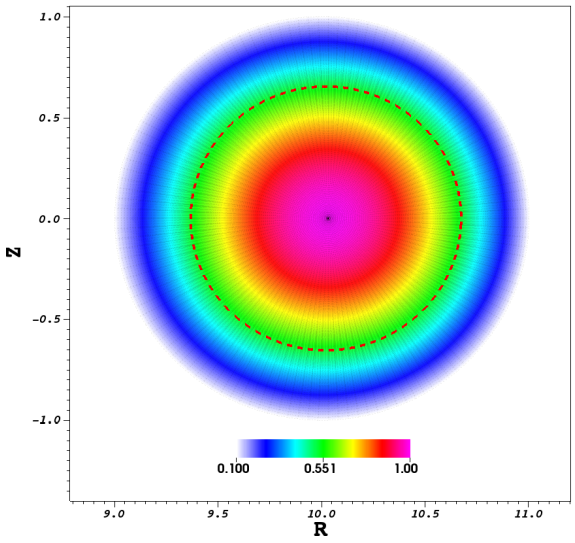

FIGURE 5.5: Density profile at $t = 3 \times 10^4 t_A$ showing that the discontinuity at the center does not affect scalar quantities

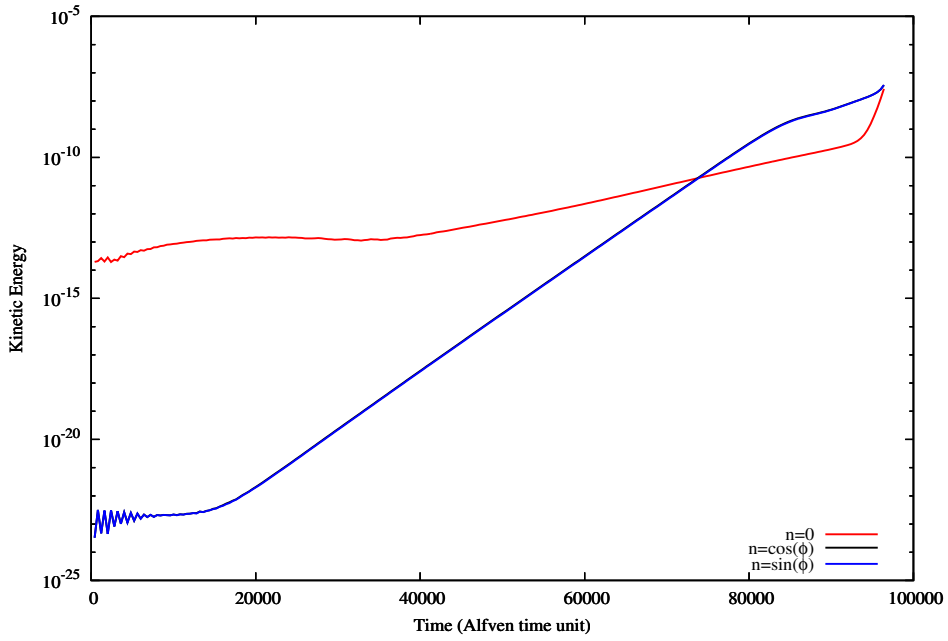

FIGURE 5.6: Evolution of the kinetic energy when the derivatives at the center are restrained. The growth rate typical of the kink mode is observed

at $t = 6 \times 10^4 t_A$ and the layer formation around the surface $q = 1$ can be observed as well. It confirms that restraining the derivatives on the axis nodes improves both stability and accuracy of the simulation. Therefore, this condition is retained and all the results obtained from here have taken it into account.

The possibility of reproducing an internal kink mode has been settled. Nonetheless, it is important to study this instability in further details in order to establish the robustness

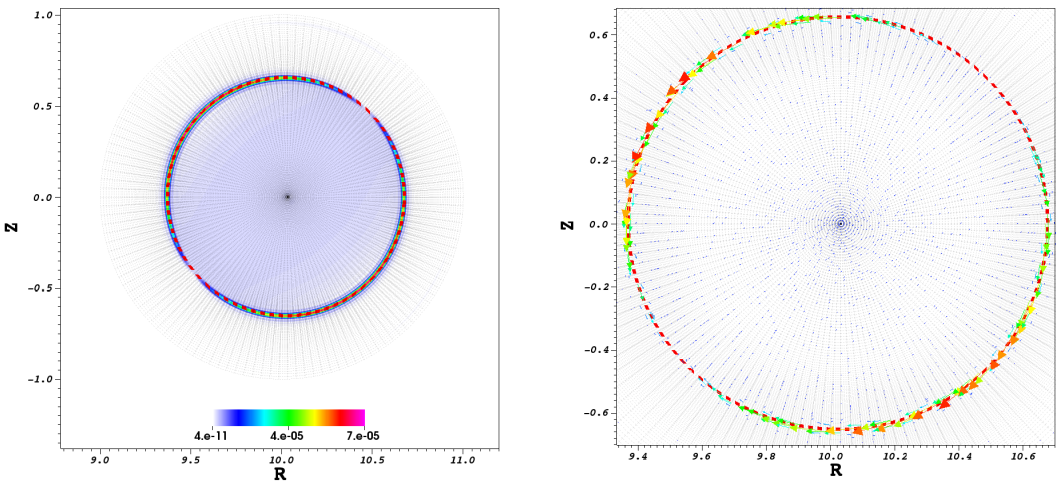

FIGURE 5.7: Velocity profiles without perturbation at the center. The thin layer around the surface $q = 1$ can be now observed.

and the limitations of the numerical scheme. For that, a rigorous study on the effects of the VMS stabilization has been done.

5.2.1.2 Effects of the VMS-stabilization

To test the effects of the numerical stabilization, two test-cases were taken into consideration. In the first one, only a uniform numerical viscosity $\mu_{num} = 10^{-5}$ was applied in the whole domain to play the stabilizing role, while for the second one the VMS-stabilization method described in Chapter 3 was implemented. All the others parameters were the same as before.

It can be seen in Figure (5.8) that only the presence of a numerical viscosity (right) is not enough to stabilize the scheme. The velocity profile obtained (top right) for the Fourier mode $cos(\phi)$ is very noisy and contains several oscillations. For the density profile (bottom right) the scenario is even worse. When only a constant artificial viscosity is considered it is almost impossible to see the formation of the expected profile and the result is mainly composed of noise.

Details of these profiles are shown below (Figure (5.9)) for the toroidal velocity, for example. The effects of the spurious waves are clearly seen when the VMS technique is not implemented (left). When it is acting (right), on the other hand, the profile can be distinguished.

This section has shown the robustness and the importance of a well-posed stabilization technique when using finite element methods to solve partial differential equations. In

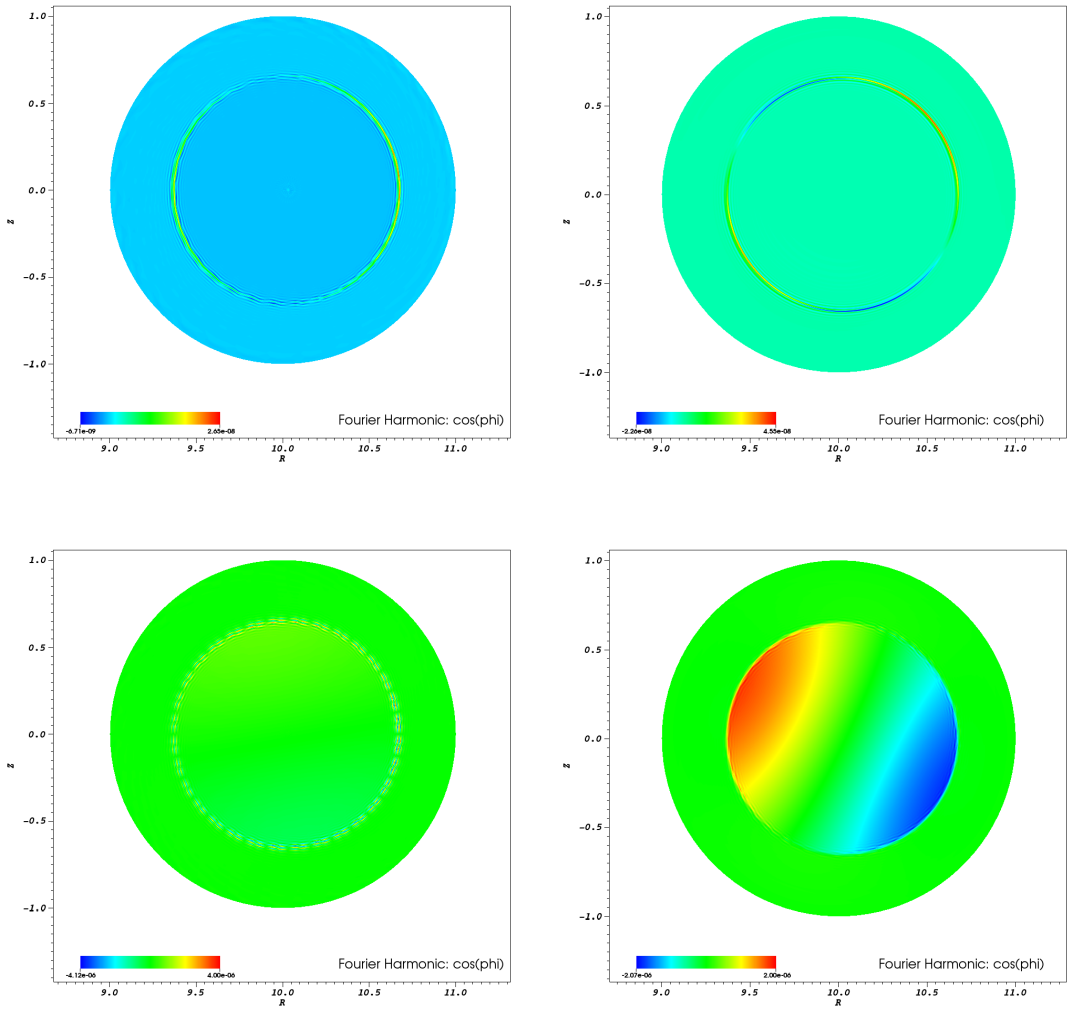

FIGURE 5.8: Effect of the VMS stabilization on the spurioous waves. The fluctuations of the toroidal velocity (top) and the density (bottom) are shown for the case in which an artifical viscosity $\mu_{num} = 10^{-5}$ is applied (left) and anoher in whic the VMS strategy is implemented (right)

the context of simulating tokamak plasmas with the Full MHD model, the main source of numerical noise are the fast acoustic waves and the main goal of the stabilization technique is to act exactly on these waves in order to avoid the divergence of the numerical scheme.

Nonetheless, as it was discussed in Chapter 3, several options are available for the stabilization matrix $\underline{\mathcal{T}}$ and the choice is not always straightforward. What is important to have in mind is that the stabilization objective is to control the numerical perturbations which are strictly related to the scheme that has been chosen to solve the system. This means that an optimal stabilization is one that can avoid the numerical noise without severely affecting the physical characteristics of the problem. In fact, the main objective

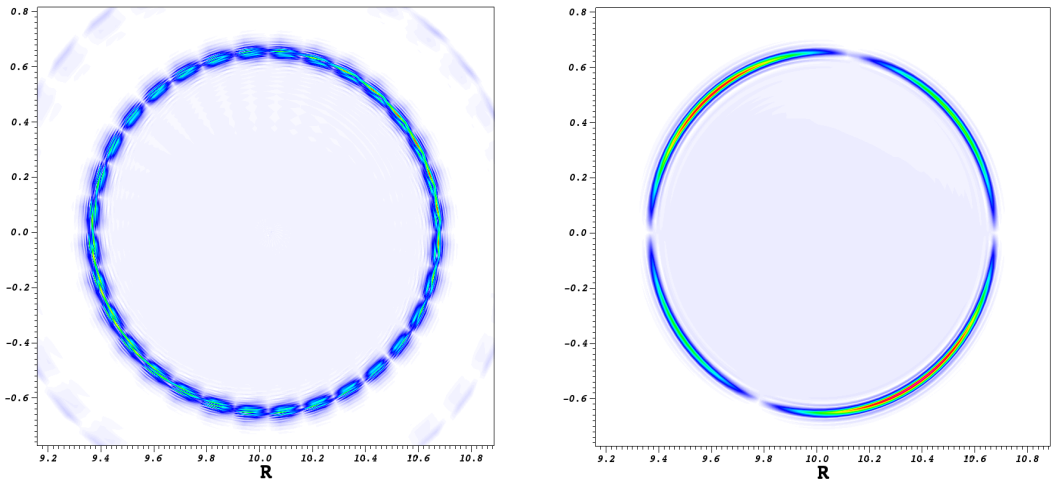

FIGURE 5.9: The efffects of the VMS stabilization: not implemented (left) and implemented (right). The details of the profile can be observed under this strategy.

here is to validate the strategy by studying a very known physical instability present in tokamks. Therefore, the choice of this parameter must be carefully taken.

In order to ensure that our stabilization strategy is not affecting the dynamics of the internal kink mode, a study of the growth rates was done before and after its implementation. As the resistive internal kink mode is a current triggered instability, it is expected that its behavior is somehow dependent on the magnetic Reynolds number S and this because its definition can be written as

$$S \equiv \frac{VL}{\eta}, \tag{5.30}$$

where V is the typical velocity of the flow, L the typical legth scale and η the resistivity. Well, the behavior of the parallel current $j_{\|}$ is dependent on the resistivity and so will be the case as well for the instability.

Several almost identical simulations have then been run for different magnetic Reynolds numbers and their growth rates were calculated as a function of S. The result can be seen in Figure (5.10).

Before discussing the result it is important to precise some characteristics of the simulations that have been run. A closer look at the Figure (5.10) shows that there are two different sets of points. The dark circles labeled Semi-Linear MHD and the red squares labeled Non-linear MHD. In fact, the numerical tool used for this simulations (JOREK Code) allows us to set the fluctuations of the Fourier mode $n = 0$ to zero. It means that all the variables are fixed for this mode, staying constant throughout the simulation. With this feature, an approximate but faster study can be performed giving insights

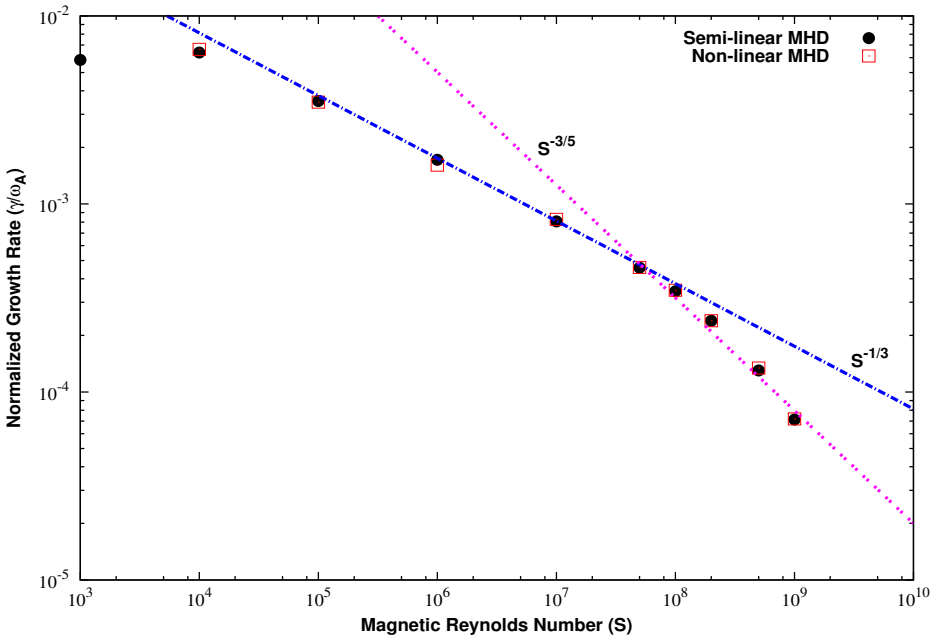

FIGURE 5.10: Computed growth rate for the internal kink mode as a function of the Magnetic Reynolds number (S). The asymptotic behavior, $S^{-1/3}$ for S smaller than a threshold and $S^{-3/5}$ for larger S is expected and has been observed before

about the characteristics of the instability that is being simulated. It is important however to verify if this approximation is consistent with the case under study. For that, we analyzed the behavior of the variables for the $n = 0$ mode and the results are shown in Figure (5.11).

The top figures show the variation on the magnetic flux ψ for the modes $n = 0$ (left) and $cos(\phi)$ (right) for the semi and non linear simulations. The bottom figures show the same information but for the vertical component of the velocity v_Z. The suitability of the semi-linear approximation can be clearly seen. Indeed, the fluctuations of $\psi^{(n=0)}$ are constant even when there is no condition applied to this mode. For the velocity there is an increasing at the beginning and at the end but during the most part of the simulation it stays constant. In fact, the fast increase at the end can be explained by the fact that at this point the kink mode enters on its non-linear phase. It can be seen by the saturation ocurring on the mode $cos(\phi)$. Therefore, there is no point in using a semi-linear approach when it happens. Nonetheless, the figures on the left show that the growth rate, for example, is kept unchanged by this approximation meaning that it is reasonable enough to give some concluding information about the problem studied.

Thus, knowing that the semi-linear case is a valid approach, the growth rate study has been performed for both cases. Going back to Figure (5.10), several conclusions can be made. First, the dependence on the magnetic Reynolds number obtained agrees with previous results obtained with the linear MHD code Phoenix [91, 92] and also with

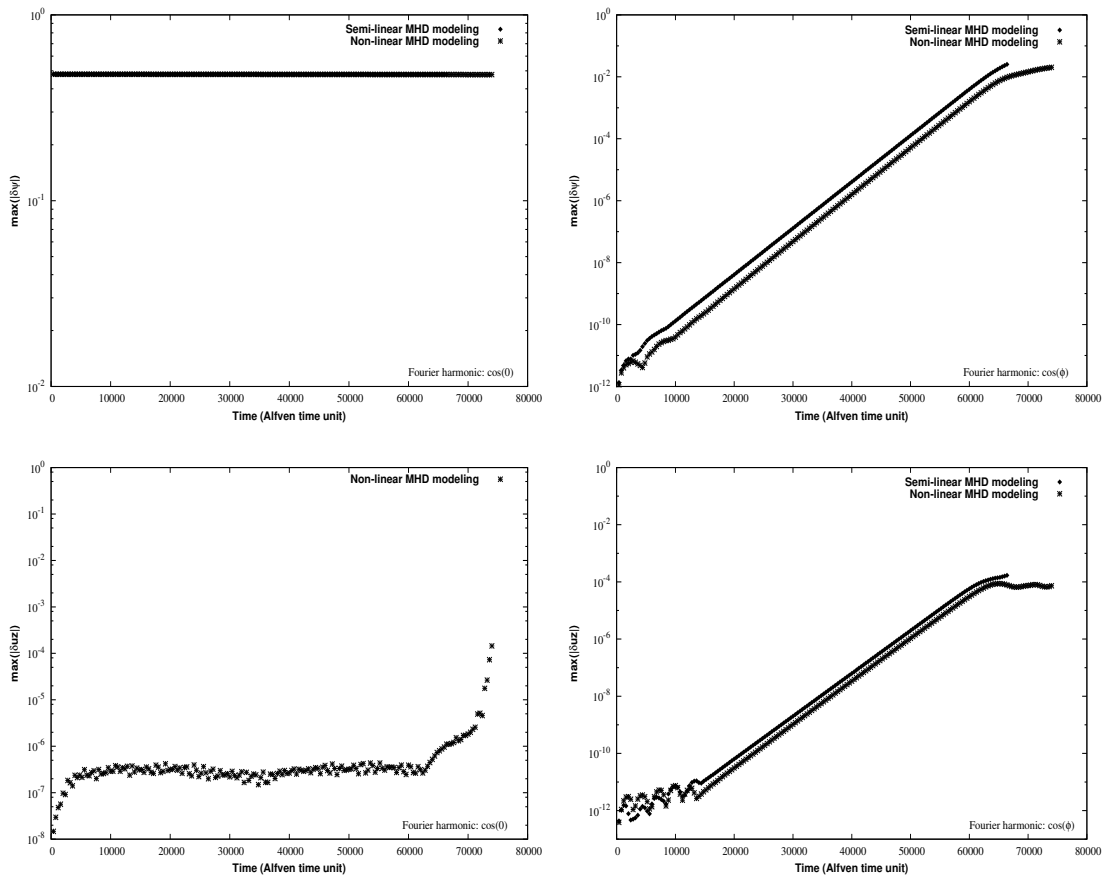

FIGURE 5.11: Dynamic of the kink mode for $S = 10^8$ using semi-linear modeling (when the mode $n = 0$ is assumed to be constant) and fully nonlinear modeling. The evolution of ψ (top) and the vertical component of the velocity v_Z (bottom) are shown for $n = 0$ (left) and $n = 1$ ($cos(\phi)$) (right).

results obtained by Hastiel *et al* [93] showing that the stabilization does not affect the physical instability, restraining its effects to the numerical level. For $S < 10^4$ the mode width becomes comparable to the machine size and the scaling is lost entirely.

For higher S, a transition is observed and the asymptotic behavior of the growth rates shifts from $S^{-\frac{1}{3}}$ to $S^{-\frac{3}{5}}$ which has been also observed by [93] and described by [90] and extended by Bussac *et al* [35]. In fact, the second asymptotic behavior, i.e., $S^{-\frac{3}{5}}$ is a characteristic of another current triggered MHD instability known as Tearing Modes.

5.2.2 Resistive Internal Kink Dynamics

After establishing that the effects of the stabilization were not interfering with the physical behavior it was possible the analyze different characteristics of the kink instability. The first one is the typical movement performed by the plasma column under its action (Described in Chapter 1). This movement can be seen in Figure (5.12).

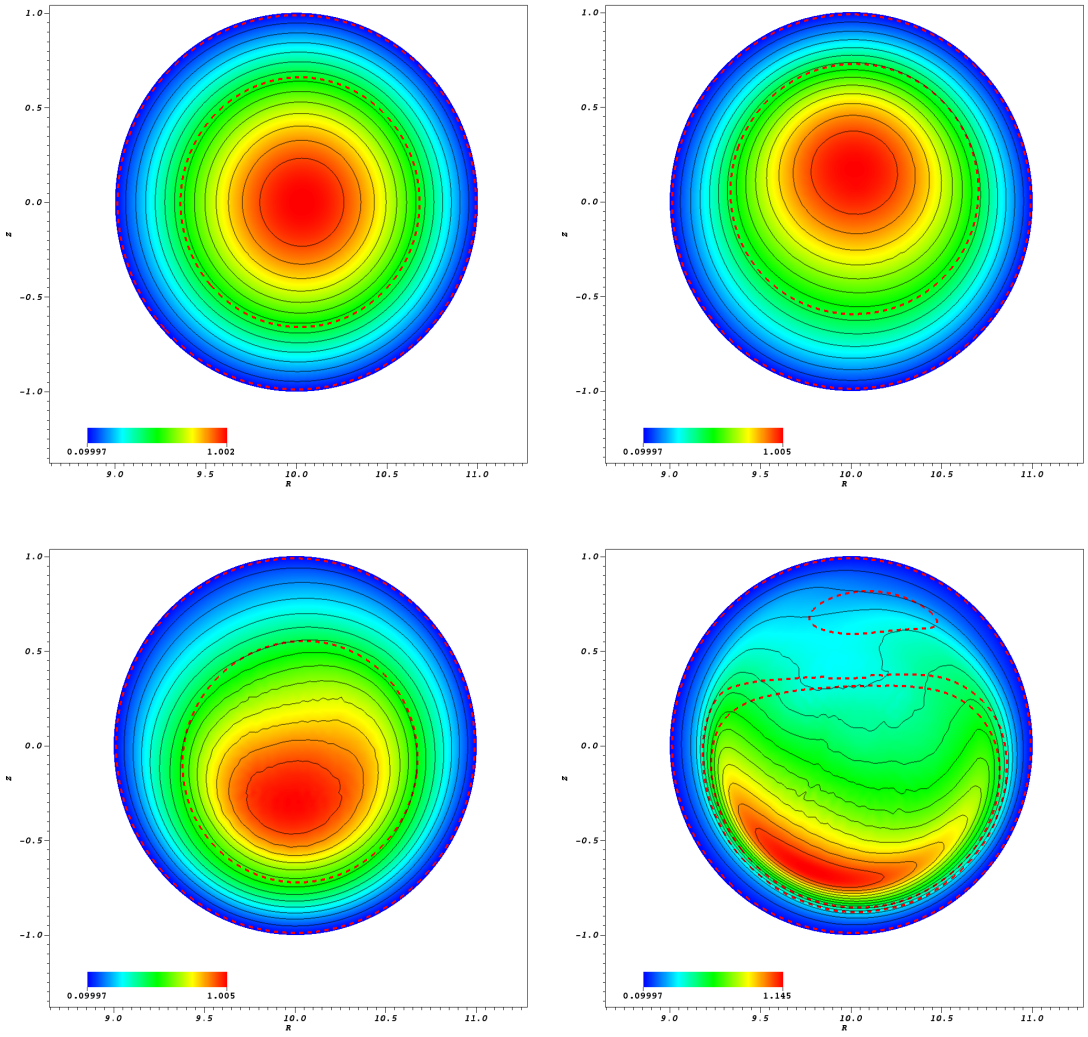

FIGURE 5.12: Evolution of the density profiles during the motion of the plasma column. $2D$ plot of the poloidal plane located at $\phi = 0$

Since the whole plasma column is moving it is expected that the magnetic field configuration will move with it. In fact this is the fundamental theorem the the MHD, known as Alfvén Theorem. The surface in which $q = 1$ moves with the column because is directly related to the magnetic configuration which is now being dragged by the movement of the density.

Another characteristic of the internal kink modes is the formation of a thin layer around the surface $q = 1$. In fact, the size of this layer, as the growth rates, depends on the magnetic Reynolds number S. This is shown in Figure (5.13) for $S = 10^5$ (left) and $S = 10^8$ (right). As it was stated before, decreasing S increases the layer width and it imposes a limitation on a minimum S for which the scaling will be lost. For our simulations this limit is $S = 10^4$.

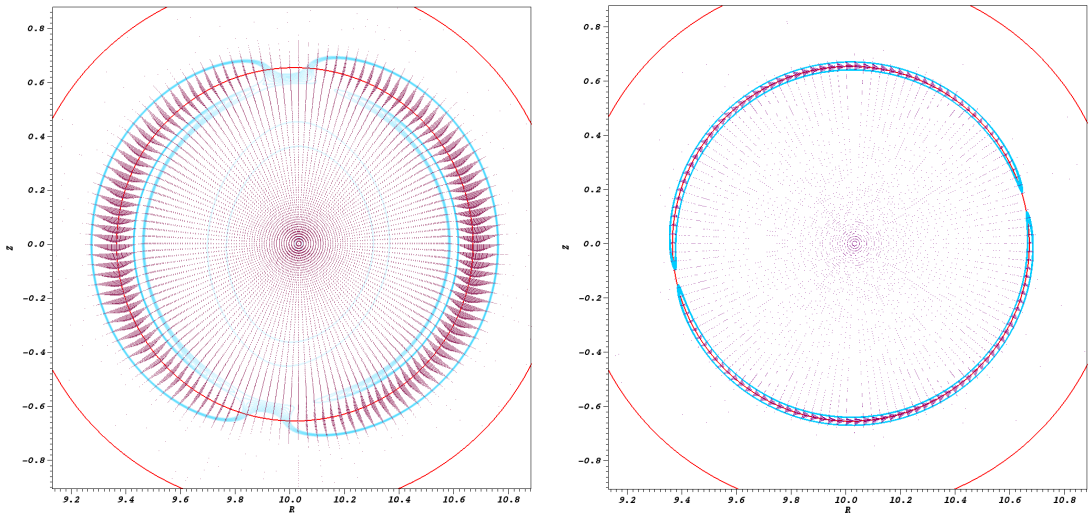

FIGURE 5.13: Kink structure comparison for $S = 10^5$ (left) and $S = 10^8$ (right). The width of the layers depends on the magnetic Raynolds number, going from 10^{-1}(left) to 3×10^{-2} (right)

5.2.2.1 Magnetic Reconnection

Finally, the phenomenon of magnetic reconnection, which is one of the main physical processes allowing self-organization and relaxation on time scales faster than global dissipation times in the plasma has been observed. This process is only possible if dissipative and other physical locally important processes take place.

In nature this phenomenon has been directly measured in different solar phenomena, like solar wind and solar flares. In the magnetic fusion context it has been identified as one important mechanism acting on the redistribution of energy and relaxation of the magnetic field. Often it has a destructive effect, acting in a way that degrades the magnetic confinement. For this reason it is a crucial issue that must be taken into account when modeling tokamak plasmas.

Our stabilized simulations were able to reproduce the beginning of this phenomenon and, specially, the initial formation of a magnetic island. One of the expected effects of this reconfiguration is the triggering of an instability known as Saw tooth instability. Unfortunately, it has not been observed in our simulations and there are different reasons for that, among which we can name the discontinuity on the center that becomes important when a strong movement is happening in this region but also the model that has been used in which diamagnetic effects (to which the Saw tooth is related) are not taken into account, for example.

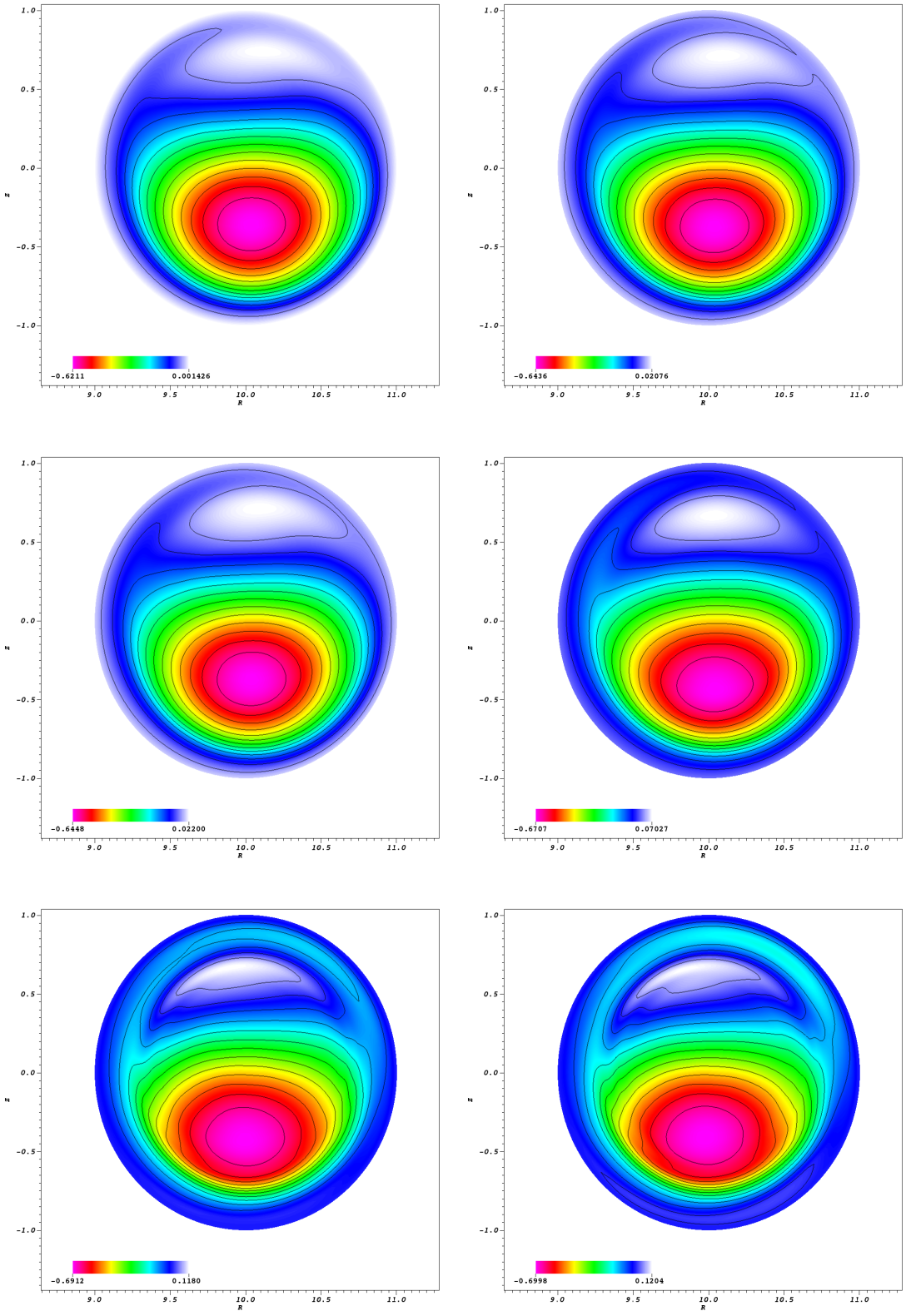

FIGURE 5.14: Reconnection of the magnetic flux surfaces ψ.

5.3 Conclusions

This Chapter was entirely dedicated to the numerical results related to the resistive internal kink instability. Its main goal is tha validation of the numerical strategy that is the core of this thesis. For that, the initial equilibrium obtained in Chapter 4 has been perturbed in such a way as to create the physical instability.

Then, we started by analyzing the effects of the discretization and the construction of the grid over the evolution of the equations. It has been shown that special attention must be paid to the center of the grid because it can affect in a severe way the physics of the problem. This conclusion allowed us to show that adding a condition on the derivatives, as discussed in the previous chapter, is justified and necessary if we are using aligned grids.

After that, the discussion is focused on the effects of the VMS method. This is very important because it allows to validate the whole numerical strategy. Indeed, it has been shown that the VMS method can improve considerably the results by controlling the numerical noise. Furhermore, it was shown that it has no impact on the physical properties of the problem. In order to show that, an extensive anlysis of several properties of the instabilitiy has been done and the results were confronted either to analytic solutions or other results obtained before.

In the end, the stabilized finite element strategy developed here for the numerical approximation of MHD equation has been validated. The divergence free of the magnetic field is achieved under a potential vector formulation and the stability of the scheme is done via the Variational Multi Scale (VMS) technique.

All the validations here were performed with a circular plasma that can be seen as a simplification with respect to the configurations used in the current and future tokamaks. The next chapter is dedicated to the divertor configuration.

Chapter 6

Divertor Configuration: X-point plasmas

In the previous chapter we dealt with circular plasmas where there were no interactions between the plasma and any material wall. For the divertor configuration, on the other hand, these interactions cannot be neglected since the open field lines in the SOL region can transport plasma to material targets, i.e., the divertors.

Then, while Dirichlet conditions are enough for simulating plasma systems without X-point, it is not the case for X-point plasmas. For this case, special boundary conditions, known as Bohm boundary conditions must be taken into account. This happens because when the plasma comes in contact with a material wall a layer is formed around it in which the quasi-neutrality condition is violated. This layer, known as Debye Sheath is characterized by a negative charged wall that will act to repulse the electrons and attract to ions until a new equilibrium is established in this region. It is a direct consequence of the high mobility of the electrons compared to those of the ions due to their difference of mass, $m_e << m_i$.

This phenomenon will induce an acceleration of the ions towards the wall and, in fact, they must enter this region with a velocity superior to a certain threshold. Otherwise, the unbalanced potential formed at the sheath will "eat" its way into the plasma in order to balance itself. This threshold was established by David Bohm in 1949 and for this reason is known as Bohm Sheath Criterion.

In this Chapter we start by giving the theoretical basis related to the Bohm criterion (6.1), then the implementation of this condition (6.2) is discussed in terms of the formulation given in Chapter 3. In fact, some changes must be performed in the boundary

conditions terms of the weak formulation. Finally, the first results obtained for an X-point configuration simulation are shown (6.3).

6.1 Bohm Criterion

When the plasma comes in contact with a wall or any surface a sheath region is formed. In this region, electron and ion densities no longer balance. The reason for this comes from the fact that electrons have a very much greater mobility than ions. It means that any surface in contact with a plasma will be attained first by electrons acquiring rapidly a negative charge. This will lead to the creation of a (negative) potential that will act to reduce the electron flux and increase the flux of positive ions to the surface. This will go until a stage is reached where the two balance and the net current to the surface disappears. In this steady state the surface potential is known as the floating potential.

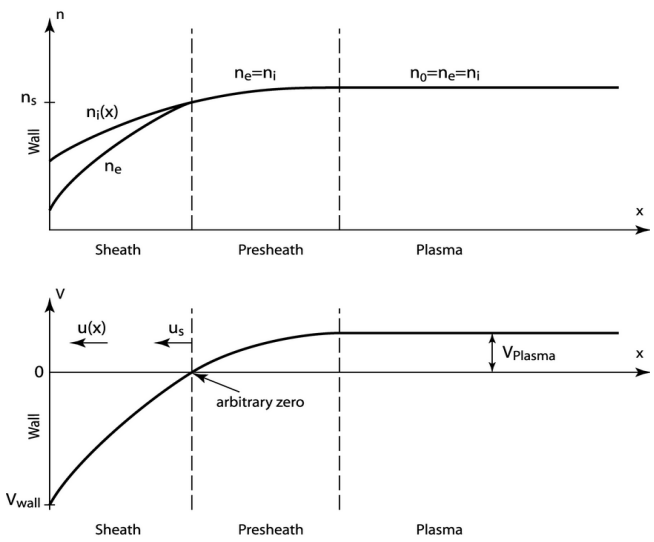

FIGURE 6.1: Scheme of the sheath formation around a plasma boundary

To understand the sheath dynamics one must solve Poisson's equation along with the dynamical equations for both ions and electrons with suitably chosen boundary conditions. A general solution can only be found numerically because of the non-linearity of the governing equations together with the fact that the plasma parameters are strongly inhomogeneous across the sheath. However, in plane geometry an approximate analytic solution is possible. The key approximation lies in the distinct assumptions made about ions and electrons dynamics. For the electron fluid, the pressure gradient is dominant over the momentum term while for the ion fluid the reverse is the case, i.e., the ions are cold.

Let us start by assuming a Boltzmann distribution for the electron density

$$n_e(x) = n_0 e^{\left(\frac{eV(x)}{k_B T_e}\right)}, \tag{6.1}$$

where $V(x)$ is the electrostatic potential and we have made use of the boundary condition $V(x \to \infty) = 0$ and $n_e(x \to \infty) = n_0$ considering that the wall is located at $x = 0$. For the ions, for a hydrogen plasma, the density has the following profile

$$n_i(x) = n_0 \left[1 - \frac{2eV(x)}{m_i u_{0i}^2}\right]^{-\frac{1}{2}}, \tag{6.2}$$

where $u_{0i} = u_i(x \to \infty)$, u_i is the ion velocity.

The potential distribution within the sheath is described by Poisson's equation

$$\frac{d^2V(x)}{dx^2} = -\frac{\rho_q}{\epsilon_0} = \frac{e(n_e - n_i)}{\epsilon_0}. \tag{6.3}$$

Hence, replacing equations (6.1) and (6.2) above leads to

$$\frac{d^2V(x)}{dx^2} = \frac{n_0 e}{\epsilon_0}\left[e^{\left(\frac{eV(x)}{k_B T_e}\right)} - \left(1 - \frac{2eV(x)}{m_i u_{0i}^2}\right)^{-\frac{1}{2}}\right]. \tag{6.4}$$

This non-linear equation is the plasma sheath equation in plane geometry. It helps to rewrite it in terms of the following dimensionless parameters

$$\phi(x) = -\frac{eV(x)}{k_B T_e}, \qquad M = \frac{u_{0i}}{(k_b T_e/m_i)^{\frac{1}{2}}} \text{ and } \xi = \frac{x}{\lambda_D};$$

where λ_D is the Debye length, defined by $\lambda_D = \left(\frac{\epsilon_0 k_B T_e}{n_0 e^2}\right)^{\frac{1}{2}}$. Equation (6.4) then becomes

$$\frac{d^2\phi}{d\xi^2} = \left(1 + \frac{2\phi}{M^2}\right)^{-\frac{1}{2}} - e^{-\phi},$$

which can be multiplied by $\frac{d\phi}{d\xi}$ and then integrated, leading to

$$\frac{1}{2}\left(\frac{d\phi}{d\xi}\right)^2 = M^2\left[\left(1 + \frac{2\phi}{M^2}\right) - 1\right]^{\frac{1}{2}} + \left(e^{-\phi} - 1\right). \tag{6.5}$$

It is important to notice that equation (6.5) effectively determines $\phi(\xi)$ in terms of the Mach number M. A second integration can only be done numerically unless we make an additional approximation. If we confine our attention to the plasma side of the sheath

where ϕ is small we may approximate (6.5) by

$$\left(\frac{d\phi}{d\xi}\right)^2 = \left(1 - \frac{1}{M^2}\right)\phi^2, \tag{6.6}$$

which has a monotonic solution provided $M^2 > 1$. In other words

$$u_{0i} > \left(\frac{k_B T_e}{m_i}\right)^{\frac{1}{2}}, \tag{6.7}$$

a result due to Bohm (1949) and known as the Bohm sheath criterion. A sheath forms at a material boundary provided the streaming velocity of ions entering the region close to a wall exceeds the ion acoustic velocity c.

6.2 Bohm Boundary Conditions: Implementation

This criterion was not relevant for the circular cases described in Chapter 5 because, in that case, the wall is aligned with the magnetic flux surfaces for this reason only boundary condition of type Dirichlet were considered. This it not the case, though, for X-point plasmas. In fact, in this case there are two types of boundary walls: the flux aligned non-resistive walls and non-resistive divertor boundary.

It is important to consider this division because the dynamics of these two boundaries are different since one is aligned with the magnetic field lines - flux aligned wall - while the other is basically perpendicular to it - the divertor. Well, for our simulations it is assumed that the particles escaping through the separatrix will be all trapped by an open field line and eventually will hit the divertor. Thus, the Bohm criterion has to be taken into account only at those boundaries. In order to understand how it is done, let us retake the RHS of our weak formulation defined in Equation (3.82), in which two terms are related to the boundary: $\boldsymbol{\Psi}_i^{\boldsymbol{F}}$ and $\frac{1}{\epsilon}\boldsymbol{\Psi}_i^S$. The first is a result of the integration by parts while the second comprises the penalized Dirichlet type boundary conditions.

Therefore, for the aligned walls, these terms remain the same as for the previous test case. For the divertor, on the other hand, some changes must be made. Let us first consider $\boldsymbol{\Psi}_i^{\boldsymbol{F}}$ which is a consequence of the integration by parts, it can be written as

$$\boldsymbol{\Psi}_i^{\boldsymbol{F}} = \begin{pmatrix} \rho(\boldsymbol{v}\cdot\boldsymbol{n})\mathcal{N}_i \\ (\rho\boldsymbol{v}(\boldsymbol{v}\cdot\boldsymbol{n}) + p\boldsymbol{n} + \pi\boldsymbol{n} - \boldsymbol{B}(\boldsymbol{B}\cdot\boldsymbol{n})))\cdot\boldsymbol{\mathcal{N}}_i \\ p(\boldsymbol{v}\cdot\boldsymbol{n})\mathcal{N}_i \\ 0 \end{pmatrix}, \tag{6.8}$$

where $\boldsymbol{\mathcal{N}}_i = \mathcal{N}_i\hat{\boldsymbol{R}} + \mathcal{N}_i\hat{\boldsymbol{\phi}} + \mathcal{N}_i\hat{\boldsymbol{Z}}$ and there is no contribution in $\boldsymbol{A}$ because it has been taken into account in another term and there are no changes in these conditions when dealing with the divertors. As usual, $\boldsymbol{n}$ is the normal pointing outwards from the wall.

A close look at (6.8) shows that there are velocities involved and thus, they must satisfy the Bohm criterion at the divertor. The physical condition states that the velocity close to the boundary must be superior to the acoustic velocity, still, for practical reasons, the equality can be assumed as a first approximation. Then, knowing that $c = \left(\frac{\gamma p}{\rho}\right)^{\frac{1}{2}}$, makes it possible to define a Bohm velocity at the divertors, called $\boldsymbol{v}_{Bd}$. For that, one must take into account the fact that the particles are guided to the divertors following the magnetic field. Thus, the direction of $\boldsymbol{v}_{Bd}$ is parallel to $\boldsymbol{B}$. Therefore

$$\boldsymbol{v}_{Bd} \equiv \pm\frac{\sqrt{\gamma T}}{||\boldsymbol{B}||}\boldsymbol{B}, \tag{6.9}$$

where the $\pm$ is necessary to ensure that the particles are going out at the divertor and not in.

Therefore, a Bohm Boundary Condition flux can be defined as

$$\tilde{\boldsymbol{\Psi}}_i^{\boldsymbol{F}} = \begin{pmatrix} \pm\rho(\boldsymbol{v}_{Bd}\cdot\boldsymbol{n})\mathcal{N}_i \\ (\rho\boldsymbol{v}_{Bd}(\boldsymbol{v}_{Bd}\cdot\boldsymbol{n}) + p\boldsymbol{n} + \pi\boldsymbol{n} - \boldsymbol{B}(\boldsymbol{B}\cdot\boldsymbol{n})))\cdot\boldsymbol{\mathcal{N}}_i \\ \pm p(\boldsymbol{v}_{Bd}\cdot\boldsymbol{n})\mathcal{N}_i \\ 0 \end{pmatrix}. \tag{6.10}$$

Moreover, the penalized term is also $\frac{1}{\epsilon}\boldsymbol{\Psi}_i^S$ redefined as

$$\tilde{\boldsymbol{\Psi}}_i^S = \begin{pmatrix} 0 \\ \rho(\boldsymbol{v}\mp\boldsymbol{v}_{Bd})\mathcal{N}_i\boldsymbol{\mathcal{X}}(\partial\tilde{\Omega}_{x,h}^{\boldsymbol{v}}) + (\rho\boldsymbol{v}\mp\boldsymbol{m}_{Bd})\mathcal{N}_i\boldsymbol{\mathcal{X}}(\partial\tilde{\Omega}_{x,h}^{\boldsymbol{m}}) \\ 0 \\ (\boldsymbol{A}-\boldsymbol{A}_b)\mathcal{N}_i\boldsymbol{\mathcal{X}}(\partial\tilde{\Omega}_{x,h}^{\boldsymbol{A}}) + (\boldsymbol{B}-\boldsymbol{B}_p)\mathcal{N}_i\boldsymbol{\mathcal{X}}(\partial\tilde{\Omega}_{x,h}^{\boldsymbol{B}}) \end{pmatrix}, \tag{6.11}$$

where $\partial\tilde{\Omega}_{x,h}^{\rho}$ stands for the divertor boundary only. A free outflow of the density and temperature is applied which means that it must be compensated by a heat and particle sources terms that must be included in the model.

Once the boundary conditions for the divertor configuration have established the simulations can be run. This configuration is generally used for simulating the Balooning modes that could eventually trigger the edge localized modes (ELM) briefly described in Chapter 1.

6.3 X-point Plasmas: Quasi-stationary equilibriuim

Adding the Bohm boundary conditions to the models leads to the development of a large parallel flow close to the divertors. This is an expected consequence since a velocity field is created at those boundaries. Before perturbing the equilibrium in order to simulate the instabilities, it becomes, then, important to achieve a first quasi-steady state in which the poloidal and parallel flows have adapted to the Bohm conditon applied [10] and are well established.

In order to do that, the Grad-Shafranov equilibrium obtained for this configuration using the profiles described in (4.29), in which the H-mode edge pedestal is imposed by the shape of the input profiles is run with only one Fourier harmonic $n = 0$ and without any perturbation. Then, after 1 time-step the velocity field at the divertors can be seen. A $3D$ representation of the tokamak can be seen in Figure (6.2) and the details of the velocity field close to the divertors are shown in Figure (6.3).

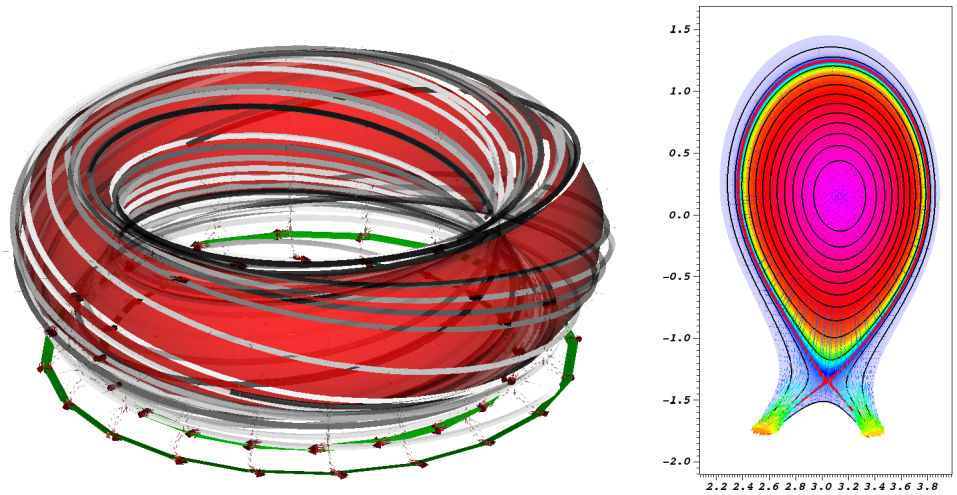

FIGURE 6.2: 3D magnetic field lines, plasma density and velocity field near the divertors (left) and a poloidal cut showing the cross section of the reactor (right)

The value of the velocity at this point must be the acoustic velocity c. It is then useful to express the velocity in terms of the Mach number M because in this case it scales as one. This representation is shown in Figure (6.4).

With these conditions, the simulation was ran considering only one Fourier harmonic with the goal of finding the quasi-steady state that will serve as the basis for the perturbations. It is important to remark that there are several possible quasi-static equilibria from this point. The most correct one to obtain would be reached after a long time when the pressure gradient has adapted to the diffusion profiles. As these time-scales are usually too long, another state is searched in practice.

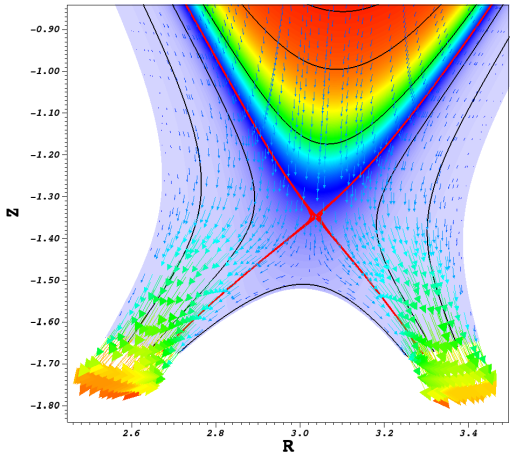

FIGURE 6.3: Details of the velocity field near to the divertor plates when Bohm boundary conditions are taken into account

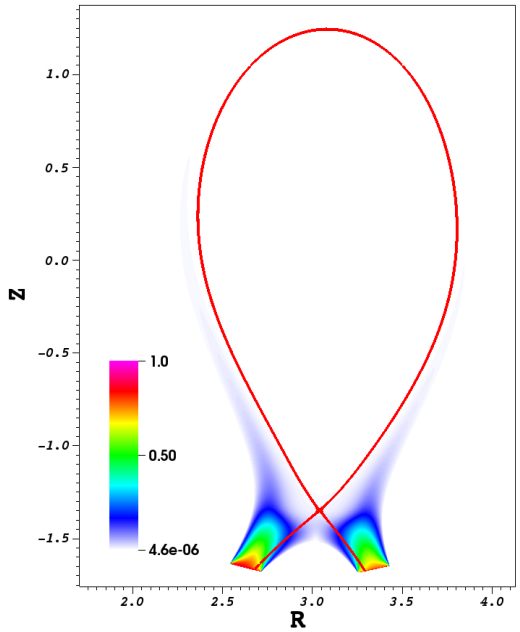

FIGURE 6.4: Velocity profile written in terms of the Mach number M at $t = 1$

This quasi-steady state that requires far less simulation time is obtained when the velocity profile has adapted to the conditions, meaning that it becomes almost constant. Thus, the goal becomes to find rather this one then the pressure related quasi-equilibrium. Figure (6.5) shows the evolution of the kinetic energy for this case.

As it can be remarked, the quasi-stationary equilibrium searched has not been found. In fact, Figure (6.5) shows that the kinetic energy is tending to an equilibrium value since its variation is becoming smaller. However, some other problems interfere with the simulation before this state is reached, namely a density hole that appears near the

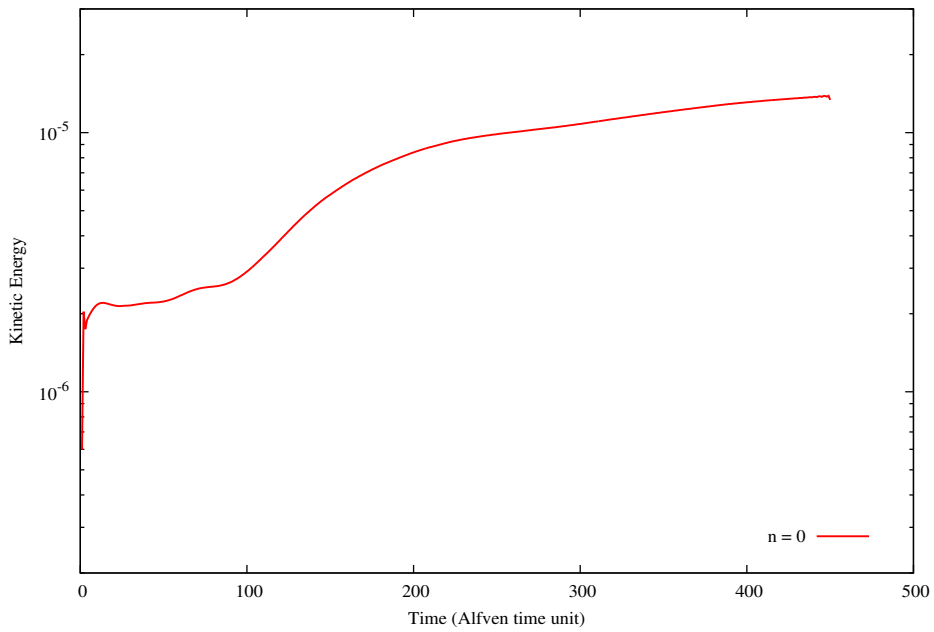

FIGURE 6.5: Evolution of the kinetic energy for the harmonic $n = 0$ when Bohm boundary conditions are applied

divertors. This problem can be related to the fact that the sources and the outflow of particles are still not well balanced. It is not the only possible reason, though, as this problem could be also related to the strong diffusion happening in this region, which could create numerical discontinuities between two neighbor elements from one time-step to another. If this is the case, one possible solution (that has not been tested yet) would be the implementation of a shock capturing stabilization.

The important thing to retain here is that the main goal has been to verify the suitability and robustness of the stabilized scheme and this has been verified. Actually, without the stabilized scheme even the simulation of this one Fourier mode case is not possible, as the calculation diverges after just a few iterations. There are still improvements to be done but the basis for achieving the simulation of Edge localized Modes using the full MHD model has been settled.

6.4 Conclusions

In this chapter we extended the discussion of the numerical simulations to the so called X-point plasmas. This is the configuration that allows the development of the H-mode of confinement and, thus, is the one chosen for the operation of tokamaks like JET and the future ITER.

It has been shown here the details that must be taken into account when dealing with numerical simulations of plasmas having this configuration. In fact, special boundary conditions were implemented for the divertors and these conditions are related to the velocity of the plasma reaching the targets. The so called Bohm criterion establishes that it must be superior to the acoustic speed c. As a first approximation, the equality $\boldsymbol{v}_{Bd} = \pm c$ has been implemented. Indeed, this is often the condition used for calculations involving the X-point and it has already been used for the reduced MHD model.

Bohm conditions generate a great flow near the divertors, such that, before triggering an instability, a quasi-steady equilibrium in which the parallel and poloidal flows would be well established, must be reached. For this, the axis-symmetric equilibrium obtained with GS was let to evolve without any harmonics until the kinetic energy would reach a constant value. We could observe with our results that the velocity field was well aligned with the magnetic lines and respected the Mach-1 condition. Moreover, even though the kinetic energy has not reached a steady state, its growth rate is decreasing indicating that eventually it will be the case.

Unfortunately, another problems developed during the calculation before the quasi-equilibrium could be reached. This means that some corrections are still to be done in the model. Nonetheless, this simulation, as well as the kink instability have allowed us to verify once more the suitability and the robustness of the VMS stabilization. It was not possible to obtain a simulation using the full MHD model with X-point that does not diverge after just a few timesteps without the stabilization technique developed here.

Conclusions and Perspectives

The simulations of tokamak plasmas is not simple. It involves different phenomena happening in different time scales and presenting instabilities. For this reason, a robust and well posed numerical method is necessary in order to solve the models describing the physics inside the device.

In Chapter 2 we have developed the magnetohydrodynamic plasma models having at their basis the kinetic model. The single fluid MHD model, which is the one used in our simulations was obtained and from appropriated and justified simplifications other models, e.g., ideal and resistive, were derived. The Grad-Shafranov equilibrium that plays a crucial role in our simulations has also been obtained. The solenoid condition of the magnetic field, i.e., $\nabla \cdot \boldsymbol{B} = 0$, was discussed and possible ways to properly deal with it have been presented. In our case, the vector potential formulation was the choice and under that formulation the Coulomb gauge has been used.

Next, once the models were well established, we presented in Chapter 3 the numerical approach chosen for our simulations. It is based in the finite element method. More precisely, since the tokamak presents axis-symmetry, the 3D domain is decomposed in a tensor product of a 2D poloidal domain and a 1D toroidal domain. For the poloidal planes, a finite element using Bézier surfaces was used and for the toroidal part, a Fourier decomposition is done. Moreover, as it is widely known, when dealing with convection dominated fluxes, finite element method alone is not robust enough. Hence, we presented here a stabilization method known as Variational Multi-Scale (VMS) stabilization as it has to role of taking into account the effects of the unresolved scales over the coarse ones. All the derivation of the method and its application on the MHD equations via the Jacobian operator has been shown. Finally, the assembling of the system and the ways to solve it are presented and discussed.

In Chapter 4, we were able to show the first results of the numerical approach. This chapter was dedicated the solution of the Grad-Shafranov equilibrium. It was shown that, giving the appropriate profiles as the input to this equation, it is possible not only to establish the initial conditions for the MHD simulation bat also to build a grid of the

domain that is aligned with the magnetic field lines. An important and detailed analysis of the residual of the GS equation and how it can be coupled with the full MHD model has been done. It was shown that even if, analytically, the equilibrium is preserved this could not be the case numerically. In fact, as the construction of the grid itself leads to meshes containing singularities, the solution of the equilibrium may be perturbed. Indeed, the residuals tend to grow around the two possible singularities present in the tokamak configuration, i.e., the magnetic axis ans the X-point. Some techniques to attenuate this problems have been discussed. This analysis is very important because problems can occur during the simulation that are not related to the modeling itself but to particularities of the grid and it is important to be able to distinguish them.

Then, in Chapter 5 the internal kink instability has been extensively discussed. The main goal was the validation of the VMS stabilized finite element technique. Indeed, it has been clearly shown that the stabilization is fundamental in order to obtain proper results of this instability. Once it has been shown, different studies of the kink dynamics have been performed because it was necessary to ensure that the stabilization was not only properly dealing with the numerical perturbations but also not affecting the physics of the problem. For that, the growth rate of the instability has been studied and the results were compared with other simulations but also with analytic results. After that, other properties of the kink mode have been shown like the dependence of the mode layers on the resistivity and the movement of the plasma column. Also, the beginning of the magnetic reconnection, which is a very important phenomenon since it changes the magnetic configuration of the system, has been observed. It is important to highlight that all these results were obtained with the Full MHD model and thanks to the stabilization technique used. This chapter allowed us to validate the technique and this opens up a scenario for more detailed simulations of tokamak plasmas.

Finally, the more complex X-point geometry has been briefly tested under this technique and the first results are shown in Chapter 6. Although, not so many results could be obtained for this configuration, it represents already a great step towards the simulation of the Edge Localized Modes. These first results could not have been obtained if not for the stabilization technique implemented here. The stabilized full MHD model implemented and validated here opens up a scenario for more powerful and detailed simulations for tokamak plasmas, specially in the context of ITER for which a better understanding of the physics inside the device will be needed. The goal now is to use this model to better describe the Edge-localized modes. In recent years a large number of detailed measurements of these modes has become available allowing the validations of numerical simulations.

Conclusions et Perspectives

Les simulations des plasmas de tokamaks ne sont pas simples. Elles doivent traiter différents phénomènes ayant lieux sur différentes échelles temporelles et présentant des instabilités. Pour cette raison, une méthode robuste et bien posée est nécessaire pour résoudre les modèles décrivant la physique à l'intérieur de la machine.

Dans le Chapitre 2 nous avons devéloppé les modèles magnétohydrodynamiques des plasmas ayant pour base le modèle cinétique. Le modèle monofluide de la MHD complète, celui utilisé dans nos simulations, a été obtenu. Ensuite, en faisant des simplifictions appropriées et justifiées, d'autres modèles - idéal et résistif - ont été dérivés. L'équilibre de Grad-Shafranov qui joue un rôle essentiel dans nos simulations a été lui aussi obtenu. La condition solenoïdale du champ magnétique, $\nabla \cdot \boldsymbol{B} = 0$, a été discutée et les possibilités de la surmonter ont été présentées. Dans notre cas, la formulation potentiel vecteur a été choisie et sous cette formulation la jauge de Coulmob a été utilisée.

Ensuite, une fois les modèles établis, nous avons présenté, dans le Chapitre 3, l'approche numérique uilisée dans nos simulations. Elle est basée sur la méthode des éléments finis. Plus précisement, compte tenu la symétrie axiale des tokamaks, le domaine 3D est decomposé sous forme d'un produit tensoriel entre un domaine poloïdal 2D et un domaine toroïdal 1D. Pour les plans poloïdaux, des éléments finis composés des surfaces de Bézier ont été utilisés tandis que la partie toroïdale a été discretisée par une décomposition de Fourier. De plus, lorsque l'on traite des flux dominés par convection, la méthode éléments finis seule n'est pas assez robuste. Nous avons, donc, présenté une méthode de stabilisation connue sous le nom de stabilisation Variationnelle Multi-Échelles (VMS) dont le rôle est de prendre en compte les effets des échelles non-résolues sur celles résolues. La dérivation complète de la méthode et son application dans les équations de la MHD via l'opérateur Jacobien y ont été présentées et discutées.

Dans le Chapitre 4, nous avons pu présenter les prémiers résultats de l'approche numérique. Ce chapitre a été dédié à la solution de l'équilibre de Grad-Shafranov. Il a été démontré que, si les paramètres d'entrée appropriés sont donnés, il est possible non seulement d'établir la condition initiale de la simulation MHD mais aussi de construire la grille

du domaine alignée aux lignes du champ magnétique. Une analyse detaillée des résidus de l'équation GS et la manière de la coupler au modèle de la MHD complète a été faite. Nous avons démontré que, même si l'équilibre est préservé analytiquement, cela pourrait ne pas être le cas numériquement. En effet, la construction de la grille mène à des maillages contenant des singularités et cela peut perturber la solution de l'équilibre. Par conséquent, les résidus ont tendence à croître autour des deux singularités possibles dans la configuration d'un tokamak, c'est-à-dire, l'axe magnétique et le point-X. Des techniques pour réduire ces problèmes ont été discutées. Cette analyse est impérative car des problèmes peuvent avoir lieu pendant la simulation qui ne seraient pas liés à la modélisation elle-même mais aux particularités du maillage. Il est très important de les identifier.

Dans le chapitre 5, l'instabilité dite de ≪kink≫ interne a été largement discutée. Le but principal est la validation de la méthode d'éléments finis stabilisés via l'approche VMS. En effet, nous avons montré que la stabilisation est essentielle afin d'obtenir des résultats cohérents pour cette instabilité. Une fois la validation faite, différentes études de la dynamique du kink ont été menées puisqu'il fallait s'assurer que la stabilisation contrôlait les perturbations numériques tout en préservant la physique du problème. Pour cela, le taux de croissance de l'instabilité a été étudié et les résultats obtenus ont été comparés à ceux d'autres simulations ainsi qu'à des résultats analytiques. Après cela, d'autres propriétés du mode kink ont été présentées, notamment la dépendence entre l'épaisseur de la couche du mode et la résistivité ainsi que le mouvement de la colonne de plasma. Aussi, le début du phénomène de reconnexion magnétique, un phénomène très important vu qu'il change la configuration magnétique du système, a été observé. Il est très important de souligner que tous ces résultats ont été obtenus avec le modèle de la MHD complète et grâce à la méthode de stabilisation utilisée. Ce chapitre nous a permis de valider la stratégie ouvrant un scénario pour des simulations plus détaillées des plasmas de tokamak.

Finalement, une géométrie plus complexe des plasmas, contenant un point-X, a été brièvement testée avec notre méthode et les résultats sont dans le Chapitre 6. Malgré le fait que nous n'avons pas pu obtenir beaucoup de résultats pour cette configuration, cela réprésente déjà une avancée vers les simulations des ≪Edge Localized Modes≫. Ces premiers résultats n'auraient pas pu être obtenus si la stabilisation discutée ici n'avait pas été implémentée . Le modèle de la MHD complète stabilisé et validé ici peut ouvrir le chemin à des simulations plus puissantes des plasmas de tokamak, notamment dans le cadre du projet ITER pour lequel une meilleure compréhension de la physique dans la machine est nécessaire. Le but, maintenant, est d'utiliser ce modèle pour obtenir une meilleure description des ELMS. Récemment, un grand nombre de mesures détaillées

de ces modes ont été mises à disposition permettant ainsi la validation des simulations numériques.

Appendix A

Details of the evaluations used to derive the Reduced MHD model

A.1 For any scalar A, the relation $\nabla\times(\nabla A \times \nabla\phi) = -\nabla\phi(\Delta^* A) + \frac{1}{R^2}\nabla_{\boldsymbol{\xi}}(\partial_\phi A)$ holds.

Let's start by rewriting $\nabla \times (\nabla A \times \nabla\phi)$ as $\nabla \times (\nabla \times (A\nabla\phi))$, then

$$\begin{aligned} \nabla \times (\nabla \times (A\nabla\phi)) &= -\Delta(A\nabla\phi) + \nabla(\nabla \cdot (A\nabla\phi)) && \text{(A.1)} \\ &= -\Delta(A\nabla\phi) + \nabla(A\nabla \cdot \nabla\phi + \nabla\phi \cdot \nabla A). && \text{(A.2)} \end{aligned}$$

Knowing that $\nabla\phi = \frac{1}{R}\hat{\boldsymbol{\phi}}$, then

$$A\nabla \cdot \nabla\phi = A\nabla \cdot \left(\frac{1}{R}\hat{\boldsymbol{\phi}}\right), \tag{A.3}$$

wiriting the divergence explicitly gives

$$\nabla \cdot \left(\frac{1}{R}\hat{\boldsymbol{\phi}}\right) = \hat{\boldsymbol{R}} \cdot \partial_R \left(\frac{1}{R}\hat{\boldsymbol{\phi}}\right) + \frac{1}{R^2}\hat{\boldsymbol{\phi}} \cdot \partial_\phi\hat{\boldsymbol{\phi}} + \frac{1}{R}\hat{\boldsymbol{Z}} \cdot \partial_Z\hat{\boldsymbol{\phi}}, \tag{A.4}$$

and since the only derivatives of the unitary vectors that are different from zero are $\partial_\phi\hat{\boldsymbol{R}} = \hat{\boldsymbol{\phi}}$ and $\partial_\phi\hat{\boldsymbol{\phi}} = -\hat{\boldsymbol{R}}$, it yields

$$\nabla \cdot \left(\frac{1}{R}\hat{\boldsymbol{\phi}}\right) = \cancelto{0}{-\frac{1}{R^2}\hat{\boldsymbol{\phi}} \cdot \hat{\boldsymbol{R}}}. \tag{A.5}$$

Therefore, (A.36) becomes

$$\nabla \times (\nabla \times (A\nabla\phi)) = -\Delta(A\nabla\phi) + \nabla\left(\frac{1}{R^2}\partial_\phi A\right). \tag{A.6}$$

Now, the term $\nabla\left(\frac{1}{R^2}\partial_\phi A\right)$ is

$$\begin{aligned}
\nabla\left(\frac{1}{R^2}\partial_\phi A\right) &= \nabla\left(\frac{1}{R^2}\right)\partial_\phi A + \frac{1}{R^2}\nabla(\partial_\phi A) \\
&= -\frac{2}{R^3}\partial_\phi A\hat{\boldsymbol{R}} + \frac{1}{R^2}\nabla(\partial_\phi A) \\
&= -\frac{2}{R^3}\partial_\phi A\hat{\boldsymbol{R}} + \frac{1}{R^2}(\nabla_{\boldsymbol{\xi}}\partial_\phi A + \nabla\phi\partial_\phi^2 A),
\end{aligned} \tag{A.7}$$

and the term $\Delta(A\nabla\phi)$ is

$$\begin{aligned}
\Delta(A\nabla\phi) &= \Delta\left(\frac{A}{R}\hat{\boldsymbol{\phi}}\right) \\
&= -\frac{2}{R^3}\partial_\phi A\hat{\boldsymbol{R}} + \left(\Delta\left(\frac{A}{R}\right) - \frac{A}{R^3}\right)\hat{\boldsymbol{\phi}} \\
&= -\frac{2}{R^3}\partial_\phi A\hat{\boldsymbol{R}} + \left(\frac{1}{R}\partial_R\left(R\partial_R\frac{A}{R}\right) + \frac{1}{R^2}\partial_\phi^2\frac{A}{R} + \partial_Z^2\frac{A}{R} - \frac{A}{R^3}\right)\hat{\boldsymbol{\phi}} \\
&= -\frac{2}{R^3}\partial_\phi A\hat{\boldsymbol{R}} + \left(\partial_R\left(\partial_R A - \frac{A}{R}\right) + \frac{1}{R^2}\partial_\phi^2 A + \partial_Z^2 A - \frac{A}{R^2}\right)\nabla\phi \\
&= -\frac{2}{R^3}\partial_\phi A\hat{\boldsymbol{R}} + \left(\partial_R^2 A + \frac{A}{R^2} - \frac{1}{R}\partial_R A + \frac{1}{R^2}\partial_\phi^2 A + \partial_Z^2 A - \frac{A}{R^2}\right)\nabla\phi \\
&= -\frac{2}{R^3}\partial_\phi A\hat{\boldsymbol{R}} + \left(\partial_R^2 A - \frac{1}{R}\partial_R A + \frac{1}{R^2}\partial_\phi^2 A + \partial_Z^2 A\right)\nabla\phi \\
&= -\frac{2}{R^3}\partial_\phi A\hat{\boldsymbol{R}} + \left(\Delta^* A + \frac{1}{R^2}\partial_\phi^2 A\right)\nabla\phi.
\end{aligned} \tag{A.8}$$

Now, putting (A.7) and (A.8) in (A.6) yields

$$\nabla \times (\nabla \times (A\nabla\phi)) = -\nabla\phi(\Delta^* A) + \frac{1}{R^2}\nabla_{\boldsymbol{\xi}}(\partial_\phi A). \tag{A.9}$$

Relation (A.9) is exactly the one shown in (2.128) in Chapter 2.

A.2 Derivation of $\boldsymbol{v} \cdot \nabla\boldsymbol{v}$

First of all, the following vector indentity is considered

$$\nabla \cdot (\boldsymbol{a} \cdot \boldsymbol{b}) = \boldsymbol{a} \times (\nabla \times \boldsymbol{b}) + \boldsymbol{b} \times (\nabla \times \boldsymbol{a}) + \boldsymbol{a} \cdot \nabla\boldsymbol{b} + \boldsymbol{b} \cdot \nabla\boldsymbol{a}. \tag{A.10}$$

When $\boldsymbol{a} = \boldsymbol{b} = \boldsymbol{v}$,

$$\begin{aligned}
\nabla \cdot (\boldsymbol{v} \cdot \boldsymbol{v}) &= \boldsymbol{v} \times (\nabla \times \boldsymbol{v}) + \boldsymbol{v} \times (\nabla \times \boldsymbol{v}) + \boldsymbol{v} \cdot \nabla \boldsymbol{v} + \boldsymbol{v} \cdot \nabla \boldsymbol{v} \\
\nabla |\boldsymbol{v}|^2 &= 2(\boldsymbol{v} \times (\nabla \times \boldsymbol{v})) + 2(\boldsymbol{v} \cdot \nabla \boldsymbol{v}) \\
\boldsymbol{v} \cdot \nabla \boldsymbol{v} &= \nabla \left(\frac{|\boldsymbol{v}|^2}{2} \right) - \boldsymbol{v} \times (\nabla \times \boldsymbol{v}). \qquad \text{(A.11)}
\end{aligned}$$

If we define the quantity $\boldsymbol{\Omega} = \nabla \times \boldsymbol{v}$, the expression above becomes

$$\boldsymbol{v} \cdot \nabla \boldsymbol{v} = \nabla \left(\frac{|\boldsymbol{v}|^2}{2} \right) - \boldsymbol{v} \times \boldsymbol{\Omega}. \qquad \text{(A.12)}$$

Now, let's consider the following profile for the velocity $\boldsymbol{v} = \vartheta F \nabla \phi + \boldsymbol{v}_{2D}$ and treat the equation above, term by term. First of all, Equation (2.146) gives, for $\boldsymbol{v}'_{\perp} = 0$ and $F_0 \approx F$

$$\boldsymbol{v}_{2D} = \vartheta (\nabla \psi \times \nabla \phi) + R^2 (\nabla \phi \times \nabla U). \qquad \text{(A.13)}$$

Hence,

$$\boldsymbol{v} = \vartheta F \nabla \phi + \vartheta (\nabla \psi \times \nabla \phi) + R^2 (\nabla \phi \times \nabla U). \qquad \text{(A.14)}$$

For the evaluation of $\boldsymbol{\Omega}$, let's consider it term by term. First

$$\begin{aligned}
\nabla \times (\vartheta F \nabla \phi) &= \nabla (F \vartheta) \times \nabla \phi + \cancelto{0}{F \vartheta (\nabla \times \nabla \phi)}, \\
&= \nabla (F \vartheta) \times \nabla \phi. \qquad \text{(A.15)}
\end{aligned}$$

Then,

$$\nabla \times (\vartheta (\nabla \psi \times \nabla \phi)) = -\nabla \vartheta \times (\nabla \phi \times \nabla \psi) - \vartheta (\nabla \times (\nabla \phi \times \nabla \psi)), \qquad \text{(A.16)}$$

for the second term on the RHS, we use the relation (A.9) developped before, to obtain

$$\nabla \times (\vartheta (\nabla \psi \times \nabla \phi)) = -\nabla \vartheta \times (\nabla \phi \times \nabla \psi) - \vartheta \left(\nabla \phi (\Delta^* \psi) - \frac{1}{R^2} \nabla_{\boldsymbol{\xi}} (\partial_\phi \psi) \right), \qquad \text{(A.17)}$$

finally,

$$\begin{aligned}
\nabla \times R^2 (\nabla \phi \times \nabla U) &= \nabla R^2 \times (\nabla \phi \times \nabla U) + R^2 (\nabla \times (\nabla \phi \times \nabla U)), \\
&= 2R \nabla R \times (\nabla \phi \times \nabla U) + R^2 \left(\nabla \phi (\Delta^* U) - \frac{1}{R^2} \nabla_{\boldsymbol{\xi}} (\partial_\phi U) \right) \\
&= R^2 \left(\frac{2}{R} \nabla R \times (\nabla \phi \times \nabla U) + \nabla \phi (\Delta^* U) - \frac{1}{R^2} \nabla_{\boldsymbol{\xi}} (\partial_\phi U) \right).
\end{aligned}$$

Therefore

$$\begin{aligned}\boldsymbol{\Omega} = \nabla(F\vartheta)\times\nabla\phi - \nabla\vartheta\times(\nabla\phi\times\nabla\psi) - \vartheta\left(\nabla\phi(\Delta^*\psi) - \frac{1}{R^2}\nabla_{\boldsymbol{\xi}}(\partial_\phi\psi)\right)\\ +R^2\left(\frac{2}{R}\nabla R\times(\nabla\phi\times\nabla U) + \nabla\phi(\Delta^* U) - \frac{1}{R^2}\nabla_{\boldsymbol{\xi}}(\partial_\phi U)\right).\end{aligned} \tag{A.18}$$

In order to avoid explicit compuation of second order derivatives, we introduce the variables j_ϕ and ω defined as $j_\phi = \Delta^*\psi$ and $\omega = \Delta^* U + \frac{2}{R}\partial_R U$, as $\nabla R\times(\nabla\phi\times\nabla U) = \partial_R U\nabla\phi$. Thus,

$$\begin{aligned}\nabla\vartheta\times(\nabla\phi\times\nabla\psi) &= (\nabla\vartheta\cdot\nabla\psi)\nabla\phi - (\nabla\vartheta\cdot\nabla\phi)\nabla\psi,\\ &= (\nabla\vartheta\cdot\nabla\psi)\nabla\phi - \frac{1}{R^2}\partial_\phi\vartheta\nabla\psi,\end{aligned} \tag{A.19}$$

$\nabla\psi$ can be decomposed to sort out its poloidal and toroidal components, yielding

$$\begin{aligned}\nabla\vartheta\times(\nabla\phi\times\nabla\psi) &= (\nabla\vartheta\cdot\nabla\psi)\nabla\phi - \frac{1}{R^2}\partial_\phi\vartheta(\nabla_{\boldsymbol{\xi}}\psi + \nabla\phi\partial_\phi\psi),\\ &= (\nabla_{\boldsymbol{\xi}}\vartheta\cdot\nabla_{\boldsymbol{\xi}}\psi)\nabla\phi - \frac{1}{R^2}\partial_\phi\vartheta\nabla_{\boldsymbol{\xi}}\psi.\end{aligned} \tag{A.20}$$

Therefore

$$\boldsymbol{\Omega} = \nabla\phi(R^2\omega - \vartheta j_\phi - \nabla_{\boldsymbol{\xi}}\vartheta\cdot\nabla_{\boldsymbol{\xi}}\psi) + \nabla(F\vartheta)\times\nabla\phi + \frac{1}{R^2}(\vartheta\nabla_{\boldsymbol{\xi}}(\partial_\phi\psi) - R^2\nabla_{\boldsymbol{\xi}}(\partial_\phi U) + \partial_\phi\vartheta\nabla_{\boldsymbol{\xi}}\psi).$$

In order to simplify the computation, we will use

$$\boldsymbol{v} = \vartheta F\nabla\phi + R\mathbb{V}_{2D}\times\nabla\phi \quad\text{and}\quad \boldsymbol{\Omega} = R\boldsymbol{\Omega}_\phi\nabla\phi + \nabla(F\vartheta)\times\nabla\phi + (\nabla\phi\times\mathbb{H}_{2D})\times\nabla\phi \tag{A.21}$$

where

$$R\mathbb{V}_{2D} = \vartheta\nabla_{\boldsymbol{\xi}}\psi - R^2\nabla_{\boldsymbol{\xi}}U \tag{A.22}$$

$$R\Omega_\phi = R^2\omega - \vartheta j_\phi - \nabla_{\boldsymbol{\xi}}\vartheta\cdot\nabla_{\boldsymbol{\xi}}\psi \tag{A.23}$$

$$\mathbb{H}_{2D} = \vartheta\nabla_{\boldsymbol{\xi}}(\partial_\phi\psi) - R^2\nabla_{\boldsymbol{\xi}}(\partial_\phi U) + \partial_\phi\vartheta\nabla_{\boldsymbol{\xi}}\psi. \tag{A.24}$$

Now, the term $\boldsymbol{v}\times\boldsymbol{\Omega}$ can be written as

$$\begin{aligned}\boldsymbol{v}\times\boldsymbol{\Omega} = F\vartheta R\Omega\phi\cancelto{0}{(\nabla\phi\times\nabla\phi)} + F\vartheta(\nabla\phi\times(\nabla(F\vartheta)\times\nabla\phi)) + F\vartheta\nabla\phi\times((\nabla\phi\times\mathbb{H}_{2D})\times\nabla\phi)\\ -R\boldsymbol{\Omega}_\phi(\nabla\phi\times(R\mathbb{V}_{2D}\times\nabla\phi)) - R(\mathbb{V}_{2D}\times\nabla\phi)\times(\nabla\phi\times(\nabla(F\vartheta) + \nabla\phi\times\mathbb{H}_{2D})).\end{aligned}$$

Again, let's deal with it term by term

$$\begin{aligned} F\vartheta(\nabla\phi\times(\nabla(F\vartheta)\times\nabla\phi)) &= F\vartheta((\nabla\phi\cdot\nabla\phi)\nabla(F\vartheta)-(\nabla\phi\cdot\nabla(F\vartheta))\nabla\phi), \\ &= \frac{F\vartheta}{R^2}\nabla_{\boldsymbol{\xi}}(F\vartheta)-\frac{F\vartheta}{R}\cancelto{0}{(\partial_\phi(F\vartheta))}\nabla\phi, \\ &= \frac{1}{R^2}\nabla_{\boldsymbol{\xi}}\left(\frac{F^2\vartheta^2}{2}\right), \end{aligned} \tag{A.25}$$

where $\partial_\phi(F\vartheta)\to 0$ because F and ϑ depend only on the poloidal coordinates. For the same reason, $\nabla(F\vartheta)\to\nabla_{\boldsymbol{\xi}}(F\vartheta)$. For the second one

$$\begin{aligned} F\vartheta\nabla\phi\times((\nabla\phi\times\mathbb{H}_{2D})\times\nabla\phi) &= -F\vartheta\nabla\phi\times(\nabla\phi\times(\nabla\phi\times\mathbb{H}_{2D})), \\ &= -F\vartheta\nabla\phi\times(\cancelto{0}{(\nabla\phi\cdot\mathbb{H}_{2D})}\nabla\phi-(\nabla\phi\cdot\nabla\phi)\mathbb{H}_{2D}), \\ &= \frac{F\vartheta}{R^2}(\nabla\phi\times\mathbb{H}_{2D}), \end{aligned} \tag{A.26}$$

where $(\nabla\phi\cdot\mathbb{H}_{2D})\to 0$ for the same reason. Then

$$\begin{aligned} -R\boldsymbol{\Omega}_\phi(\nabla\phi\times(R\mathbb{V}_{2D}\times\nabla\phi)) &= -R^2\boldsymbol{\Omega}_\phi((\nabla\phi\cdot\nabla\phi)\mathbb{V}_{2D}-\cancelto{0}{(\nabla\phi\cdot\mathbb{V}_{2D})}\nabla\phi), \\ &= -\boldsymbol{\Omega}_\phi\mathbb{V}_{2D}. \end{aligned} \tag{A.27}$$

Finally,$-R(\mathbb{V}_{2D}\times\nabla\phi)\times(\nabla\phi\times(\nabla(F\vartheta)+\nabla\phi\times\mathbb{H}_{2D}))$ can be rewritten as

$$-R(((\mathbb{V}_{2D}\times\nabla\phi)\cdot(\nabla(F\vartheta)+\nabla\phi\times\mathbb{H}_{2D}))\nabla\phi-\cancelto{0}{((\mathbb{V}_{2D}\times\nabla\phi)\cdot\nabla\phi)}(\nabla(F\vartheta)+\nabla\phi\times\mathbb{H}_{2D}),$$

yielding

$$-R(\mathbb{V}_{2D}\times\nabla\phi)\times(\nabla\phi\times(\nabla(F\vartheta)+\nabla\phi\times\mathbb{H}_{2D}))=-R\nabla\phi((\mathbb{V}_{2D}\times\nabla\phi)\cdot(\nabla(F\vartheta)+\nabla\phi\times\mathbb{H}_{2D})).$$

Therefore

$$\boldsymbol{v}\times\boldsymbol{\Omega}=\frac{1}{R^2}\nabla_{\boldsymbol{\xi}}\left(\frac{F^2\vartheta^2}{2}\right)+\frac{F\vartheta}{R^2}(\nabla\phi\times\mathbb{H}_{2D})-\boldsymbol{\Omega}_\phi\mathbb{V}_{2D}-R\nabla\phi((\mathbb{V}_{2D}\times\nabla\phi)\cdot(\nabla(F\vartheta)+\nabla\phi\times\mathbb{H}_{2D})). \tag{A.28}$$

Now, $R((\mathbb{V}_{2D}\times\nabla\phi)\cdot(\nabla(F\vartheta)+\nabla\phi\times\mathbb{H}_{2D}))$ can be evaluated as

$$(R\mathbb{V}_{2D}\times\nabla\phi)\cdot\nabla(F\vartheta)+(R\mathbb{V}_{2D}\times\nabla\phi)\cdot(\nabla\phi\times\mathbb{H}_{2D}), \tag{A.29}$$

wich by using $(R\mathbb{V}_{2D}\times\nabla\phi)=\boldsymbol{v}-F\vartheta\nabla\phi$ and

$$(R\mathbb{V}_{2D}\times\nabla\phi)\cdot(\nabla\phi\times\mathbb{H}_{2D})=\cancelto{0}{(R\mathbb{V}_{2D}\cdot\nabla\phi)}\cancelto{0}{(\nabla\phi\cdot\mathbb{H}_{2D})}-\frac{1}{R^2}(R\mathbb{V}_{2D}\cdot\mathbb{H}_{2D}). \tag{A.30}$$

Thus

$$\begin{aligned} R((\mathbb{V}_{2D} \times \nabla\phi) \cdot (\nabla(F\vartheta) + \nabla\phi \times \mathbb{H}_{2D}) &= (\boldsymbol{v} - F\vartheta\nabla\phi) \cdot \nabla(F\vartheta) - \frac{1}{R^2}(R\mathbb{V}_{2D} \cdot \mathbb{H}_{2D}), \\ &= \boldsymbol{v} \cdot \nabla(F\vartheta) - \partial_\phi \left(\frac{F^2\vartheta^2}{2}\right) - \frac{1}{R^2}(R\mathbb{V}_{2D} \cdot \mathbb{H}_{2D}). \end{aligned}$$

Now, for $R\mathbb{V}_{2D} \cdot \mathbb{H}_{2D}$

$$\begin{aligned} R\mathbb{V}_{2D} \cdot \mathbb{H}_{2D} &= \vartheta\nabla_{\boldsymbol{\xi}}\psi \cdot \left(\vartheta\nabla_{\boldsymbol{\xi}}(\partial_\phi\psi) - R^2\nabla_{\boldsymbol{\xi}}(\partial_\phi U) + \partial_\phi\vartheta\nabla_{\boldsymbol{\xi}}\psi\right) \\ &\quad -R^2\nabla_{\boldsymbol{\xi}}U \cdot \left(\vartheta\nabla_{\boldsymbol{\xi}}(\partial_\phi\psi) - R^2\nabla_{\boldsymbol{\xi}}(\partial_\phi U) + \partial_\phi\vartheta\nabla_{\boldsymbol{\xi}}\psi\right), \\ &= \partial_\phi \left(\frac{|\vartheta\nabla_{\boldsymbol{\xi}}\psi|^2 - 2R^2\vartheta\nabla_{\boldsymbol{\xi}}\psi \cdot \nabla_{\boldsymbol{\xi}}U + |R^2\nabla_{\boldsymbol{\xi}}U|^2}{2}\right), \\ &= \partial_\phi \left(\frac{|\vartheta\nabla_{\boldsymbol{\xi}}\psi - |R^2\nabla_{\boldsymbol{\xi}}U|^2}{2}\right), \\ &= R^2\partial_\phi \left(\frac{|\mathbb{V}_{2D}|^2}{2}\right). \end{aligned} \tag{A.31}$$

Thus

$$R((\mathbb{V}_{2D} \times \nabla\phi) \cdot (\nabla(F\vartheta) + \nabla\phi \times \mathbb{H}_{2D}) = \boldsymbol{v} \cdot \nabla(F\vartheta)\partial_\phi \left(\frac{|\boldsymbol{v}|^2}{2}\right). \tag{A.32}$$

Putting everything together

$$\boldsymbol{\Omega} = R\boldsymbol{\Omega}_\phi\nabla\phi + \nabla(F\vartheta) \times \nabla\phi + (\nabla\phi \times \mathbb{H}_{2D}) \times \nabla\phi \tag{A.33}$$

which yields

$$\boldsymbol{v} \times \boldsymbol{\Omega} = \nabla\phi \left(-\boldsymbol{v} \cdot \nabla(F\vartheta) + \partial_\phi \left(\frac{|\boldsymbol{v}|^2}{2}\right)\right) + \frac{1}{R^2}\nabla_{\boldsymbol{\xi}} \left(\frac{F^2\vartheta^2}{2}\right) + \frac{F\vartheta}{R^2}\nabla\phi \times \mathbb{H}_{2D} - \boldsymbol{\Omega}_\phi\mathbb{V}_{2D} \tag{A.34}$$

Therefore

$$\nabla\left(\frac{|\boldsymbol{v}|^2}{2}\right) - \boldsymbol{v} \times \boldsymbol{\Omega} = \nabla\phi\,(\boldsymbol{v} \cdot \nabla(F\vartheta)) + \nabla_{\boldsymbol{\xi}} \left(\frac{|\boldsymbol{v}|^2}{2}\right) - \frac{1}{R^2}\nabla_{\boldsymbol{\xi}} \left(\frac{F^2\vartheta^2}{2}\right) - \frac{F\vartheta}{R^2}\nabla\phi \times \mathbb{H}_{2D} + \boldsymbol{\Omega}_\phi\mathbb{V}_{2D}, \tag{A.35}$$

which is the same as

$$\boldsymbol{v} \cdot \nabla\boldsymbol{v} = \nabla\phi\,(\boldsymbol{v} \cdot \nabla(F\vartheta)) + \nabla_{\boldsymbol{\xi}} \left(\frac{|\boldsymbol{v}|^2}{2}\right) - \frac{1}{R^2}\nabla_{\boldsymbol{\xi}} \left(\frac{F^2\vartheta^2}{2}\right) - \frac{F\vartheta}{R^2}\nabla\phi \times \mathbb{H}_{2D} + \boldsymbol{\Omega}_\phi\mathbb{V}_{2D}. \tag{A.36}$$

Equation (A.36) is exactly the same as Equation (2.157).

Appendix B

Coefficients of the Discrete Fourier Transform

B.1 Modes retained when evaluating the RHS

The relations are shown in (3.134) and are

$$\begin{aligned}
\underline{\boldsymbol{\mathcal{R}}}^{(k)}_{i_{2D},1} &= \boldsymbol{RE}\left((-i0)^k Z_0^{(k)}\right), \\
\underline{\boldsymbol{\mathcal{R}}}^{(k)}_{i_{2D},2m} &= \boldsymbol{RE}\left((-im)^k Z_m^{(k)}\right), \\
\underline{\boldsymbol{\mathcal{R}}}^{(k)}_{i_{2D},2m+1} &= -\boldsymbol{IM}\left((-im)^k Z_m^{(k)}\right).
\end{aligned} \tag{B.1}$$

Only the first modes will be retained, yielding

$$\begin{aligned}
\underline{\boldsymbol{\mathcal{R}}}^{(0)}_{i_{2D},1} &= \boldsymbol{RE}\left(Z_0^{(0)}\right), \\
\underline{\boldsymbol{\mathcal{R}}}^{(0)}_{i_{2D},2m} &= \boldsymbol{RE}\left(Z_m^{(0)}\right), \qquad 0 < m < \frac{N_\phi + 1}{2}, \\
\underline{\boldsymbol{\mathcal{R}}}^{(0)}_{i_{2D},2m+1} &= -\boldsymbol{IM}\left(Z_m^{(0)}\right),
\end{aligned} \tag{B.2}$$

and

$$\begin{aligned}
\underline{\boldsymbol{\mathcal{R}}}^{(1)}_{i_{2D},1} &= \boldsymbol{RE}\left(0 Z_0^{(1)}\right) &&= 0, \\
\underline{\boldsymbol{\mathcal{R}}}^{(1)}_{i_{2D},2m} &= m\boldsymbol{RE}\left(-i Z_m^{(1)}\right) &&= m\boldsymbol{IM}\left(Z_m^{(1)}\right), \quad 0 < m\frac{N_\phi + 1}{2}. \\
\underline{\boldsymbol{\mathcal{R}}}^{(1)}_{i_{2D},2m+1} &= -m\boldsymbol{IM}\left(-i Z_m^{(1)}\right) &&= m\boldsymbol{RE}\left(Z_m^{(1)}\right),
\end{aligned} \tag{B.3}$$

B.2 Modes retained when evaluating the Jacobian

They are separated into two case: the non-degenerated ones first and the degenerated after.

B.2.1 Non-degenerated cases

The relations are shown in (3.138) and are

$$\begin{cases} \underline{\mathbb{A}}^{kl}_{2m,2n} - \underline{\mathbb{A}}^{kl}_{2m+1,2n+1} - i(\underline{\mathbb{A}}^{kl}_{2m,2n+1} + \underline{\mathbb{A}}^{kl}_{2m+1,2n}) &= (-i)^{k+l} m^k n^l Z^{(kl)}_{m+n} \\ \underline{\mathbb{A}}^{kl}_{2m,2n} + \underline{\mathbb{A}}^{kl}_{2m+1,2n+1} + i(\underline{\mathbb{A}}^{kl}_{2m,2n+1} - \underline{\mathbb{A}}^{kl}_{2m+1,2n}) &= i^{k+l}(-1)^k m^k n^l Z^{(kl)}_{m-n} \\ \underline{\mathbb{A}}^{kl}_{2m,2n} + \underline{\mathbb{A}}^{kl}_{2m+1,2n+1} - i(\underline{\mathbb{A}}^{kl}_{2m,2n+1} - \underline{\mathbb{A}}^{kl}_{2m+1,2n}) &= i^{k+l}(-1)^l m^k n^l Z^{(kl)}_{n-m} \end{cases} \tag{B.4}$$

For $m \geq n > 0$, they are

$$\begin{aligned} \underline{\mathbb{A}}^{kl}_{2m,2n} &= m^k n^l \frac{+\boldsymbol{RE}\left((-i)^{k+l} Z^{(kl)}_{m+n}\right) + \boldsymbol{RE}\left(i^l (-i)^k Z^{(kl)}_{m-n}\right)}{2}, \\ \underline{\mathbb{A}}^{kl}_{2m+1,2n} &= m^k n^l \frac{-\boldsymbol{IM}\left((-i)^{k+l} Z^{(kl)}_{m+n}\right) - \boldsymbol{IM}\left(i^l (-i)^k Z^{(kl)}_{m-n}\right)}{2}, \\ \underline{\mathbb{A}}^{kl}_{2m,2n+1} &= m^k n^l \frac{-\boldsymbol{IM}\left((-i)^{k+l} Z^{(kl)}_{m+n}\right) + \boldsymbol{IM}\left(i^l (-i)^k Z^{(kl)}_{m-n}\right)}{2}, \\ \underline{\mathbb{A}}^{kl}_{2m+1,2n+1} &= m^k n^l \frac{-\boldsymbol{RE}\left((-i)^{k+l} Z^{(kl)}_{m+n}\right) + \boldsymbol{RE}\left(i^l (-i)^k Z^{(kl)}_{m-n}\right)}{2}. \end{aligned} \tag{B.5}$$

For $n > m > 0$, they are

$$\begin{aligned} \underline{\mathbb{A}}^{kl}_{2m,2n} &= m^k n^l \frac{+\boldsymbol{RE}\left((-i)^{k+l} Z^{(kl)}_{m+n}\right) + \boldsymbol{RE}\left(i^k (-i)^l Z^{(kl)}_{n-m}\right)}{2}, \\ \underline{\mathbb{A}}^{kl}_{2m+1,2n} &= m^k n^l \frac{-\boldsymbol{IM}\left((-i)^{k+l} Z^{(kl)}_{m+n}\right) + \boldsymbol{IM}\left(i^k (-i)^l Z^{(kl)}_{n-m}\right)}{2}, \\ \underline{\mathbb{A}}^{kl}_{2m,2n+1} &= m^k n^l \frac{-\boldsymbol{IM}\left((-i)^{k+l} Z^{(kl)}_{m+n}\right) - \boldsymbol{IM}\left(i^k (-i)^l Z^{(kl)}_{n-m}\right)}{2}, \\ \underline{\mathbb{A}}^{kl}_{2m+1,2n+1} &= m^k n^l \frac{-\boldsymbol{RE}\left((-i)^{k+l} Z^{(kl)}_{m+n}\right) + \boldsymbol{RE}\left(i^k (-i)^l Z^{(kl)}_{n-m}\right)}{2}. \end{aligned} \tag{B.6}$$

For any of these cases, $0 < m$, $n < \frac{N_\phi+1}{2}$, $m+n < \frac{N_p+1}{2}$ and $|m-n| < \frac{N_p+1}{2}$. Details of thses expressions in different contexts that appear in practice are given below

- **Case of** $k = l = 0$

$k = l = 0$	when $m \geq n > 0$	when $0 < m < n$
$\underline{\mathbb{A}}^{00}_{2m,2n}$	$\dfrac{+\boldsymbol{RE}\left(Z^{(00)}_{m+n}\right) + \boldsymbol{RE}\left(Z^{(00)}_{m-n}\right)}{2}$	$\dfrac{+\boldsymbol{RE}\left(Z^{(00)}_{m+n}\right) + \boldsymbol{RE}\left(Z^{(00)}_{n-m}\right)}{2}$
$\underline{\mathbb{A}}^{00}_{2m+1,2n}$	$\dfrac{-\boldsymbol{IM}\left(Z^{(00)}_{m+n}\right) - \boldsymbol{IM}\left(Z^{(00)}_{m-n}\right)}{2}$	$\dfrac{-\boldsymbol{IM}\left(Z^{(00)}_{m+n}\right) + \boldsymbol{IM}\left(Z^{(00)}_{n-m}\right)}{2}$
$\underline{\mathbb{A}}^{00}_{2m,2n+1}$	$\dfrac{-\boldsymbol{IM}\left(Z^{(00)}_{m+n}\right) + \boldsymbol{IM}\left(Z^{(00)}_{m-n}\right)}{2}$	$\dfrac{-\boldsymbol{IM}\left(Z^{(00)}_{m+n}\right) - \boldsymbol{IM}\left(Z^{(00)}_{n-m}\right)}{2}$
$\underline{\mathbb{A}}^{00}_{2m+1,2n+1}$	$\dfrac{-\boldsymbol{RE}\left(Z^{(00)}_{m+n}\right) + \boldsymbol{RE}\left(Z^{(00)}_{m-n}\right)}{2}$	$\dfrac{-\boldsymbol{RE}\left(Z^{(00)}_{m+n}\right) + \boldsymbol{RE}\left(Z^{(00)}_{n-m}\right)}{2}$

- **Case of** $k = 0,\ l = 1$

$k = 0,\ l = 1$	when $m \geq n > 0$	when $0 < m < n$
$\underline{\mathbb{A}}^{01}_{2m,2n}$	$n\dfrac{+\boldsymbol{IM}\left(Z^{(01)}_{m+n}\right) - \boldsymbol{IM}\left(Z^{(01)}_{m-n}\right)}{2}$	$n\dfrac{+\boldsymbol{IM}\left(Z^{(01)}_{m+n}\right) + \boldsymbol{IM}\left(Z^{(01)}_{n-m}\right)}{2}$
$\underline{\mathbb{A}}^{01}_{2m+1,2n}$	$n\dfrac{+\boldsymbol{RE}\left(Z^{(01)}_{m+n}\right) - \boldsymbol{RE}\left(Z^{(01)}_{m-n}\right)}{2}$	$n\dfrac{+\boldsymbol{RE}\left(Z^{(01)}_{m+n}\right) - \boldsymbol{RE}\left(Z^{(01)}_{n-m}\right)}{2}$
$\underline{\mathbb{A}}^{01}_{2m,2n+1}$	$n\dfrac{+\boldsymbol{RE}\left(Z^{(01)}_{m+n}\right) + \boldsymbol{RE}\left(Z^{(01)}_{m-n}\right)}{2}$	$n\dfrac{+\boldsymbol{RE}\left(Z^{(01)}_{m+n}\right) + \boldsymbol{RE}\left(Z^{(01)}_{n-m}\right)}{2}$
$\underline{\mathbb{A}}^{01}_{2m+1,2n+1}$	$n\dfrac{-\boldsymbol{IM}\left(Z^{(01)}_{m+n}\right) - \boldsymbol{IM}\left(Z^{(01)}_{m-n}\right)}{2}$	$n\dfrac{-\boldsymbol{IM}\left(Z^{(01)}_{m+n}\right) + \boldsymbol{IM}\left(Z^{(01)}_{n-m}\right)}{2}$

- **Case of** $k = 1,\ l = 0$

$k = 1,\ l = 0$	when $m \geq n > 0$	when $0 < m < n$
$\underline{\mathbb{A}}^{10}_{2m,2n}$	$m\dfrac{+\boldsymbol{IM}\left(Z^{(10)}_{m+n}\right) + \boldsymbol{IM}\left(Z^{(10)}_{m-n}\right)}{2}$	$m\dfrac{+\boldsymbol{IM}\left(Z^{(10)}_{m+n}\right) - \boldsymbol{IM}\left(Z^{(10)}_{n-m}\right)}{2}$
$\underline{\mathbb{A}}^{10}_{2m+1,2n}$	$m\dfrac{+\boldsymbol{RE}\left(Z^{(10)}_{m+n}\right) + \boldsymbol{RE}\left(Z^{(10)}_{m-n}\right)}{2}$	$m\dfrac{+\boldsymbol{RE}\left(Z^{(10)}_{m+n}\right) + \boldsymbol{RE}\left(Z^{(10)}_{n-m}\right)}{2}$
$\underline{\mathbb{A}}^{10}_{2m,2n+1}$	$m\dfrac{+\boldsymbol{RE}\left(Z^{(10)}_{m+n}\right) - \boldsymbol{RE}\left(Z^{(10)}_{m-n}\right)}{2}$	$m\dfrac{+\boldsymbol{RE}\left(Z^{(10)}_{m+n}\right) - \boldsymbol{RE}\left(Z^{(10)}_{n-m}\right)}{2}$
$\underline{\mathbb{A}}^{10}_{2m+1,2n+1}$	$m\dfrac{-\boldsymbol{IM}\left(Z^{(10)}_{m+n}\right) + \boldsymbol{IM}\left(Z^{(10)}_{m-n}\right)}{2}$	$m\dfrac{-\boldsymbol{IM}\left(Z^{(10)}_{m+n}\right) - \boldsymbol{IM}\left(Z^{(10)}_{n-m}\right)}{2}$

- **Case of** $k = l = 1$

$k=l=1$	when $m \geq n > 0$	when $0 < m < n$
$\underline{\mathbb{A}}^{11}_{2m,2n}$	$mn\dfrac{-\boldsymbol{RE}\left(Z^{(11)}_{m+n}\right)+\boldsymbol{RE}\left(Z^{(11)}_{m-n}\right)}{2}$	$mn\dfrac{-\boldsymbol{RE}\left(Z^{(11)}_{m+n}\right)+\boldsymbol{RE}\left(Z^{(11)}_{n-m}\right)}{2}$
$\underline{\mathbb{A}}^{11}_{2m+1,2n}$	$mn\dfrac{+\boldsymbol{IM}\left(Z^{(11)}_{m+n}\right)-\boldsymbol{IM}\left(Z^{(11)}_{m-n}\right)}{2}$	$mn\dfrac{+\boldsymbol{IM}\left(Z^{(11)}_{m+n}\right)+\boldsymbol{IM}\left(Z^{(11)}_{n-m}\right)}{2}$
$\underline{\mathbb{A}}^{11}_{2m,2n+1}$	$mn\dfrac{+\boldsymbol{IM}\left(Z^{(11)}_{m+n}\right)+\boldsymbol{IM}\left(Z^{(11)}_{m-n}\right)}{2}$	$mn\dfrac{+\boldsymbol{IM}\left(Z^{(11)}_{m+n}\right)-\boldsymbol{IM}\left(Z^{(11)}_{n-m}\right)}{2}$
$\underline{\mathbb{A}}^{11}_{2m+1,2n+1}$	$mn\dfrac{+\boldsymbol{RE}\left(Z^{(11)}_{m+n}\right)+\boldsymbol{RE}\left(Z^{(11)}_{m-n}\right)}{2}$	$mn\dfrac{+\boldsymbol{RE}\left(Z^{(11)}_{m+n}\right)+\boldsymbol{RE}\left(Z^{(11)}_{n-m}\right)}{2}$

B.2.2 Degenerated cases

There are three degenrated cases

- $i_\phi = 1$ **and** $j_\phi > 1$ In this case, it is enough to consider the general expressions in (B.6) by doing $m = 0$ but $2m = 1$. It leads to

when $0 = m < n$	$0 = m < n$
$\underline{\mathbb{A}}^{00}_{1,2n} = \dfrac{+\boldsymbol{RE}\left(Z^{(00)}_n\right)+\boldsymbol{RE}\left(Z^{(00)}_n\right)}{2}$	$\underline{\mathbb{A}}^{01}_{1,2n} = n\dfrac{+\boldsymbol{IM}\left(Z^{(01)}_n\right)+\boldsymbol{IM}\left(Z^{(01)}_n\right)}{2}$
$\underline{\mathbb{A}}^{00}_{2,2n} = \dfrac{-\boldsymbol{IM}\left(Z^{(00)}_n\right)+\boldsymbol{IM}\left(Z^{(00)}_n\right)}{2}$	$\underline{\mathbb{A}}^{01}_{2,2n} = n\dfrac{+\boldsymbol{RE}\left(Z^{(01)}_n\right)-\boldsymbol{RE}\left(Z^{(01)}_n\right)}{2}$
$\underline{\mathbb{A}}^{00}_{1,2n+1} = \dfrac{-\boldsymbol{IM}\left(Z^{(00)}_n\right)-\boldsymbol{IM}\left(Z^{(00)}_n\right)}{2}$	$\underline{\mathbb{A}}^{01}_{1,2n+1} = n\dfrac{+\boldsymbol{RE}\left(Z^{(01)}_n\right)+\boldsymbol{RE}\left(Z^{(01)}_n\right)}{2}$
$\underline{\mathbb{A}}^{00}_{2,2n+1} = \dfrac{-\boldsymbol{RE}\left(Z^{(00)}_n\right)+\boldsymbol{RE}\left(Z^{(00)}_n\right)}{2}$	$\underline{\mathbb{A}}^{01}_{2,2n+1} = n\dfrac{-\boldsymbol{IM}\left(Z^{(01)}_n\right)+\boldsymbol{IM}\left(Z^{(01)}_n\right)}{2}$

In the end

when $0 = m < n$	$0 = m < n$
$\underline{\mathbb{A}}^{00}_{1,2n} = \boldsymbol{RE}\left(Z^{(00)}_n\right)$	$\underline{\mathbb{A}}^{01}_{1,2n} = n\boldsymbol{IM}\left(Z^{(01)}_n\right)$
$\underline{\mathbb{A}}^{00}_{1,2n+1} = -\boldsymbol{IM}\left(Z^{(00)}_n\right)$	$\underline{\mathbb{A}}^{01}_{1,2n+1} = n\boldsymbol{RE}\left(Z^{(01)}_n\right)$

- $i_\phi > 1$ **and** $j_\phi > 0$ In this case, it is enough to consider the general expressions in (B.5) by doing $n = 0$ but $2n = 1$. It leads to

when $m \geq n = 0$	$m \geq n = 0$
$\underline{\mathbb{A}}^{00}_{2m,1} = \dfrac{+\boldsymbol{RE}\left(Z^{(00)}_m\right) + \boldsymbol{RE}\left(Z^{(00)}_m\right)}{2}$	$\underline{\mathbb{A}}^{10}_{2m,1} = m\dfrac{+\boldsymbol{IM}\left(Z^{(10)}_m\right) + \boldsymbol{IM}\left(Z^{(10)}_m\right)}{2}$
$\underline{\mathbb{A}}^{00}_{2m+1,1} = \dfrac{-\boldsymbol{IM}\left(Z^{(00)}_m\right) - \boldsymbol{IM}\left(Z^{(00)}_m\right)}{2}$	$\underline{\mathbb{A}}^{10}_{2m+1,1} = m\dfrac{+\boldsymbol{RE}\left(Z^{(10)}_m\right) + \boldsymbol{RE}\left(Z^{(10)}_m\right)}{2}$
$\underline{\mathbb{A}}^{00}_{2m,2} = \dfrac{-\boldsymbol{IM}\left(Z^{(00)}_m\right) + \boldsymbol{IM}\left(Z^{(00)}_m\right)}{2}$	$\underline{\mathbb{A}}^{10}_{2m,2} = m\dfrac{+\boldsymbol{RE}\left(Z^{(10)}_m\right) + \boldsymbol{RE}\left(Z^{(10)}_m\right)}{2}$
$\underline{\mathbb{A}}^{00}_{2m+1,2} = \dfrac{-\boldsymbol{RE}\left(Z^{(00)}_m\right) + \boldsymbol{RE}\left(Z^{(00)}_m\right)}{2}$	$\underline{\mathbb{A}}^{10}_{2m+1,2} = m\dfrac{-\boldsymbol{IM}\left(Z^{(10)}_m\right) + \boldsymbol{IM}\left(Z^{(10)}_m\right)}{2}$

In the end

when $m \geq n = 0$	$m \geq n = 0$
$\underline{\mathbb{A}}^{00}_{2m,1} = \boldsymbol{RE}\left(Z^{(00)}_m\right)$	$\underline{\mathbb{A}}^{10}_{2m,1} = m\boldsymbol{IM}\left(Z^{(10)}_m\right)$
$\underline{\mathbb{A}}^{00}_{2m+1,1} = -\boldsymbol{IM}\left(Z^{(00)}_m\right)$	$\underline{\mathbb{A}}^{10}_{2m+1,1} = m\boldsymbol{RE}\left(Z^{(10)}_m\right)$

- $i_\phi = 1$ **and** $j_\phi = 0$ In this case, we simply have $\underline{\mathbb{A}}_{ij} = Z^{(00)}_0$.

List of Figures

1 Tokamak 11

1.1 Illustration of a fusion reaction involving hydrogen isotopes 18
1.2 Reactivity of the three more common reactions as a function of the energy 19
1.3 Tokamak scheme 23
1.4 Toroidal coordinates 23
1.5 Scheme of the magnetic field lines forming differente flux surfaces. At each surface ψ_θ is constant [28] 24
1.6 Scheme showing the main components of a a) limiter plasma and b)X-point plasma [29] 26
1.7 A scheme of the profiles for L and H-mode. The sharp gradient region, i.e., the pedestal can be clearly seen (the straight part of the red line)[32] 27
1.8 A scheme of the ELM dynamics: a relaxation of the transport barrier (pedestal) leads to a mass ejection and a possible collapsing of the pressure profile 29
1.9 Deformation caused by a kink instability occurring in a plasma column . . 30
1.10 Representation of the future tokamak [36] 31
1.11 Comparison between current and future tokamaks 32

3.1 Simple $1D$ convection-diffusion example: a)two element discretization and b)analytic solution 71
3.2 Examples of Bézier curves with $P_i \in \mathbb{R}^2$ 89
3.3 Bézier patch with $P_{ij} \in \mathbb{R}^3$ 90
3.4 Continuity between two adjacent Bézier patches 90
3.5 Scheme of the transformation from a curved element to the reference square element 92

4.1 Unaligned meshes (grey) and aligned ones (red) for both, limiter and divertor, configurations. 107
4.2 Coordinate points used to define the boundaries of the different domains of the plasma 107
4.3 Scheme with the differente domains of the plasma. The red line represents the separatrix wich is defined as $\mathcal{S}^{sep} = \mathcal{S}(\boldsymbol{\xi}^l_\times, \boldsymbol{\xi}_\times) \cup \mathcal{S}(\boldsymbol{\xi}_\times, \boldsymbol{\xi}_\times) \cup \mathcal{S}(\boldsymbol{\xi}_\times, \boldsymbol{\xi}^r_\times)$ 108
4.4 Example of a X-point grid (left) with the detail of the separation between two regions below and above the X-point (right) 110
4.5 Example of an aligned circular grid 111

4.6 Residual of the Grad-Shafranov equation $\overline{\mathcal{R}}_i^{GS}$ over the domain for two different grids. A polar grid (left) and a X-point one (right). They were obtained for stop criterion $\epsilon = 10^{-7}$. Around the singularities, however this value can go up to 10^{-3} for the X-point grid. This can be seen in more details in Figures (4.7) and (4.8) 113
4.7 Perturbation of the residual of the GS equation at the magnetic axis. Its maximum value is $\approx 10^{-8} < \epsilon$ 113
4.8 Perturbations of the equilibrium related ot the singularities of the grid: one at the magnetic axis (left) and one at the X-point (right). Their maximum residual is $\approx 10^{-3}$. 114
4.9 The norm of $\nabla\psi^{(0)}$ for both grids: poloidal (left) and X-point (right) . . . 114
4.10 Residual od the momentum equation, $\overline{\mathcal{R}}_i^{\boldsymbol{m}}$, for the poloidal (left) and X-point grids (right). The difference from the previous residual can be clearly seen. The perturbations, however were attenuated, for the poloidal case it is $\approx 10^{-9}$ and for the X-point case $\approx 5.10^{-4}$ 115
4.11 Orientation related to the nodes associated to the global mesh 116
4.12 Orientations related to the particular points of the grid: the magnetic axis (left) and the X-point (right) 116
4.13 Four different frames meeting at the X-point. As a consequence, this node has 16 degrees of freedom per variable 117
4.14 Perturbation around the center due to the derivatives conditions. Its maximum value is $\approx 10^{-8}$. 118
4.15 Residual od the momentum equation, $\overline{\mathcal{R}}_i^{\boldsymbol{m}}$ when the derivatives of all variables on the nodes belonging to the center are fixed as zero. In this case, the perturbation value goes from $\approx 5 \times 10^{-4}$ to $\approx 10^{-3}$ as it can be seen in the detail (right) 118
4.16 Density and magnetic fluw profiles used to initialize the circular plasma simulations 120
4.17 Density and potential flux profiles for the X-point plasma. The black lines represent the flux surfaces and the bold one, the separatrix. In the cut for the density (bottom-left), it is possible to identify the pedestal region by its sharp gradient. 121

5.1 Initial data for $3D$ computation with the density and magnetic stramlines (top) and perturbation of the first Fourier mode of the velocity (bottom). The perturbation has an order of magnitude of 10^{-12}. 131
5.2 Safety factor as a function of the minor radius r. Its minimum value is 0.73 at the center and its maximum is 1.6 at the edge. The sharp decreasing at the end is a consequence of getting near to the wall 131
5.3 Kinetic energy evolution of the Fourier modes for an internal kink simulation. The oscillations at the beginning are expected but not those at the end which are a result of numerical noise related to the singularity of the grid 132
5.4 The abolute value of the poloidal velocity (top) for two different times - $2.5 \times 10^4 t_A$ (left) and $3 \times 10^4 t_A$ (right)- shows that the instabilities are located close to the singularity at the center. The vector shape of the field for the same time-steps are shown (below). The red dotted line represents the surface $q = 1$ where $\psi = -0.229$ 133

5.5 Density profile at $t = 3 \times 10^4 t_A$ showing that the discontinuity at the center does not affect scalar quantities 134
5.6 Evolution of the kinetic energy when the derivatives at the center are restrained. The growth rate typical of the kink mode is observed 134
5.7 Velocity profiles without perturbation at the center. The thin layer around the surface $q = 1$ can be now observed. 135
5.8 Effect of the VMS stabilization on the spurioous waves. The fluctuations of the toroidal velocity (top) and the density (bottom) are shown for the case in which an artifical viscosity $\mu_{num} = 10^{-5}$ is applied (left) and anoher in whic the VMS strategy is implemented (right) 136
5.9 The efffects of the VMS stabilization: not implemented (left) and implemented (right). The details of the profile can be observed under this strategy. 137
5.10 Computed growth rate for the internal kink mode as a function of the Magnetic Reynolds number (S). The asymptotic behavior, $S^{-1/3}$ for S smaller than a threshold and $S^{-3/5}$ for larger S is expected and has been observed before 138
5.11 Dynamic of the kink mode for $S = 10^8$ using semi-linear modeling (when the mode $n = 0$ is assumed to be constant) and fully nonlinear modeling. The evolution of ψ (top) and the vertical component of the velocity v_Z (bottom) are shown for $n = 0$ (left) and $n = 1$ ($cos(\phi)$) (right). 139
5.12 Evolution of the density profiles during the motion of the plasma column. $2D$ plot of the poloidal plane located at $\phi = 0$ 140
5.13 Kink structure comparison for $S = 10^5$ (left) and $S = 10^8$ (right). The width of the layers depends on the magnetic Raynolds number, going from 10^{-1}(left) to 3×10^{-2} (right) 141
5.14 Reconnection of the magnetic flux surfaces ψ. 142

6.1 Scheme of the sheath formation around a plasma boundary 146
6.2 3D magnetic field lines, plasma density and velocity field near the divertors (left) and a poloidal cut showing the cross section of the reactor (right) 150
6.3 Details of the velocity field near to the divertor plates when Bohm boundary conditions are taken into account 151
6.4 Velocity profile written in terms of the Mach number M at $t = 1$ 151
6.5 Evolution of the kinetic energy for the harmonic $n = 0$ when Bohm boundary conditions are applied 152

Bibliography

[1] A.N. Brooks and T.J.R. Hughes. Streamlineupwind/Petrov-Galerkin formulation for convection dominanted flows with particular emphasis on the incompressible navier-stokes equations. *Computer Methods in Applied Mechanics and Engineering*, **32**(1-3):199–259, 1982.

[2] T.J.R. Hughes. A simple scheme for developing upwind finite elements. *Journal for Numerical Methods in Engineering*, **12**(9):1359–1365, 1978.

[3] J. von Neumann and R.D. Richtmyer. A method for the numerical calculations of hydrodynamical schocks. *J.Appl.Phys.*, (21):232–238, 1950.

[4] M.L Wilkins. Calculation of elastic plastic flow. *Methods in Computational Physics*, (3), 1964.

[5] M.L Wilkins. Use of artificial viscosity in multidimensional fluid dynamic calculations. *J. Comput. Phys*, (36):381–403, 1980.

[6] S. Godunov, A. Zabrodine, M. Ivanov, A. Kraiko, and G. Prokopov. Résolution numérique des problèmes multidimensionnels de la dynamique des gaz. *Mir*, 1979.

[7] C.R. Sovinec, A.H. Glasser, T.A. Gianakon, D.C. Barnes, R.A. Nebel, S.E. Kruger, D.D. Schnack, A. Plimpton, S.J. Terditi, M.S. Chu, and Nimrod team. Nonlinear magnetohydrodynamis simulation using high-order finite elements. *Journal of Computational Physics*, (195):355–386, 2004.

[8] J. Breslau, N. Ferraro, and S. Jardin. Some properties of the M3D-C1 form of the three-dimensional magnetohydrodynamics equations. *Phys Plasmas*, 2009.

[9] O. Czarny and G. Huysmans. Bézier surfaces and finite elements for MHD simulations. *Journal of Computational Physics*, **227**(16):7423–7445, 2008.

[10] G. Huysmans, S. Pamela, E. van der Plas, and P. Ramet. Non-linear MHD simulations of edge localized modes (ELMs). *Plasma Physics and Controlled Fusion*, **51** (12), 2009.

[11] D.S. Harned and W. Kerner. Semi-implicit method for three-dimensional compressible magnetohydrodynamic simulation. *Journal of Computational Physics*, **60**(1): 62–75, 1985.

[12] S. Jardin. Review of implicit methods for the magnetohydrodynamic description of magnetically confined plasmas. *Journal of Computational Physics*, **231**(3):822–838, 2012.

[13] H. Lutjens and J.F. Luciani. Xtor-2F: A fully implicit Newton-Krylov solver applied to nonlinear 3D extended MHD in tokamaks. *Journal of Computational Physics*, **229**(21):8130–8143, 2010.

[14] T. Hughes, M. Mallet, and A. Mizukami. A new finite element formulation for computational fluid dynamics: II beyond SUPG. *Computer methods in Applied Mechanics and Engineering*, **54**:341–355, 1986.

[15] T.J.R. Hughes, G. Scovazzi, and T. Tezduyar. Stabilzed methods for compressible flows. *Journal of Scientific Computing*, **43**:343–368, 2010.

[16] J. Donea, S. Giuliani, H. Laval, and L. Quartapelle. Time-accurate solution of advection-diffusion problems by finite elements. *Computer Methods in applied Mechanics and Engineering*, **45**(1-3):123–145, 1984.

[17] J. Donea, L. Quartapelle, and V. Selmin. An analysis of time discretization in the finite element solution of hyperbolic problems. *Journal of Computational Physics*, **70**(2):463–499, 1987.

[18] D. Ambrosi and L. Quartapelle. A Taylor-Galerkin method for simulating nonlinear dispersive water waves. *Journal of Computational Physics*, **146**(2):546–569, 1998.

[19] N. Ferraro and S. Jardin. Calculations of two-fluid magnetohydrodynamic axyssimmetric steady-states. *Journal of Computational Physics*, **228**(20):7742–7770, 2009.

[20] P. Hénon, P. Ramet, and J. Roman. Pastix: a high-performance perallel direct solver for sparse symmetric positive systems. *Parallel Computing*, **28**(2):301–321, 2002.

[21] Energey Information Administration (EIA). *International Energy Outlook, 2016*. 2016.

[22] A Einstein. Ist die Trägheit eines Körpers von seinem Energieinhalt abhängig? *Annalen der Physik*, **18**:639–641, 1905.

[23] H. Bethe and R Bacher. Nuclear Physics. A: Stationary States of Nuclei. *Reviews of Modern Physics*, **8**(2):8–229, 1936.

[24] H. Bethe. Nuclear Physics. B: Nuclear Dynamics, Theoretical. *Reviews of Modern Physics*, **9**(2):8–229, 1937.

[25] H. Bethe and R Bacher. Nuclear Physics. C: Nuclear Dynamics, Experimental. *Reviews of Modern Physics*, **9**(2):8–229, 1937.

[26] C.F. von Weizsäcker. On transformations of elements in the interiors of stars. I). *Physikalische Zeitschrift*, **38**:176–191, 1937.

[27] J.D. Lawson. Some criteria for a power producing thermonuclear reactor. *Proceedings of the Physical Society, section B*, **70**(1,6), 1957.

[28] J. Ball, F.I. Parral, M. Barnes, W. Dorland, G.W. Hammett, and N.F. Rodrigues, P. Loureiro. Intrinsic momentum transport in updown asymmetric tokamaks. *Plasma Physics and Controlled Fusion*, **56**(9), 2014.

[29] J. Ongena, R. Koch, R. Wolf, and H. Zohm. Magnetic-confinement fusion. *Nature Physics*, **12**:398–410, 2016.

[30] F. *et al.* Wagner. Regime of improved confinement and high beta in neutral-beam-heated divertor discharges of the ASDEX tokamak. *Phys. Rev. Letters*, **49**:1408, 1982.

[31] F. Wagner. A quarter century of H-mode studies. *Plasma Physics and Controlled Fusion*, **49**(12B), 2007.

[32] T. *et al.* Koabyashi. Experimental identification of electric field excitation mechanisms in a structural transition of tokamak plasmas. *Scientific reports*, **6**, 2016.

[33] S. Pamela. Simulation magnéto-hydro-dynamique des edge localized modes dans un tokamak. PhD Thesis, 2010.

[34] F. Orain, M. Bécoulet, J. Morales, G.T.A. Huijsmans, G. Dif-Pradalier, M. Hoelzl, S. Garbet, X.and Pamela, E. Nardon, and C. Passeron. Non-linear MHD modeling of edge localized mode cycles and mitigation by resonant magnetic perturbations. *Plasma Physics and Controlled Fusion*, **57**(1), 2014.

[35] Bussac;M., R. Pellat, D. Edery, and J. Soule. Internal kink modes in toroidal plasmas with circular cross sections. *Phys. Rev. Lett.*, **35**:1638, 1975.

[36] ITER webpage. URL https://www.iter.org.

[37] H. Alfven. Existence of electromagnetic-hydrodynamic waves. *Nature*, **150**(3805): 405–406, October 1942.

[38] H. Alfven. On the existence of electromagnetic-hydrodynamic waves. *Arkiv f. Mat., Astron. o. Fys.*, **29B**(2):1–7, 1943.

[39] H.R. Strauss, R. Paccagnella, and J. Breslau. Wall forces produced during ITER disruptions. *Physics of Plasmas*, **17**(8), 2010.

[40] L.E. Sugiyama and H.R. Strauss. Magnetic X-points, edge localized modes, and stochasticity. *Physics of Plasmas*, **17**(6), 2010.

[41] B.D. Dudson, M.V. Umansky, X.Q. Xu, P.B. Snyder, and H.R. Wilson. Bout++:A framework for parallel plasma fluid simulations. *Computer Physics Communications*, **180**(9):1467–1480, 2009.

[42] P. Bellan. Fundamentals of plasma physics. *Cambridge University Press*, 2006.

[43] S.I. Braginsky. Reviews of plasma physics. 1965.

[44] F. Chen. Introduction to plasma physics and controlled fusion. *Plenum Press*, 1984.

[45] E.M. Epperlein and M.G. Haines. Plasma transport coeffcients in a magnetic field by a direct numerical solution of the Fokker-Planck equation. *Physics of fluids*, **29** (4):1029–1041, 1986.

[46] H. Grad. 1949.

[47] W.B. Thompson. *An introduction to plasma physics.* Pergamon London, 1962.

[48] M. Martin. Modlisations fluides pour les plasmas de fusion : approximation par lments finis C1 de Bell. PhD Thesis, 2013.

[49] J.D. Huba. NRL Plasma Formulary, 2013.

[50] A. Dedner, F. Kemm, and D. Kröner. Hyperbolic divergence cleaning for MHD equations. *Journal of Computational Physics*, **175**(2):645–673, 2002.

[51] J. Brackbill. Fluid modeling of magnetized plasmas. *Space Science Reviews*, **42**: 153–167, 1985.

[52] J. Brackbill and D. Barnes. The effect of nonzero product of magnetic gradient and B on the numerical solution of magnetohydrodynamics equations. *Journal of Computational Physics*, **35**:426–430, 1980.

[53] D.S. Balsara and D.S. Spicer. A staggered mesh algorithm using high-order Godunov fluxes to ensure solenoidal magnetic fields in magnetohydrodynamic simulations. *Journal of Computational Physics*, **149**(2):270–292, 199.

[54] J. Vides. Godunov-type schemes for hydrodynamic and magnetohydrodynamic modeling. PhD Thesis, 2014.

[55] J.P. Freidberg. Ideal magnetohydrodynamics.

[56] J.D. Lawson. Some criteria for a power producing thermonuclear reactor. *Proceedings of the Physical Society*, Section B **70**(1,6), 1957.

[57] K.G. Powell. An approximate Riemann solver for the magnetohydrodynamics (that works in more than one dimension). *ICASE Report, NASA*, pages 92–94, 1994.

[58] A. Jameson. Eigenvalues, eigenvectors and symmetrization of the magnetohydrodynamic. *AFOSR, Grantees and contractors meeting*, 2006.

[59] M Brio and C.C Wu. An upwind differencing scheme for the equations of ideal magnetohydrodynamics. *Journal of computational physics*, **75**, 1988.

[60] H.R. Strauss. Nonlinear three-dimensional magnetohydrodynamics of noncircular tokamaks. *Physics of Fluids*, **19**(1):134–140, 1976.

[61] S. Briguglio, F. Zonca, and G. Vlad. Hybrid magnetohydrodynamic-particle simulation of linear and nonlinear evolution of Alfven modes in tokamaks. *Physics of Plasmas*, **5**(9):3287–3301, 1998.

[62] R. Izzo. Effects of toroidicity on resistive tearing modes. *Physics of Fluids*, **19**(1): 134–140, 1983.

[63] H. R. Strauss. Dynamics of high beta tokamaks. *Physics of Fluids*, **20**(8):1354–1360, 1977.

[64] G.T.A. Huysmans and O. Czarny. MHD stability in X-point geometry: simulation of ELMs. *Nuclear Fusion*, **47**(7), 2007.

[65] H. Grad and H. Rubin. Hydromagnetic equilibria and force-free fields. *2nd UN Conf. on the Peaceful Uses of Atomic Energy*, **31**, 1958.

[66] V.D. Shafranov. Plasma equilibrium in a magnetic field. *Reviews of Plasma Physics*, **2103**, 1966.

[67] D. Biskamp. Nonlinear magnetohydrodynamics. *Cambridge University Press*, 1997.

[68] J.P. Freidberg. Plasma physics and fusion energy. *Cambridge University Press*, 2007.

[69] J. Wesson. Tokamaks. *Oxford University Press*, 2004.

[70] T.J.R. Hughes. Multiscale phenomena: Green's functions, the Dirichlet-to-Neumann formulation, subgrid scale methods, bubbles and the origins of stabilized methods. *Computer methods in Applied Mechanics and Engineering*, **12**(1-4): 387–401, 1995.

[71] R. Codina. Analysis of a stablized finite element approximation of the Oseen equations using orthogonal subscales. *Applied Numerical Mathematics*, **58**(3):264–283, 2008.

[72] R. Corida and J Blasco. Analysis of a pressure stabilized finite element approximation of the stationary Navier-Stokes equations. *Numerische Mathematik*, **87**:59–81, 2000.

[73] R. Codina. On stabilized finite element methods for linear systems of convection-diffusion-reaction equations. *Computer methods in Applied Mechanics and Engineering*, **188**(1-3):61–82, 2000.

[74] T.J.R. Hughes, G. Scovazzi, and L.P. Franca. *Multiscale and stablized methods. Chapter.* John Wiley and Sons, Ltd, 2004.

[75] I. Christie, D. Griffiths, A.R. Mitchell, and O. Zienkiewicz. Finite element methods for second order differential equation with significant first derivatives. *Internat. J. Numer. Methods Engrg.*, **10**:1389–1396, 1976.

[76] K. Jansen, S. Collis, C. Whiting, and F. Shaki. A better consistency for low-order stabilized finite elements methods. *Computer methods in applied mechanics and engineering*, **174**:153–170, 1999.

[77] C. Whiting, K. Jansen, and S. Dey. Hierarchical basis for stabilized finite elements methods for compressible flows. *Computer methods in applied mechanics and engineering*, **192**:5167–5185, 2003.

[78] T. Tezduyar and M. Senga. Stabilization and shock-capturing parameters in SUPG formulation of compressible flows. *Computer methods in applied mechanics and engineering*, **195**:1621–1632, 2006.

[79] T.J. Barth and D.C. Jespersen. The design and applicatioin of upwind schemes on unstructured meshes. *27th AIAA Aerospace Sciences Meeting, Reno Nevada (USA)*, **Paper 89**, 1989.

[80] A. Soulaimani and M. Fortin. Finite element solution of compressible viscous flows using conservative variables. *Computer methods in applied mechanics and engineering*, **118**:319–350, 1994.

[81] A.B.H. Ali and A. Soulaimani. An unstructured finite element method for solving the compressible RANS equations and the Spalart-Allmaras turbulence model. *Computer methods in applied mechanics and engineering*, **199**:2261–2272, 2010.

[82] M. Billaud, G. Gallice, and B. Nkonga. Stabilization and shock-capturing parameters in SUPG formulation of compressible flows. *Computer methods in applied mechanics and engineering*, **200**(9-12):1272–1290, 2011.

[83] C. Wervaecke, H. Beaugendre, and B. Nkonga. A fully coupled RANS Spalart-Allmaras SUPG formulation for turbulent compressible flows on stretched-unstructured grids. *Computer methods in applied mechanics and engineering*, **233-236**:109–122, 2012.

[84] R. Abgrall. Essentially non-oscillatory residual distribution schemes for hyperbolic problems. *Journal of Computationla Physics*, **214**:773–808, 2006.

[85] R.M. Beam and R.F. Warming. Alternating direction implicit methods for parabolic equations with mixed derivatives. *SIAM J. Sci. Stat. Comput*, (1):131–159, 1980.

[86] S.C. Jardin. A triangular finite element with first-order continuity applied to fusion MHD applications. *Journal of Computational Physics*, (200):133–152, 2004.

[87] S.N. Bernstein. Démonstration du théorème de Weierstrass, fondé sur le calcul des probabilités. *Communications of the Society of Mathematics*, 13(2), 1912-1913.

[88] D. Liu. C1 continuity conditions between two adjacent rational Bézier surface patches. *Computer aided geometric design*, (7):151–163, 1990.

[89] H.P. Furth, J. Killeen, M.N. Rosenbluth, and B. Coppi. IAEA, vienna. *Plasma Phys. and Controlled Nucl. Fusion Research*, **1**, 1965.

[90] B. Coppi, R. Galvao, R. Pellat, M. Rosenbluth, and P. Rutherford. nb. *Fiz. Plazmy*, **2**(961), 1976.

[91] J.W.S. Blokland, B. van der Holst, R. Keppens, and J.P. Goedbloed. Phoenix: MHD spectral code for rotating laboratory and gravitating astrophysical plasmas. *J. Comp. Phys.*, **226**:509–533, 2007.

[92] J.P. Goedbloed, A.J.C. Belien, B. van der Holst, and R. Keppens. Unstable continuous spectra of transonic axissymmetric plasmas. *Phys. Plasmas*, **11**:28–54, 2004.

[93] R.J. Hastie, T.C. Hender, B.A. Carreras, L.A. Charlton, and J.A. Holmes. Stability of ideal and resistive internal kink modes in toroidal geometry. *Physics of FLuids*, **30**(6):1756–1766, 1987.

Éléments finis stabilisés VMS appliqués aux modèles magnétohydrodynamiques (MHD) des plasmas de fusion

L'objectif principal de cette thèse concerne la mise en oeuvre d'une méthode d'éléments finis stabilisés pour la simulation des plasmas de fusion. Pour cela, nous avons d'abord dérivé les modèles magnétohydrodynamiques depuis le modèle cinétique. Les modèles MHD sont généralement utilisés pour simuler les instabilités macroscopiques des plasmas. Nous nous sommes concentrés sur le modèle de la MHD complète. Ensuite, l'approche numérique est décrite dans le cadre de la stabilisation Varationnelle Multi-échelles (VMS). Cette stabilisation vient ajouter un terme à la formulation faible pour mimer les effets des échelles non-résolues sur celles résolues. Si les effets de ces sous-échelles ne sont pas pris en compte lorsque l'on traite des écoulements dominés par convection, comme dans le cadre des plasmas de fusion, le schéma numérique conduit à des résultats non-physiques. Une étude détaillée de l'instabilité de «kink interne» a été faite ainsi qu'une étude préliminaire des plasmas avec point-X ayant pour but la validation du schéma numérique développé ici.

Mots-clés : Magnétohydrodynamique, Éléments finis stabilisés, Stabilisation variationnelle multi-échelles (VMS), Intégration temporelle implicite, Potentiel vecteur magnétique, Kink interne

---

Variational Multi-Scale stabilized Finite Elements for the magnetohydrodynamic models of fusion plasmas

The main objective of this thesis concerns the implementation of a robust stabilized finite element method for simulating fusion plasmas. For that, we first derive the magnetohydrodynamic models from the kinetic model. MHD models are generally used for macroscopic simulations of plasma instabilities. We concentrate ou efforts on the full MHD model. Next, the numerical approach is described in the context of the Variational Multi-Scale (VMS) stabilization. This stabilization comes to add a term to the weak formulation to mimics the effects of the unresolved scales over the coarse scales. If the effects of these sub-scales are not taken into account when dealing with fluxes dominated by convection, as it is the cases for fusion plasmas, the numerical scheme can lead to unphysical results. A detailed study of the resistive internal kink instability has been done as well as an introductory study of the so called X-point plasmas in order to validate the numerical scheme developed here.

Keywords: Magnetohydrodynamics, Stabilized finite elements, Variational multi-scale stabilization, Implicit time integration, Magnetic vector potential, Internal kink mode